NASA TECHNICAL NOTE

NASA TN D-7526

NASA TN D-7526

WIND-TUNNEL INVESTIGATION OF A LARGE-SCALE SEMISPAN MODEL WITH AN UNSWEPT WING AND AN UPPER-SURFACE BLOWN JET FLAP

by Charles C. Smith, Jr., Arthur E. Phelps III, and W. Latham Copeland

Langley Research Center and
Langley Directorate, U.S. Army Air Mobility R&D Laboratory
Hampton, Va. 23665

NATIONAL AERONAUTICS AND SPACE ADMINISTRATION • WASHINGTON, D. C. • FEBRUARY 1974

1. Report No.	2. Government Accession No.	3. Recipient's Catalog No.
NASA TN D-7526		

4. Title and Subtitle	5. Report Date
WIND-TUNNEL INVESTIGATION OF A LARGE-SCALE SEMISPAN MODEL WITH AN UNSWEPT WING AND AN UPPER-SURFACE BLOWN JET FLAP	February 1974
	6. Performing Organization Code
7. Author(s) Charles C. Smith, Jr., Arthur E. Phelps III (Langley Directorate, U.S. Army Air Mobility R&D Laboratory), and W. Latham Copeland	8. Performing Organization Report No. L-9137
	10. Work Unit No. 760-61-02-01
9. Performing Organization Name and Address NASA Langley Research Center Hampton, Va. 23665	11. Contract or Grant No.
	13. Type of Report and Period Covered Technical Note
12. Sponsoring Agency Name and Address National Aeronautics and Space Administration Washington, D.C. 20546	14. Sponsoring Agency Code

15. Supplementary Notes

16. Abstract

An investigation of the static longitudinal aerodynamic characteristics of a large-scale semispan model with an unswept wing and an upper-surface blown jet flap for lift augmentation was conducted in the Langley full-scale tunnel. The wing had an aspect ratio of 7.8 (3.9 for the semispan) and a simulated turbofan engine mounted ahead of and above the wing in a nacelle with a rectangular-exit nozzle. The flap system had three spanwise flap segments: an inboard plain flap located behind the engine and having a large radius of curvature to provide a smooth upper surface to enhance the turning of the jet sheet, a double-slotted midspan flap, and a drooped aileron equipped with blowing boundary-layer control. The wing was also equipped with a full-span leading-edge Krueger flap with blowing boundary-layer control. In addition to the aerodynamic measurements, noise measurements were also included in the investigation for positions above and below the wing.

17. Key Words (Suggested by Author(s))	18. Distribution Statement
Upper-surface blown jet flap Powered lift STOL configurations High-lift devices	Unclassified – Unlimited STAR Category 02

19. Security Classif. (of this report)	20. Security Classif. (of this page)	21. No. of Pages	22. Price*
Unclassified	Unclassified	144	$4.50

*For sale by the National Technical Information Service, Springfield, Virginia 22151

WIND-TUNNEL INVESTIGATION OF A LARGE-SCALE SEMISPAN MODEL WITH AN UNSWEPT WING AND AN UPPER-SURFACE BLOWN JET FLAP

By Charles C. Smith, Jr., Arthur E. Phelps III,* and W. Latham Copeland
Langley Research Center

SUMMARY

An investigation of the static longitudinal aerodynamic characteristics of a large-scale semispan model with an unswept wing and an upper-surface blown jet flap for lift augmentation was conducted in the Langley full-scale tunnel. The wing had an aspect ratio of 7.8 (3.9 for the semispan) and a simulated turbofan engine mounted ahead of and above the wing in a nacelle with a rectangular-exit nozzle. The flap system had three spanwise flap segments: an inboard plain flap located behind the engine and having a large radius of curvature to provide a smooth upper surface to enhance the turning of the jet sheet; a double-slotted midspan flap; and a drooped aileron equipped with blowing boundary-layer control (BLC). The wing was also equipped with a full-span leading-edge Krueger flap with blowing BLC. In addition to the aerodynamic measurements, noise measurements were also included in the investigation for positions above and below the wing.

The results of the investigation showed that the upper-surface blown jet-flap concept is effective for producing the high lift necessary for powered-lift operation and the performance is generally comparable with that of other externally blown powered-lift concepts. Maximum lift coefficients of about 9.5 were obtained for thrust coefficients of 4 when partial-span trailing-edge flaps were used with no BLC. The effects of Reynolds number were generally small for powered-lift conditions. Varying the engine nozzle geometry did not significantly alter the aerodynamic characteristics of the model. Full-span trailing-edge flaps were much more effective for achieving good high-lift performance than partial-span flaps alone. The use of leading-edge BLC markedly increased the lift at high angles of attack and generally improved the overall aerodynamic performance of the model.

The shielding effects of the wing resulted in significantly lower overall noise levels being observed below the wing than above the wing. An observer located beneath the airplane would detect little effect on the overall noise levels due to fan-nozzle geometry. The effects of forward airspeed on the noise were beneficial but relatively small.

---

*Langley Directorate, U.S. Army Air Mobility R&D Laboratory.

INTRODUCTION

Considerable interest is being shown in the upper-surface blown (USB) jet-flap concept as a means of achieving the high lift necessary for efficient powered-lift operation and for reducing the noise associated with powered-lift systems. This interest comes about mainly from recent aerodynamic and noise studies in which the concept showed promising results in both these areas. (See refs. 1 to 4.) The USB jet flap produces high lift by exhausting all the jet-engine efflux above the wing in such a manner that it becomes attached to the wing and turns downward over a trailing-edge flap. Although the results of preliminary work with the USB jet flap have been very encouraging, all this work has been conducted at very low scale and the possibility exists that there might be large Reynolds number effects which could significantly alter conclusions based on the preliminary small-scale tests. The present investigation was undertaken, therefore, to provide fundamental information an the effects of Reynolds number on the overall performance of the USB jet-flap concept. The investigation also included tests to determine the effects of engine nozzle geometry, trailing-edge flap span, and blowing boundary-layer control (BLC) on the aerodynamic characteristics of the model.

Prior investigations have indicated that location of the nozzle above the wing resulted in a reduction in the noise below the wing. (See refs. 3 and 4.) In order to determine the effects of wing shielding, engine nozzle geometry, and free-stream velocity on the noise characteristics of the model, the present investigation also included noise measurements from positions above and below the wing.

The model had a full-span leading-edge Krueger flap equipped with BLC, and three spanwise trailing-edge flap segments: an inboard plain flap located behind the engine and having a large radius of curvature, a double-slotted midspan flap, and a drooped aileron equipped with blowing BLC. The model was equipped with a simulated engine which consisted of four small-diameter fans mounted in a common nacelle. Each fan had its own inlet but exhausted into a common duct which could be fitted with a rectangular nozzle having an aspect ratio of either 2, 4, or 6. The internal contour of the nozzle exit was designed so that the exhaust flow was deflected slightly downward toward the top of the wing to insure that the jet sheet was attached to the upper surface of the wing. In the present investigation, the aerodynamic tests were conducted for four different trailing-edge flap deflections (0°, 20°, 40°, and 60°) and for several different engine thrust coefficients over an angle-of-attack range through the stall. In addition, noise tests were made for several wind-tunnel speeds, two nozzle aspect ratios $(A_n = 2 \text{ and } 6)$, a flap deflection of 60°, and an angle of attack of 0°.

SYMBOLS

The data are referred to the wind-axis system. (See fig. 1.) The origin of the axes was located to correspond to a center-of-gravity position of 0.40 mean aerodynamic chord on the fuselage horizontal reference line.

In order to facilitate international usage of data, dimensional quantities are presented both in the International System of Units (SI) and the U.S. Customary Units. The measurements and calculations were made in the U.S. Customary Units. Equivalent dimensions were determined by using the conversion factors given in reference 5.

A_n engine nozzle aspect ratio, $\frac{\text{Nozzle width}}{\text{Nozzle height}}$

c local wing chord, m (ft)

$\bar{c}$ wing mean aerodynamic chord, m (ft)

C_D drag coefficient, $\frac{F_D}{qS}$

C_L lift coefficient, $\frac{F_L}{qS}$

$(C_L)_{C_\mu=0}$ lift coefficient for zero thrust, $\frac{F_L}{qS}$

$C_{L,\Gamma}$ jet-induced circulation lift coefficient, $\frac{F_{L,\Gamma}}{qS}$

C_m pitching-moment coefficient, $\frac{M_Y}{qS\bar{c}}$

C_μ gross-thrust coefficient of engines, $\frac{T}{qS}$

$C_{\mu,a}$ thrust coefficient of boundary-layer control system for drooped aileron

$C_{\mu,le}$ thrust coefficient of boundary-layer control system for wing leading edge

D_e equivalent diameter of engine exhaust nozzle (diameter of a circle which has same area as engine nozzle), m (ft)

F_A axial force, N (lb)

F_D	drag force, N (lb)
F_L	lift force, N (lb)
$F_{L,\Gamma}$	jet circulation lift, N (lb)
F_N	normal force, N (lb)
M_Y	pitching moment, m-N (ft-lb)
q	free-stream dynamic pressure, N/m^2 (lb/ft^2)
R	Reynolds number based on $\bar{c}$
S	area of semispan wing, m^2 (ft^2)
T	static thrust force, N (lb)
X,Z	body reference axes
X_w,Z_w	wind reference axes
α	angle of attack, deg (see fig. 1)
δ_a	aileron droop angle, deg
δ_f	double-slotted flap deflection, deg (see fig. 3(c))
δ_j	static-thrust jet deflection angle, $\tan^{-1}\frac{F_N}{F_A}$
δ_v	vane deflection, deg (see fig. 3(c))
η	static-thrust recovery efficiency, $\frac{\sqrt{F_A{}^2 + F_N{}^2}}{T}$

ABBREVIATIONS

BLC	boundary-layer control
USB	upper-surface blown

MODEL AND APPARATUS

Tests were conducted on the semispan, high-wing, USB model shown in figure 2. The model was assembled largely from components of an existing light airplane to provide some early information on the effects of Reynolds number for this type of powered-lift system.

Dimensional data for the model are given in table I, and details of the high-lift devices are shown in figure 3. A full-span Krueger flap with chord equal to 20 percent of the wing chord and a slot for BLC blowing (see fig. 3(a)) was fitted to the leading edge of the wing and was set at a deflection of 70° for all but the clean-wing tests. The coordinates of the Krueger flap are given in table II. For the high-lift tests, the trailing edge of the wing consisted of three spanwise elements: an inboard plain flap located behind the engine and having a large radius of curvature, a midspan double-slotted flap, and an aileron used as an outboard flap at the wing tip. The inboard flap was formed from a single sheet of metal curved so that, in most cases, it conformed to the envelope of the upper surface of the double-slotted flap and provided a smooth, large-radius, continuously curved upper surface to enhance the turning of the engine exhaust jet. (See figs. 2 and 3(b).) The flap extended from the side of the fuselage to a station 0.65 nozzle width outboard of the nozzle centerline. In some tests, however, the outboard end of this flap segment was extended to 0.75 nozzle width. For some special tests, the radius of the flap for the 60° flap deflection was increased, as shown at the top of figure 3(b). The coordinates of the double-slotted flap are given in table III, the gaps and overlaps are given in table IV, and the system used for indicating the flap deflections is shown in figure 3(c). The aileron was equipped with BLC, as indicated in figure 3(a).

The general arrangement of the engine simulator package and exhaust nozzles is shown in figure 4(a). Power was supplied by four 20.3-cm-diameter (8.0-in.) fans mounted in a common nacelle and driven by compressed nitrogen. Each fan had its own inlet, but exhausted into a common duct to which various exhaust nozzles could be attached. The nozzles were rectangular and had nozzle aspect ratios (exit width-to-height ratios) of 2, 4, and 6; and each nozzle had an exit area of 0.155 m^2 (1.67 ft^2). The nozzles were contoured to deflect the flow downward toward the top of the wing. Internal coordinates for the nozzles used in the investigation are presented in figure 4(b). The upper-surface deflection angle was not the same for the three nozzles. The aspect-ratio-2 nozzle was tested both with and without deflectors, which are shown in figure 4(c).

The instrumentation used in the noise measurements consisted of four 1/4-inch condenser-type microphones which had frequency response flat to within ±2 dB from 5 Hz to 70 kHz, preamplifiers, and a multichannel magnetic tape recorder. The overall system

response from 20 Hz to 40 kHz was flat within ±2 dB. Windscreens were also used on the microphones. The microphone orientation and locations with respect to the test model are indicated in figure 5. The microphones were located approximately 3.05 m (10 ft) above and below the model surfaces and about 1.22 m (4 ft) above the floor in a plane which contained the centerline of the engine nozzle. The outputs of all the microphones were recorded simultaneously on a multichannel magnetic tape recorder for each test. The sound measurement system was calibrated by means of a discrete-frequency calibrator before and after the tests. The data tapes were processed to provide overall sound-pressure levels and frequency spectra.

TESTS AND PROCEDURES

Tests at Zero Forward Speed

In preparation for testing, calibration of the simulated-engine static thrust over the thrust range was made for each nozzle $(A_n = 2, 4, \text{ and } 6)$ and for the aspect-ratio-2 nozzle with two deflectors. (See fig. 4(c).) The thrust calibrations of the simulated engine were obtained as a function of fan rotational speed with the nacelle mounted on the wing and the trailing-edge flaps removed. The static-thrust calibrations were made by bringing all four fans in the nacelle to the same speed, and computing the thrust as the resultant of the measured normal and axial forces $\left(T = \sqrt{F_N{}^2 + F_A{}^2}\right)$.

Static-thrust jet deflection angles and recovery efficiencies were determined from measurements of normal and axial forces made at two values of thrust and for flap settings of 20°, 40°, and 60°. Tests to determine the effects of nozzle geometry and inboard-flap span and radius were made for a flap deflection of 60° only. In addition, the aspect-ratio-2 nozzle was tested with and without deflectors. The static thrust used in computing recovery efficiency was taken directly from the engine calibrations at the appropriate fan speed.

Aerodynamic Tests

Wind-on tests with power were run by setting the engine rotational speed to give the desired thrust and holding this speed constant over the angle-of-attack range. Previous investigations have indicated that forward speeds of the magnitude used in the present tests had a negligible effect on the gross thrust of these fans.

Unless otherwise noted in the text and/or figures, the wind-on tests were made with the following conditions: the aileron not drooped and no aileron BLC, no wing leading-edge BLC, a nozzle aspect ratio of 4, an inboard-flap span of 0.65 nozzle width outboard of the nozzle centerline, an inboard-flap radius of curvature of 38.1 cm (15 in.), the

trailing-edge flap deflected 60°, and the leading-edge Krueger flap deflected 70°. The tests were made over an angle-of-attack range from -4° to 41° and a gross-thrust-coefficient range from 0 to 5. All the wind-on tests except the tests to study the effects of Reynolds number were made by setting a nominal dynamic pressure of 79 N/m^2 (1.65 lb/ft^2), which corresponds to a velocity of 11.3 m/sec (37 ft/sec) and a Reynolds number, based on the wing mean aerodynamic chord, of 1.2×10^6. Jet-boundary interference corrections caused moderate adjustments to these nominal values, and the corrected values were used in reducing the data. The parameters varied in the wind-on tests are given in the following sections.

Reynolds number.- For the Reynolds number study, the model was tested at free-stream dynamic pressures ranging from 11.9 to 575 N/m^2 (0.25 to 12 lb/ft^2), which correspond to airspeeds of 4.6 to 31 m/sec (15 to 100 ft/sec), respectively. The range of Reynolds number, based on the mean aerodynamic chord of the wing, for the test was from 0.45×10^6 to 3.1×10^6.

Boundary-layer control.- Tests to determine the effect of BLC were made by varying the leading-edge blowing only. The BLC for the aileron was used only when the aileron was drooped, and the blowing was the lowest possible level required to achieve flow attachment over the deflected aileron $\left(C_{\mu,a} = 0.04\right)$. The thrust coefficients of the BLC systems were determined by measuring the static thrust force produced by the BLC slots for each system in the wind-off condition.

Nozzle geometry.- The effect of varying nozzle geometry was determined for the flap deflection of 60° only and was accomplished by replacing the aspect-ratio-4 nozzle with nozzles having aspect ratios of 2 and 6. The aspect-ratio-2 nozzle was tested with two different deflectors. (See fig. 4(c).)

Flaps.- Tests to determine the effect of wing trailing-edge flaps on the longitudinal aerodynamic characteristics of the model were made for flap deflections of 0°, 20°, 40°, and 60° over the angle-of-attack and thrust-coefficient ranges with a leading-edge Krueger flap deflected 70°. Included in the investigation were tests to determine the effect of the drooped blown aileron in combination with the trailing-edge flap. The effects of the span of the inboard plain flap on the longitudinal characteristics of the model were determined by testing flaps with spans of 0.65 and 0.75 nozzle width outboard of the engine centerline. A few tests were made with the Krueger flap removed to provide fundamental data for determining the effects of the Krueger flap.

Noise Tests

In all the noise-measuring tests the engine rotational speed was held constant at 15 000 rpm, which provided an average thrust of 1290 N (290 lb). The wing trailing-edge flaps were deflected 60°.

Effect of free-stream velocity.- In order to determine the effect of free-stream velocity on the noise characteristics of the model, noise measurements were made for an angle of attack of 0° and free-stream velocities of 7.72 m/sec (25.32 ft/sec) and 15.43 m/sec (50.63 ft/sec).

Wing shielding.- Tests were made to determine the effect of the wing in shielding the noise by positioning microphones above and below the wing, as illustrated in figure 5. The microphone shown positioned below and behind the wing (microphone 3) turned out to be directly in the jet exhaust flow, and no means were taken to shield the microphone from such high-velocity flow. The data measured with this microphone, therefore, are not suitable for presentation.

Nozzle geometry.- Tests to determine the effect of nozzle geometry on the noise characteristics of the model were made with the nozzles having aspect ratios of 2 and 6; however, the aspect-ratio-2 nozzle was tested with deflector 2 on.

CORRECTIONS

The tests were performed in the 9.1- by 18.3-m (30- by 60-ft) open throat test section of the Langley full-scale tunnel. The semispan model is shown installed in the tunnel in the photograph of figure 6. A large vertical wall mounted along one edge of the existing tunnel floor 5.9 m (19.29 ft) from the lower surfaces of the wing provided a fixed tunnel boundary "below" the semispan model to permit the use of references 6 and 7 in correcting the data for interference induced by the wind-tunnel jet boundary. In making the interference-factor calculations, elliptic spanwise loading, with the lift of the entire system distributed over the wing, was assumed. The point at which the model pivoted as angle of attack was changed was such that the wing location relative to the vertical wall varied slightly with angle of attack; this movement has been accounted for in the correction calculations. The correction to angle of attack ($\Delta\alpha$) was found to be small and negative (approximately -1°, or less); however, the dynamic-pressure correction was fairly large (as much as a 10-percent reduction in the measured dynamic pressure).

The wall-interference theory also predicted a large spanwise gradient of boundary-induced angle of attack (washout). Flow surveys with the model removed revealed an upwash gradient in the region where the wing would normally be located. This upwash tended to minimize the theoretically predicted boundary-induced washout. Therefore, correction of the data for these two factors was not required.

The model had no horizontal tail; therefore, no corrections were applied to the pitching-moment data other than the overall changes in angle of attack and dynamic

pressure. The values of C_μ were significantly affected by the variation in dynamic pressure, and data for constant values of C_μ have been obtained by interpolation of the basic corrected data.

PRESENTATION OF DATA

The data obtained in the investigation are presented in the following figures:

RESULTS AND DISCUSSION

Static Turning

Static turning tests were made of all the configurations included in the present investigation, since the effectiveness of a jet-flap system is dependent to a large extent upon the capability of the system for turning and spreading the jet exhaust efficiently for

the static case, and the results are presented in figure 7. The data of figure 7(a) show that the aspect-ratio-4 nozzle gave jet turning angles which were generally about equal to the angle of flap upper-surface deflection (see fig. 3(b)) except for the 60° flap setting, where the turning angle was lower. The efficiency was relatively high for the model, values of η of about 0.95 and 0.87 being achieved for flap deflections of 40° and 60°, respectively. The data of figure 7(b) show that the aspect-ratio-6 nozzle gave better turning performance than the aspect-ratio-4 nozzle, whereas the aspect-ratio-2 nozzle without deflectors gave very poor turning. This difference in turning performance for the three nozzles is not solely a result of the difference in nozzle aspect ratio but is due in part to the differences in internal contour of the nozzles, as shown in figure 4.

In an attempt to improve the static turning performance for the aspect-ratio-2 nozzle, two types of configuration changes were tested: increased radius of the curved inboard flap and jet exhaust deflectors. The results of these tests, which are presented in figure 7(c), show that the increased flap radius had the opposite effect from that expected in that it caused a reduction in turning angle. Use of the jet deflectors, however, made the turning performance of the aspect-ratio-2 nozzle comparable with that of the aspect-ratio-4 nozzle.

Figure 7(d) shows that increasing the span of the inboard flap gave better static turning efficiency than that for the basic inboard flap and caused a slight increase in the turning angle. It should be pointed out that the efficiencies shown in figure 7 are based on the static thrust of the engine and nacelle installed on the wing and do not account for any installation losses. If, instead, the static thrust of the basic engine in free air with a round nozzle had been used, the efficiencies would no doubt be lower than those shown in figure 7.

Aerodynamic Characteristics

Presentation of basic data.- The basic data of the investigation are presented in figures 8 to 32 as plots of the aerodynamic forces and moments against C_{μ}. The data are presented in this manner for convenience in interpolating for constant values of C_{μ}, since C_{μ} varied with angle of attack during each test. Various summary plots have been made to show the effects of Reynolds number, engine nozzle geometry, leading-edge BLC, trailing-edge flap span, inboard-flap span, and the leading-edge Krueger flap. The closed symbols plotted in figures 12, 23, and 30 are high Reynolds number data which were measured at one thrust setting only, so that the values of C_{μ} varied slightly from the nominal value with change in α. The baseline data $\left(R = 1.2 \times 10^{6}\right)$ shown in these figures served as a guideline for extrapolating the high Reynolds number data to the nominal or selected value of C_{μ} for subsequent comparisons at constant values of C_{μ}.

Effect of flap deflection.- The longitudinal characteristics of the basic model for flap deflections of 60°, 40°, 20°, and 0° are presented in figures 33 to 36 as pitching-moment, lift, and drag coefficients plotted against angle of attack for several values of gross-thrust coefficient. These data show the usual increases in stall angle of attack, maximum lift coefficient, and effects of power at the higher flap settings associated with the use of jet-augmented flaps. (See ref. 8.) Maximum lift coefficients of about 9.5 (untrimmed) were produced for a gross-thrust coefficient of 4.0. Nose-down pitching moments were very large at high lift because of the rearward location of the flap loads.

One interesting point noted for the 0° flap configuration (fig. 36) is that considerable lift augmentation was produced and that the stall angle of attack was increased appreciably with increasing power even though the flap was undeflected. These effects are also brought out by figure 37, which is a plot of the lift generated for $C_{\mu} = 4$ at several different flap deflections. Figure 38 presents an analysis of the lift components which make up the total lift and shows that the lift for the clean configuration can be attributed primarily to the vertical component of the jet reaction $\eta C_{\mu} \sin \delta_j$. Smoke-flow and tuft studies indicated that the engine thrust was deflected downward, even though the flaps were undeflected, because of the downward contour (12°) of the airfoil upper surface at the rear of the wing.

Effect of Reynolds number.- Presented in figures 39 to 41 are data over a Reynolds number range from 0.45×10^6 to 3.1×10^6 for constant values of C_{μ} and for flap settings of 60°, 40°, and 20°. The data of figure 39(a) show that the effects of Reynolds number were large for the 60° flap setting with power off. Increasing the Reynolds number from 0.45×10^6 to 1.2×10^6 brought the data into good agreement with the data for a Reynolds number of 3.1×10^6. As the thrust was increased to $C_{\mu} = 1.0$ (fig. 39(b)), the effects of Reynolds number were still large, but the differences in lift were not as pronounced as those for $C_{\mu} = 0$. At values of thrust coefficient C_{μ} of 2.0 (fig. 39(c)) and 3.0 (fig. 39(d)), the effects of Reynolds number within the range tested were rather small.

At the flap settings of 40° and 20°, the effects of Reynolds number over the test angle-of-attack range up to the stall were much less noticeable than those for the flap setting of 60°. One interesting point noted for both the 40° and 20° flap settings with power-off (figs. 40(a) and 41(a)) is that the lift for the higher Raynolds number decreased rapidly above the stall, whereas the lift for the lower Reynolds number tended to remain at about a constant level through the stall.

An interesting point in connection with the discussion on Reynolds number effects is illustrated in figure 42, which shows the effect of adding leading-edge BLC to the 60° flap configuration for tests at a Reynolds number of 0.45×10^6. These data show that leading-edge blowing was effective for increasing the lift coefficient and stall angle of attack at

the low Reynolds number, particularly for $C_\mu = 0$. A comparison of the data of figures 39 and 42 indicates that leading-edge blowing brought the low Reynolds number data into generally good agreement with the high Reynolds number data, except that leading-edge blowing extended the stall angle of attack beyond that of the wing with no blowing.

Effect of engine nozzle geometry.- One of the objectives of this investigation was to determine the effect of engine nozzle geometry. Tests were made with nozzles having aspect ratios of 2, 4, and 6 and various internal contours, and the results are presented in figure 43. These data show in general that the effects of engine nozzle geometry were relatively small for the range of test conditions. These small effects were not entirely unexpected, since in these tests each nozzle exit was tilted downward toward the top of the wing so that the exhaust flow impinged on top of the wing in front of the flap and was therefore forced to spread out into a thin sheet. Spreading and thinning of the jet was achieved with the aspect-ratio-2 nozzle through the use of the deflectors. Spreading the jet exhaust in this manner tended to minimize the effects of nozzle aspect ratio, since in each case the jet was forced to spread much wider than the nozzle. Much more spreading was required for the aspect-ratio-2 nozzle without deflectors than for the other nozzles to achieve the thin jet necessary for good turning over the flaps, but when this spreading was accomplished, the turning efficiency for all three nozzles was probably about the same. (See figs. 7(b) and (c).)

Effects of leading-edge BLC and drooped blown aileron.- The results of tests to determine the effects of leading-edge BLC and the drooped blown aileron are presented in figures 44 to 49. The data of figure 44 show that the addition of leading-edge BLC to the 60° flap configuration generally provided an increase in maximum lift coefficient and stall angle of attack for all thrust coefficients. The use of a drooped blown aileron in combination with leading-edge BLC provided further improvement in lift throughout most of the angle-of-attack range. The data also show that the benefits of leading-edge BLC and the drooped aileron were generally additive when they were used in combination. The data of figure 45 show that the performance benefits tend to increase with an increase in leading-edge blowing for the range of leading-edge blowing coefficients $C_{\mu,le}$ of the investigation.

The data of figures 46 to 49 show that the beneficial effects of leading-edge BLC noted for the 60° flap deflection also generally occurred for the lower flap deflections. It is significant to note that the lift increases achieved through use of leading-edge BLC and the drooped blown aileron were obtained without markedly changing the drag or increasing the negative diving moments of the wing.

Tuft studies made in connection with the tests on boundary-layer control indicated that the flow on top of the wing tended to move inboard from the wing tip toward the engines as the thrust coefficient was increased. This result is opposite to that observed from

previous work with externally blown jet flaps in which the wing flow tended to follow the exhaust flow outward along the flaps after the exhaust flow impinged on the flaps. This inward flow suggests that one reason for the effectiveness of boundary-layer control with the USB configuration is that BLC forced the spanwise flow on top of the wing to turn in a more chordwise direction and thereby increased the circulation lift induced by the engine thrust.

Effect of leading-edge Krueger flap.- One question that continues to be raised in work with high-lift systems is what type of leading-edge high-lift device is needed to insure good aerodynamic performance. A few tests were made with the Krueger flap off for $\delta_f = 40^o$, and a comparison of data showing the effectiveness of the Krueger flap is presented in figure 50. The Krueger flap significantly increased the lift at high angle of attack and delayed the stall angle of attack in a manner generally similar to that found in other high-lift studies. (See, e.g., ref. 8.) For $C_\mu = 0$, the data of figure 50(a) show that the Krueger flap reduced the lift at low angles of attack, as expected.

Effect of inboard-flap span.- The inboard flap extended to a point 0.65 nozzle width outboard of the engine centerline at the start of the tests, and this flap span was used throughout most of the test program. At the higher thrust coefficients, tuft studies showed that some of the exhaust was actually spreading beyond the outboard edge of the inboard flap. This spreading suggested that some additional benefits could be achieved with a larger inboard-flap span; therefore, a few tests were performed with the span extended to 0.75 nozzle width beyond the engine centerline. The results of these tests are presented in figures 51 to 53 and show in general that extending the span of the inboard flap had little effect on the data except at the higher power setting for flap deflections of 60^o and 40^o, where some improvement in lift could be achieved with the larger flap span.

Noise Characteristics

The noise data obtained in the investigation are presented in figures 54 to 56 and are in the form of frequency spectra and overall sound pressure levels (indicated in each figure by solid symbols).

The shielding effects of the wing on the noise of the USB jet-flap system are illustrated in figure 54. The data presented in this figure are for the aspect-ratio-2 nozzle with microphones located above and below the wing (microphones 1 and 4, respectively). The spectra were predominated by fan discharge tones, as shown by the high-frequency peaks, which are associated with blade-passage frequency. Figure 54(a) shows that for zero wind velocity the overall noise level observed below the wing was substantially lower (18 dB) than that observed above the wing. Also, the noise below the wing was substantially lower throughout the frequency range from 2 kHz to 25 kHz. Similar noise

reductions were observed below the wing for forward-speed conditions in figures 54(b) amd 54(c). These results are as expected (see ref. 9) in that the wing was more effective in shielding the high-frequency noise than the low-frequency noise.

The effect of forward speed is shown more directly in figure 55, where the data are replotted, with the data for the various airspeeds shown on the same plot. These data show that the wind effects on the noise measurements were most noticeable directly above and below the wing, and generally forward velocity provided a slight decrease in noise levels.

The noise measurements obtained at microphone 1 (directly above the wing) for the nozzles with aspect ratios of 2 and 6 and presented in figure 56(a) show little difference in the overall noise levels of the two nozzles; however, the aspect-ratio-6 nozzle had higher noise levels for the frequency range up to about 5 kHz. These higher noise levels are attributed to the increased scrubbing area provided by the aspect-ratio-6 nozzle. The high-frequency peaks in the spectra, which are associated with the blade-passage frequency, show evidence of modulations, as is characteristic of fan noise, as well as the effects of the four nonsynchronous fans. Noise measurements at microphone 4 (directly below the wing) presented in figure 56(b) show a substantial reduction in the overall noise levels for both nozzles compared with the overall noise levels for the position above the wing (fig. 56(a)). However, an observer located beneath the airplane would detect little effect on the overall noise levels due to fan-nozzle geometry, for the range of aspect ratios tested.

SUMMARY OF RESULTS

From a wind-tunnel investigation of a large-scale semispan model with an unswept wing and an upper-surface blown jet flap, the following results were obtained:

1. The upper-surface blown jet-flap concept is effective for producing the high lift necessary for powered-lift operation and the performance is generally comparable with that of other externally blown powered-lift concepts. Maximum lift coefficient of about 9.5 for thrust coefficients of 4 were obtained with partial-span trailing-edge flaps and no boundary-layer control.

2. The effects of Reynolds number were generally small for moderate to high powered-lift conditions.

3. Varying the engine nozzle geometry did not significantly alter the aerodynamic characteristics of the model; however, it should be noted that a jet deflector was used on the nozzle with an aspect ratio of 2, but not on the nozzles with higher aspect ratios.

4. Full-span trailing-edge flaps were much more effective for achieving good high-lift performance than partial-span trailing-edge flaps.

5. The use of leading-edge boundary-layer control greatly increased the stall angle and the lift at high angles of attack, and generally improved the overall aerodynamic performance of the model.

6. The shielding effects of the wing resulted in significantly lower overall noise levels being observed below the wing than above the wing.

7. The effects of forward airspeed on noise were beneficial but relatively small.

8. An observer located beneath the airplane would detect little effect on the overall noise levels due to fan-nozzle geometry.

Langley Research Center,
National Aeronautics and Space Administration,
Hampton, Va., November 29, 1973.

REFERENCES

1. Phelps, Arthur E.; Letko, William; and Henderson, Robert L.: Low-Speed Wind-Tunnel Investigation of a Semispan STOL Jet Transport Wing-Body With an Upper-Surface Blown Jet Flap. NASA TN D-7183, 1973.

2. Phelps, Arthur E., III; and Smith, Charles C., Jr.: Wind-Tunnel Investigation of an Upper Surface Blown Jet-Flap Powered-Lift Configuration. NASA TN D-7399, 1973.

3. Reshotko, Meyer; Olsen, William A.; and Dorsch, Robert G.: Preliminary Noise Tests of the Engine-Over-the-Wing Concept. I. 30^{o}-60^{o} Flap Position. NASA TM X-68032, 1972.

4. Reshotko, Meyer; Olsen, William A.; and Dorsch, Robert G.: Preliminary Noise Tests of the Engine-Over-the-Wing Concept. II. 10^{o}-20^{o} Flap Position. NASA TM X-68104, 1972.

5. Mechtly, E. A.: The International System of Units – Physical Constants and Conversion Factors (Second Revision). NASA SP-7012, 1973.

6. Heyson, Harry H.: Use of Superposition in Digital Computers To Obtain Wind-Tunnel Interference Factors for Arbitrary Configurations, With Particular Reference to V/STOL Models. NASA TR R-302, 1969.

7. Heyson, Harry H.: FORTRAN Programs for Calculating Wind-Tunnel Boundary Interference. NASA TM X-1740, 1969.

8. Parlett, Lysle P.; Greer, H. Douglas; Henderson, Robert L.; and Carter, C. Robert: Wind-Tunnel Investigation of an External-Flow Jet-Flap Transport Configuration Having Full-Span Triple-Slotted Flaps. NASA TN D-6391, 1971.

9. Dorsch, Robert G.; Lasagna, Paul L.; Maglieri, Domenic J.; and Olsen, William A.: Flap Noise. Aircraft Engine Noise Reduction, NASA SP-311, 1972, pp. 259-290.

TABLE I.- PRIMARY DIMENSIONAL CHARACTERISTICS OF MODEL

Wing:	
Area (semispan), m^2 (ft^2)	8.13 (87.50)
Semispan, m (ft)	5.64 (18.50)
Length of mean aerodynamic chord, $\bar{c}$, m (ft)	1.50 (4.92)
Incidence:	
Root, deg	+1.5
Tip, deg	-1.5
Sweep:	
Leading edge, deg	0
Trailing edge, deg	-5 (forward)
Taper ratio	0.73
Aspect ratio, semispan	3.9
Airfoils:	
Root	NACA 64_2A215 (a = 0.5)
Tip	NACA 64_1A412 (a = 0.5)
Dihedral, deg	1.5
Root chord, m (ft)	1.68 (5.50)
Tip chord, m (ft)	1.22 (4.00)
Aileron chord, percent local wing chord	25
Engine nozzle:	
Exit area, m^2 (ft^2)	0.155 (1.67)
Equivalent nozzle diameter (D_e), m (ft)	0.445 (1.46)
Aspect ratio	2, 4, 6

TABLE II.- AIRFOIL COORDINATES FOR LEADING-EDGE KRUEGER FLAP

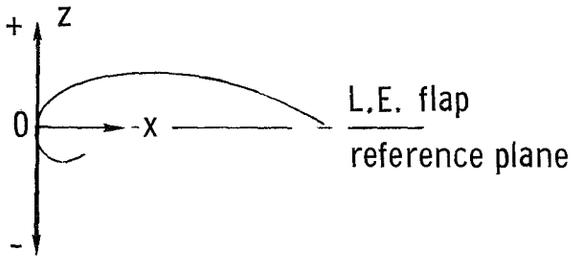

x, percent c	z_{upper}, percent c	z_{lower}, percent c
0	0	-----
.5	1.118	-1.450
1.0	1.723	-1.825
2.0	2.415	-1.980
3.0	2.910	-1.695
4.0	3.320	-----
6.0	3.825	-----
8.0	3.995	-----
10.0	4.005	-----
12.0	3.730	-----
14.0	3.250	-----
16.0	2.530	-----
18.0	1.472	-----
20.0	0	-----

TABLE III.- AIRFOIL COORDINATES FOR DOUBLE-SLOTTED FLAPS

(a) Flap coordinates

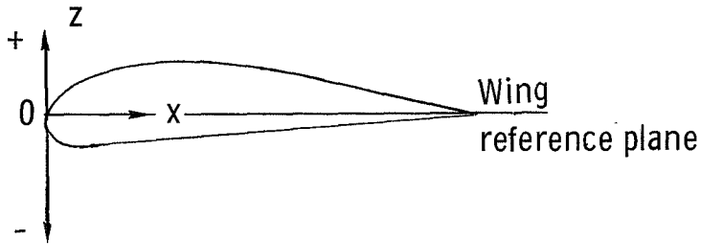

x, percent c	z_{upper}, percent c	z_{lower}, percent c
0	-1.336	-1.336
.5	-.232	-2.224
1.0	.278	-2.456
1.5	.692	-2.618
2.0	1.066	-2.718
2.5	1.375	-2.788
3.0	1.653	-2.811
4.0	2.100	-2.803
5.0	2.270	-2.703
6.0	2.672	-2.610
7.0	2.845	-2.502
8.0	2.978	-2.394
9.0	3.050	-2.301
10.0	3.073	-2.201
12.0	2.981	-1.993
14.0	2.718	-1.792
16.0	2.394	-1.583
18.0	2.039	-1.375
20.0	1.714	-1.158
22.0	1.390	-.958
26.0	.734	-.525
30.0	.06	-.06

TABLE III.- AIRFOIL COORDINATES FOR DOUBLE-SLOTTED FLAPS – Concluded

(b) Vane coordinates

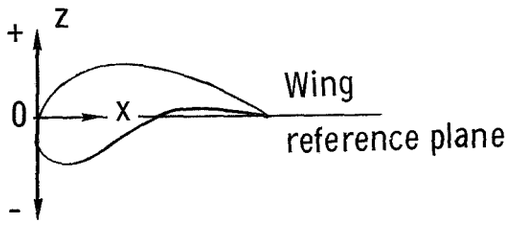

x, percent c	z_{upper}, percent c	z_{lower}, percent c
0	-0.46	-0.46
.25	.40	-.95
.50	.72	-1.14
.75	.98	-1.25
1.00	1.17	-1.30
1.25	1.32	-1.30
1.50	1.50	-1.29
1.75	1.62	-1.25
2.00	1.73	-1.21
3.00	2.04	-.90
4.00	2.11	-.52
5.00	2.07	-.20
6.00	1.90	.06
7.00	1.58	.20
8.00	1.16	.23
9.00	.61	.14
10.00	0	-.10

TABLE IV.- DEFLECTION DETAILS FOR DOUBLE-SLOTTED FLAP

δ_v, deg	δ_f, deg	Vane gap, percent c	Vane overlap, percent c	Flap gap, percent c	Flap overlap, percent c
20	60	1.45	1.52	1.50	1.50
10	40	1.45	1.52	1.50	1.50
5	20	.19	4.90	1.50	1.50

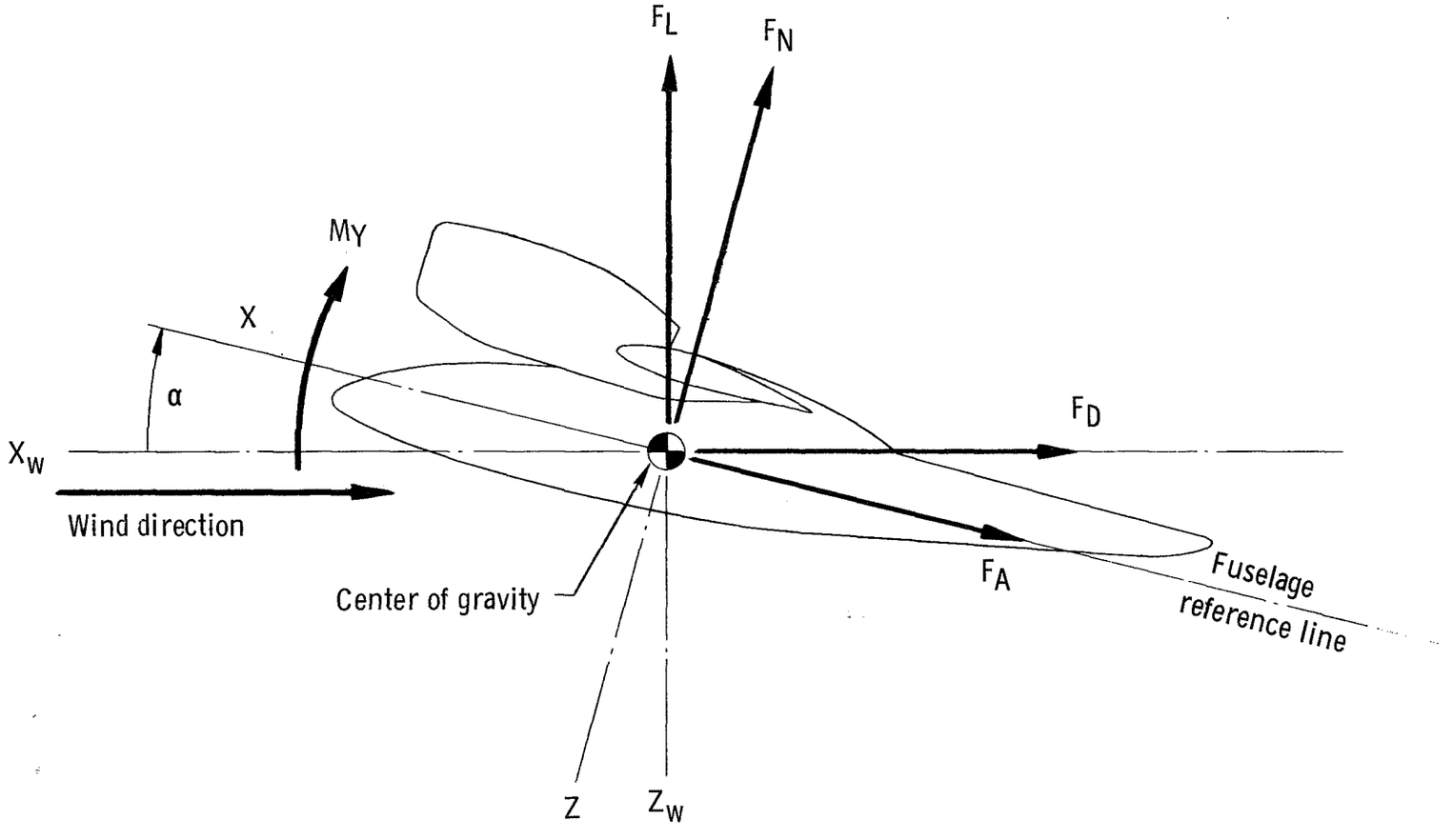

Figure 1.- Axis system used in presentation of data. Arrows indicate positive direction of forces and moments.

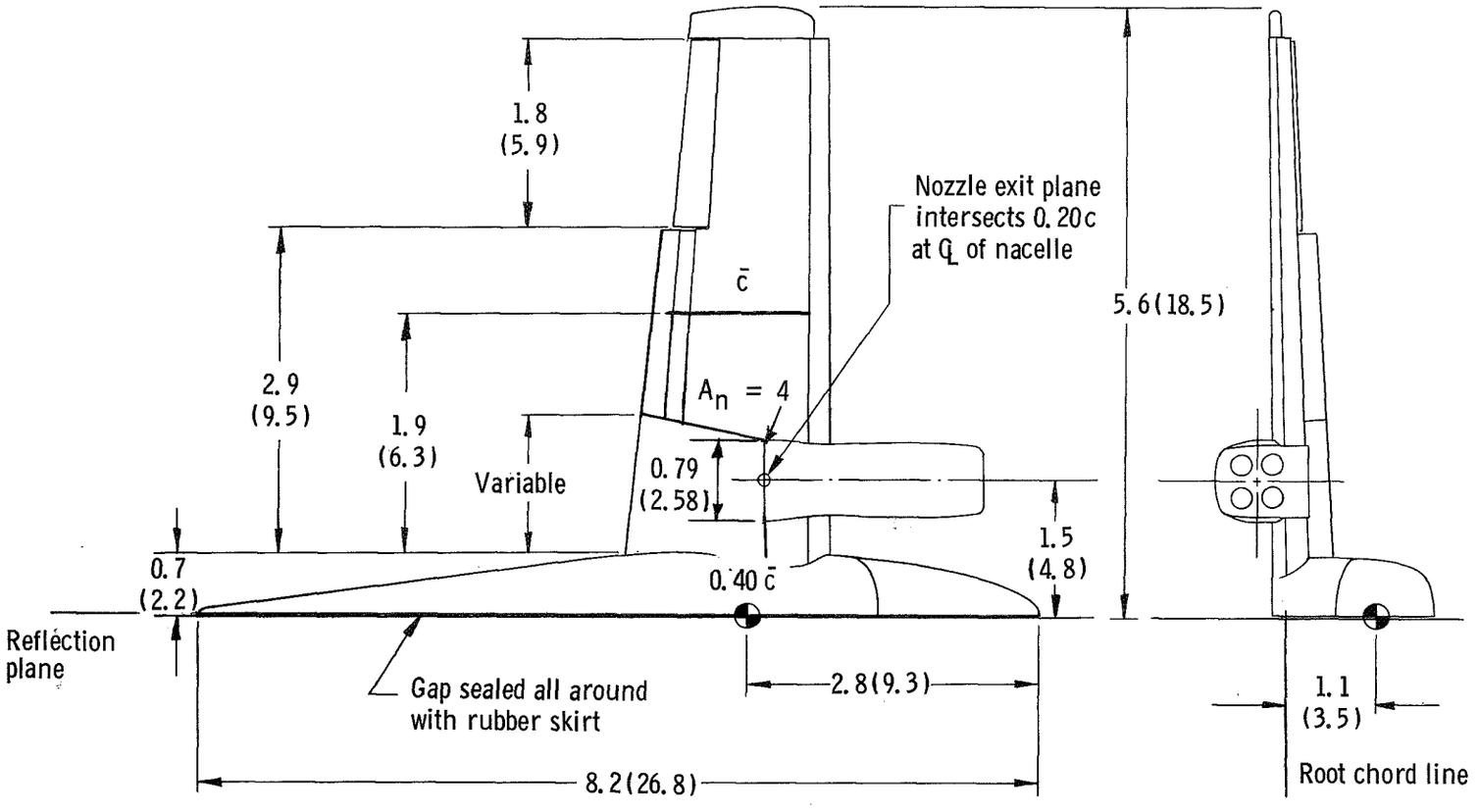

Figure 2.- General arrangement of model used in tests. Dimensions are given in meters (feet).

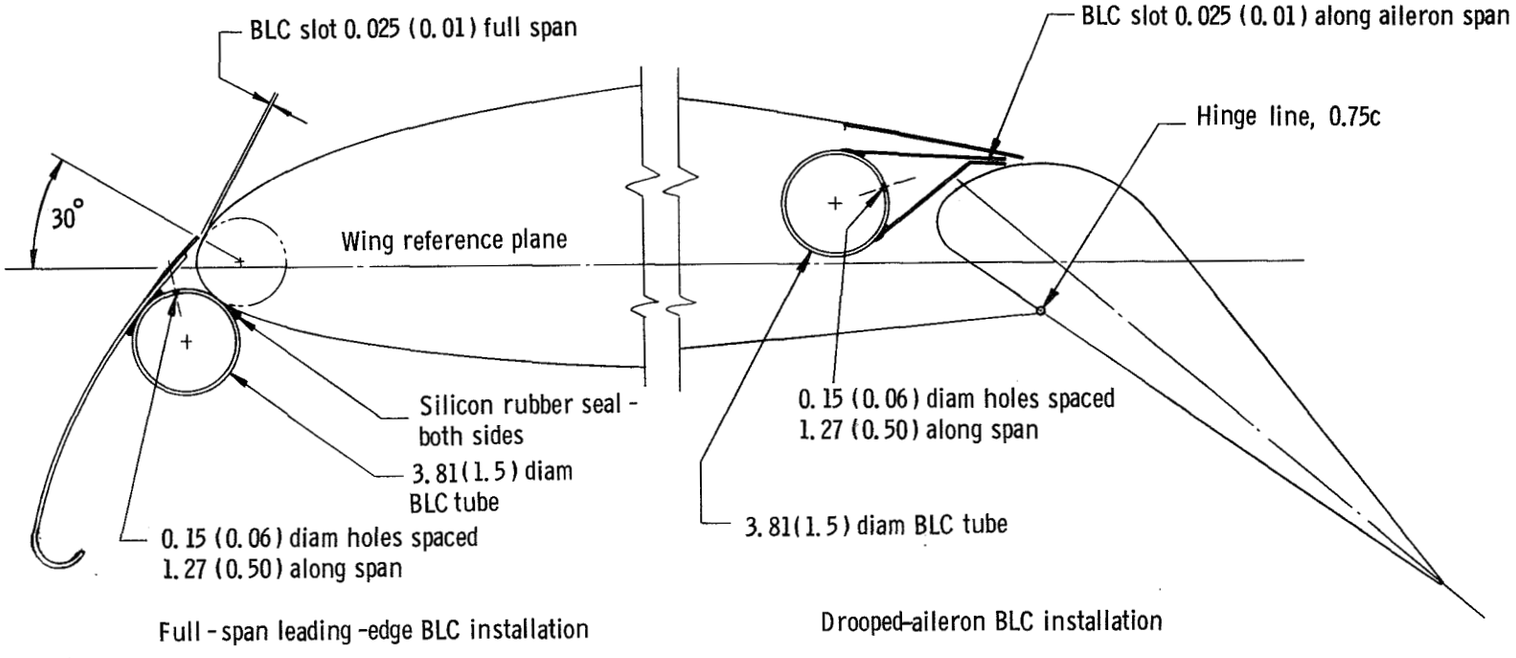

(a) Leading-edge and aileron-blowing BLC installations. Dimensions are given in centimeters (inches).

Figure 3.- Details of high-lift system.

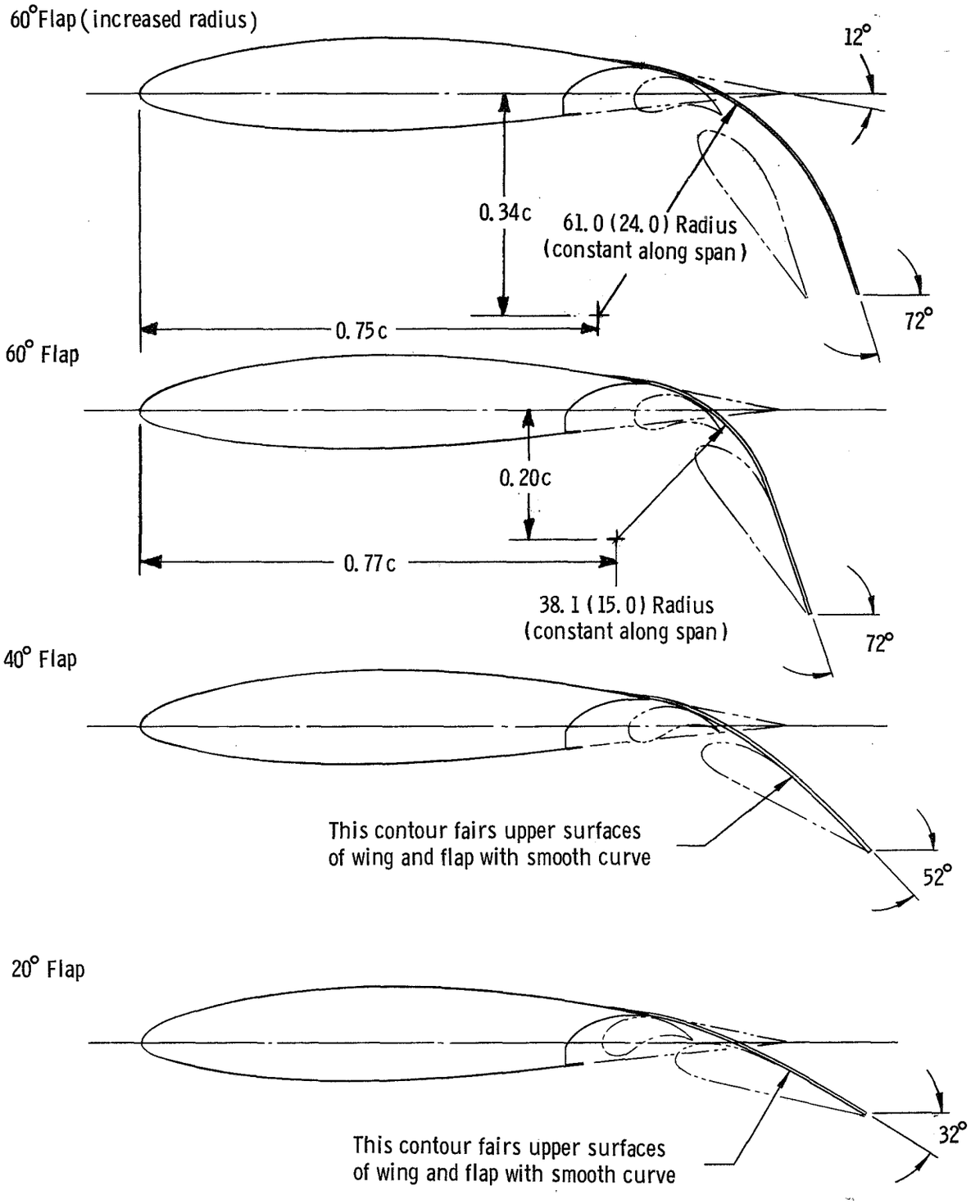

(b) Details of inboard flap. Dimensions are given in centimeters (inches).

Figure 3.- Continued.

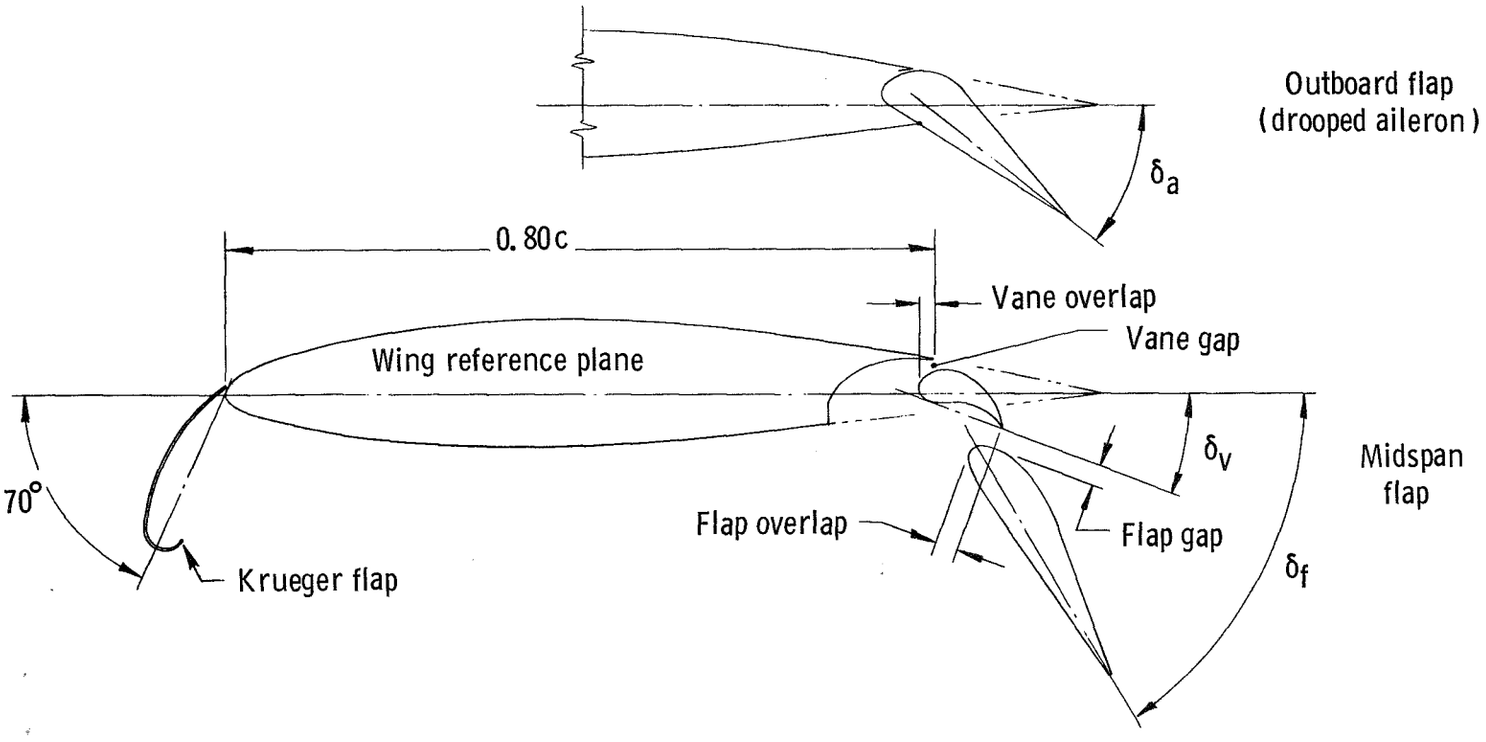

(c) Leading- and trailing-edge flap deflections.

Figure 3.- Concluded.

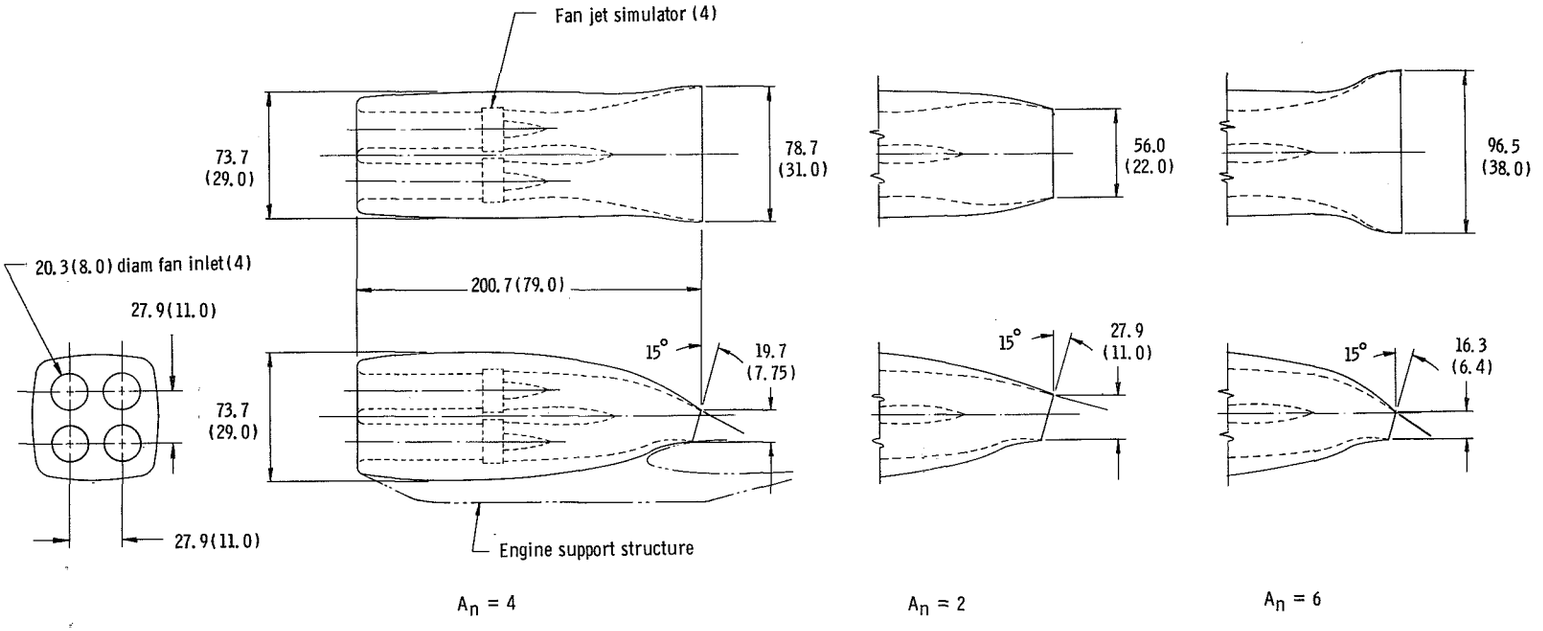

(a) General arrangement.

Figure 4.- Engine nacelle and exit nozzles used in tests. Dimensions are given in centimeters (inches).

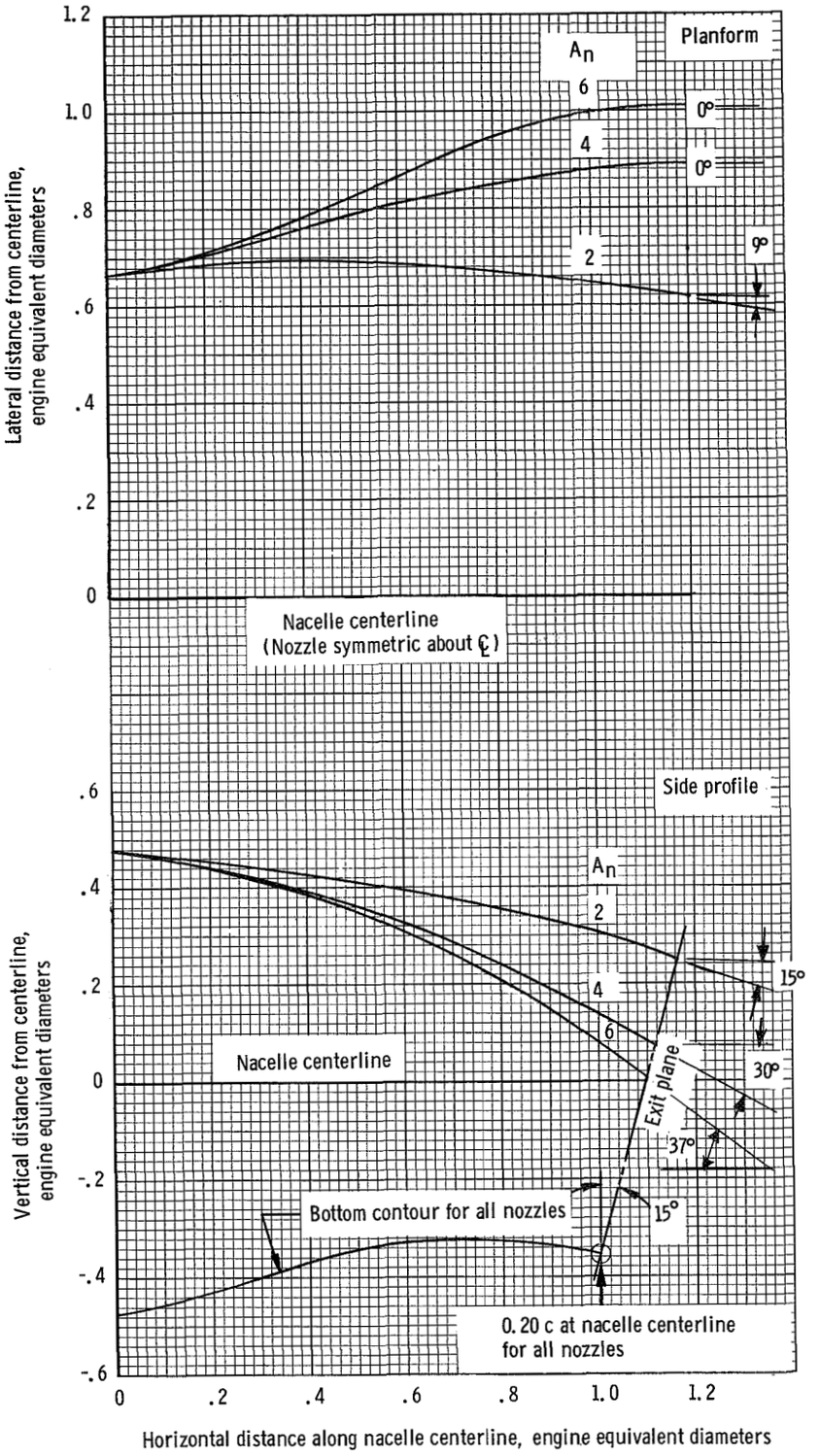

(b) Nondimensional nozzle contours.

Figure 4.- Continued.

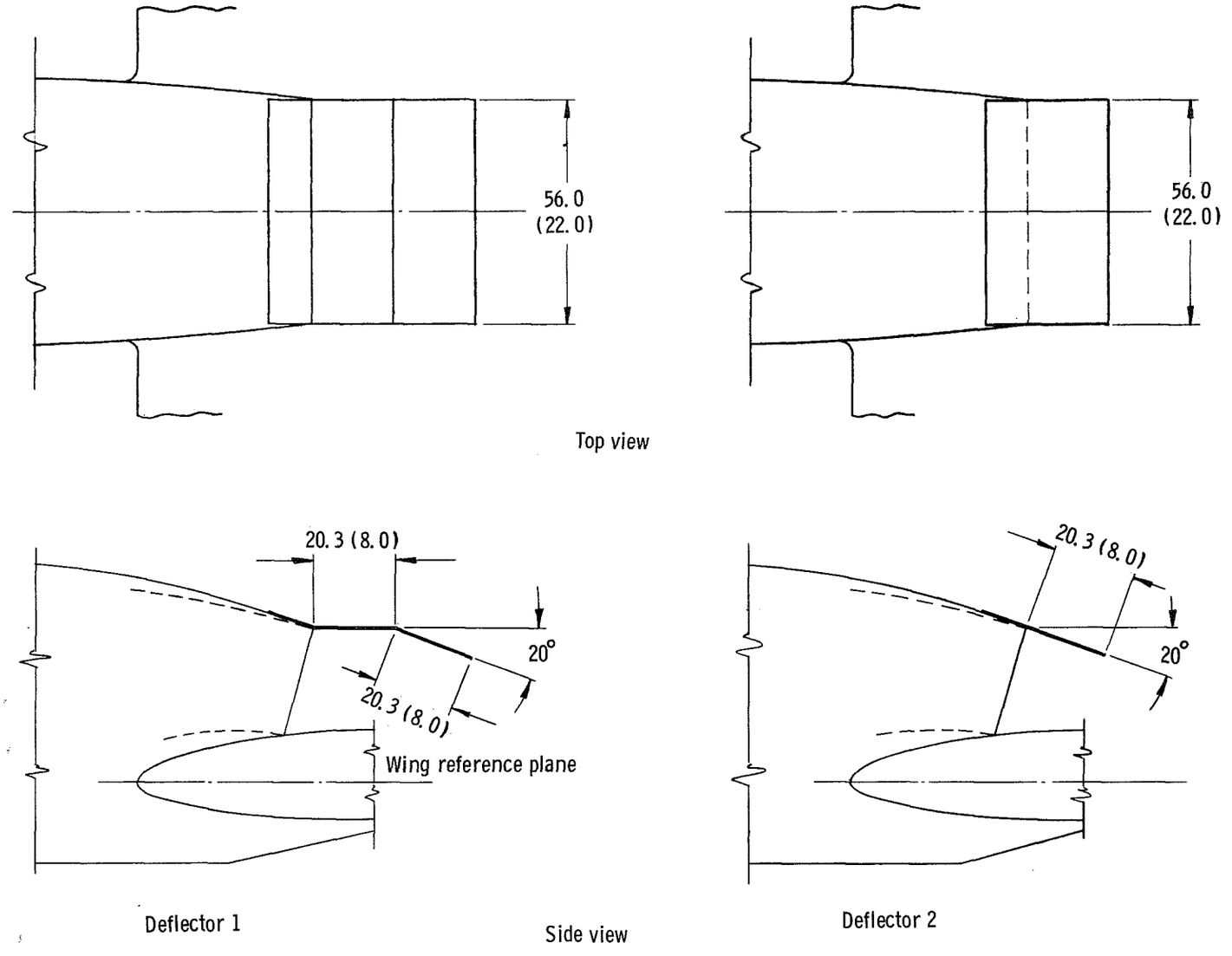

(c) Deflectors used with aspect-ratio-2 nozzle.

Figure 4.- Concluded.

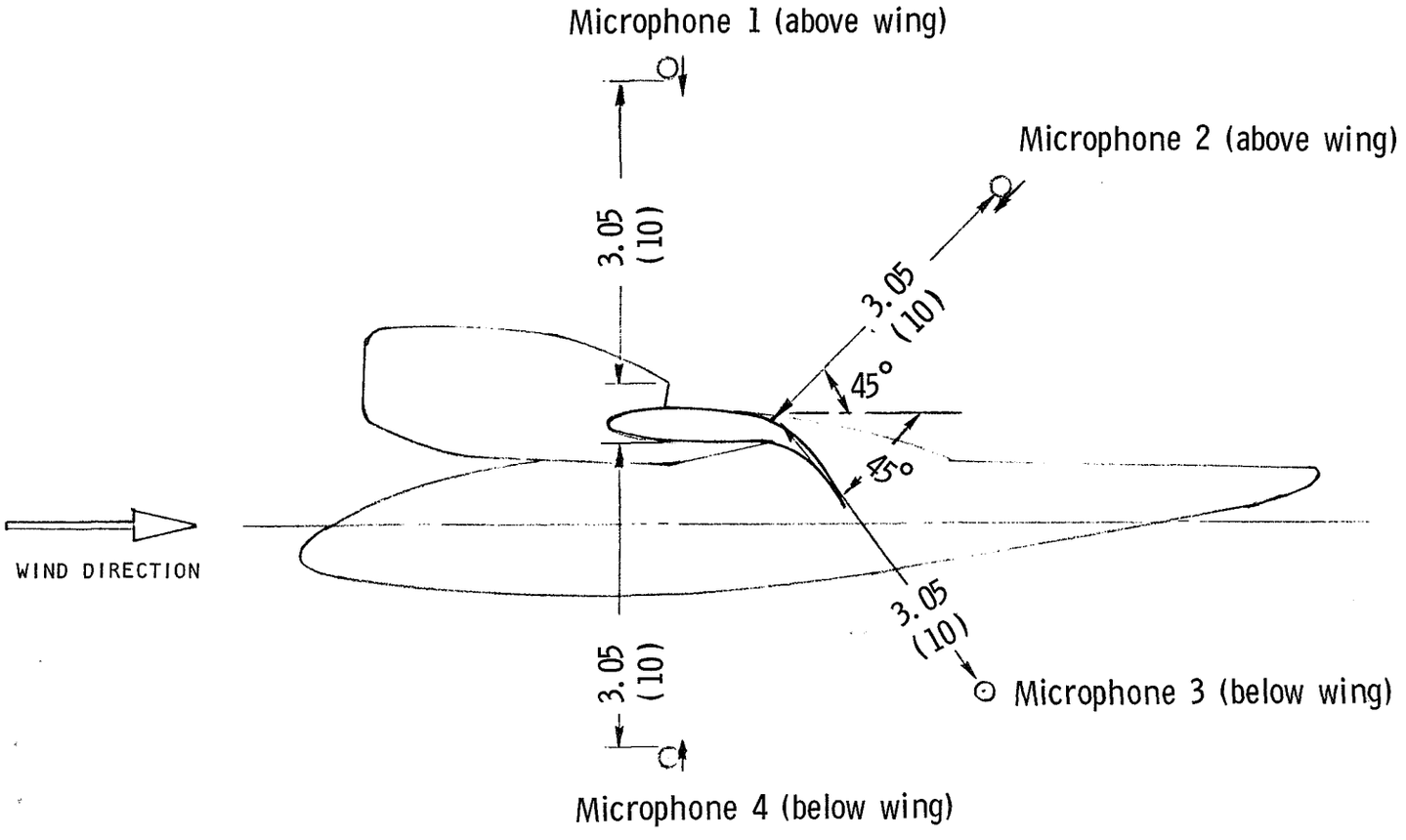

Figure 5.- Schematic of microphone locations and orientation with respect to test model. Dimensions are given in meters (feet).

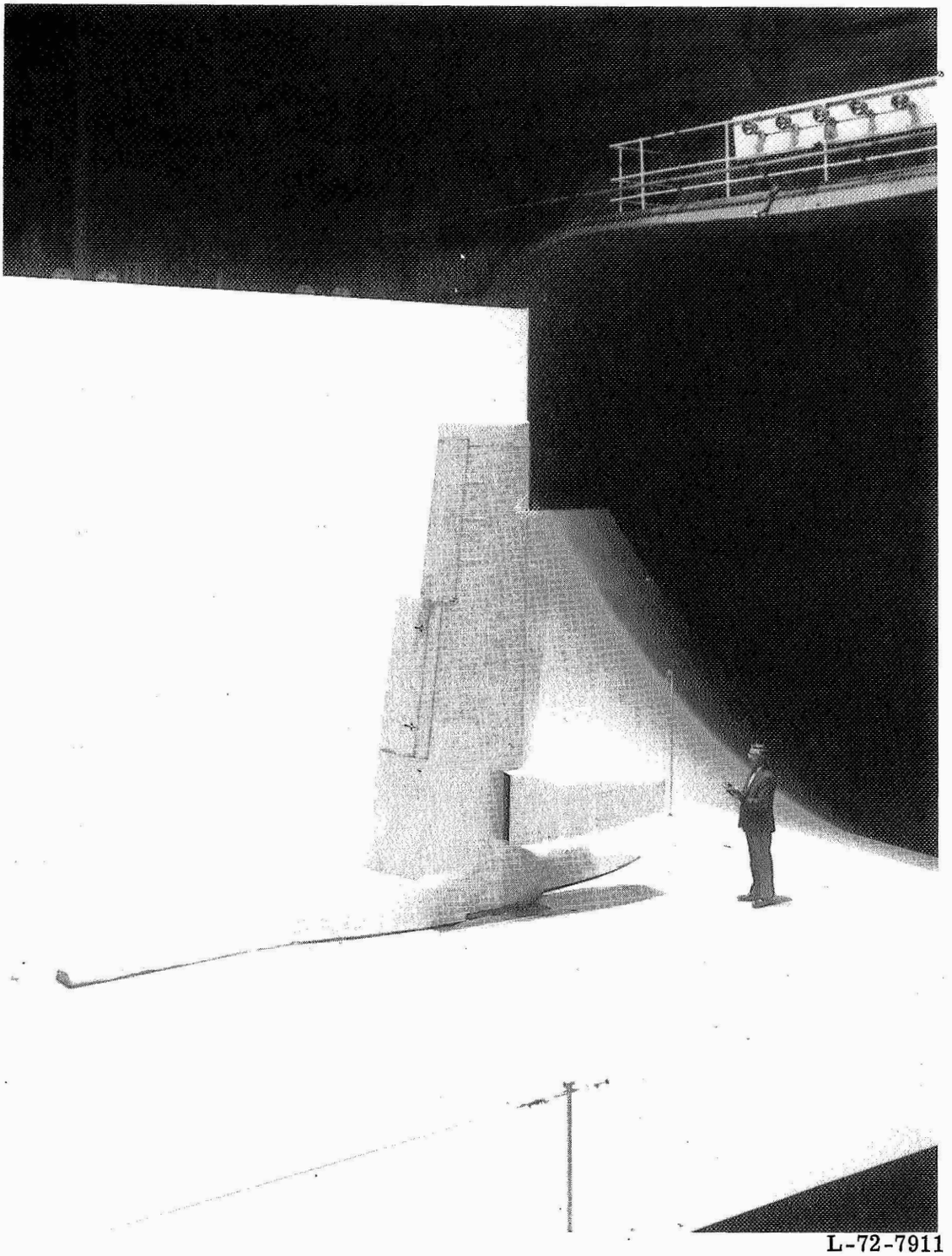

L-72-7911

Figure 6.- Photograph of model in Langley full-scale tunnel.

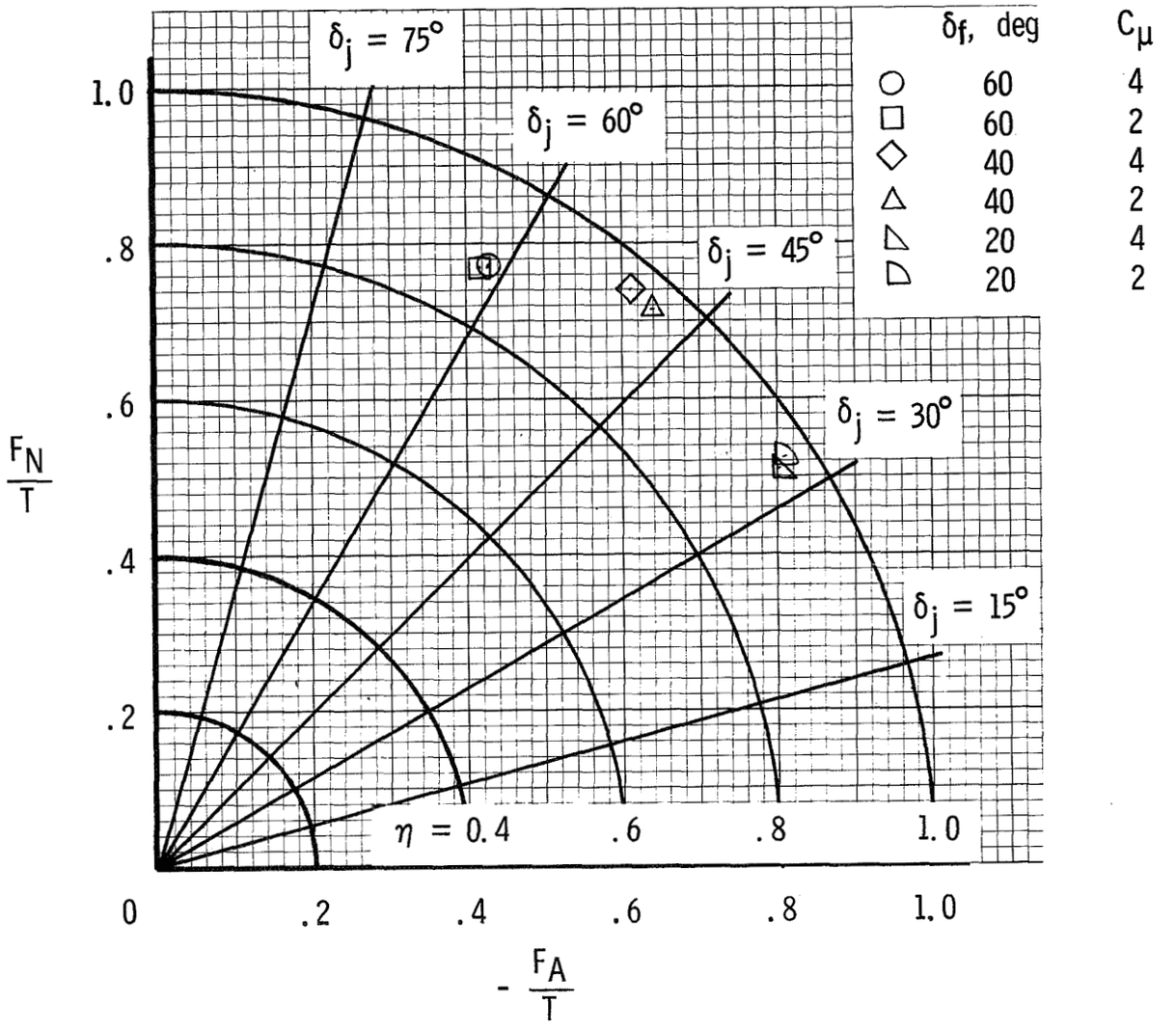

(a) Effect of flap deflection. $A_n = 4$.

Figure 7.- Summary of static turning characteristics. (For the values of C_μ quoted, a free-stream dynamic pressure of 79 N/m^2 (1.65 lb/ft^2) was assumed.)

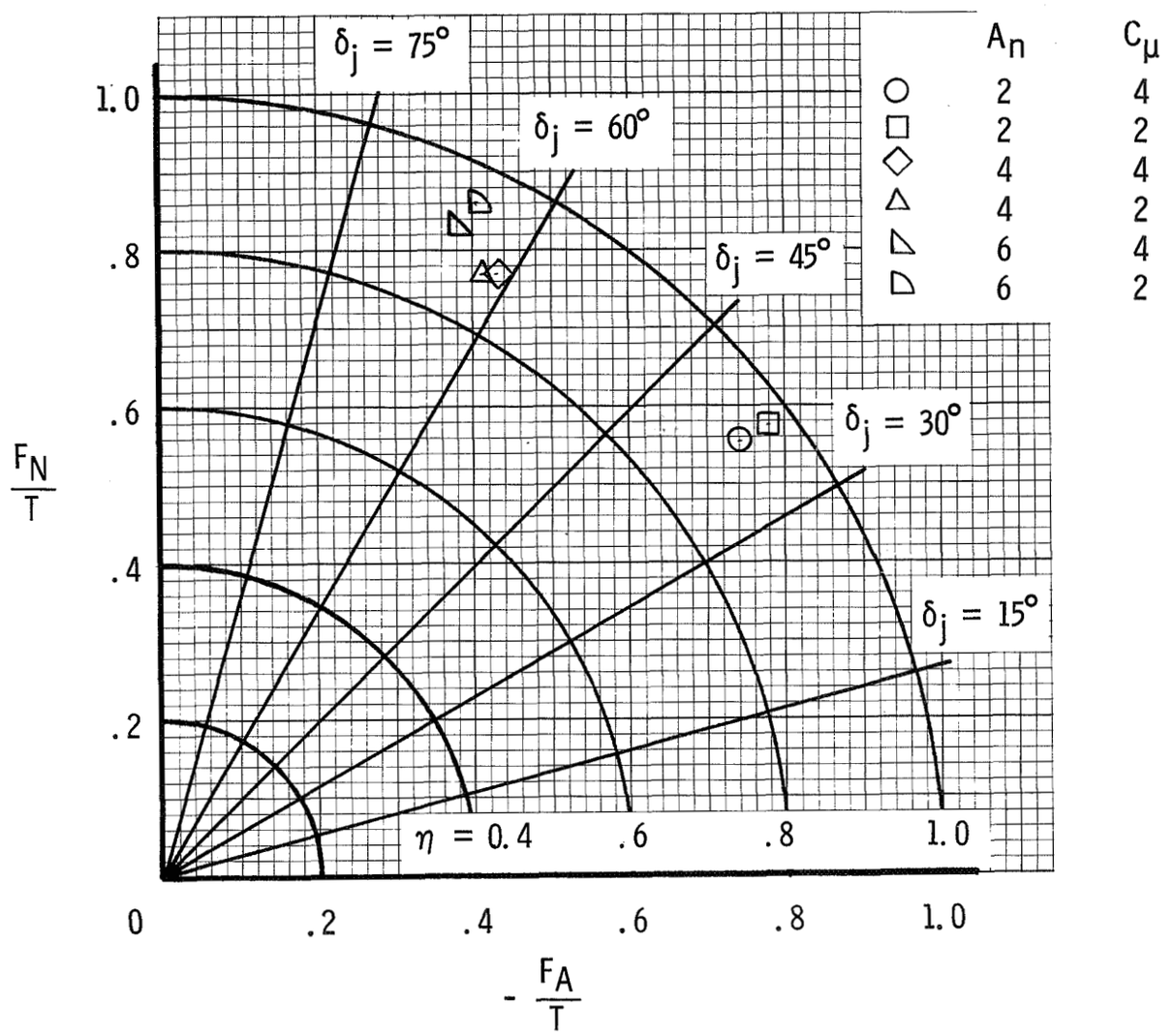

(b) Effect of nozzle geometry. $\delta_f = 60^o$.

Figure 7.- Continued.

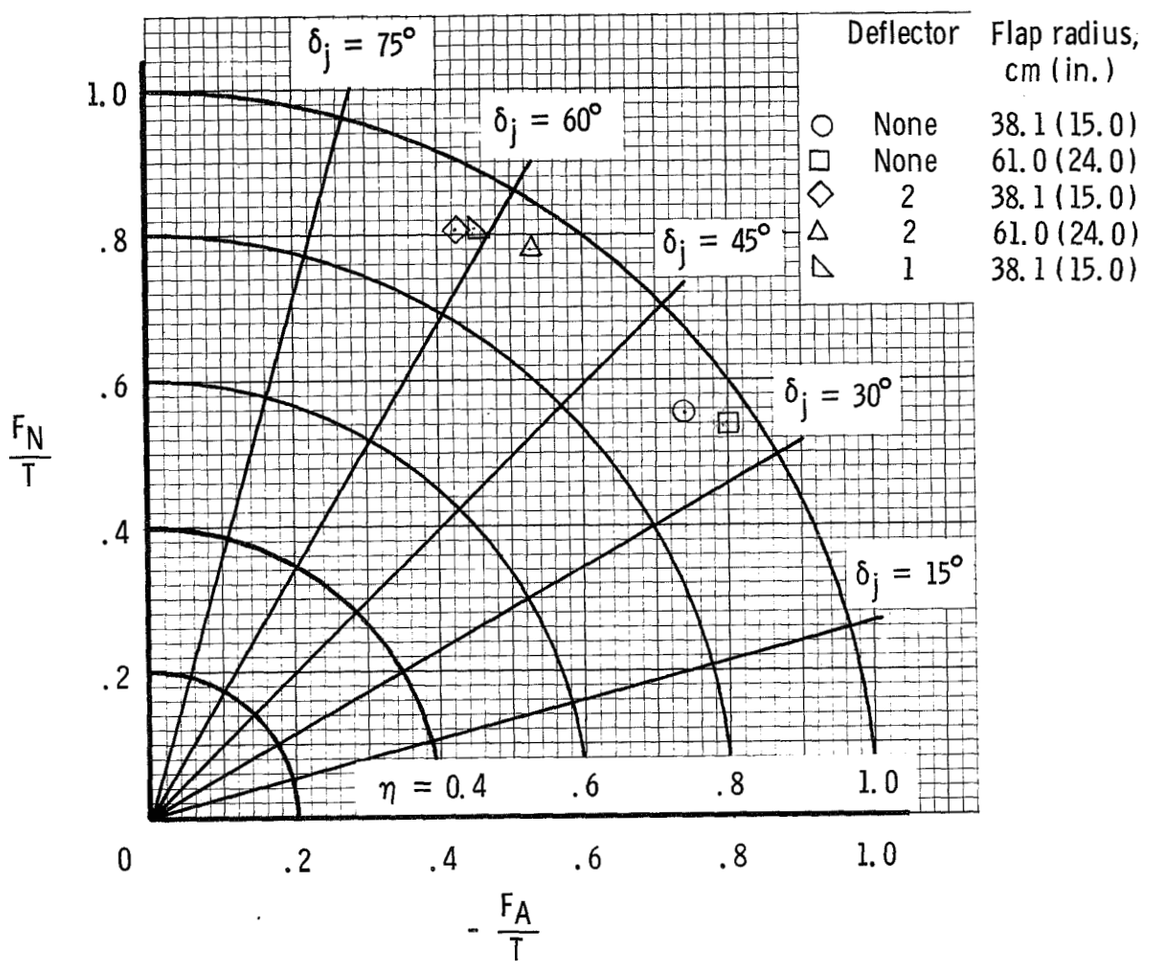

(c) Effect of nozzle deflector and inboard-flap radius. $\delta_f = 60°$; $C_\mu = 4$; $A_n = 2$.

Figure 7.- Continued.

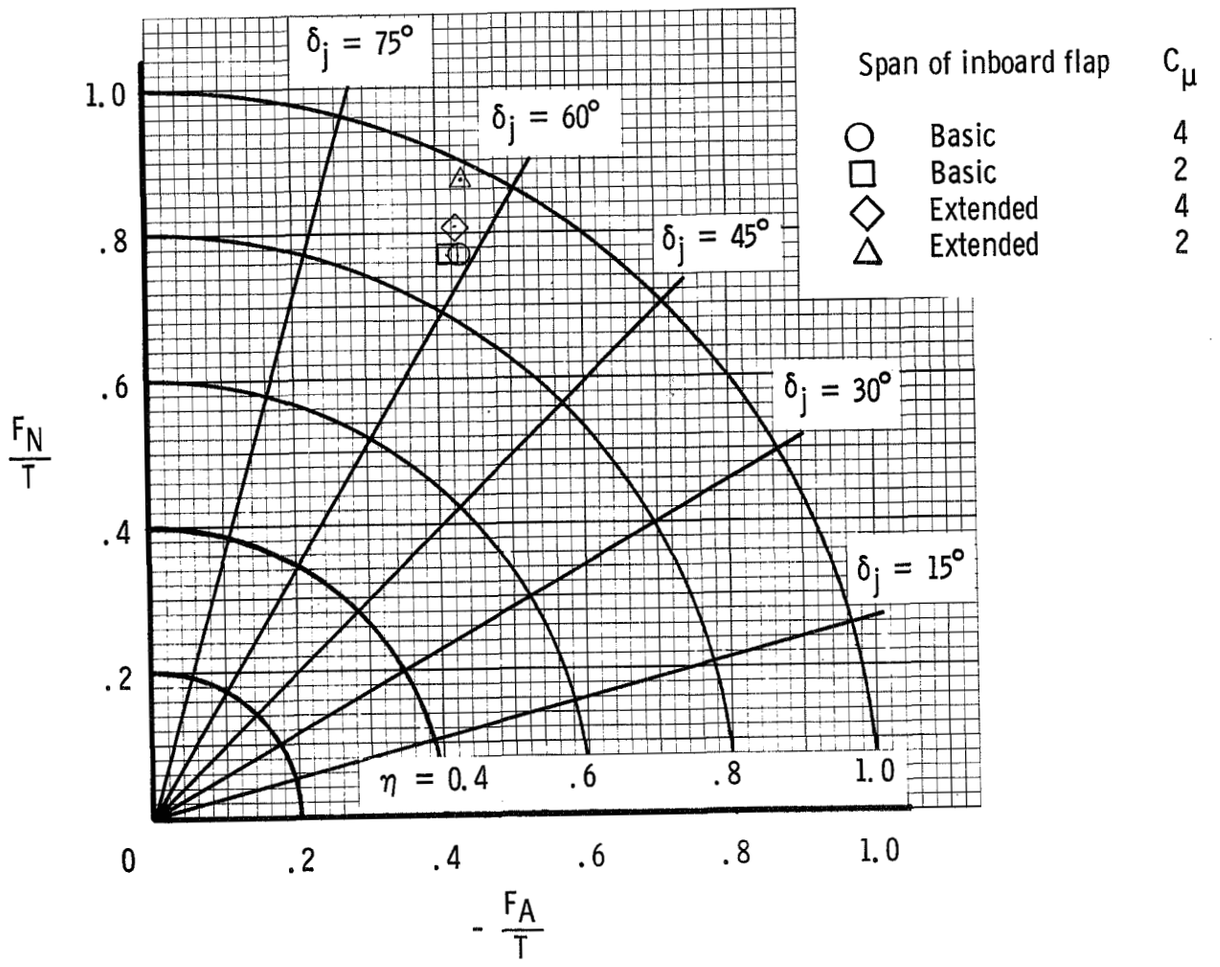

(d) Effect of inboard-flap span. $\delta_f = 60^o$; $A_n = 4$.

Figure 7.- Concluded.

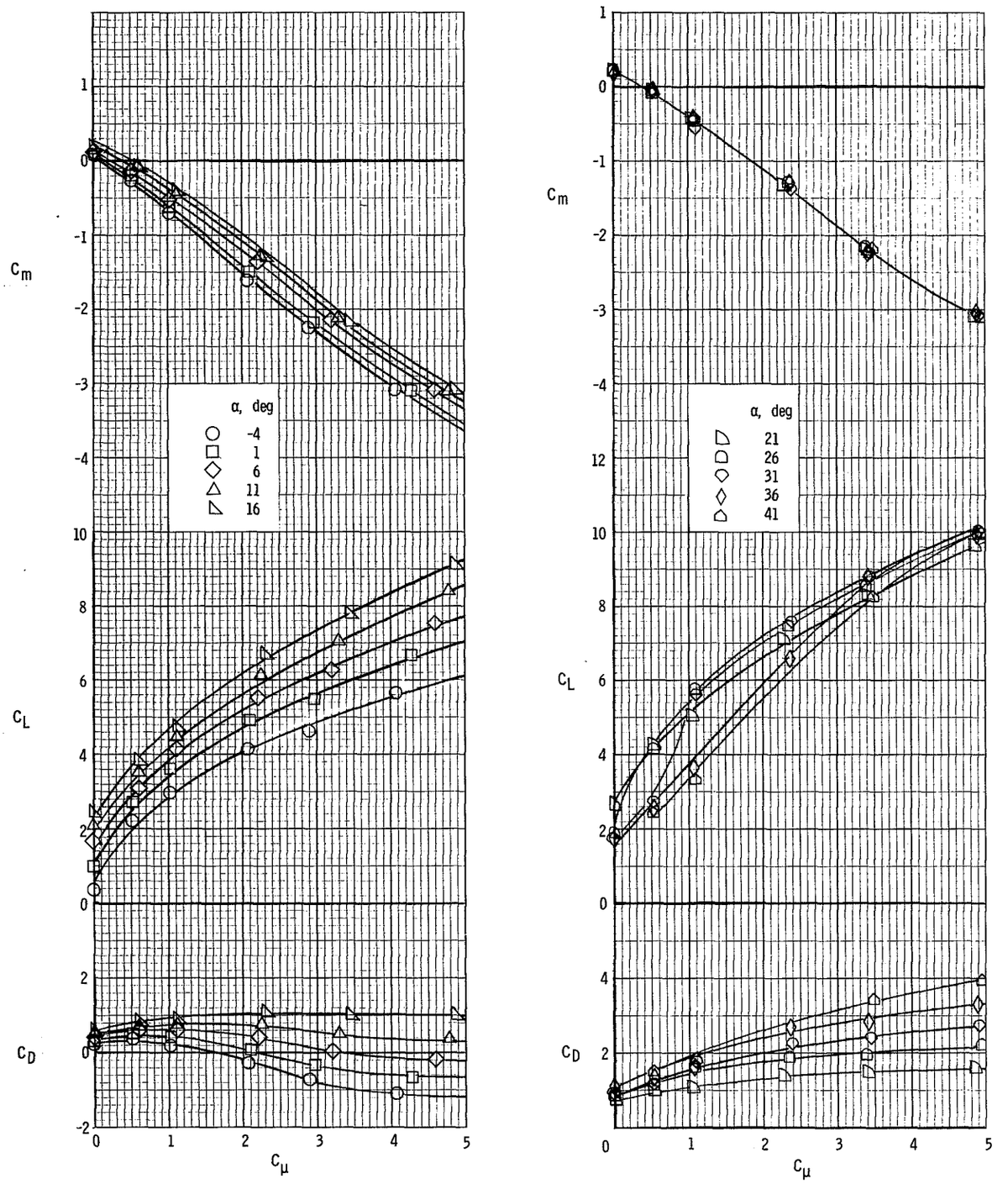

Figure 8.- Longitudinal characteristics of model. $\delta_f = 60^o$.

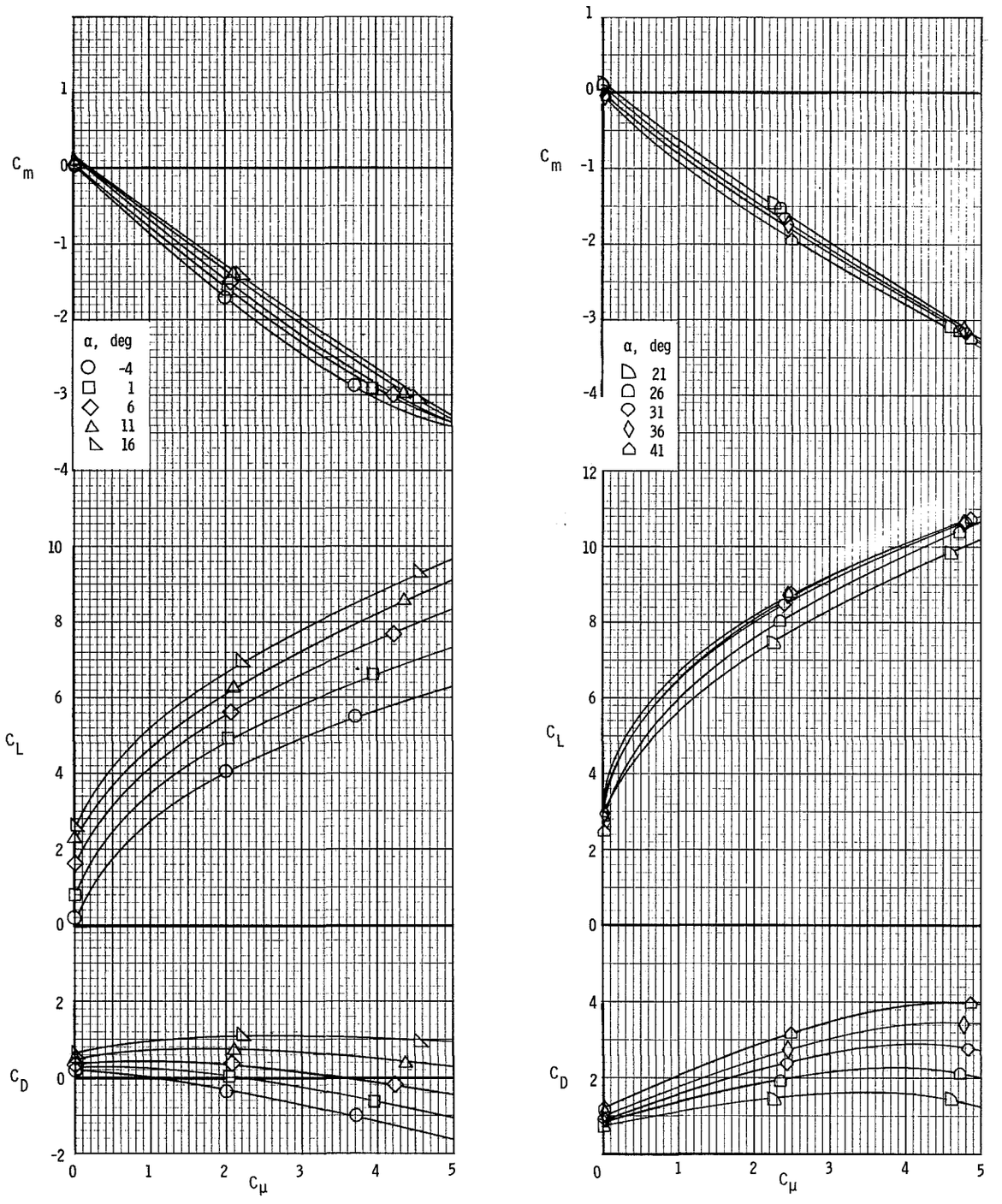

(a) $C_{\mu,le} = 0.04$.

Figure 9.- Longitudinal characteristics of the model with leading-edge BLC. $\delta_f = 60^o$.

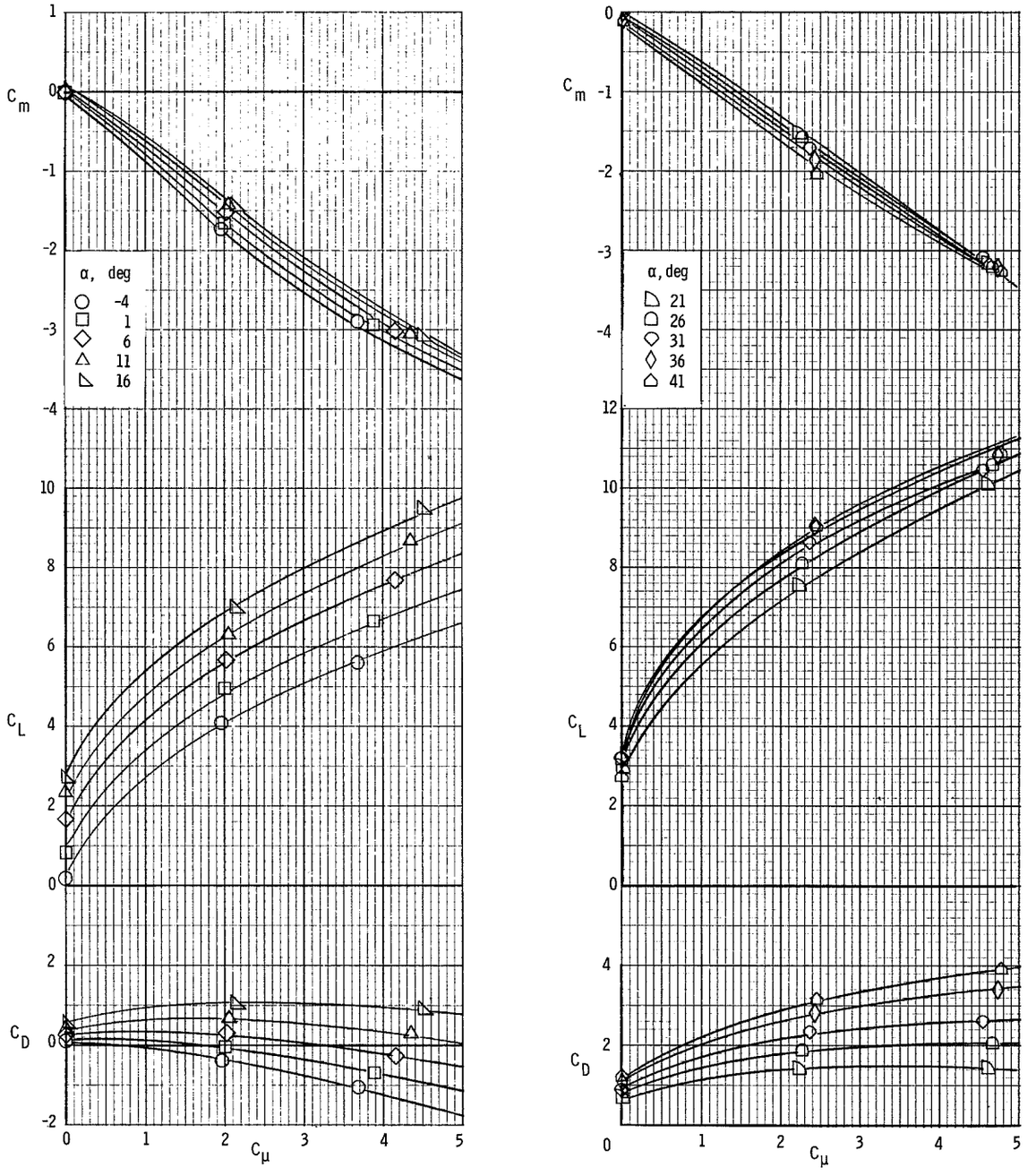

(b) $C_{\mu,le} = 0.08$.

Figure 9.- Concluded.

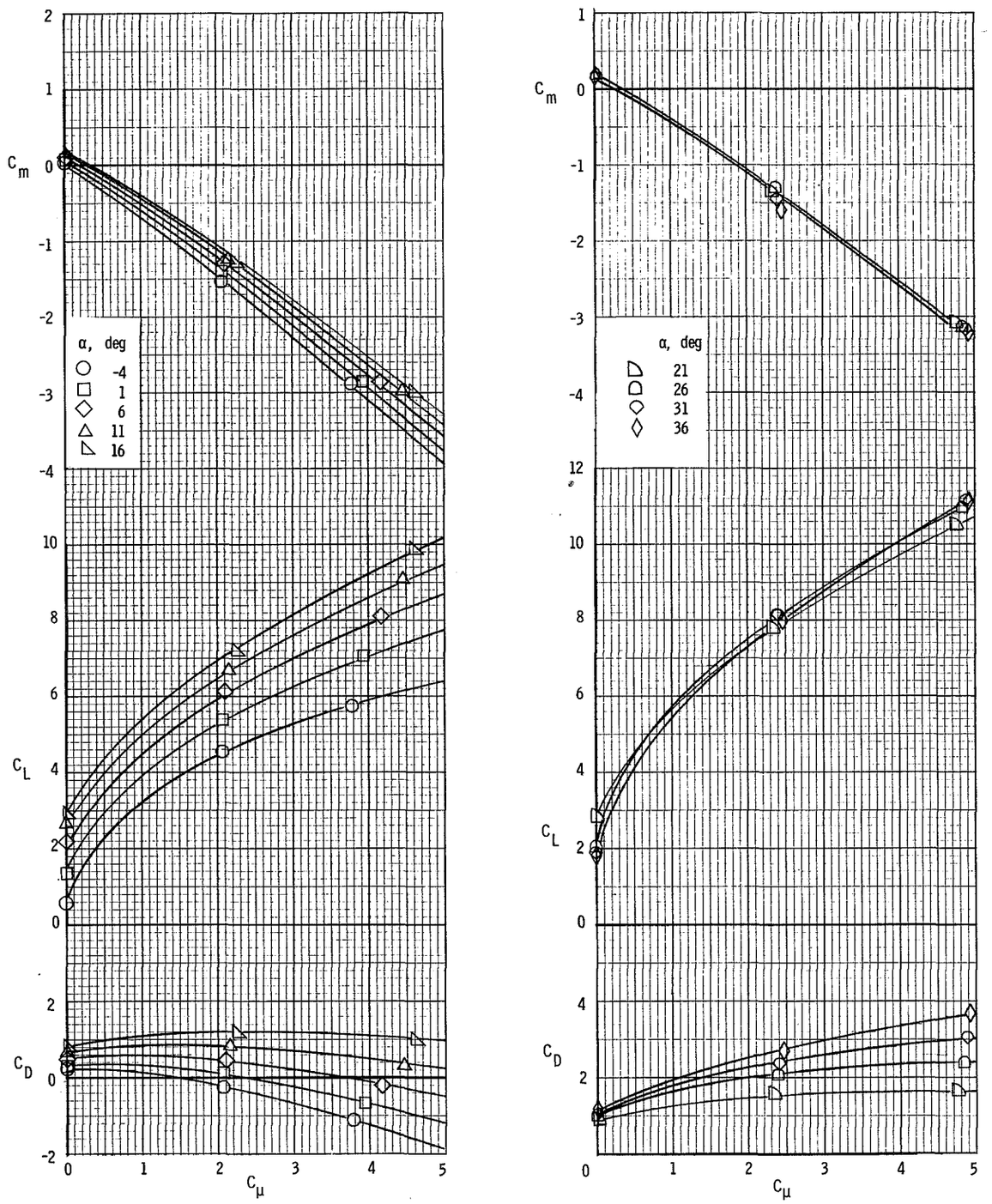

Figure 10.- Longitudinal characteristics of the model with drooped blown aileron. $\delta_f = 60^o$; $C_{\mu,a} = 0.04$; $\delta_a = 40^o$.

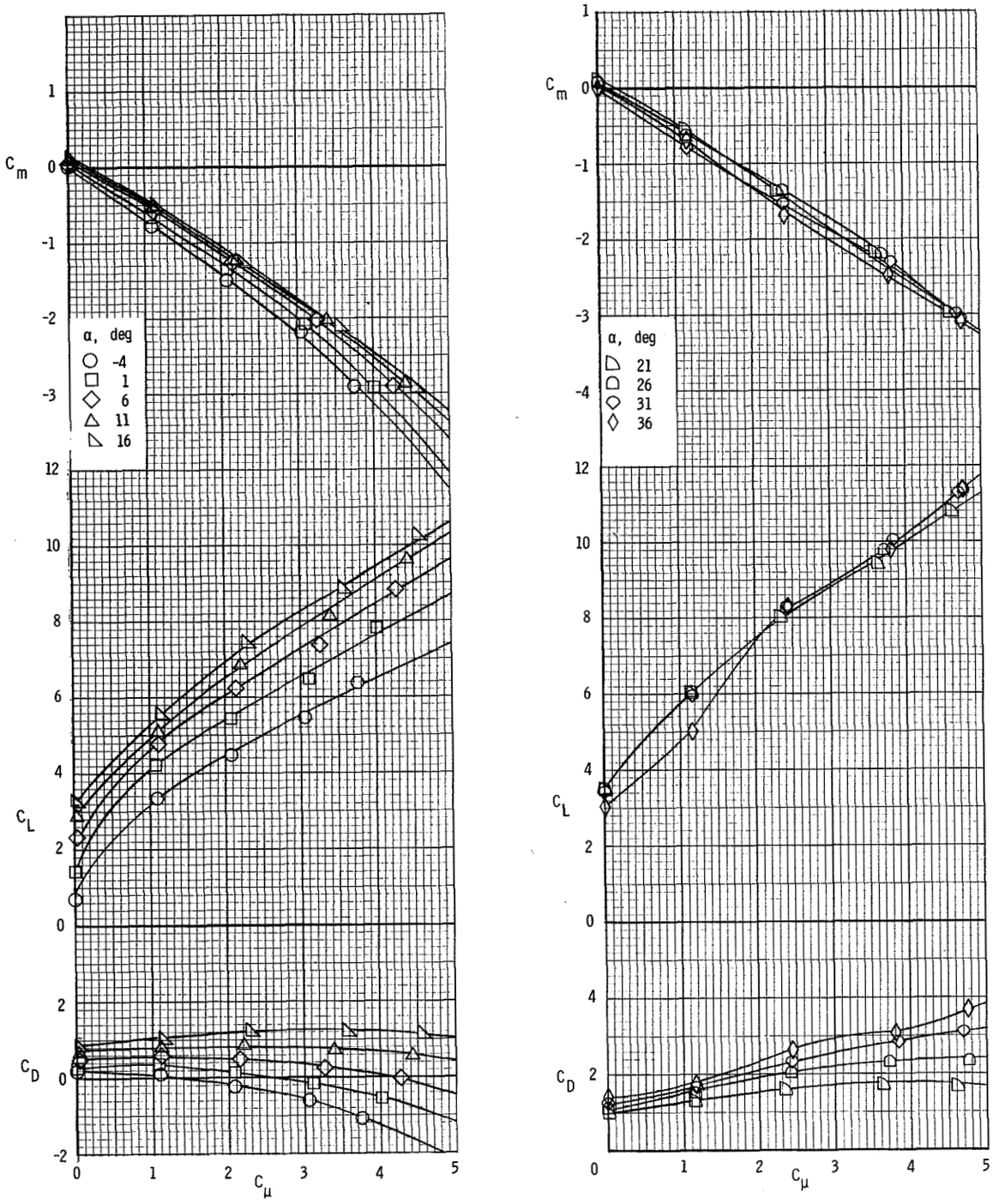

(a) $C_{\mu,le} = 0.04$. $C_{\mu,a} = 0.04$.

Figure 11.- Longitudinal characteristics of the model with leading-edge BLC and drooped blown aileron. $\delta_f = 60^o$.

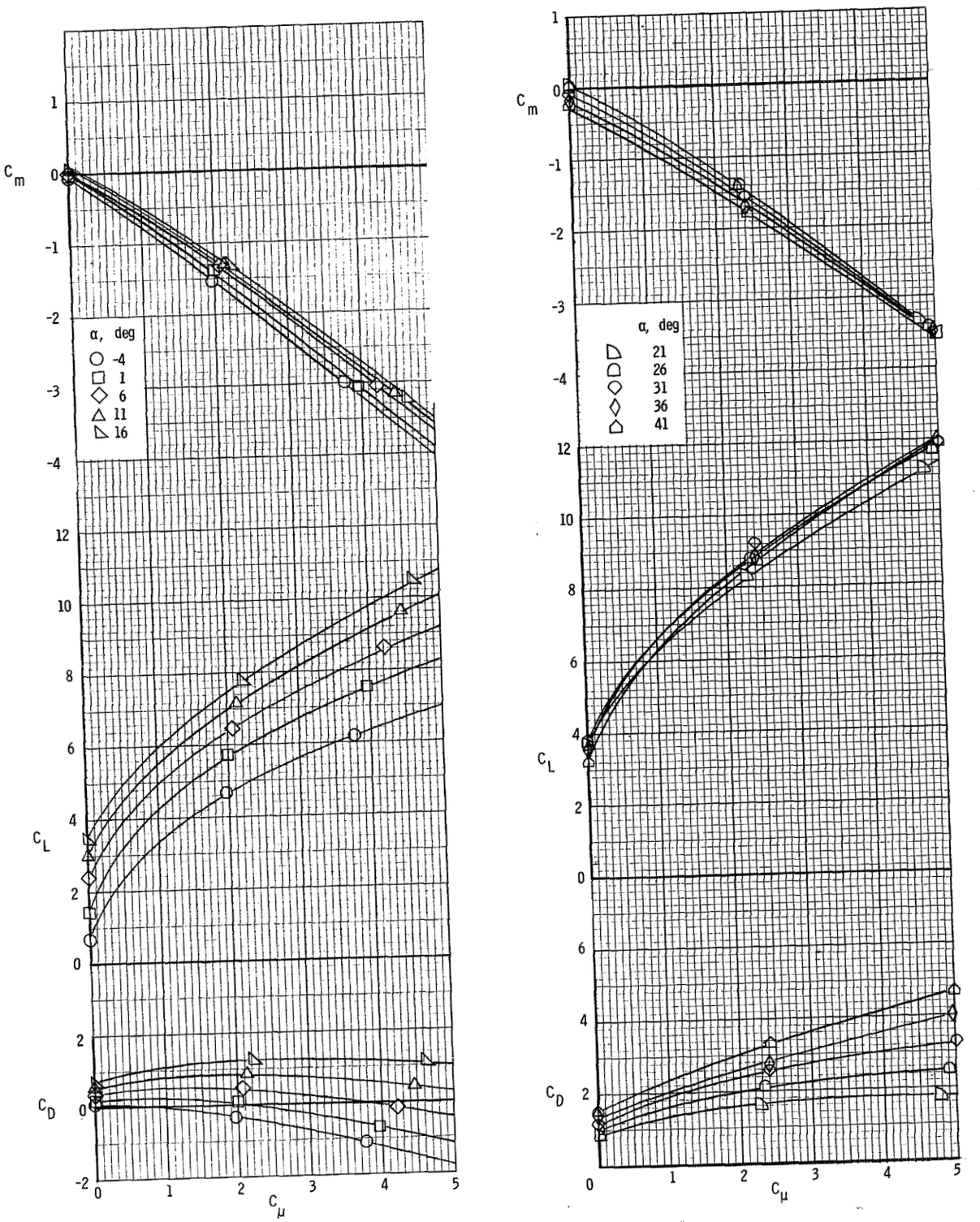

(b) $C_{\mu,le} = 0.08$. $C_{\mu,a} = 0.04$.

Figure 11.- Concluded.

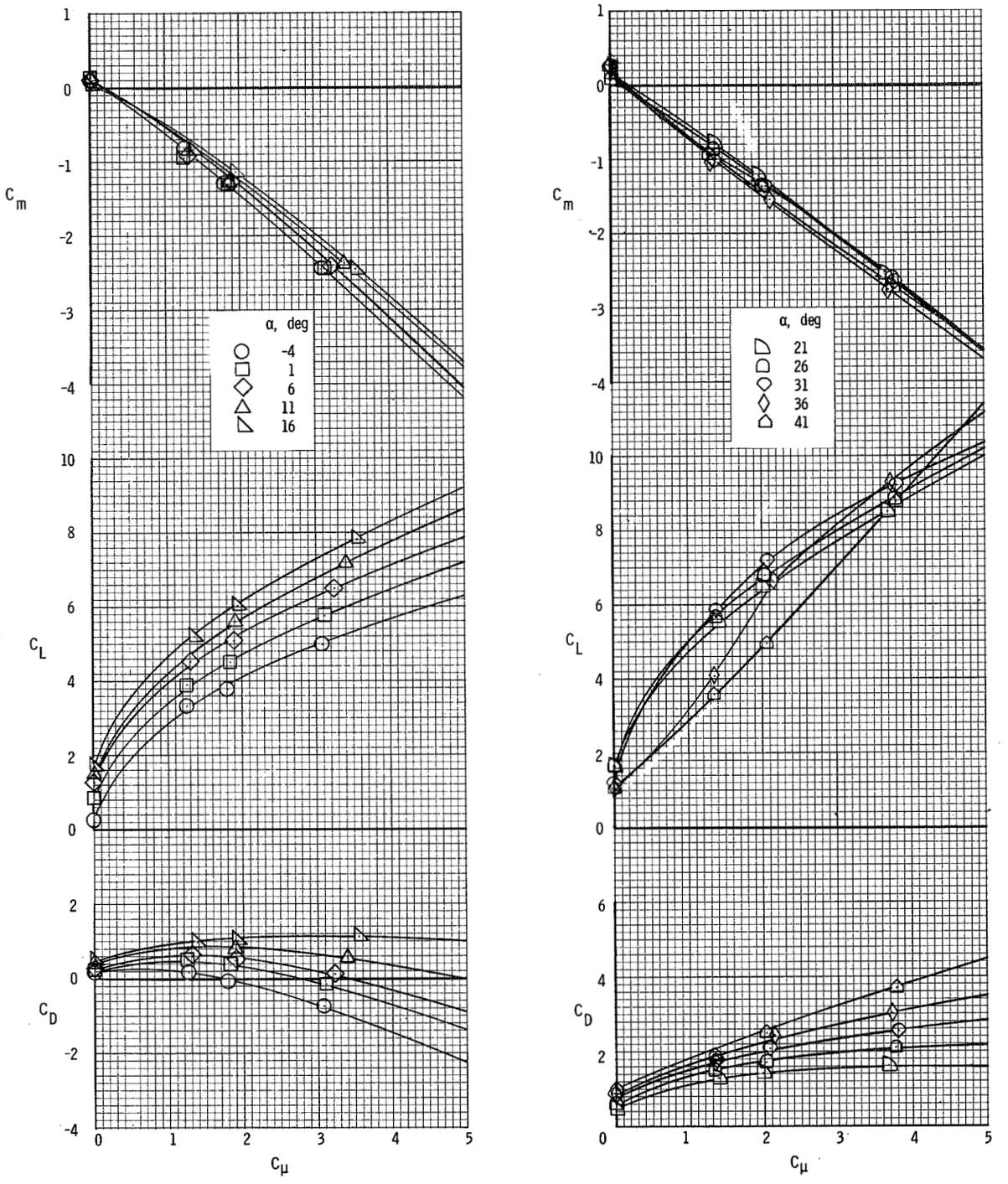

(a) $R = 0.45 \times 10^6$.

Figure 12.- Longitudinal characteristics of the model at several different values of Reynolds number. $\delta_f = 60^o$.

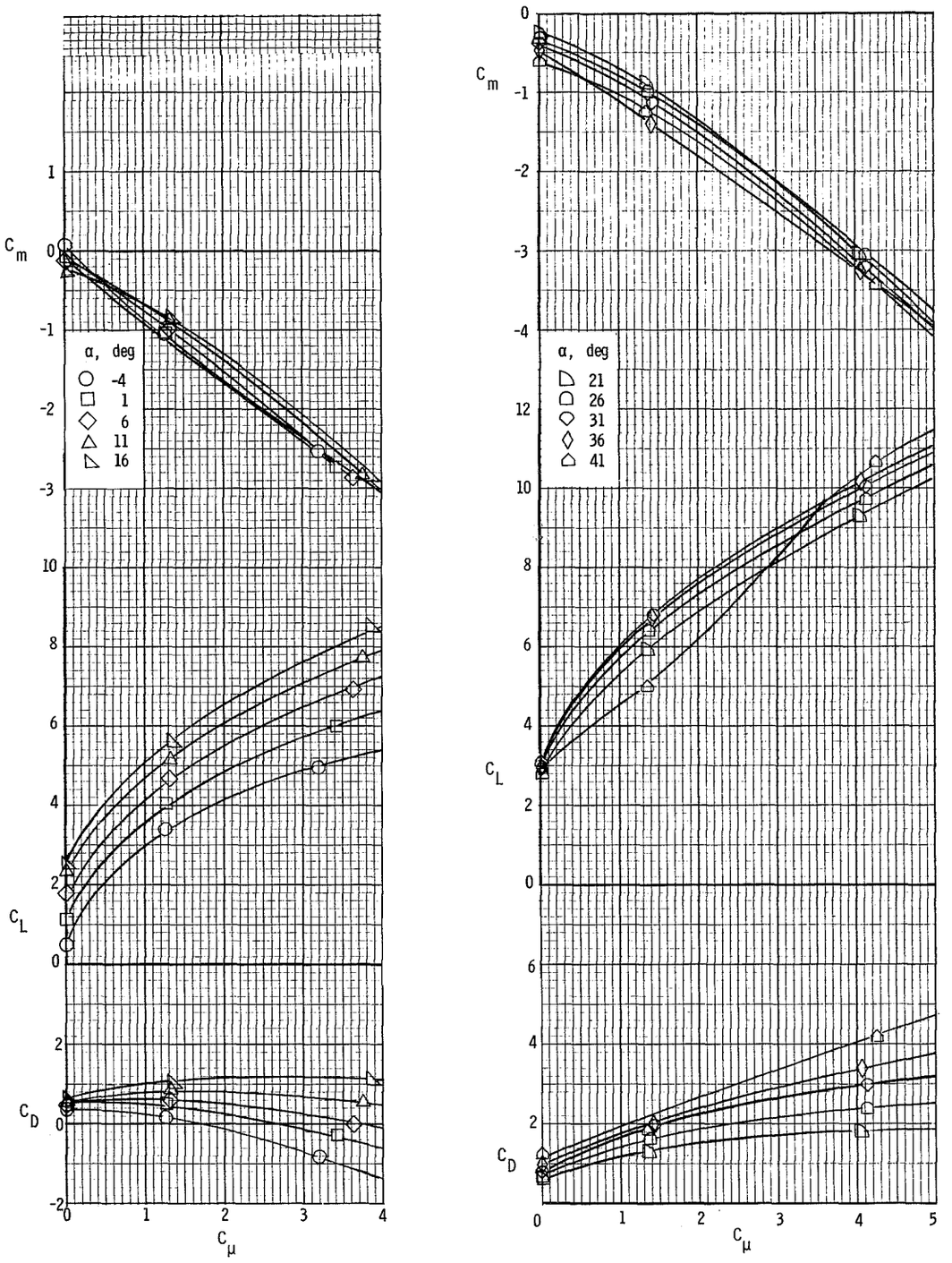

(b) $R = 0.45 \times 10^6$. $C_{\mu,le} = 0.06$.

Figure 12.- Continued.

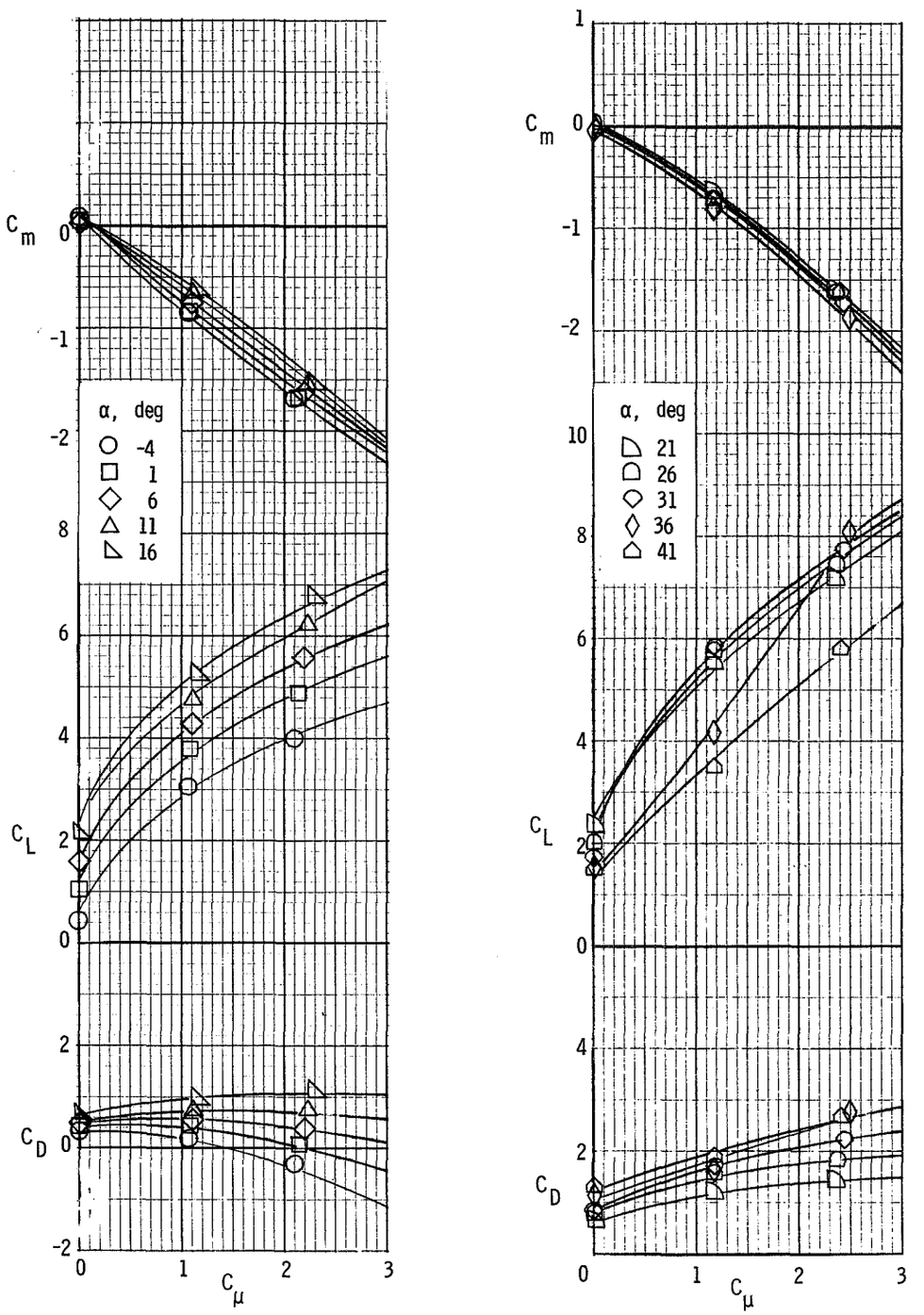

(c) $R = 0.6 \times 10^6$.

Figure 12.- Continued.

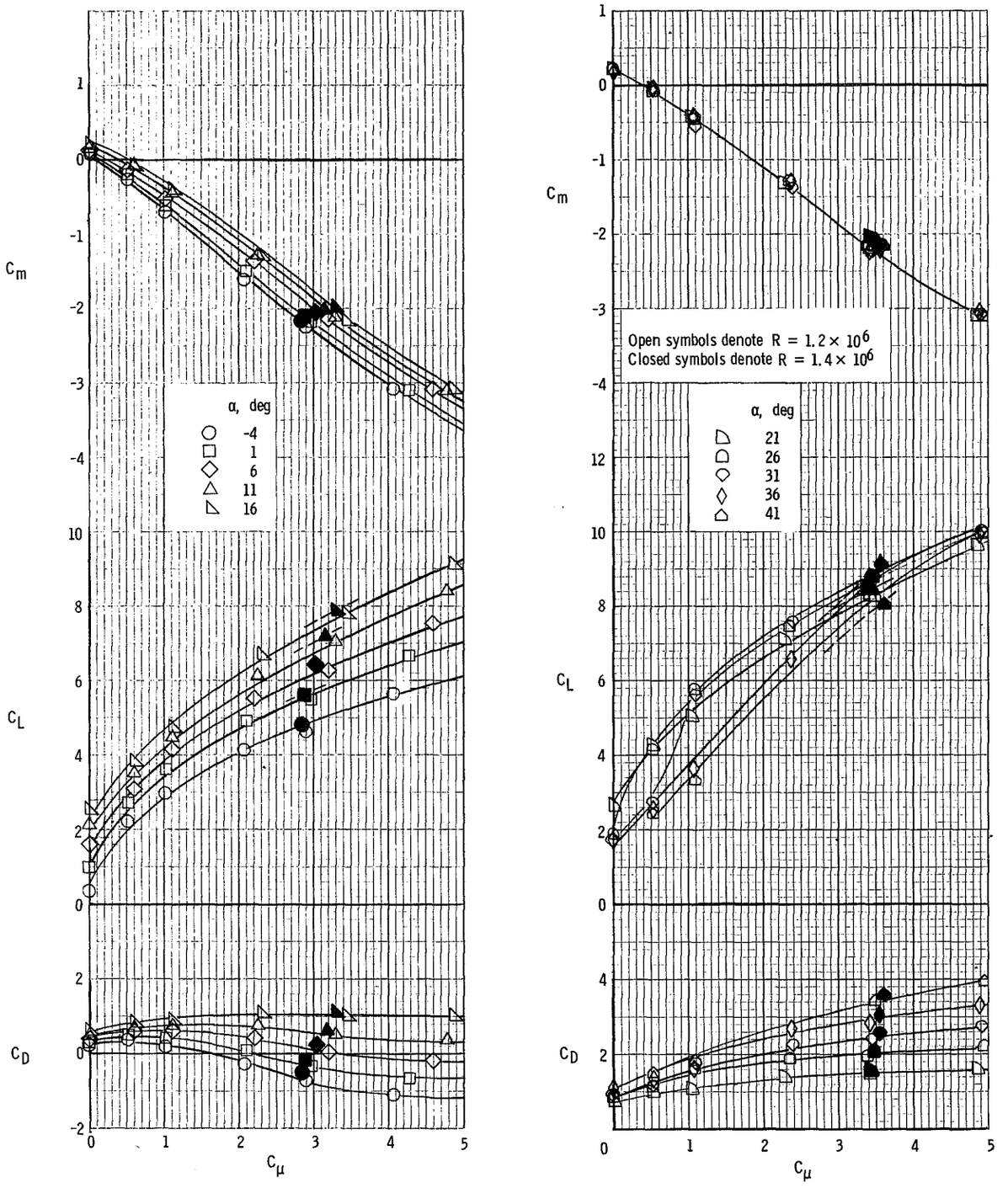

(d) Data for $R = 1.4 \times 10^6$ compared with baseline data of $R = 1.2 \times 10^6$.

Figure 12.- Continued.

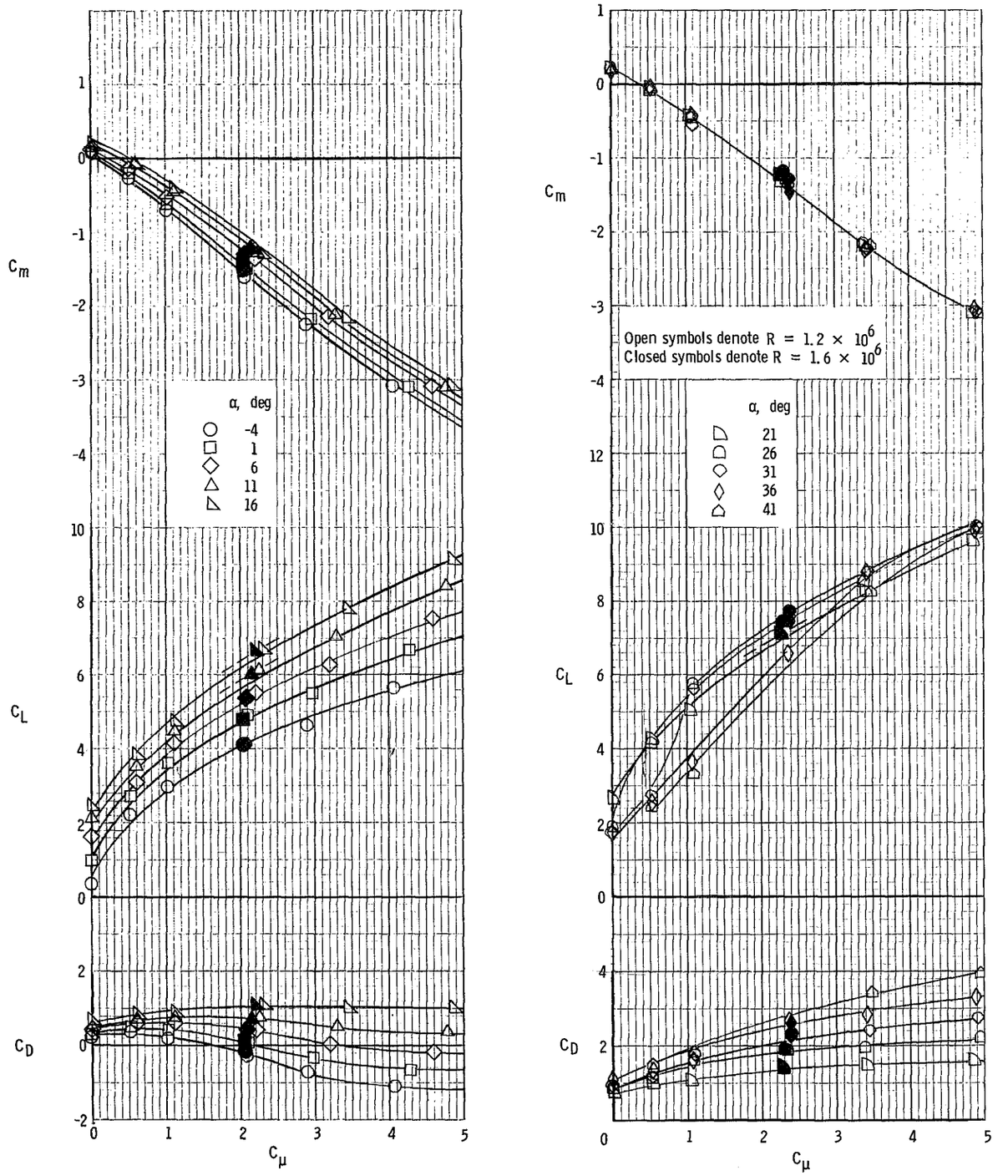

(e) Data for $R = 1.6 \times 10^6$ compared with baseline data of $R = 1.2 \times 10^6$.

Figure 12.- Continued.

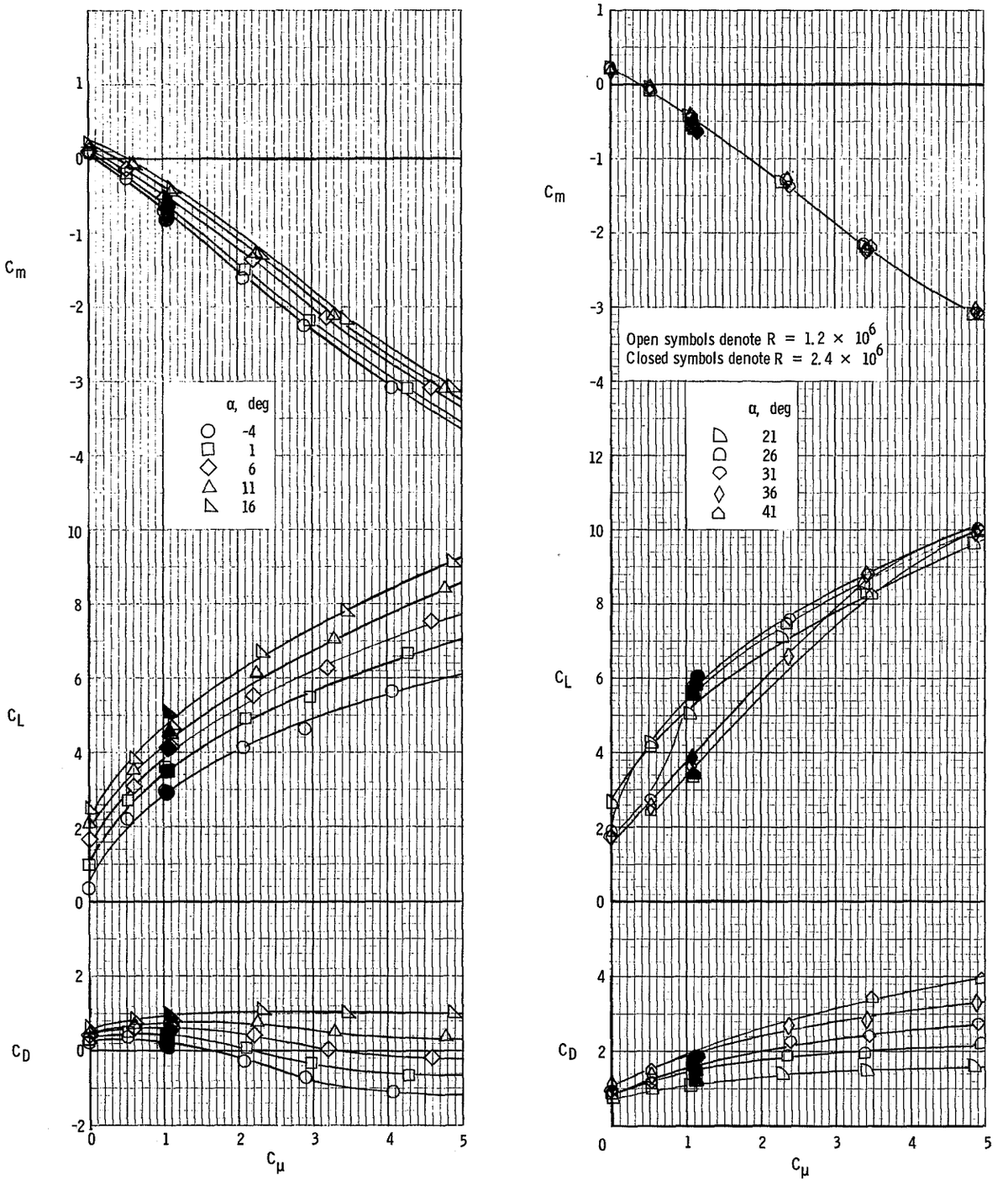

(f) Data for $R = 2.4 \times 10^6$ compared with baseline data of $R = 1.2 \times 10^6$.

Figure 12.- Continued.

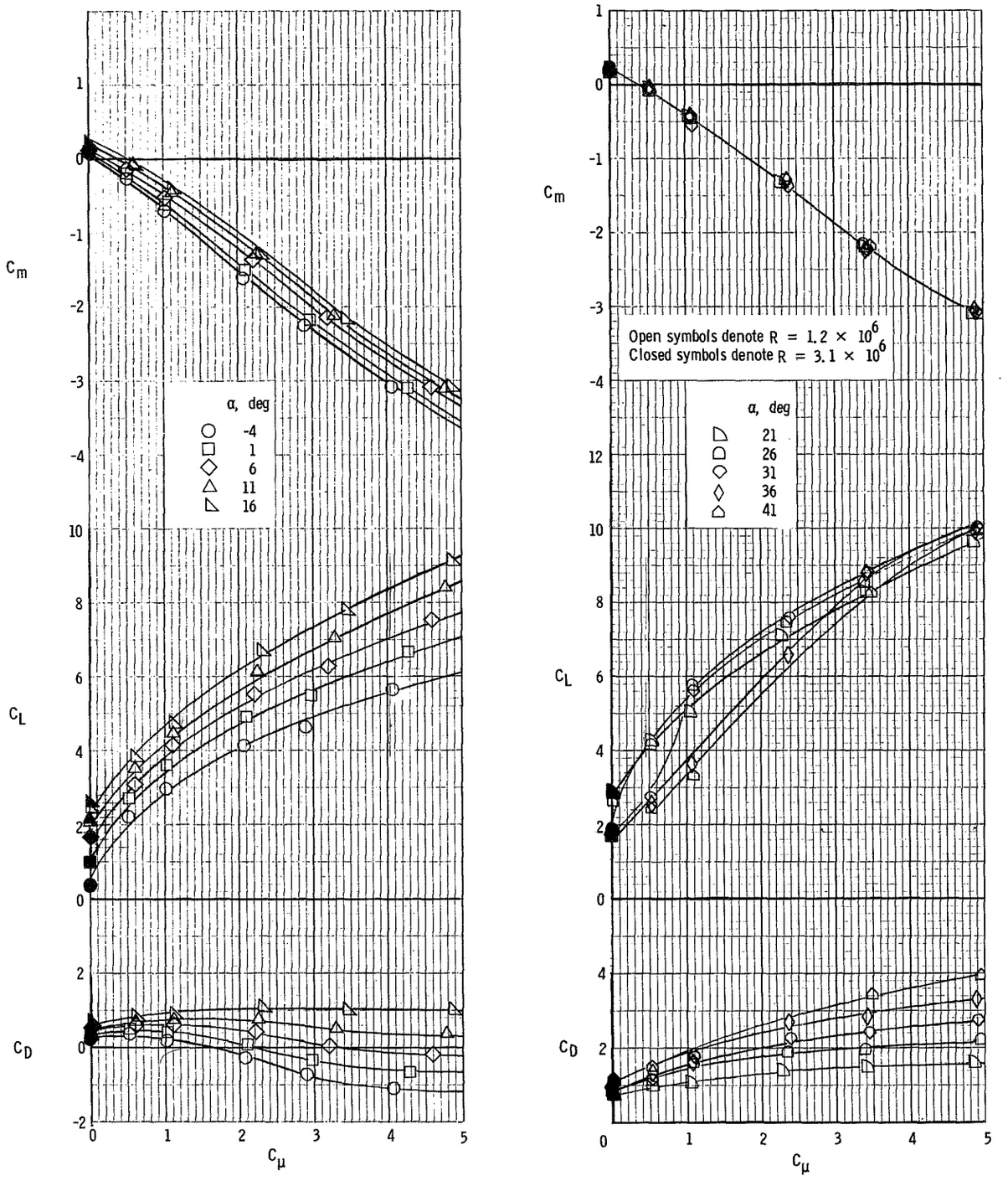

(g) Data for $R = 3.1 \times 10^6$ compared with baseline data of $R = 1.2 \times 10^6$.

Figure 12.- Concluded.

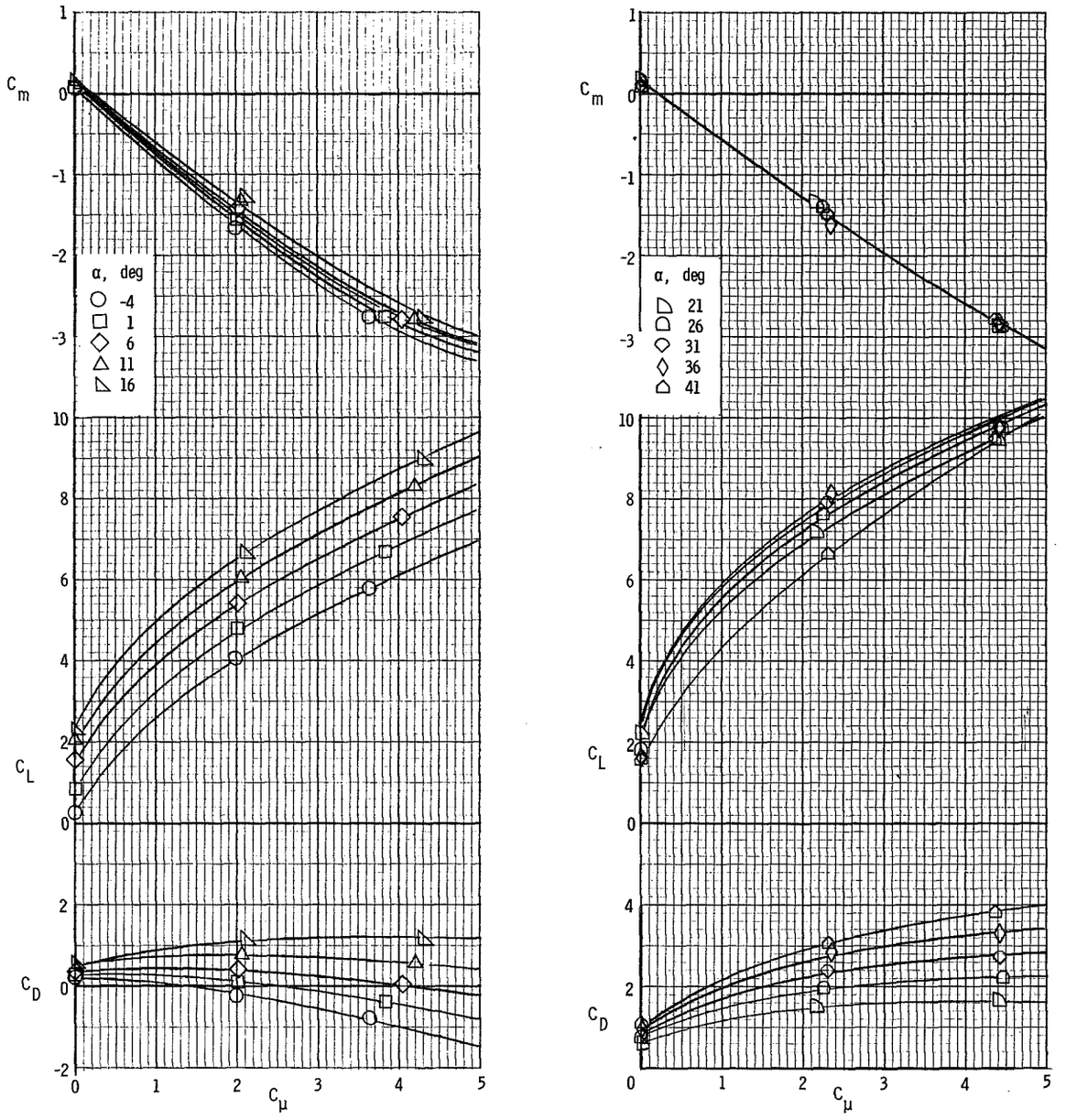

Figure 13.- Longitudinal characteristics of the model with span of inboard flap increased. $\delta_f = 60^o$.

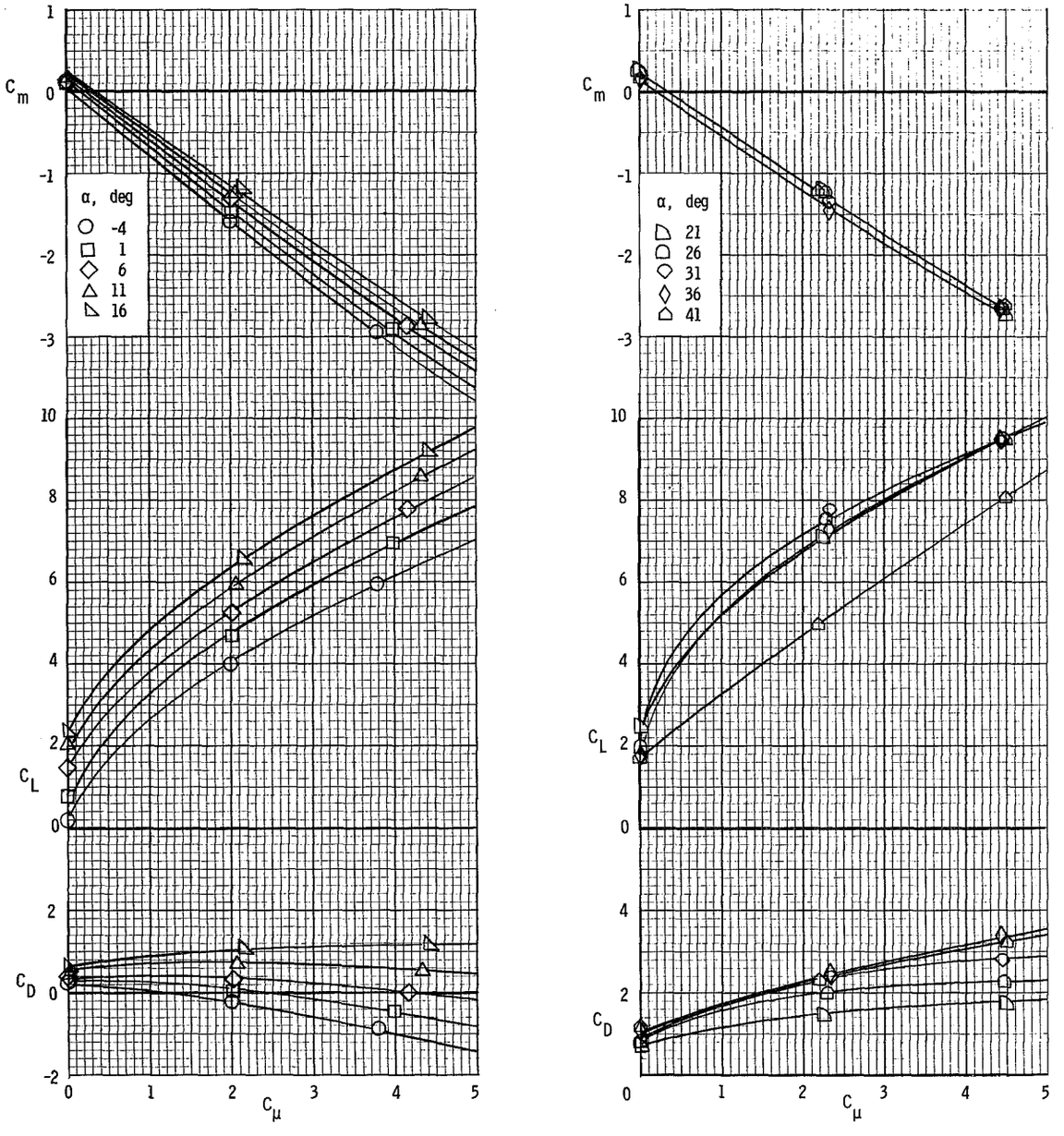

Figure 14.- Longitudinal characteristics of the model with $A_n = 6$. $\delta_f = 60^o$.

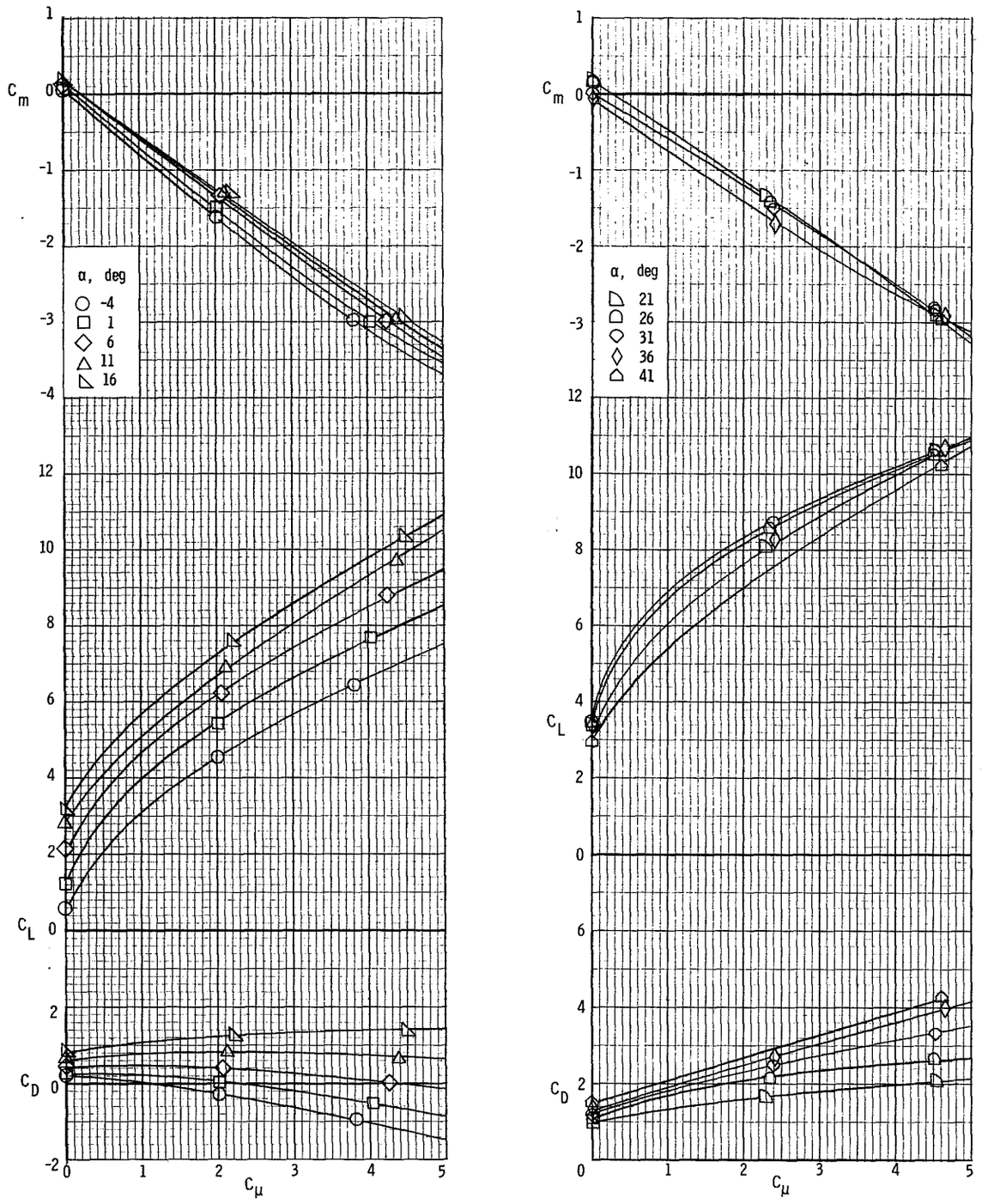

Figure 15.- Longitudinal characteristics of the model with $A_n = 6$. $\delta_f = 60^o$; $C_{\mu,le} = 0.04$; $C_{\mu,a} = 0.04$; $\delta_a = 40^o$.

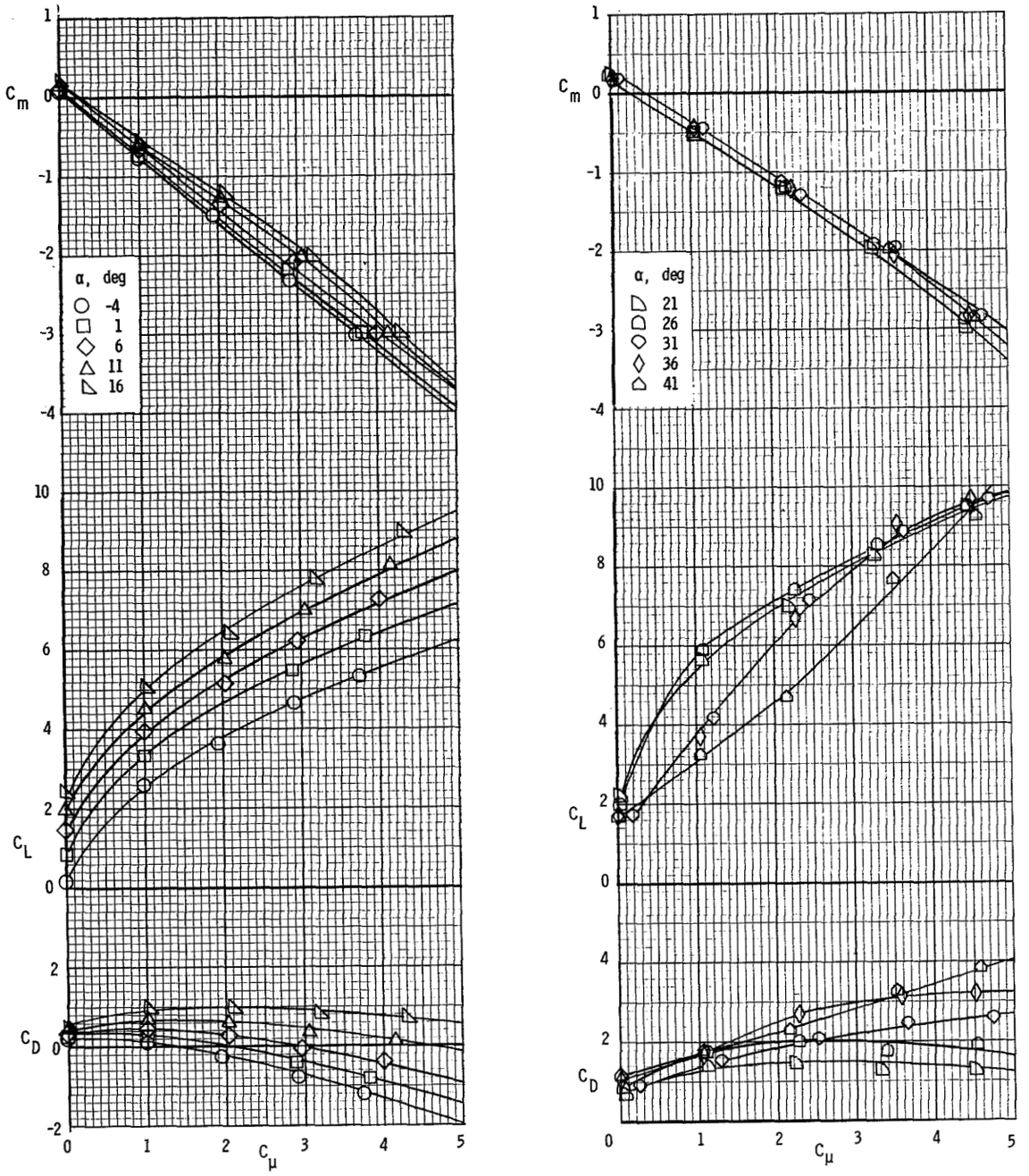

Figure 16.- Longitudinal characteristics of the model with $A_n = 2$. $\delta_f = 60^o$; deflector 1.

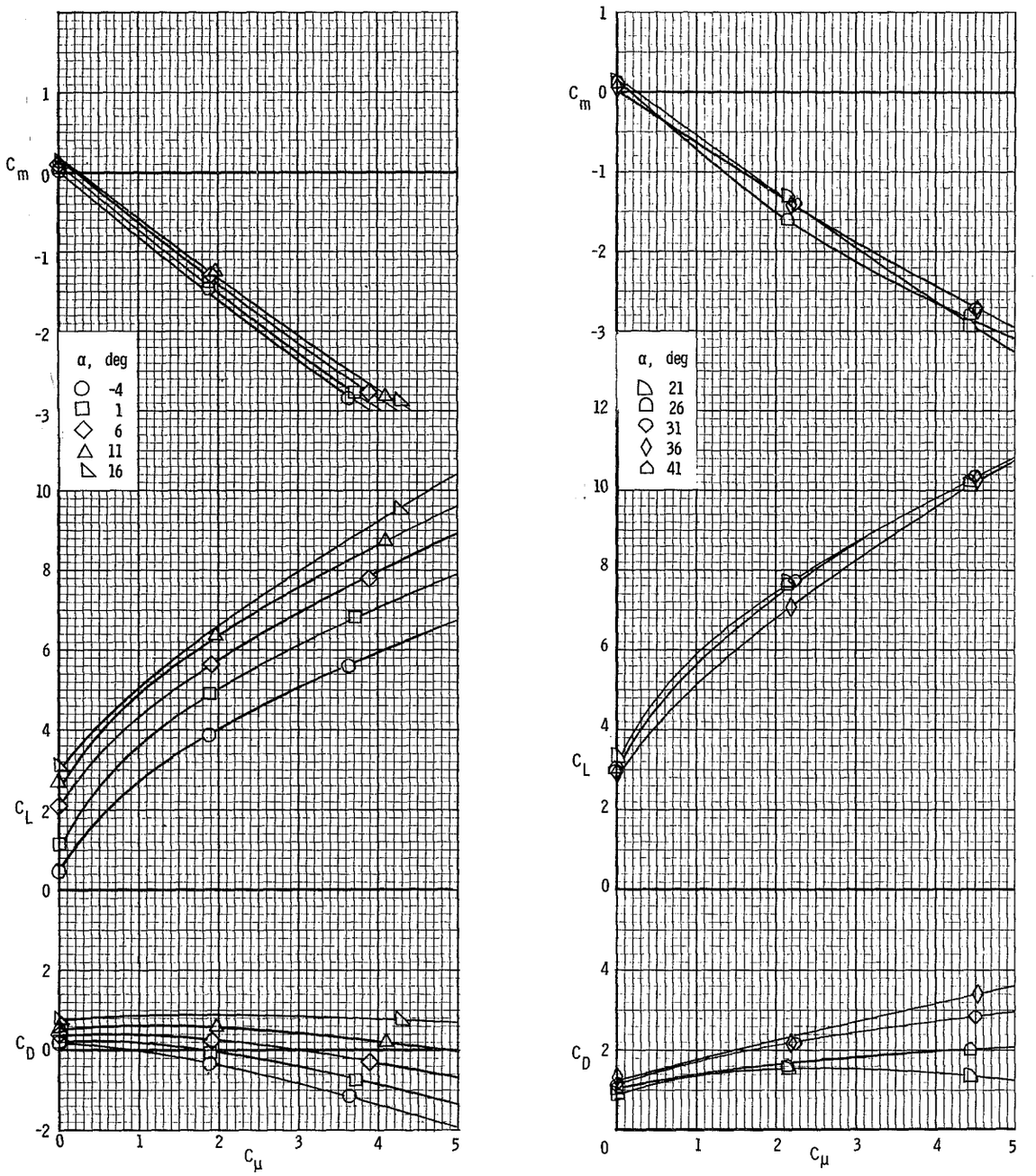

Figure 17.- Longitudinal characteristics of the model with $A_n = 2$. $\delta_f = 60^o$; $C_{\mu,le} = 0.04$; $C_{\mu,a} = 0.04$; $\delta_a = 40^o$; deflector 1.

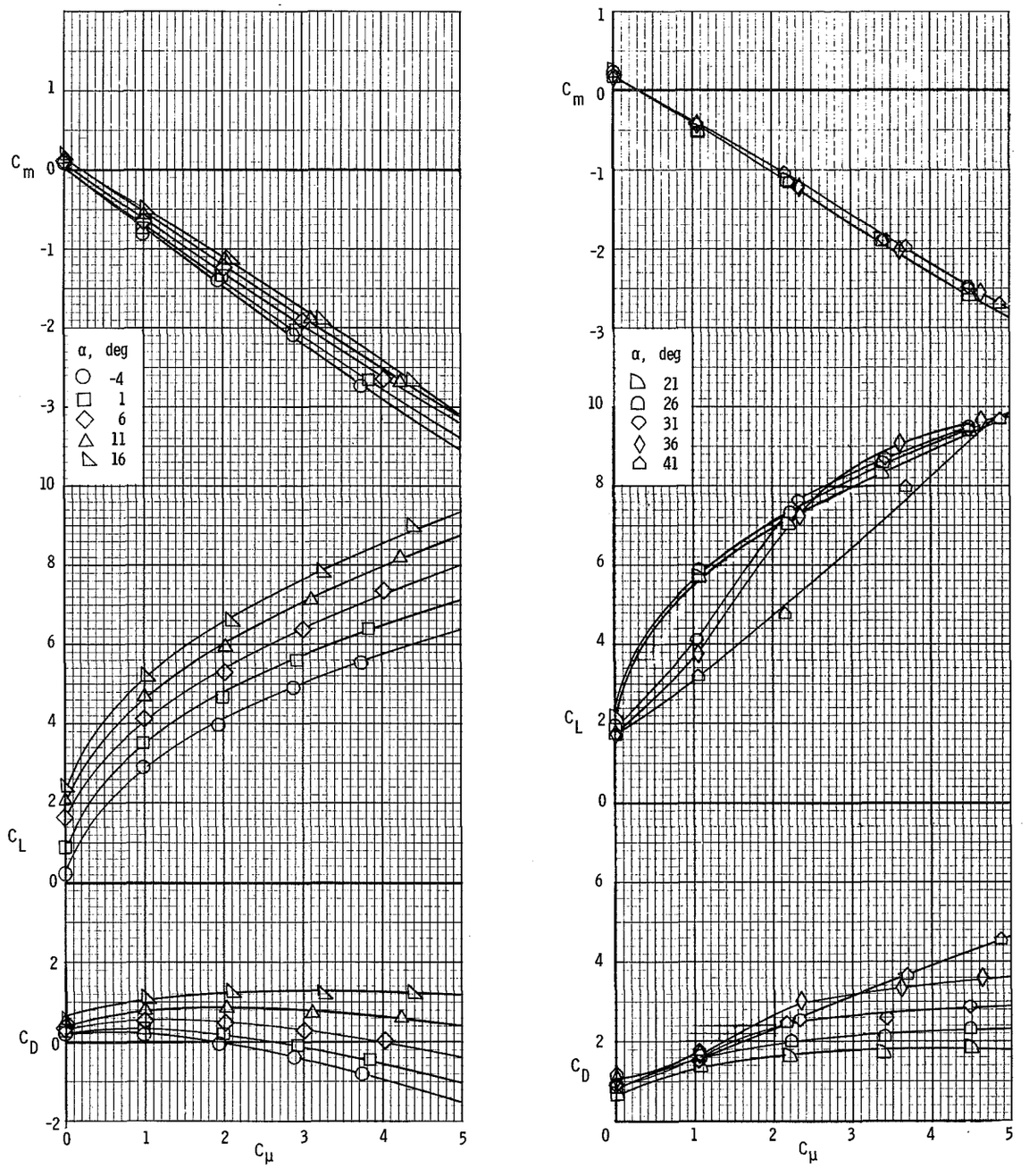

Figure 18.- Longitudinal characteristics of the model with $A_n = 2$. $\delta_f = 60^o$; deflector 2.

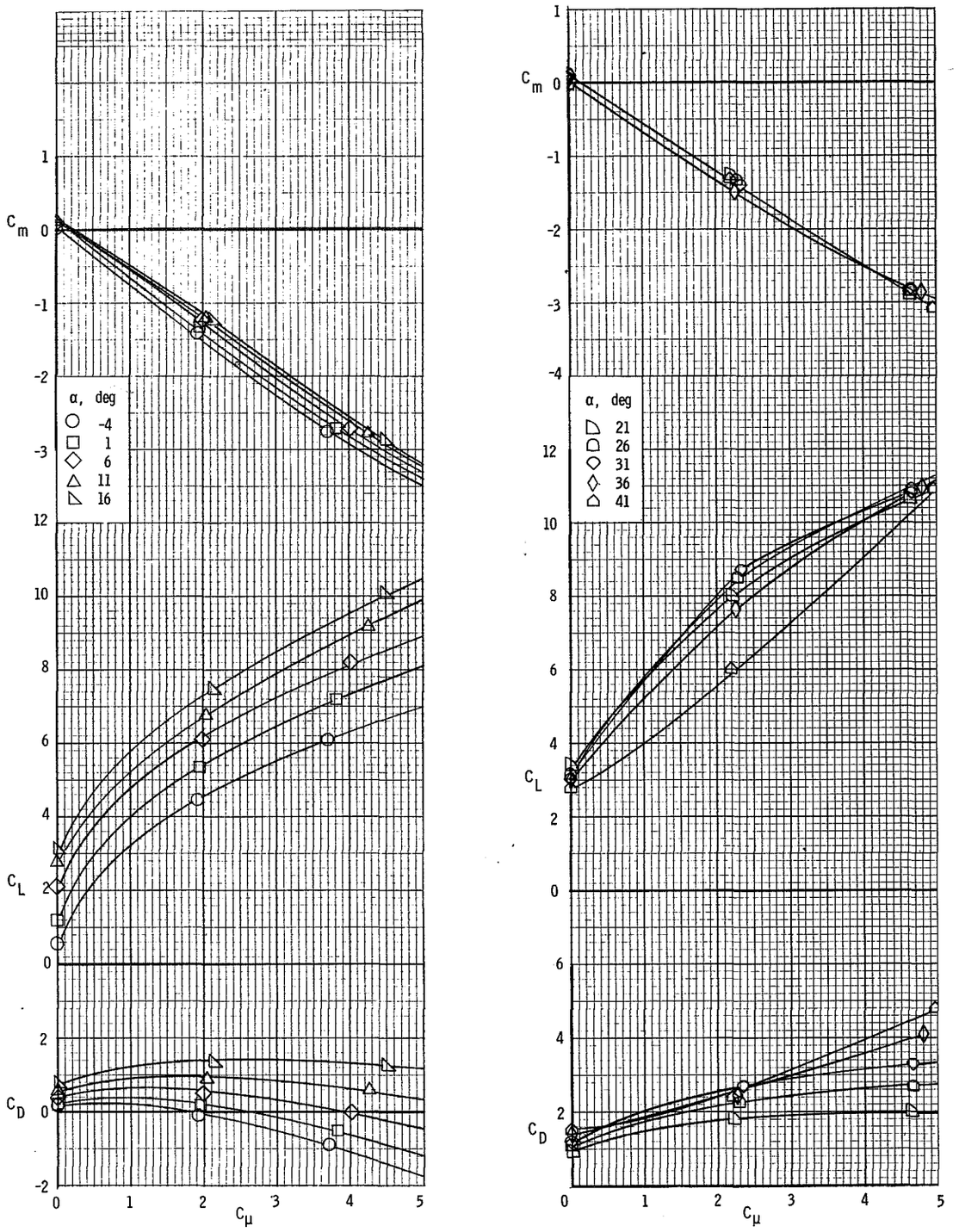

Figure 19.- Longitudinal characteristics of the model with $A_n = 2$. $\delta_f = 60^o$; $C_{\mu,le} = 0.04$; $C_{\mu,a} = 0.04$; $\delta_a = 40^o$; deflector 2.

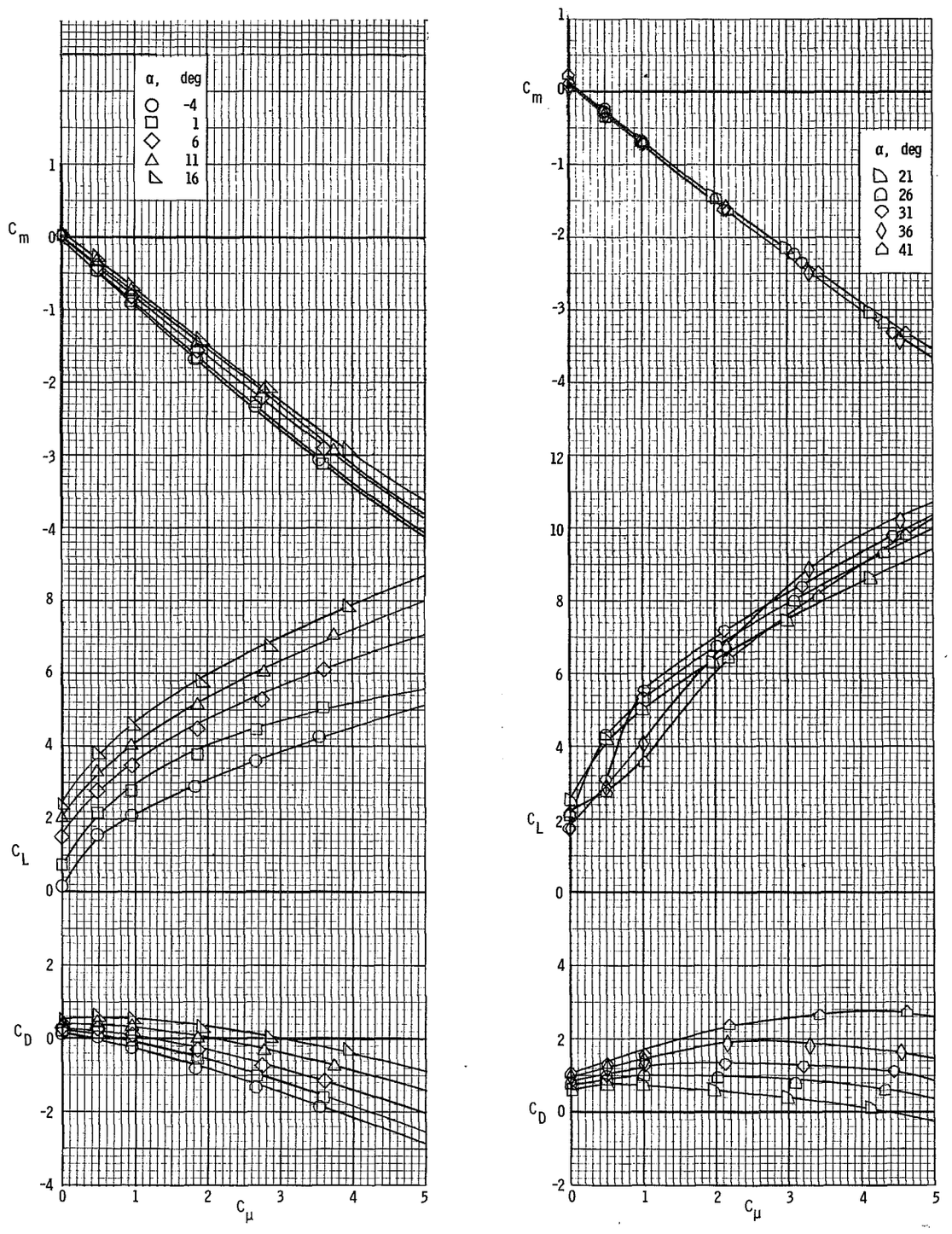

Figure 20.- Longitudinal characteristics of the model. $\delta_f = 40^o$.

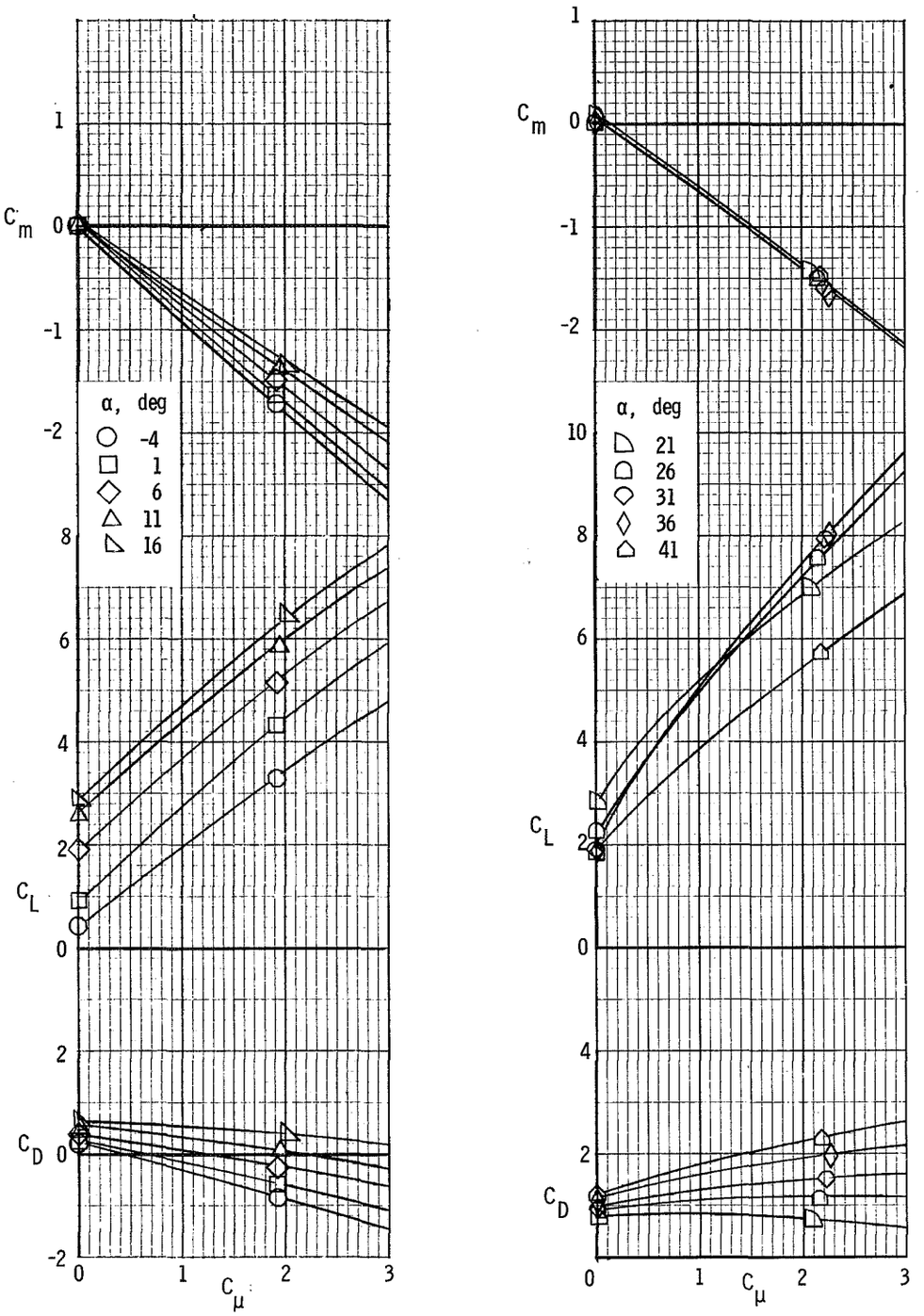

Figure 21.- Longitudinal characteristics of the model with drooped blown aileron. $\delta_f = 40^o$; $C_{\mu,a} = 0.04$; $\delta_a = 40^o$.

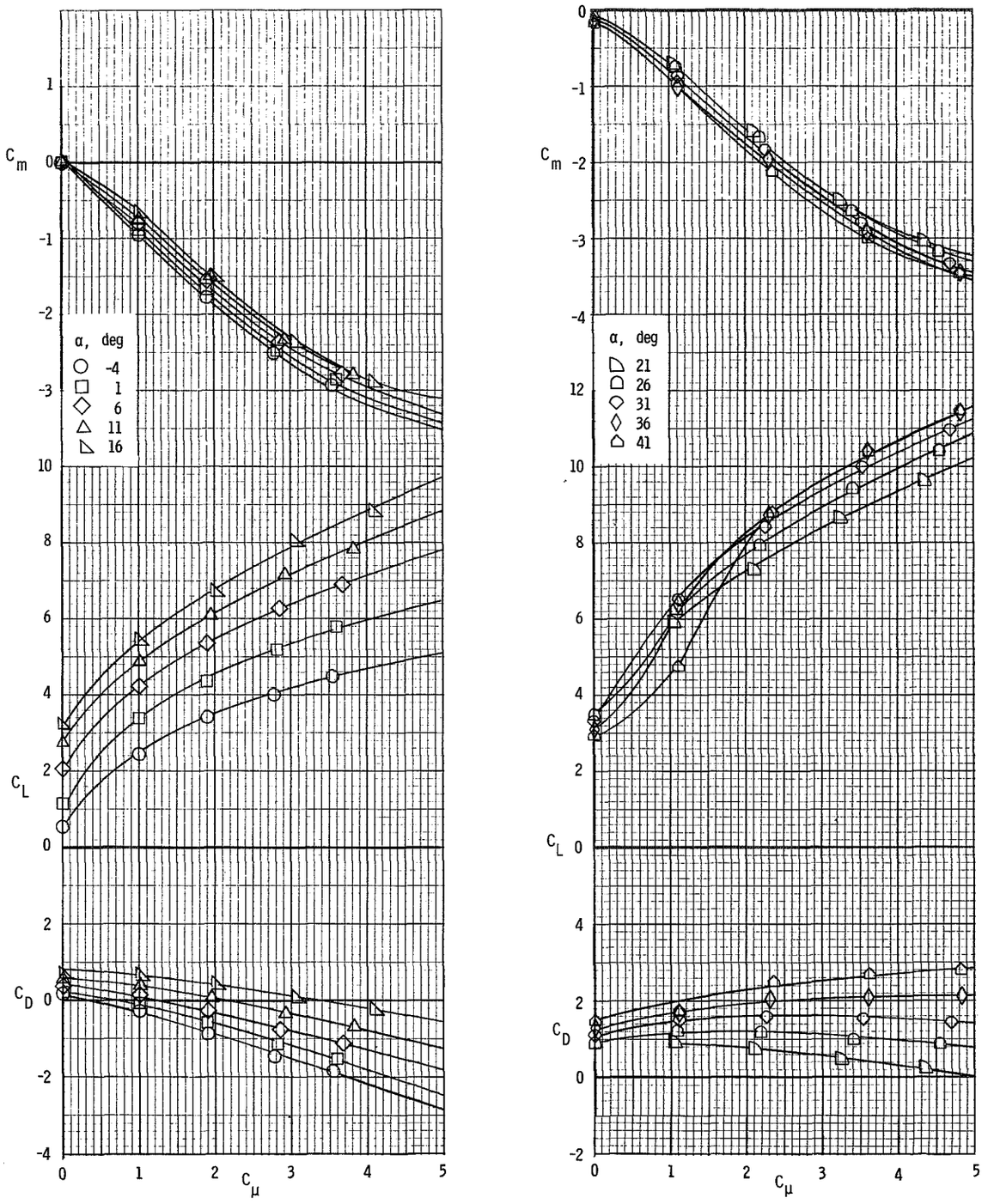

(a) $C_{\mu,le} = 0.04$. $C_{\mu,a} = 0.04$.

Figure 22.- Longitudinal characteristics of the model with leading-edge BLC and drooped blown aileron. $\delta_f = 40^o$.

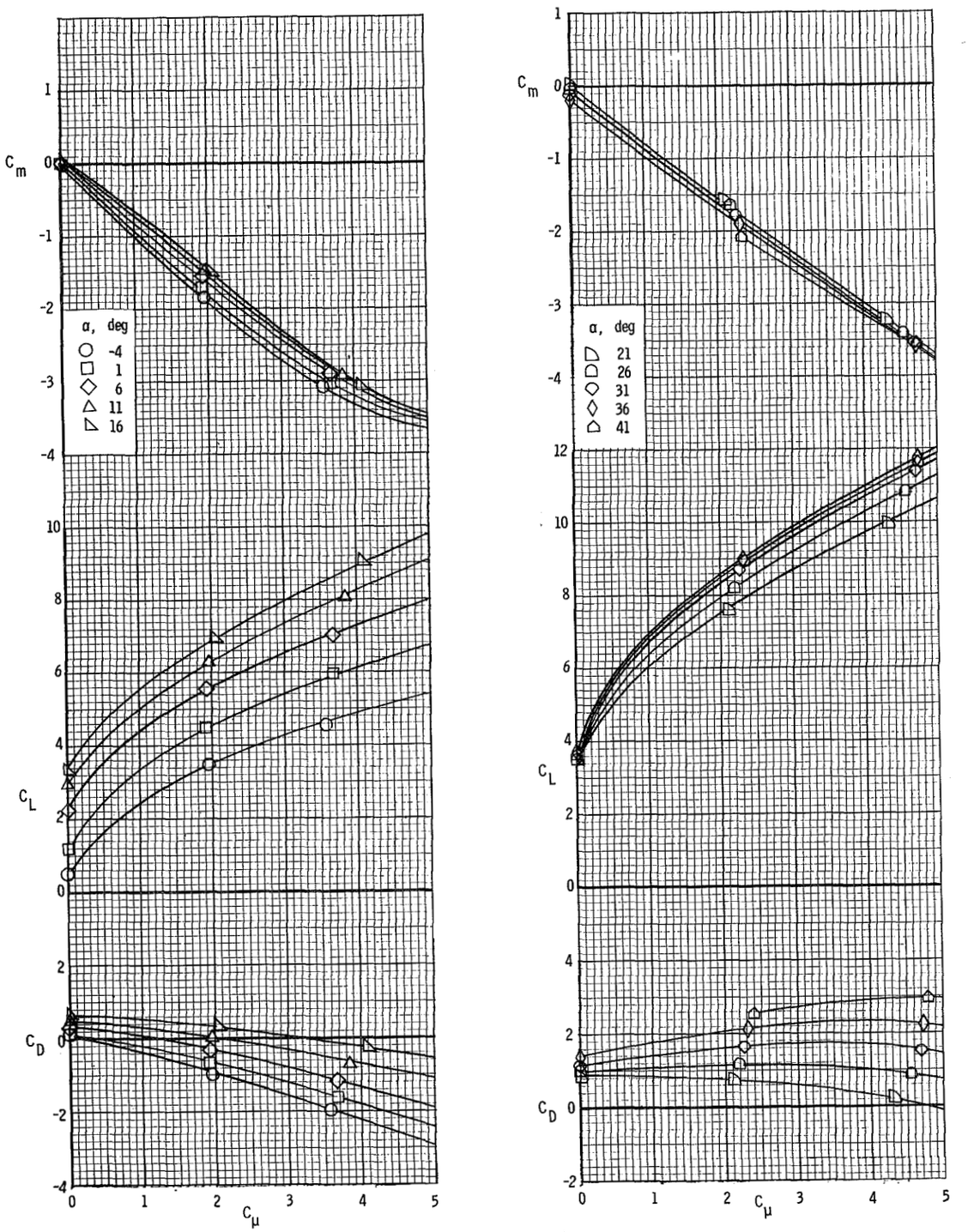

(b) $C_{\mu,le} = 0.08$. $C_{\mu,a} = 0.04$.

Figure 22.- Concluded.

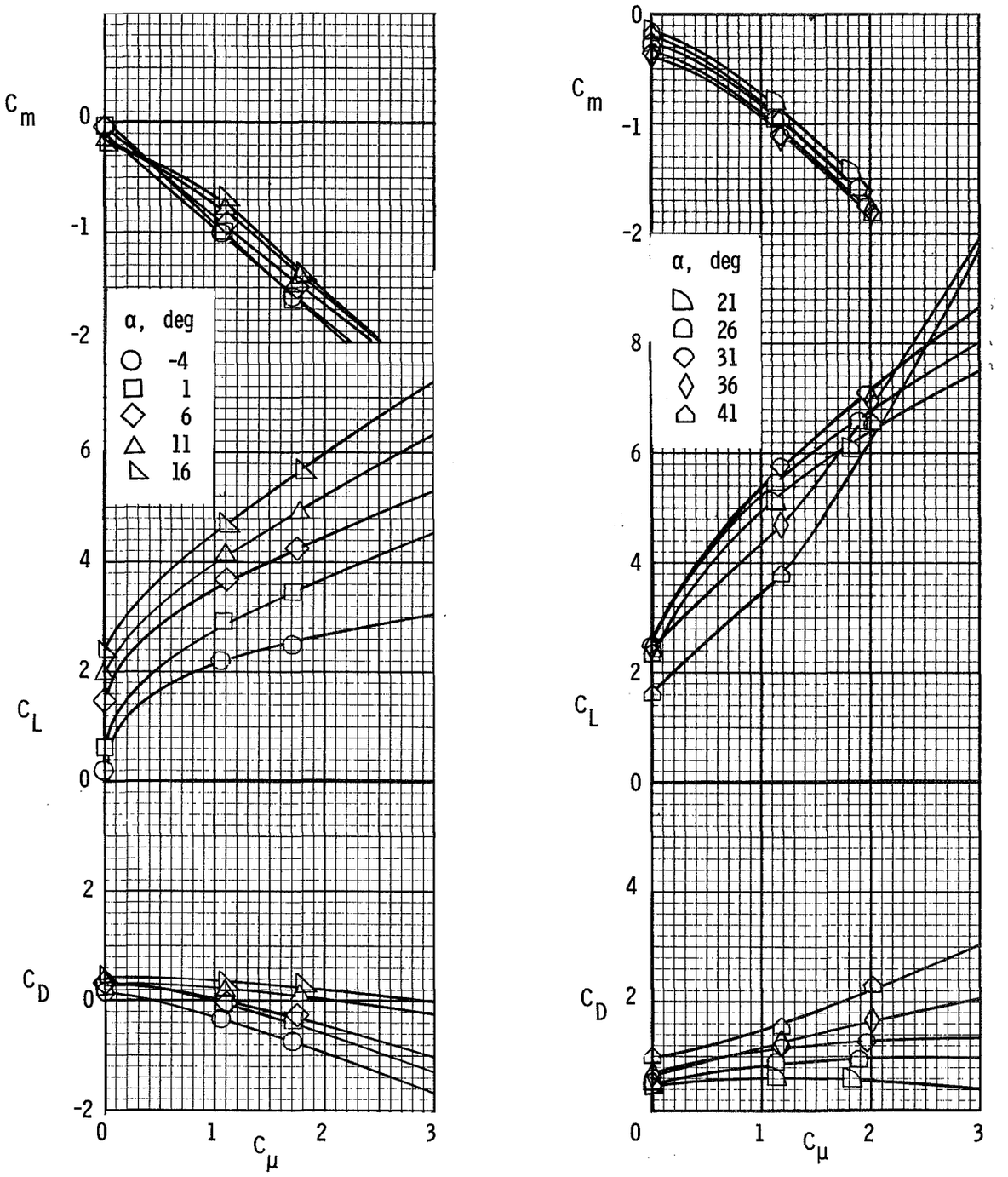

(a) $R = 0.45 \times 10^6$.

Figure 23.- Longitudinal characteristics of the model at several different values of Reynolds number. $\delta_f = 40^o$.

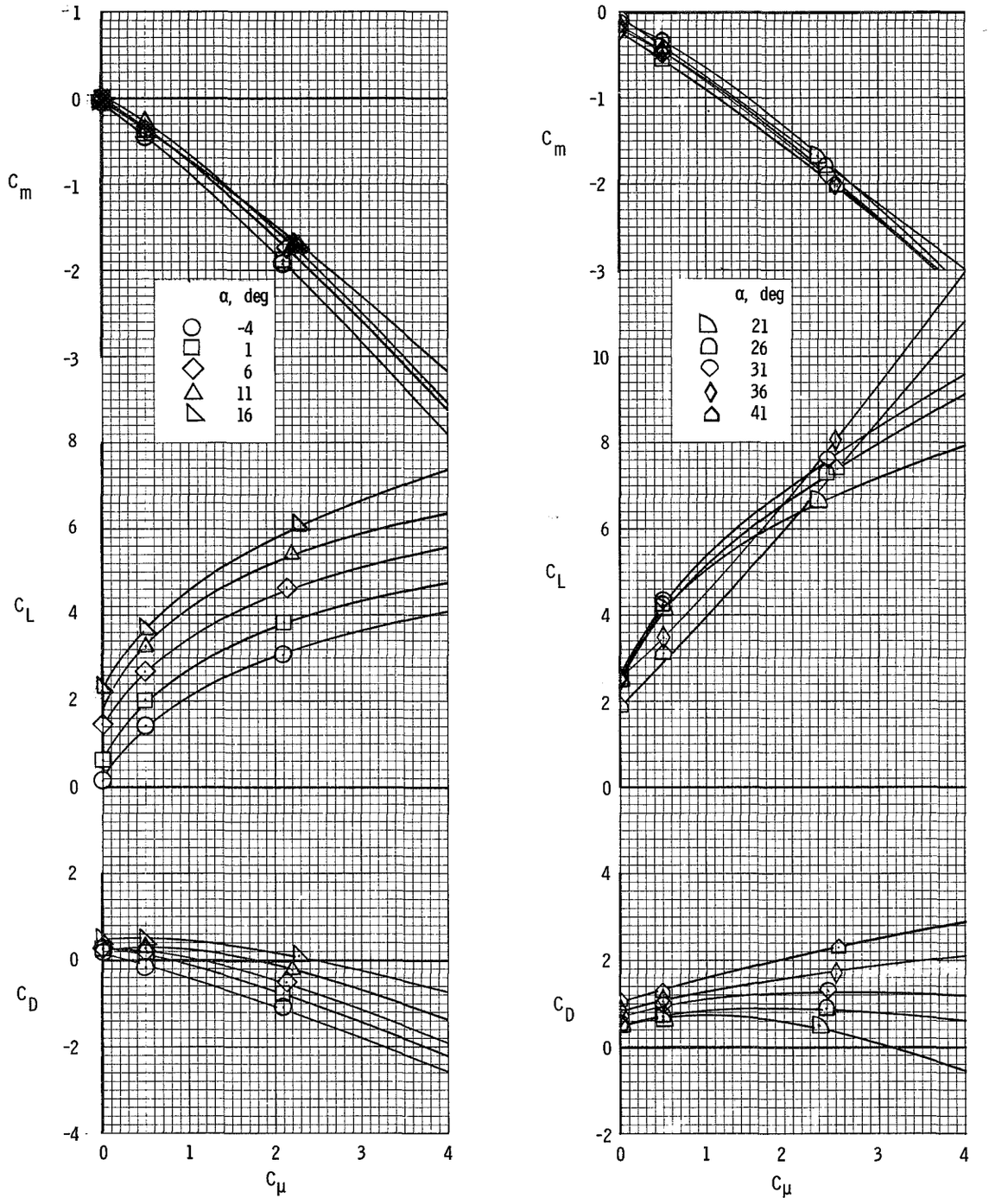

(b) $R = 0.6 \times 10^6$.

Figure 23.- Continued.

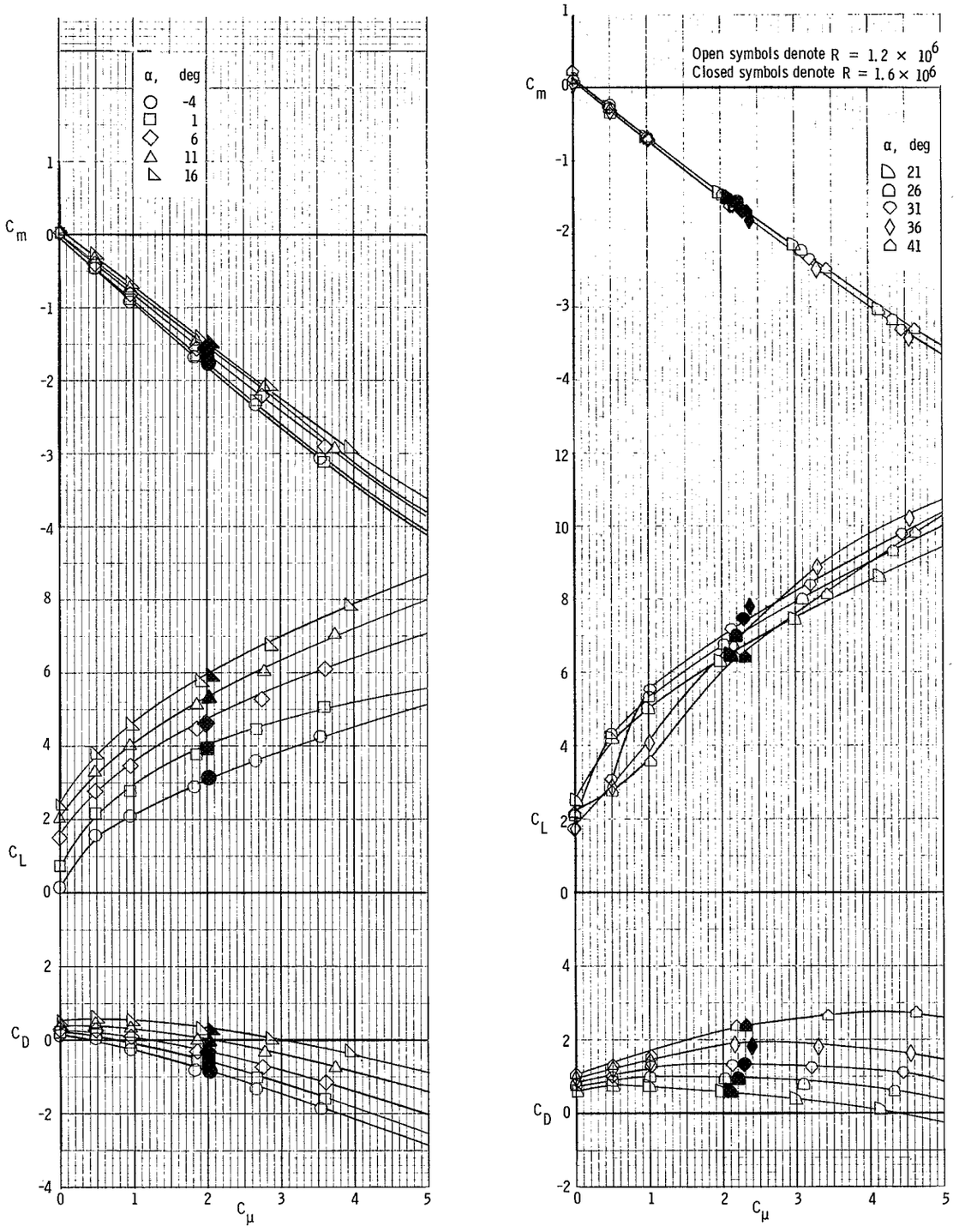

(c) Data for $R = 1.6 \times 10^6$ compared with baseline data of $R = 1.2 \times 10^6$.

Figure 23.- Continued.

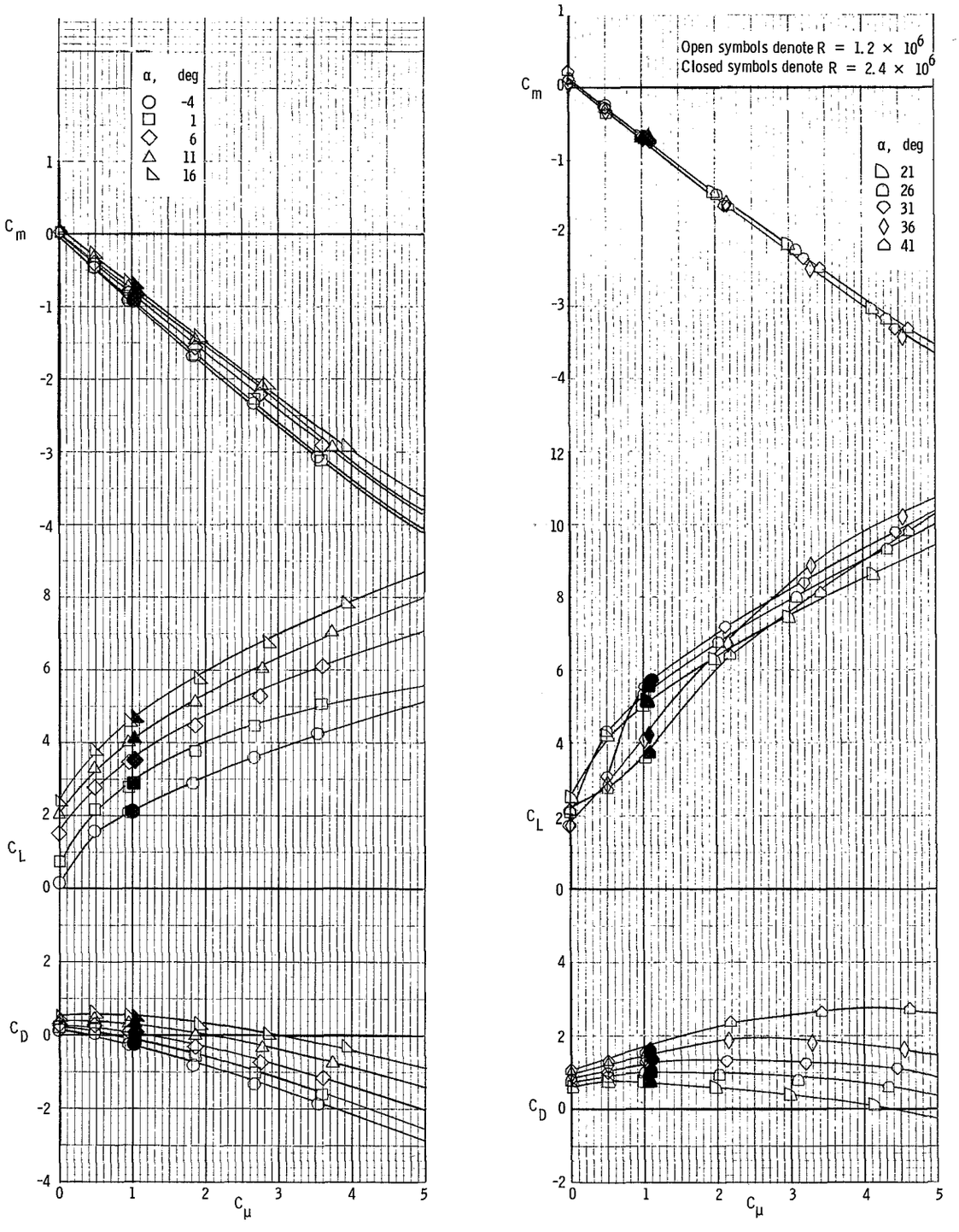

(d) Data for $R = 2.4 \times 10^6$ compared with baseline data of $R = 1.2 \times 10^6$.

Figure 23.- Continued.

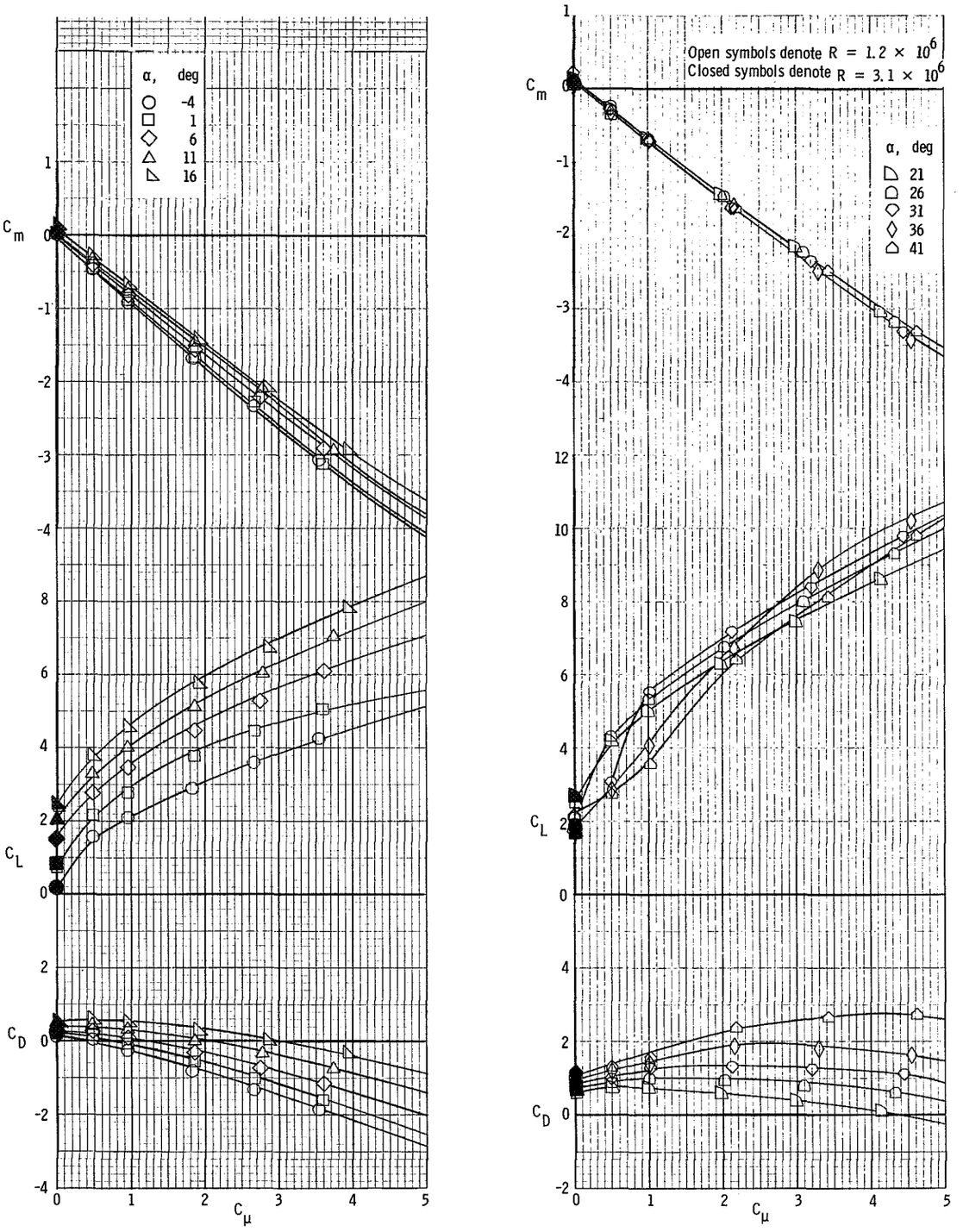

(e) Data for $R = 3.1 \times 10^6$ compared with baseline data of $R = 1.2 \times 10^6$.

Figure 23.- Concluded.

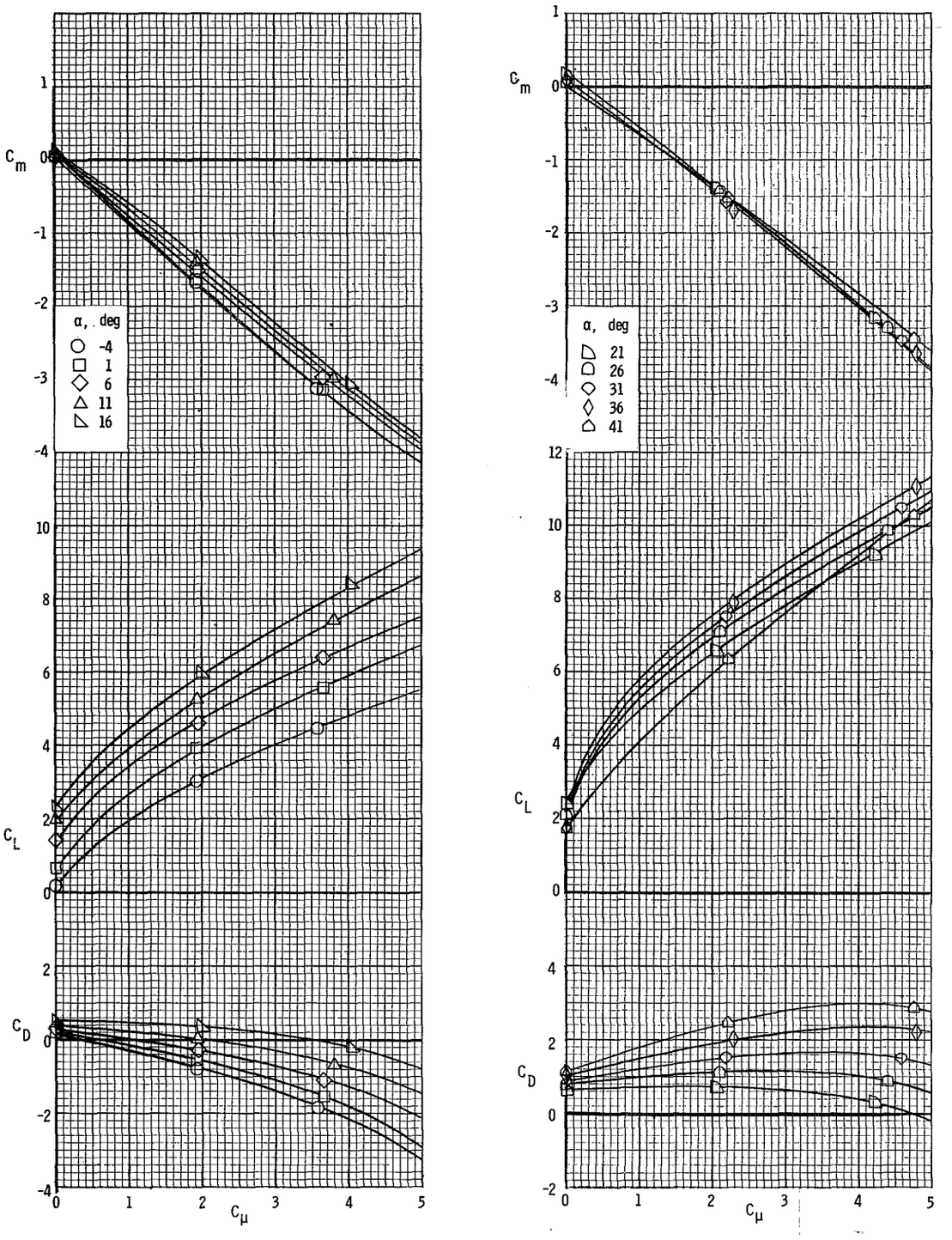

Figure 24.- Longitudinal characteristics of the model with span of inboard flap increased. $\delta_f = 40^o$.

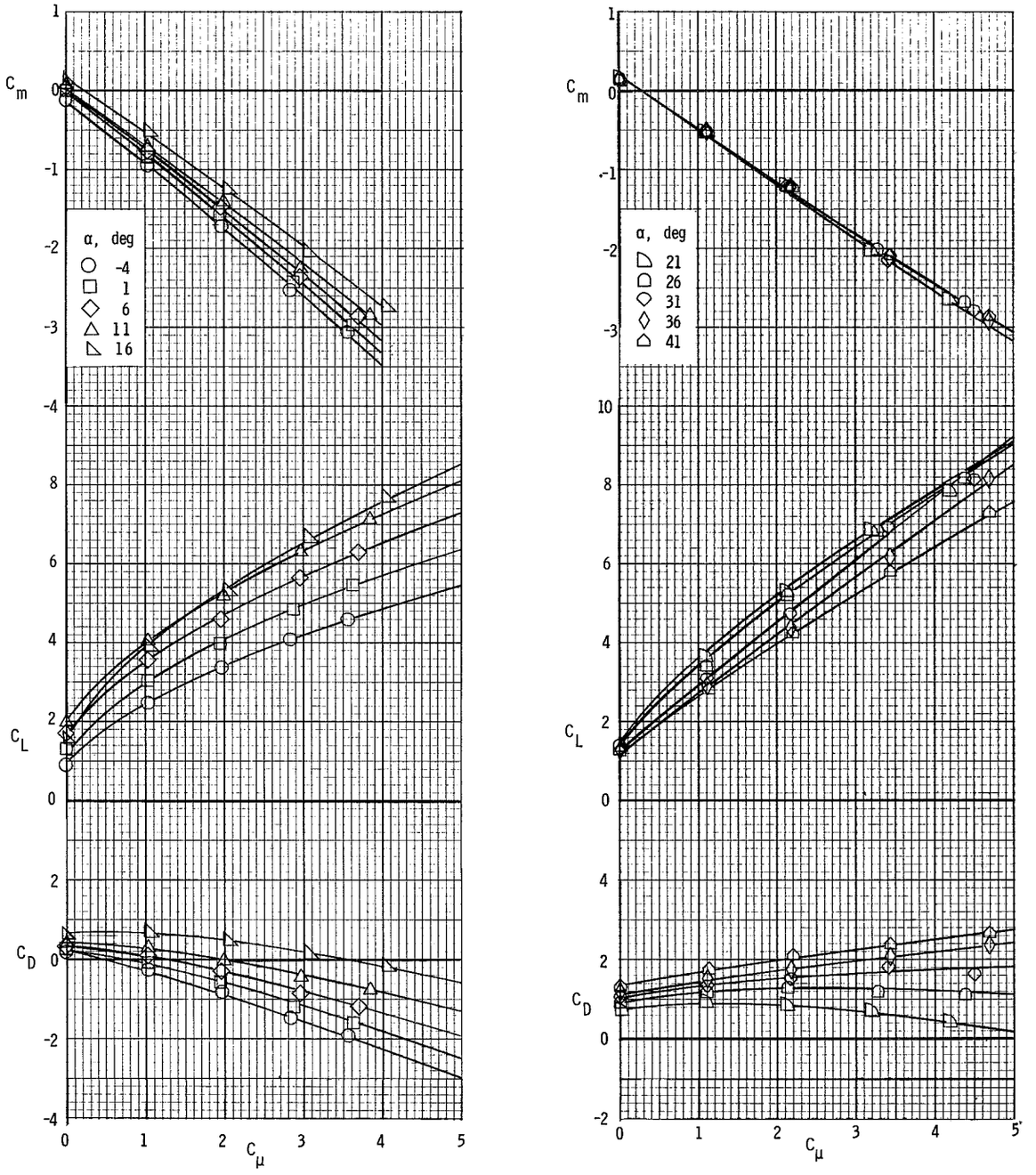

Figure 25.- Longitudinal characteristics of the model with L.E. Krueger flap removed. $\delta_f = 40^o$.

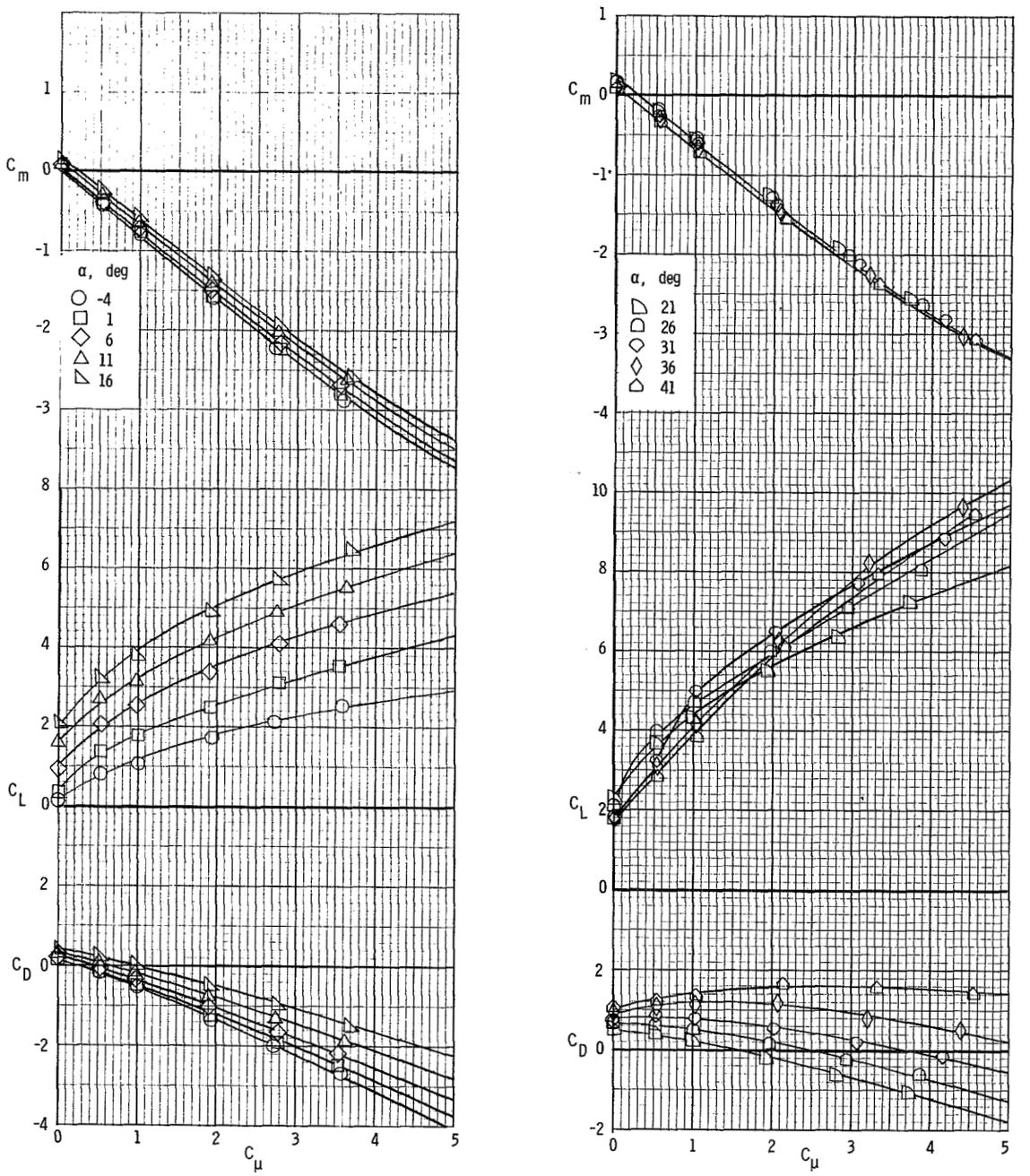

Figure 26.- Longitudinal characteristics of the model. $\delta_f = 20^o$.

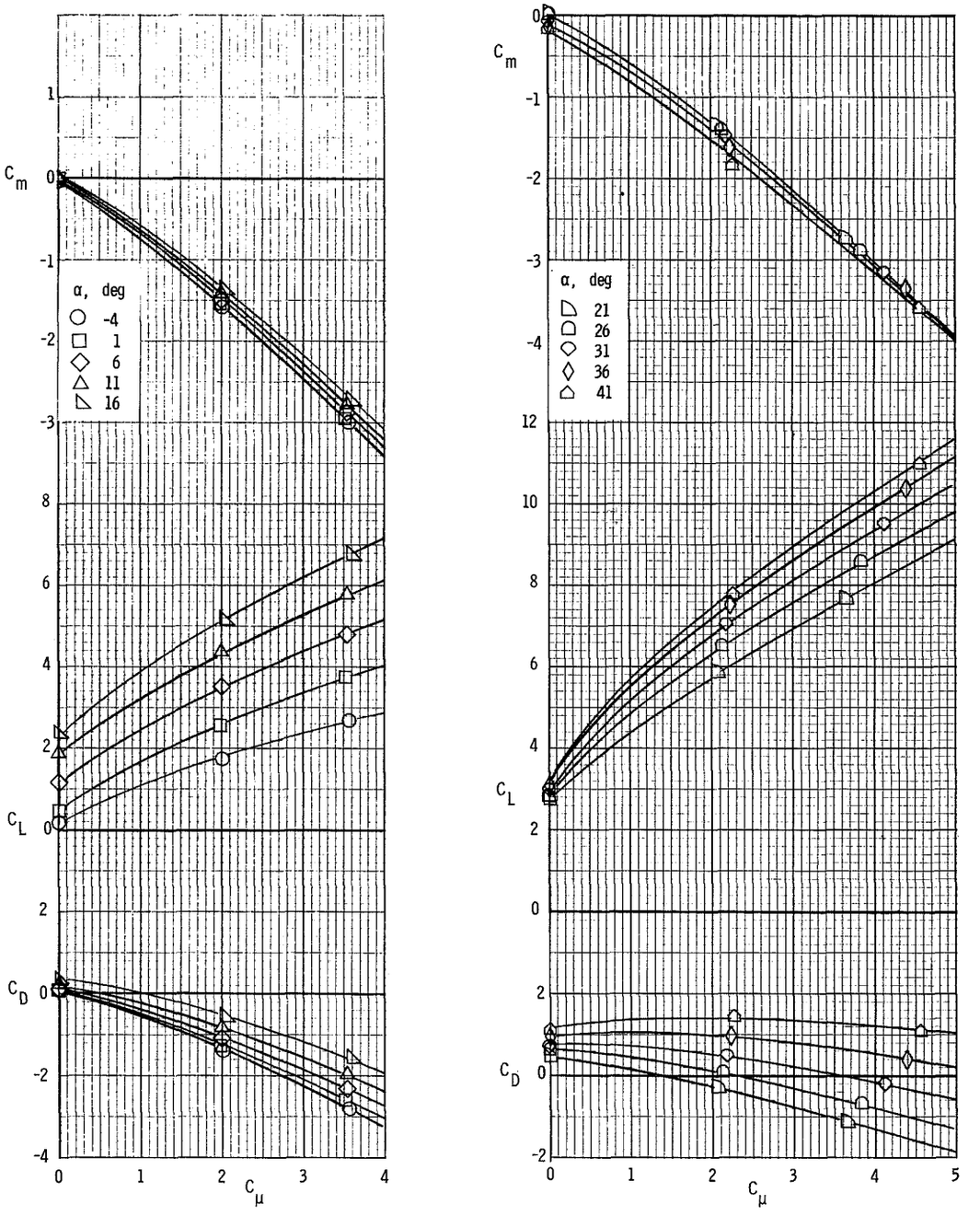

(a) $C_{\mu,le} = 0.04$.

Figure 27.- Longitudinal characteristics of the model with leading-edge BLC. $\delta_f = 20^o$.

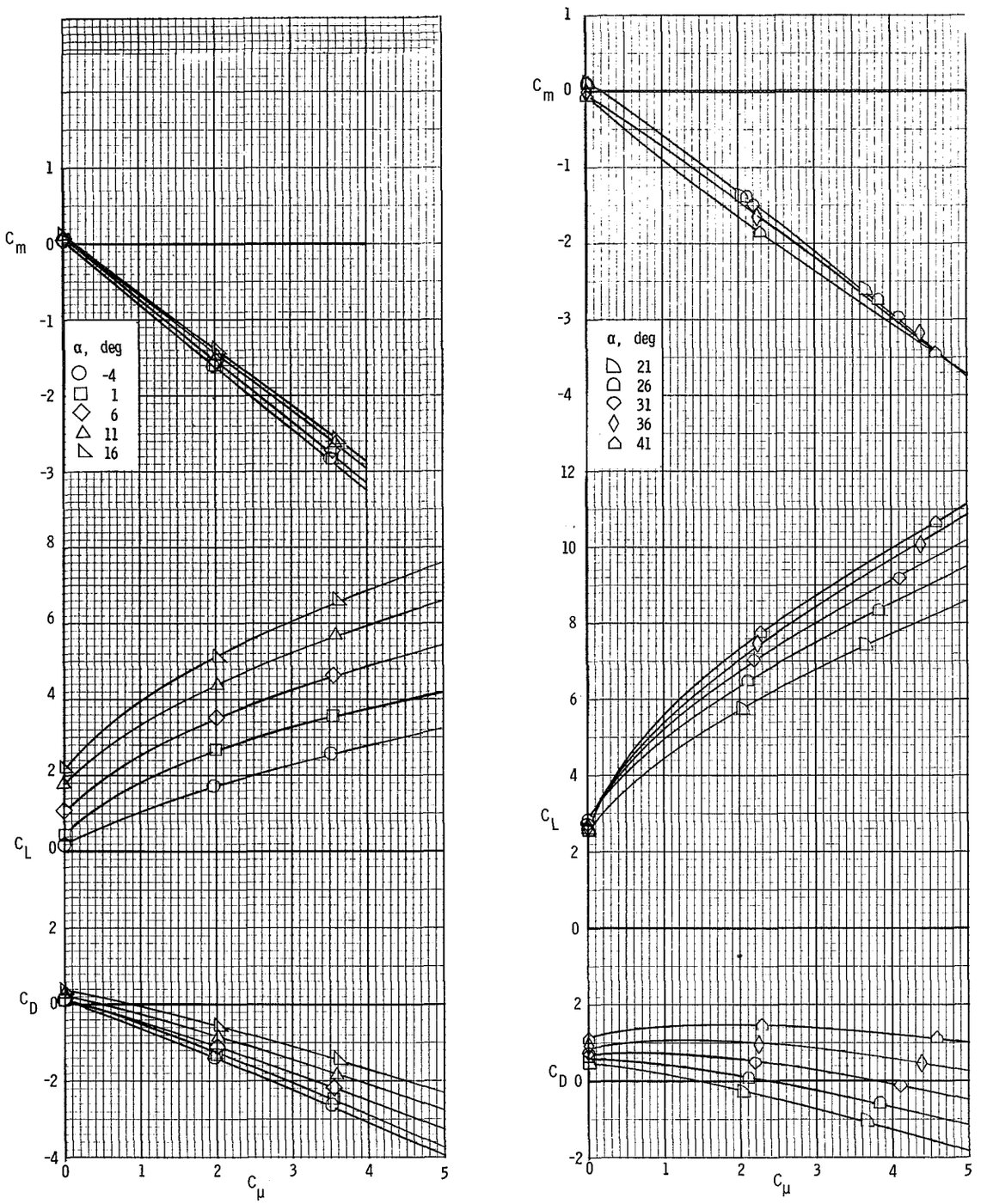

(b) $C_{\mu,le} = 0.08$.

Figure 27.- Concluded.

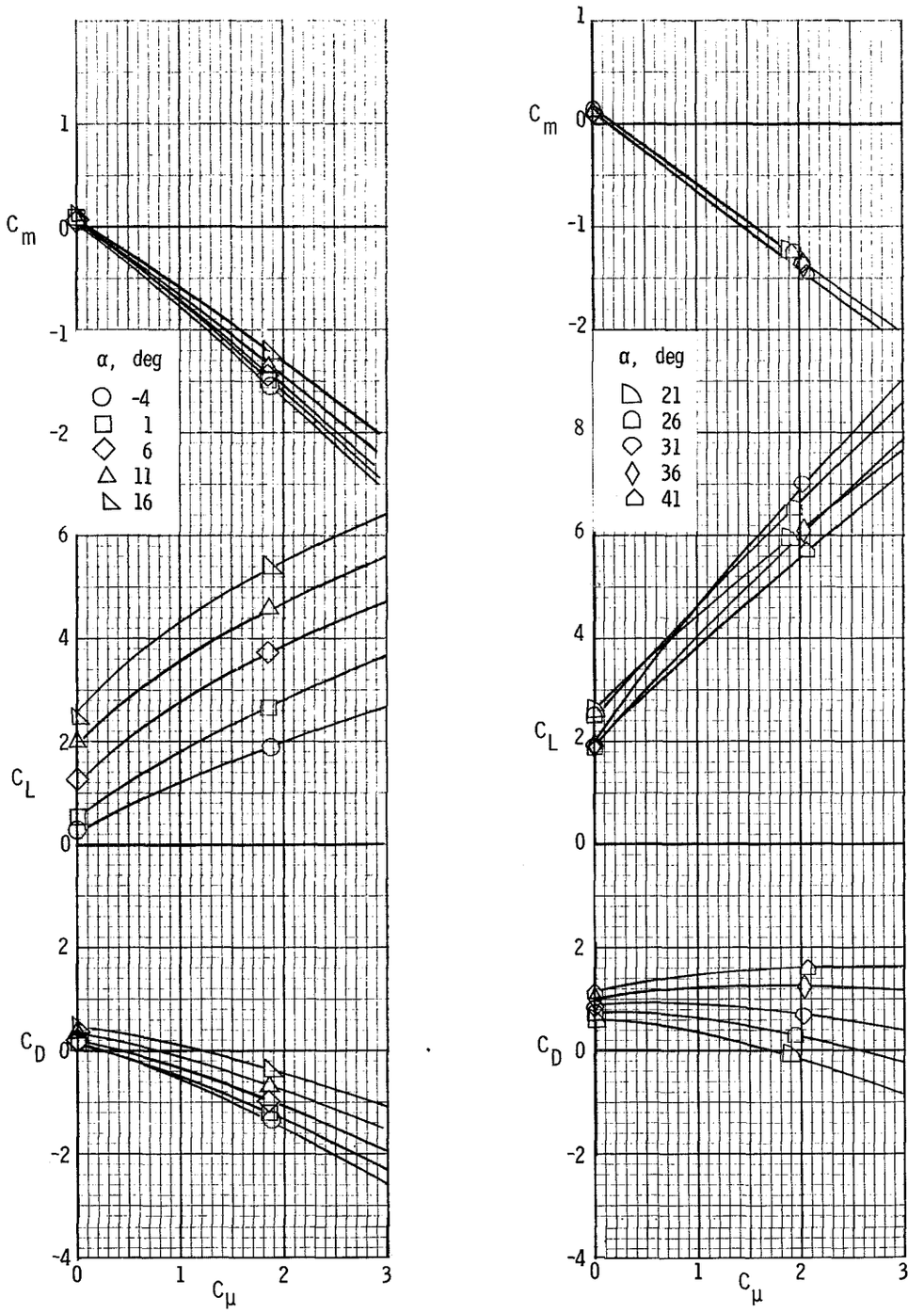

Figure 28.- Longitudinal characteristics of the model with drooped blown aileron.
$\delta_f = 20^o$; $C_{\mu,a} = 0.04$; $\delta_a = 20^o$.

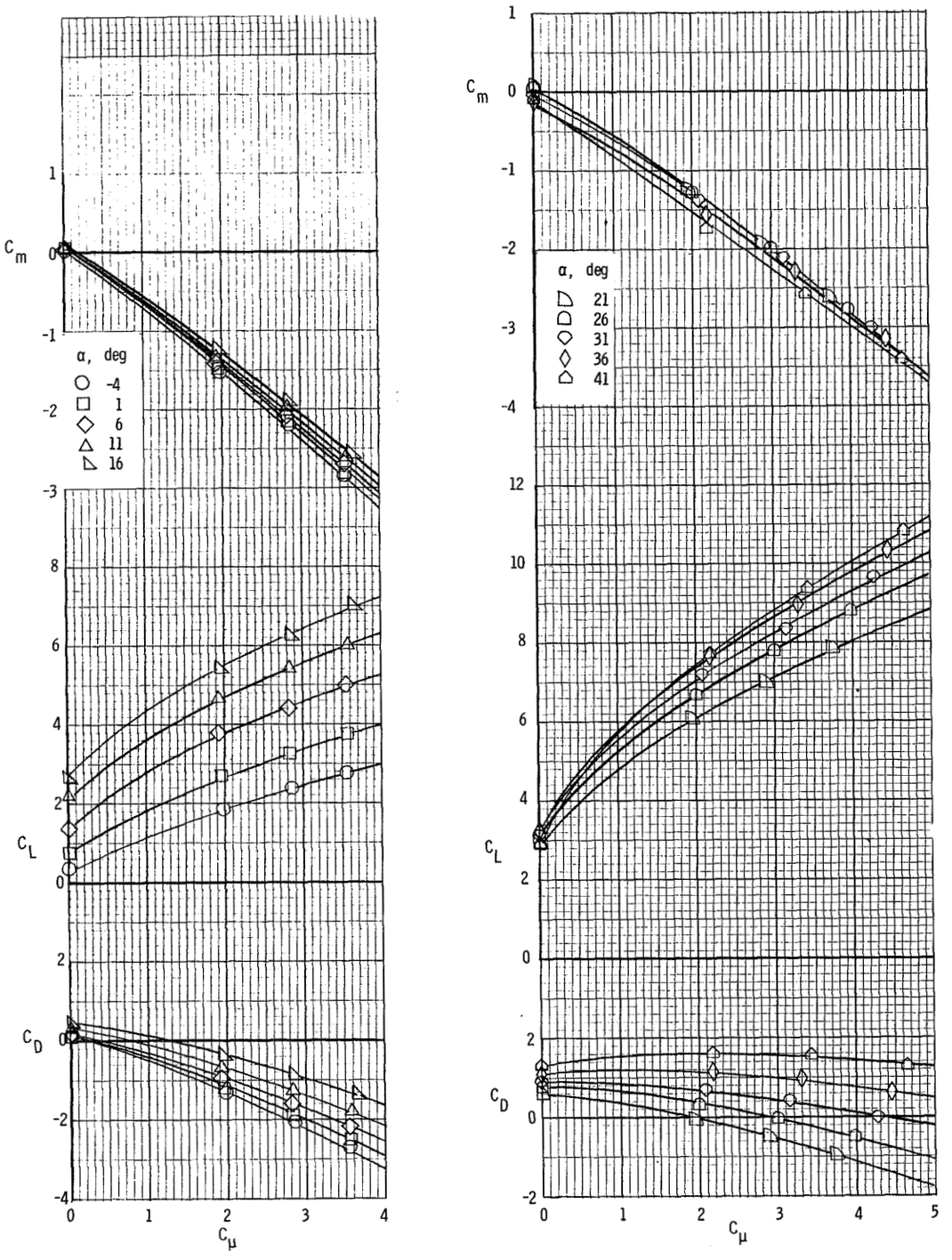

(a) $C_{\mu,le} = 0.04$. $C_{\mu,a} = 0.04$.

Figure 29.- Longitudinal characteristics of the model with leading-edge BLC and drooped blown aileron. $\delta_f = 20^o$; $\delta_a = 20^o$.

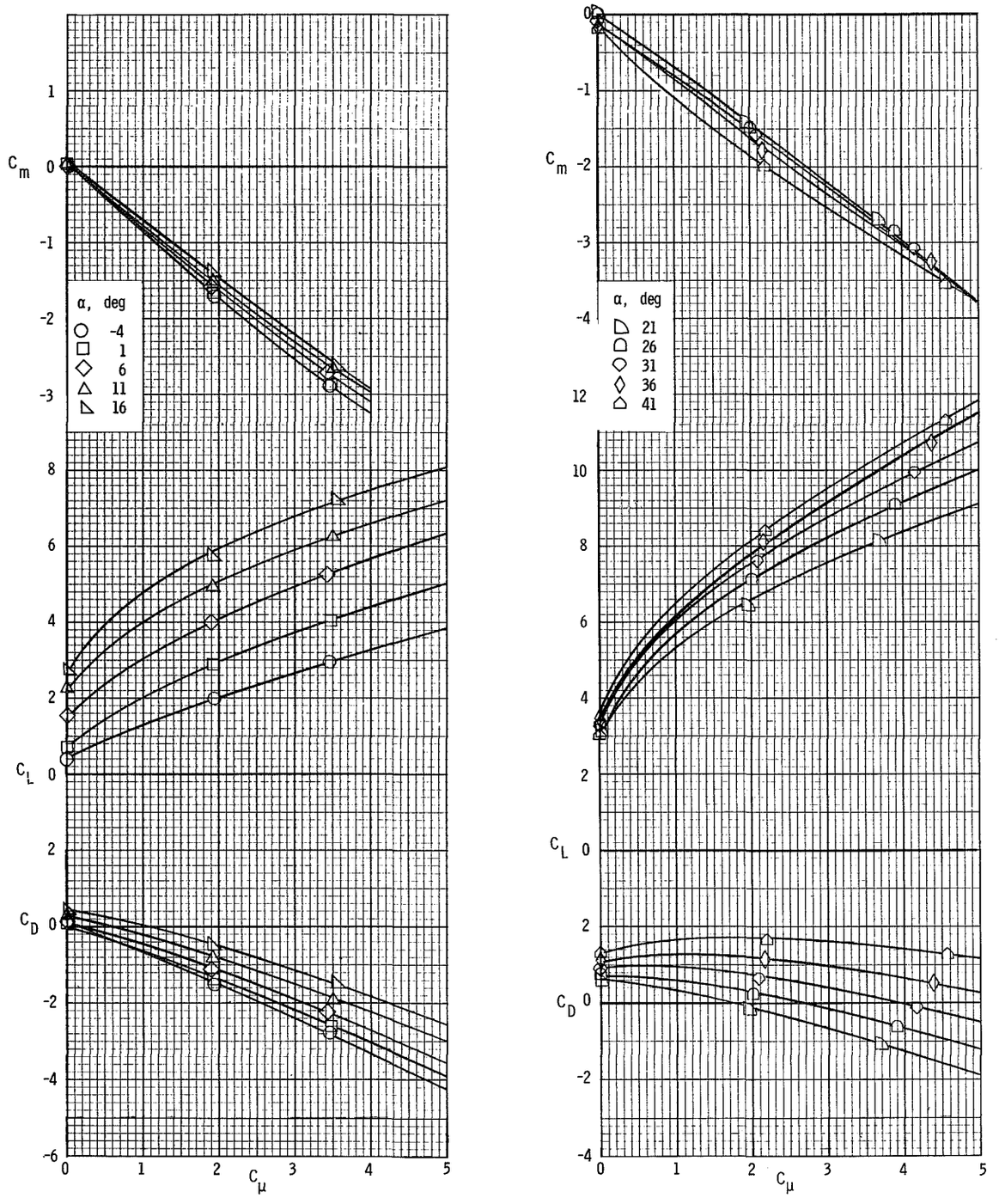

(b) $C_{\mu,le} = 0.08$. $C_{\mu,a} = 0.04$.

Figure 29.- Concluded.

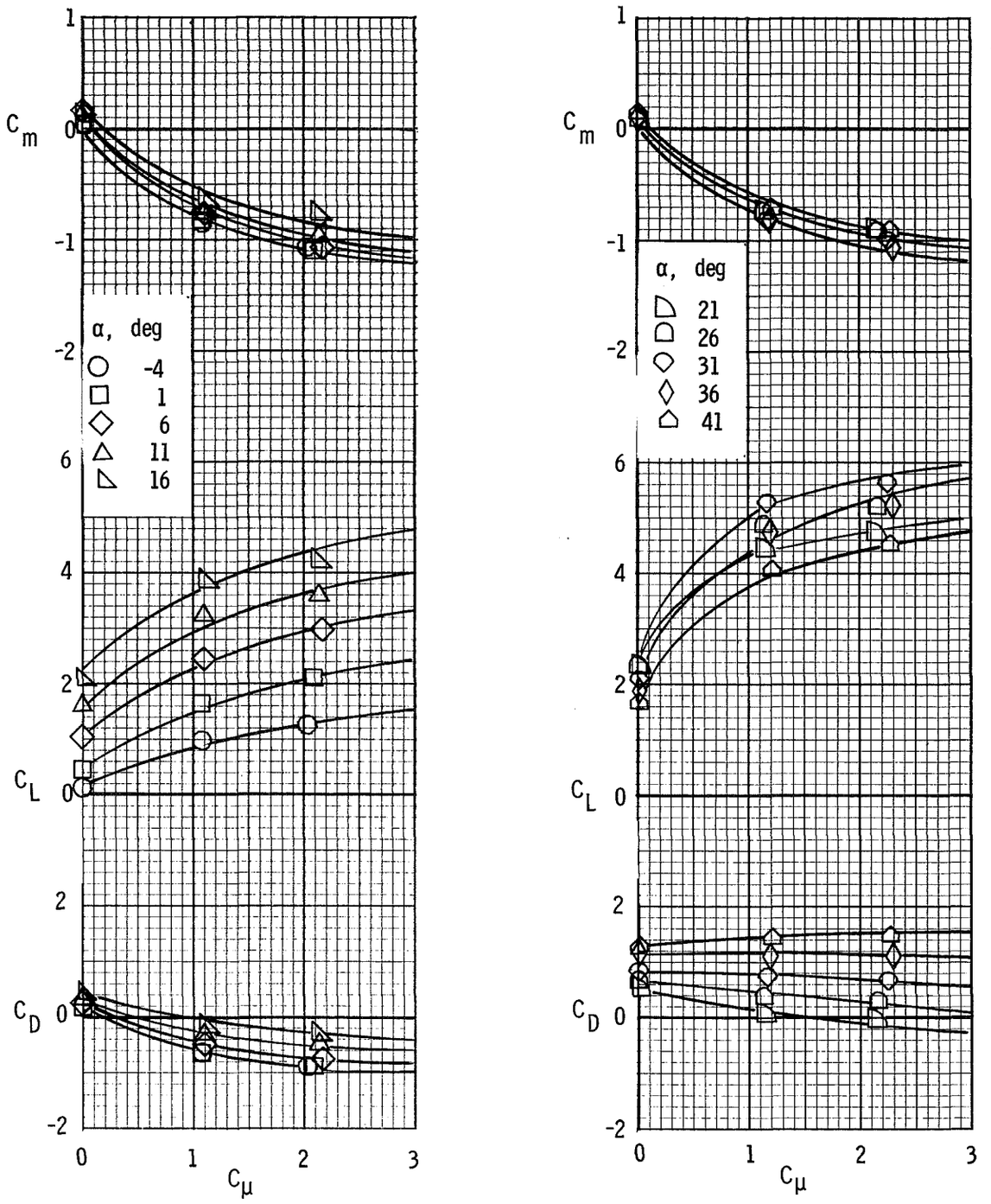

(a) $R = 0.45 \times 10^6$.

Figure 30.- Longitudinal characteristics of the model at several different values of Reynolds number. $\delta_f = 20^o$.

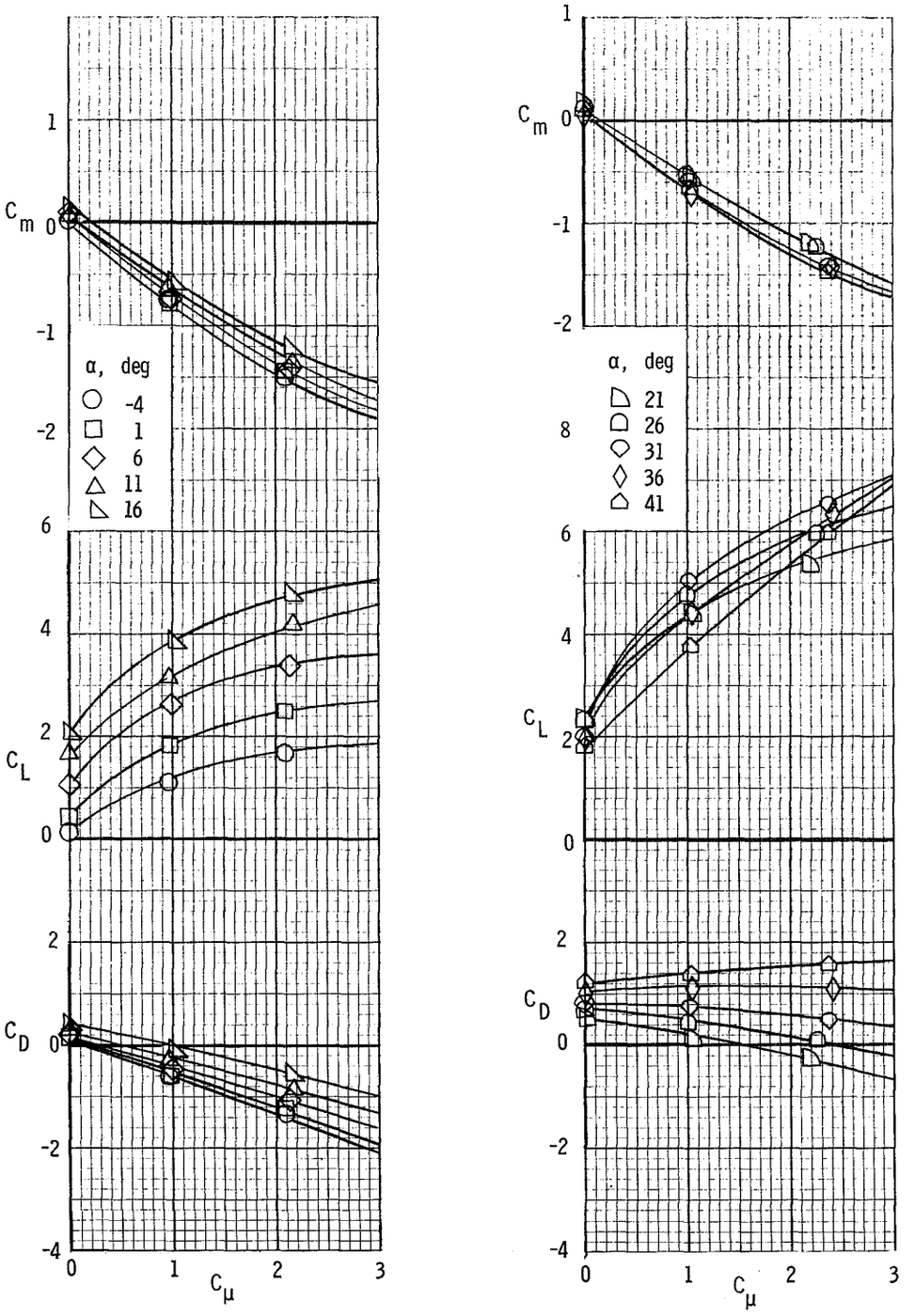

(b) $R = 0.6 \times 10^6$.

Figure 30.- Continued.

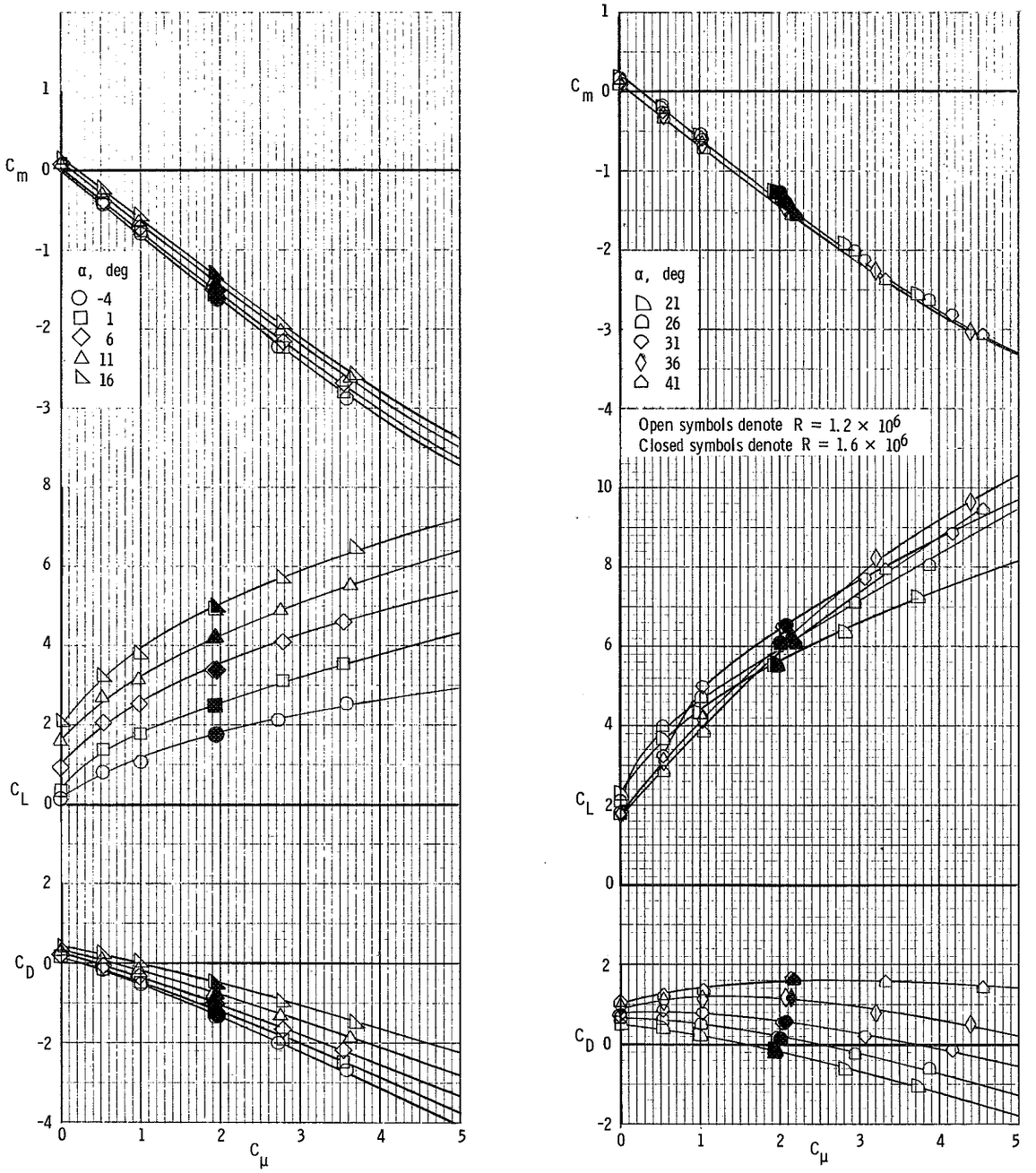

(c) Data for $R = 1.6 \times 10^6$ compared with baseline data of $R = 1.2 \times 10^6$.

Figure 30.- Continued.

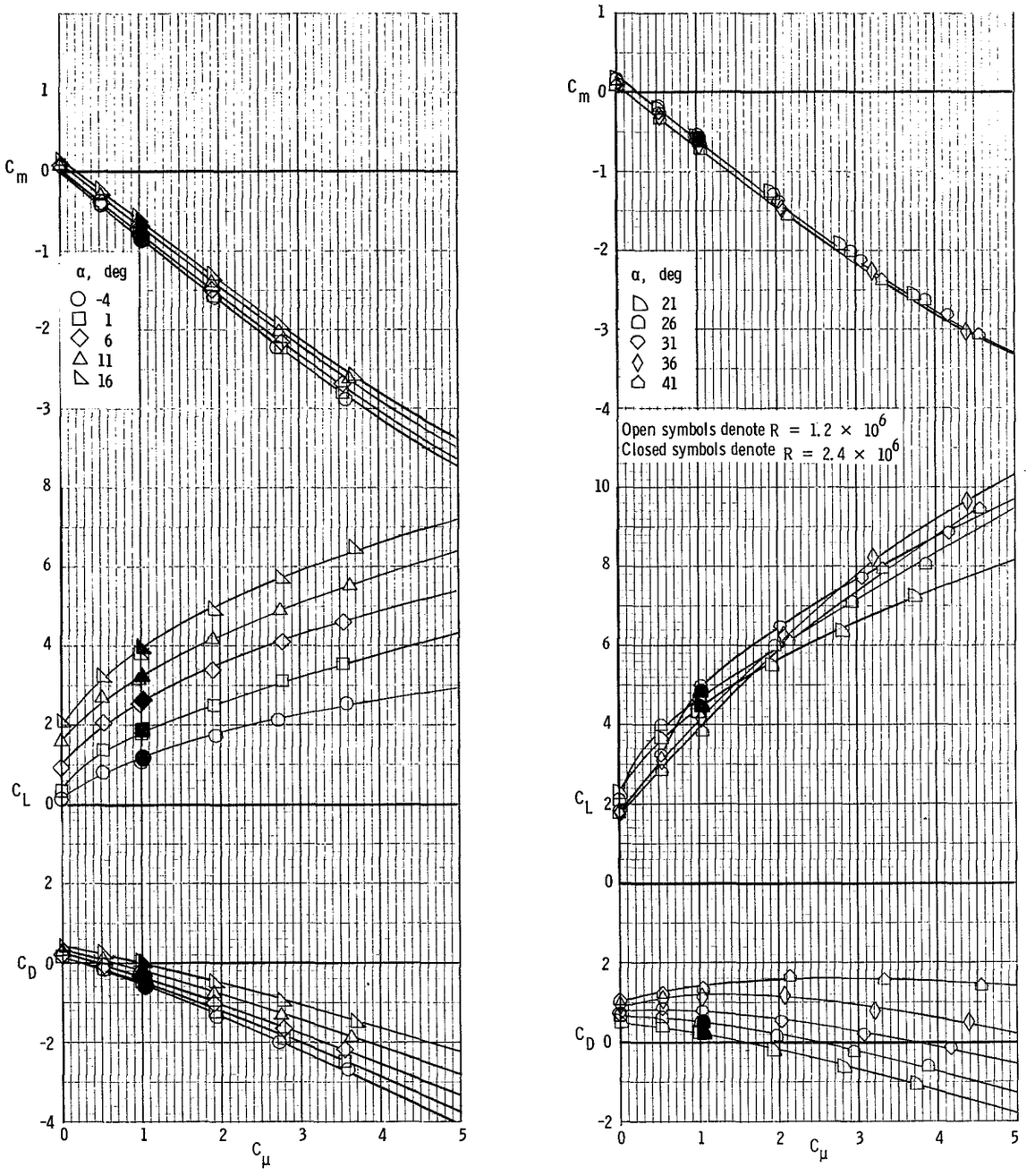

(d) Data for $R = 2.4 \times 10^6$ compared with baseline data of $R = 1.2 \times 10^6$.

Figure 30.- Continued.

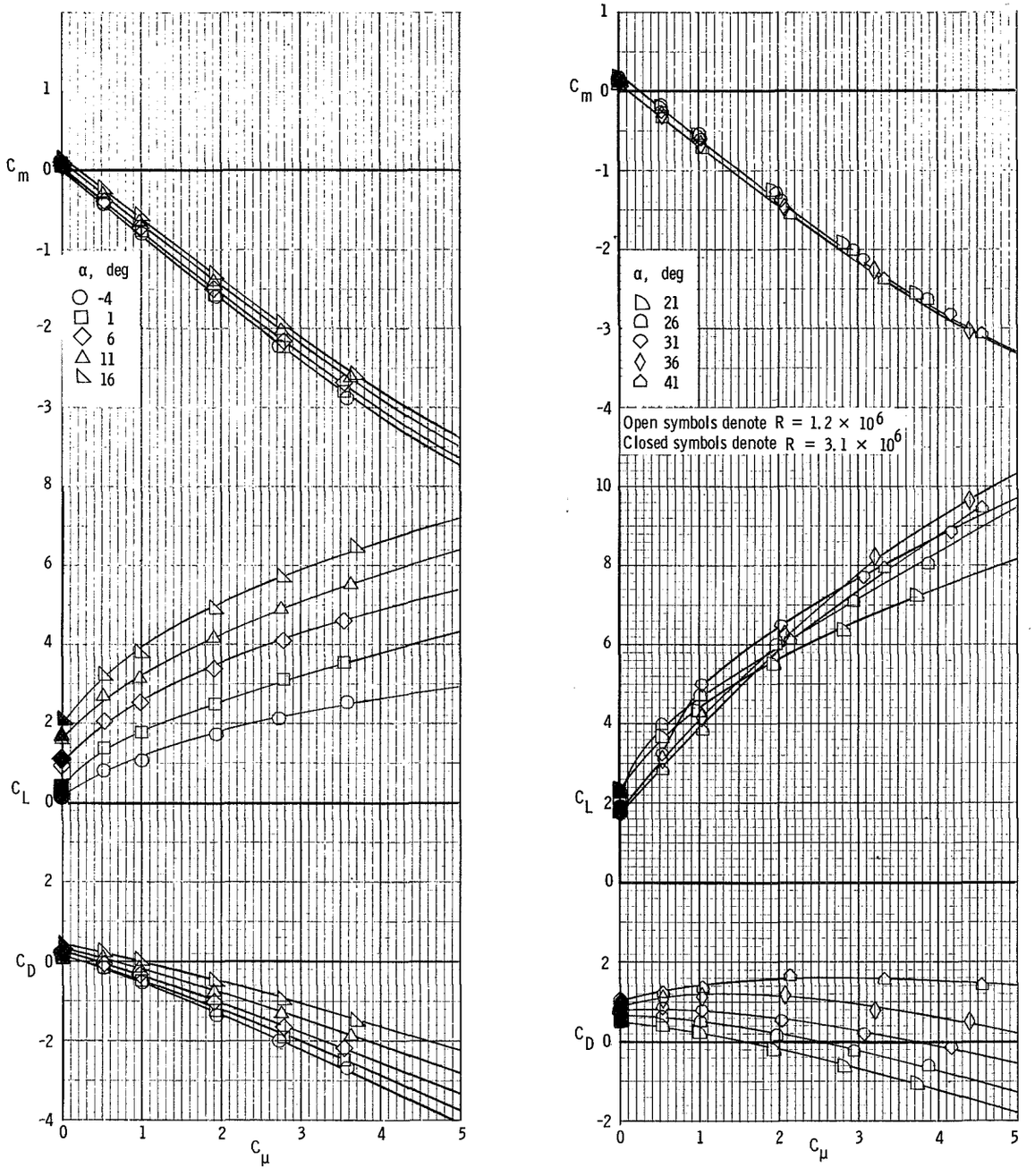

(e) Data for $R = 3.1 \times 10^6$ compared with baseline data of $R = 1.2 \times 10^6$.

Figure 30.- Concluded.

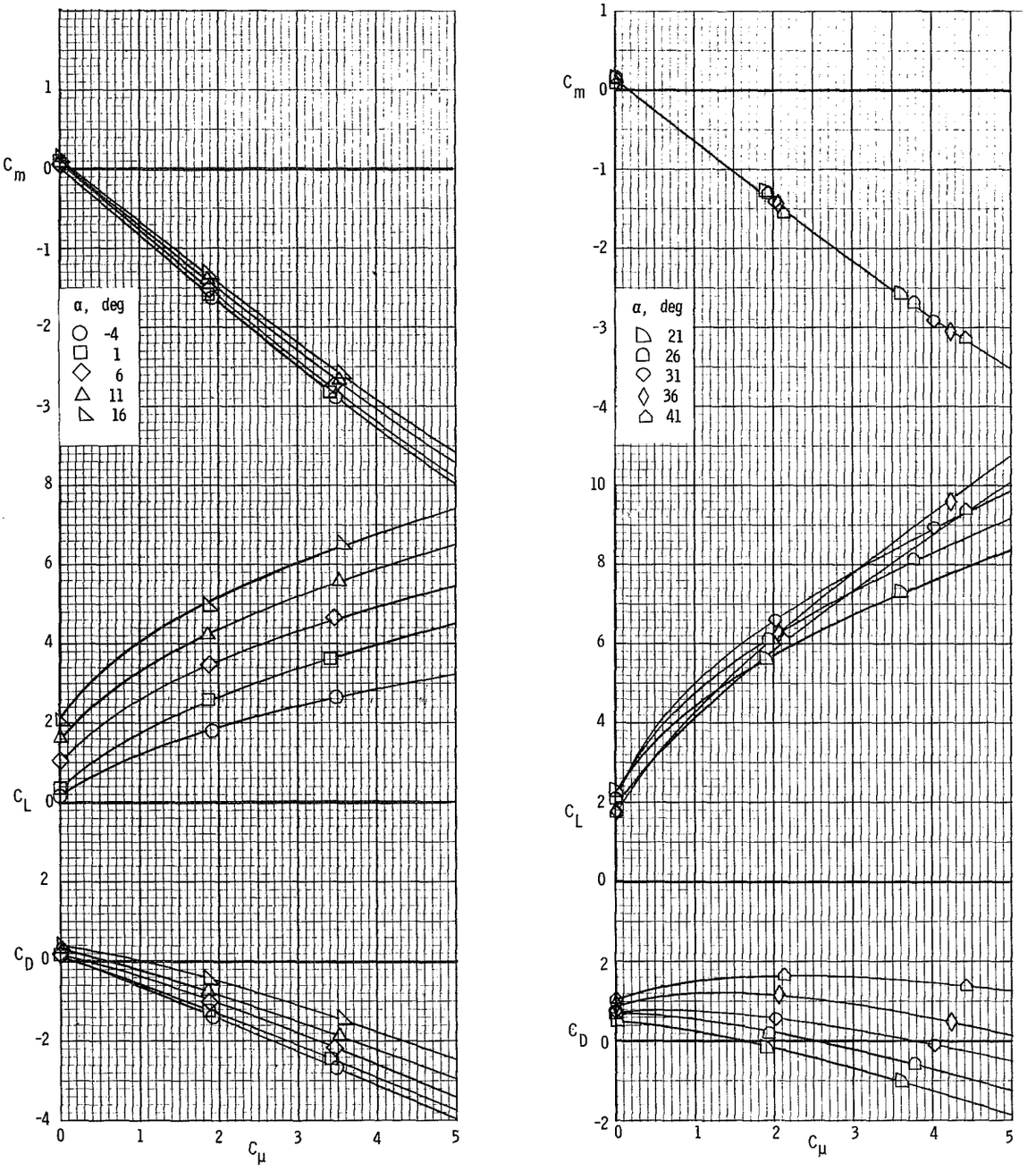

Figure 31.- Longitudinal characteristics of the model with span of inboard flap increased. $\delta_f = 20^o$.

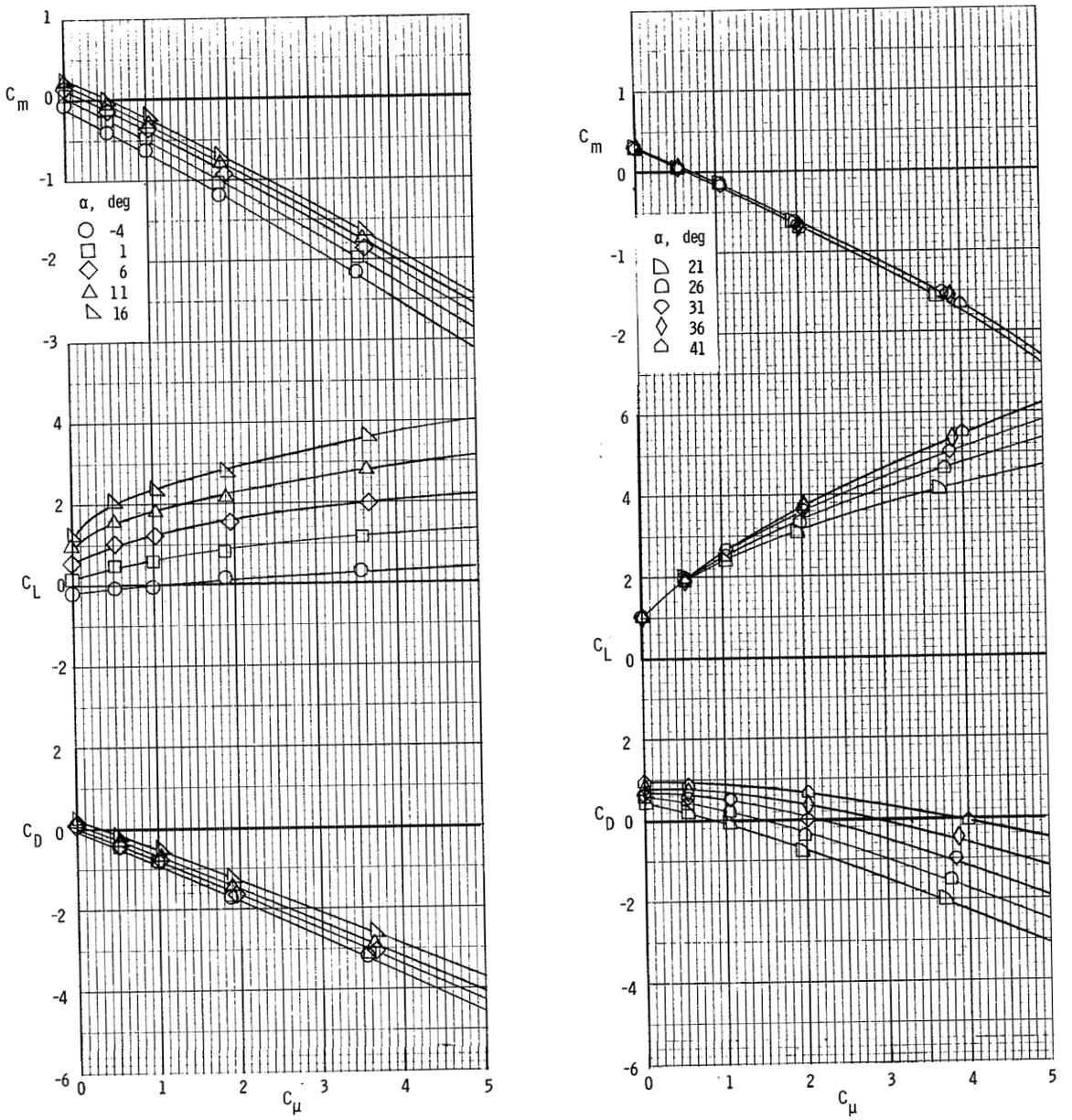

Figure 32.- Longitudinal characteristics of the model. $\delta_f = 0^o$.

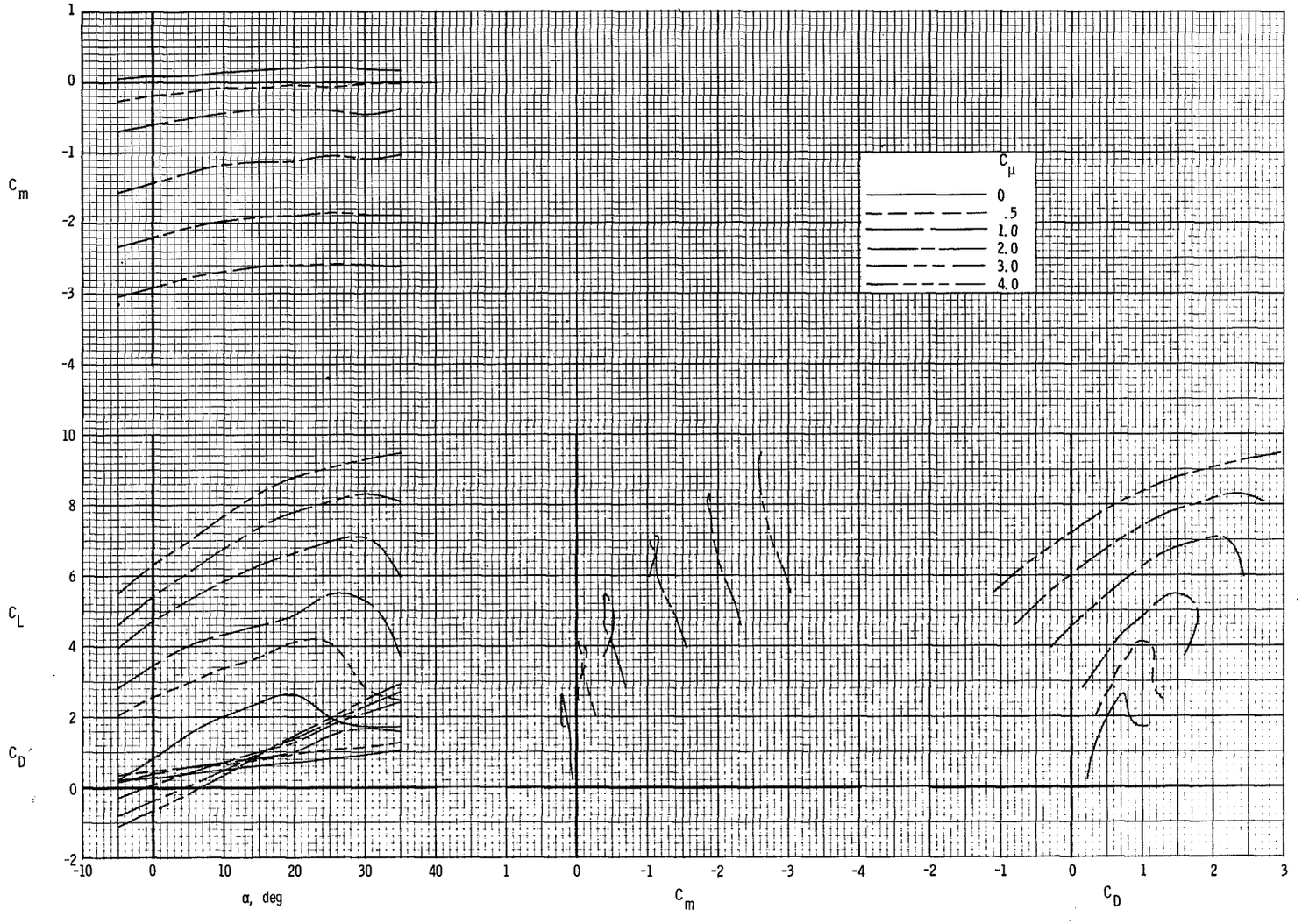

(a) $A_n = 4$.

Figure 33.- Summary of longitudinal characteristics of the model. $\delta_f = 60^o$.

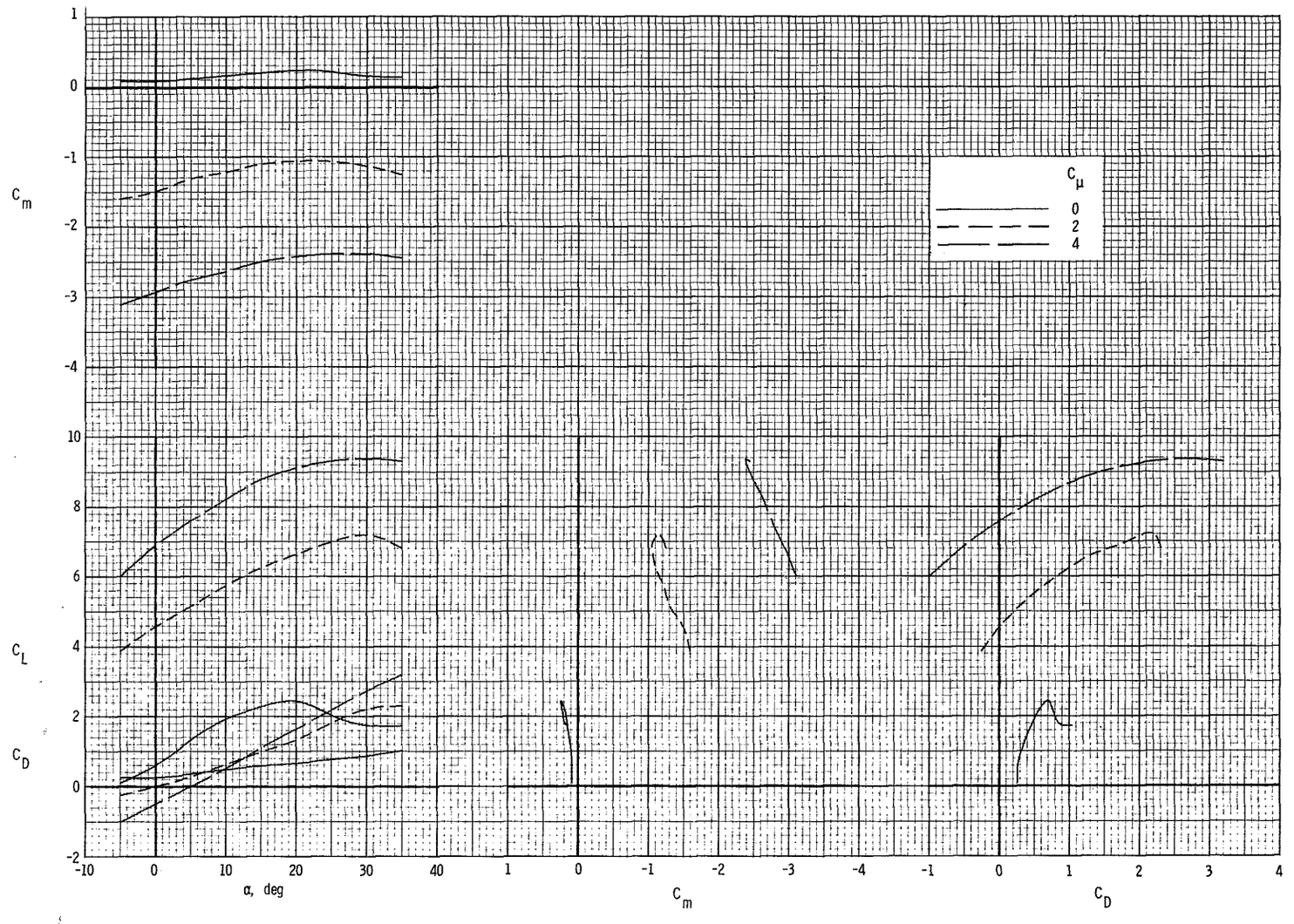

(b) $A_n = 6$.

Figure 33.- Continued.

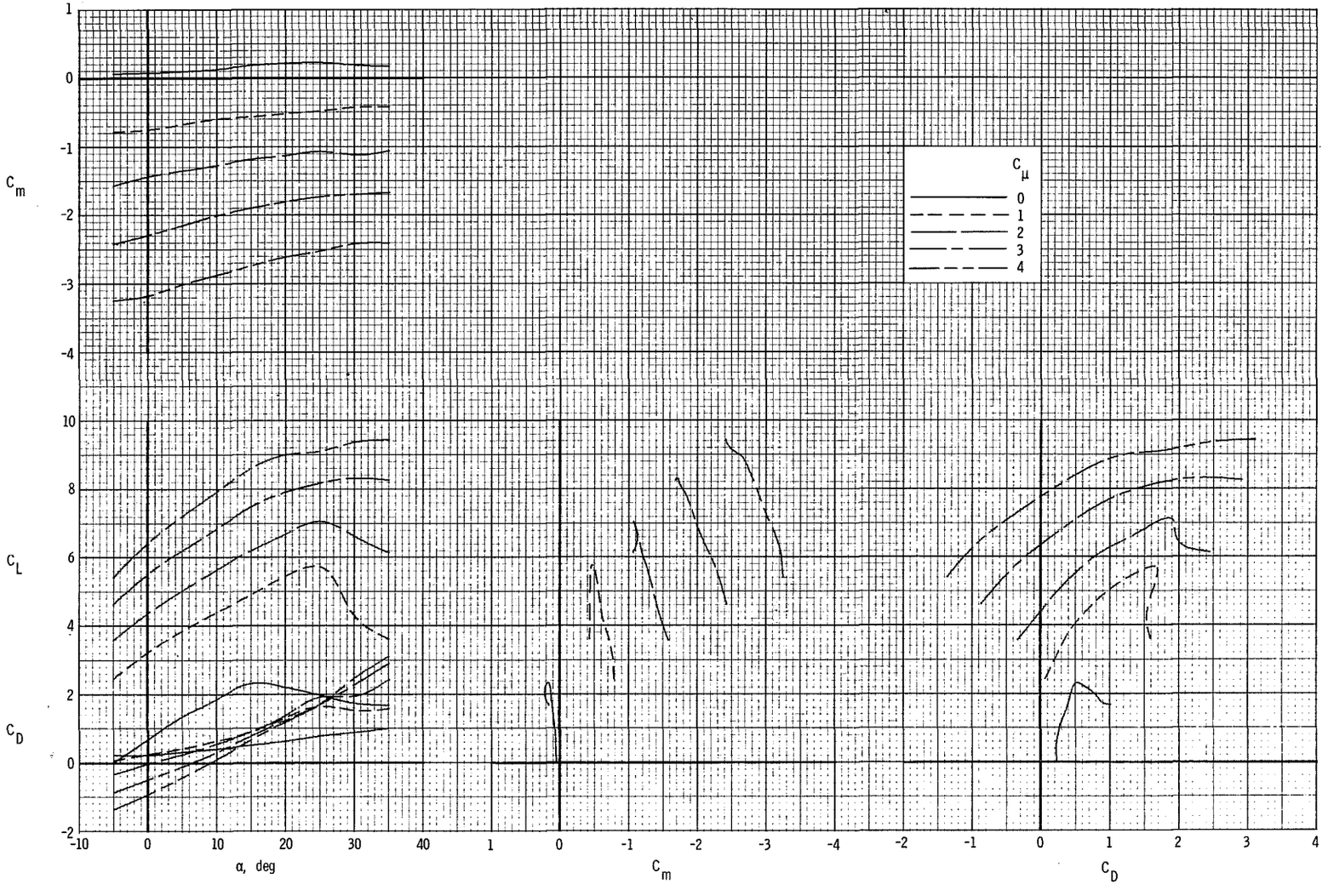

(c) $A_n = 2$. Deflector 1.

Figure 33.- Continued.

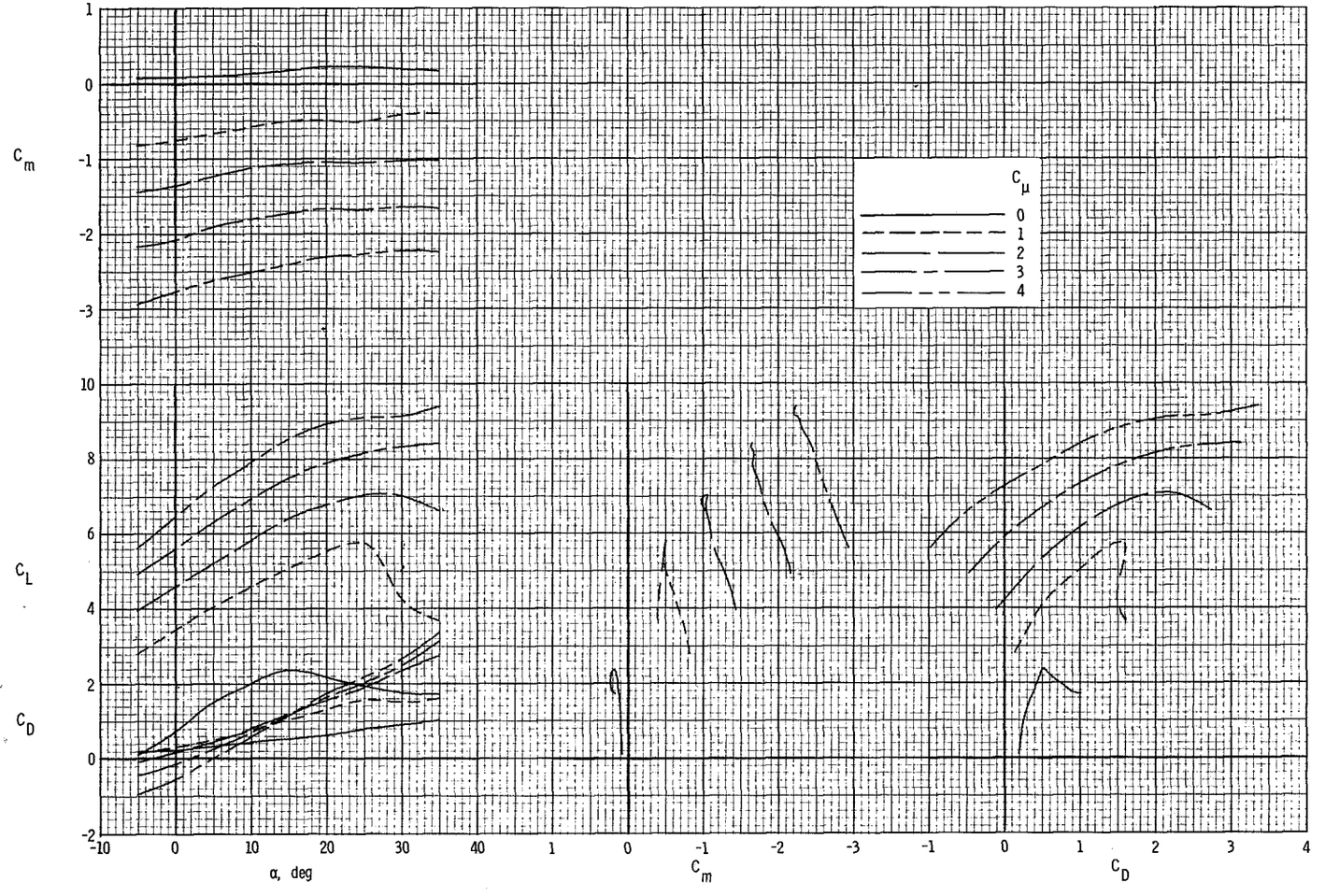

(d) $A_n = 2$. Deflector 2.

Figure 33.- Concluded.

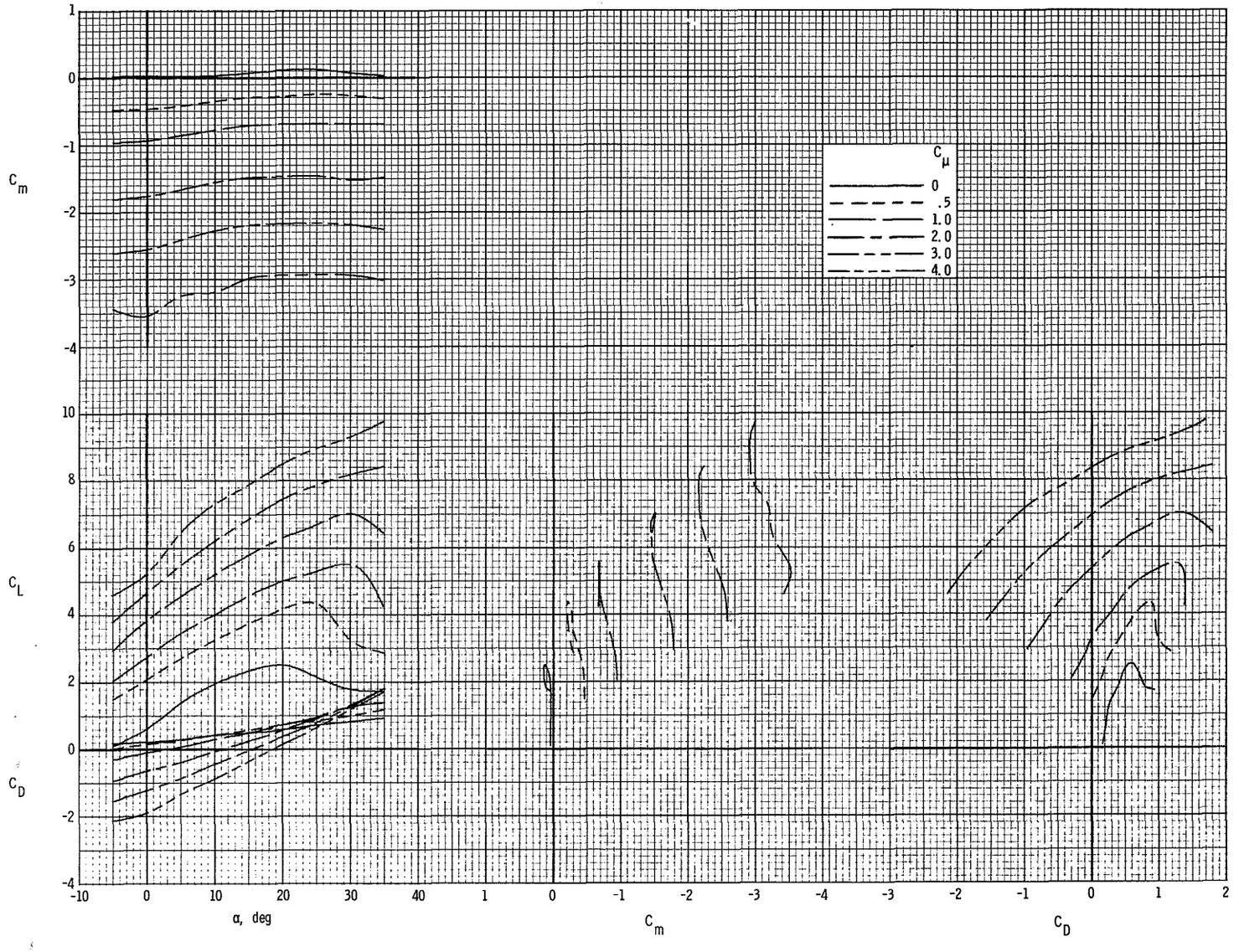

Figure 34.- Summary of longitudinal characteristics of the model. $\delta_f = 40^o$.

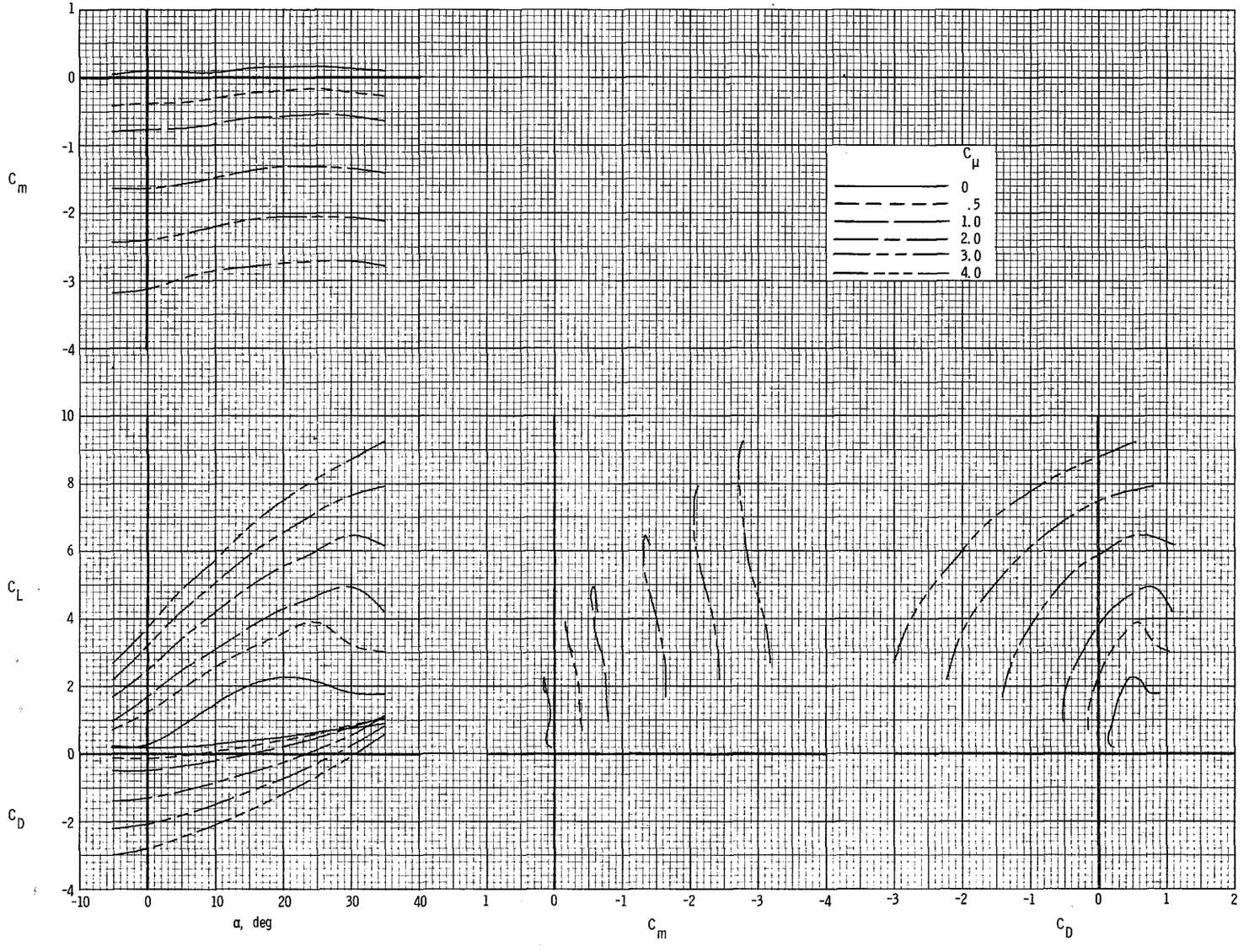

Figure 35.- Summary of longitudinal characteristics of the model. $\delta_f = 20^o$.

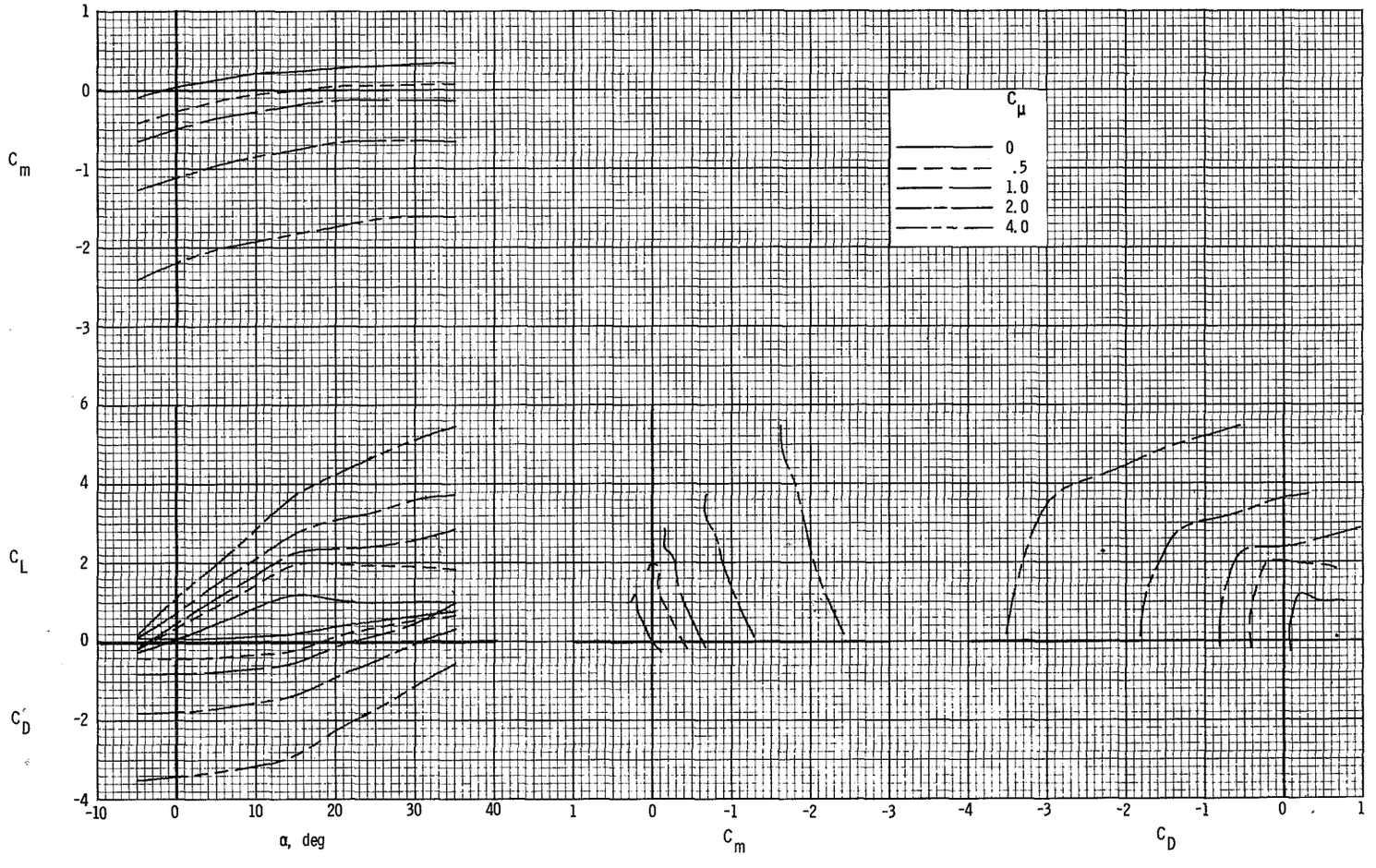

Figure 36.- Summary of longitudinal characteristics of the model with leading-edge flap off. $\delta_f = 0^o$.

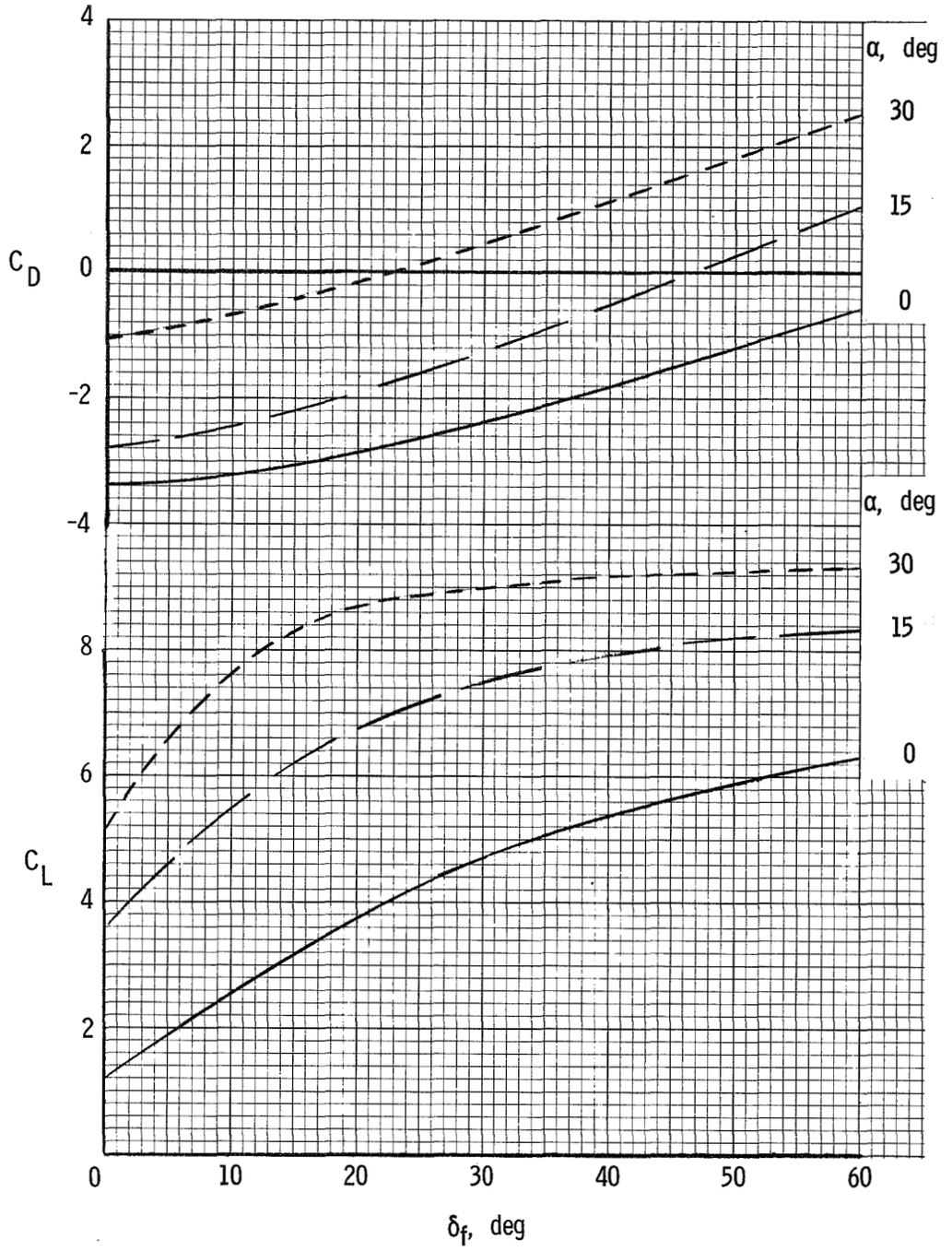

Figure 37.- Effect of flap deflection on the lift and drag characteristics of the model. C_μ = 4.0.

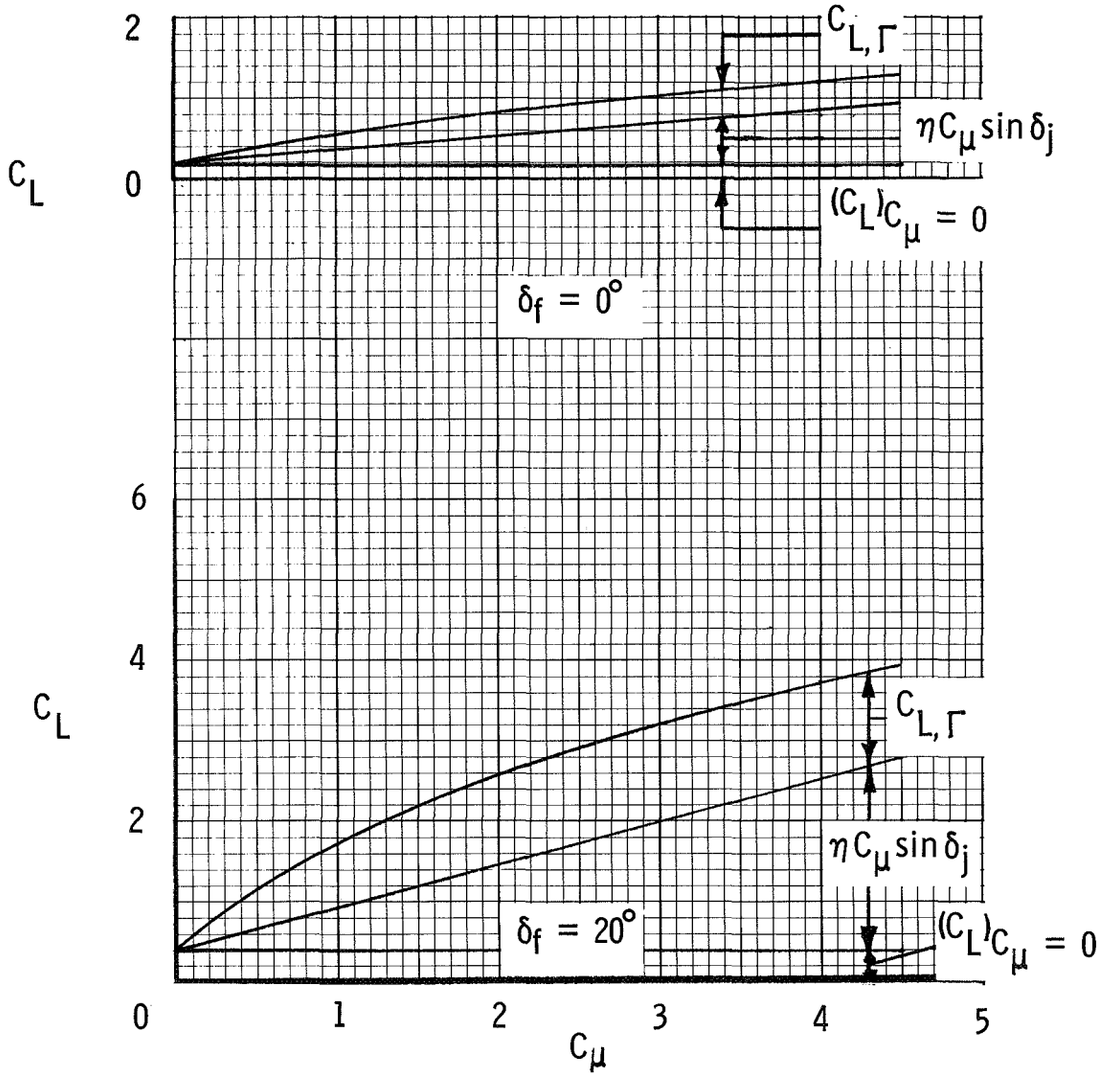

(a) $\delta_f = 0^o$ and 20^o.

Figure 38.- Lift components of the model. $C_\mu = 4.0$; $\alpha = 0^o$.

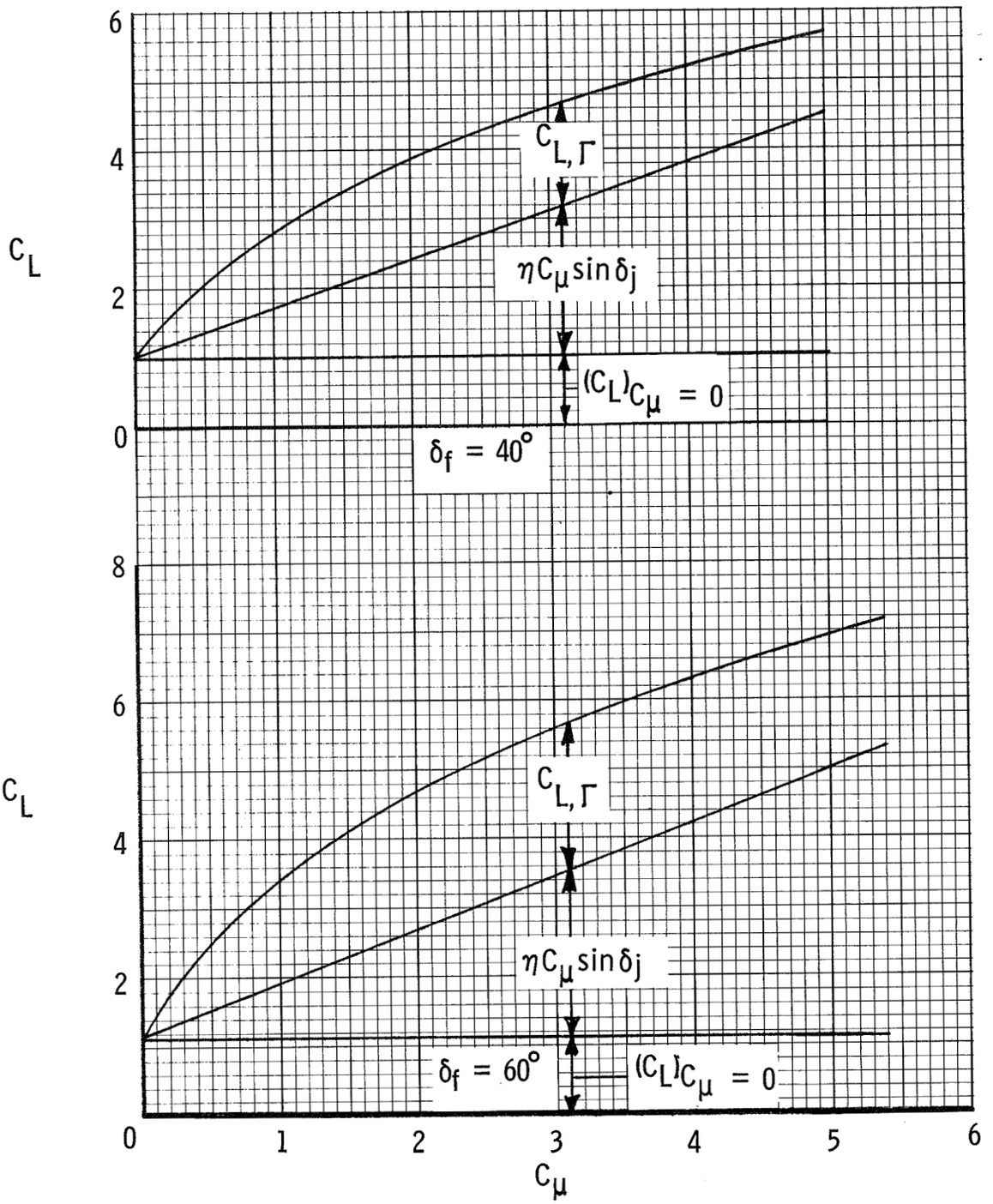

(b) $\delta_f = 40^o$ and 60^o.

Figure 38.- Concluded.

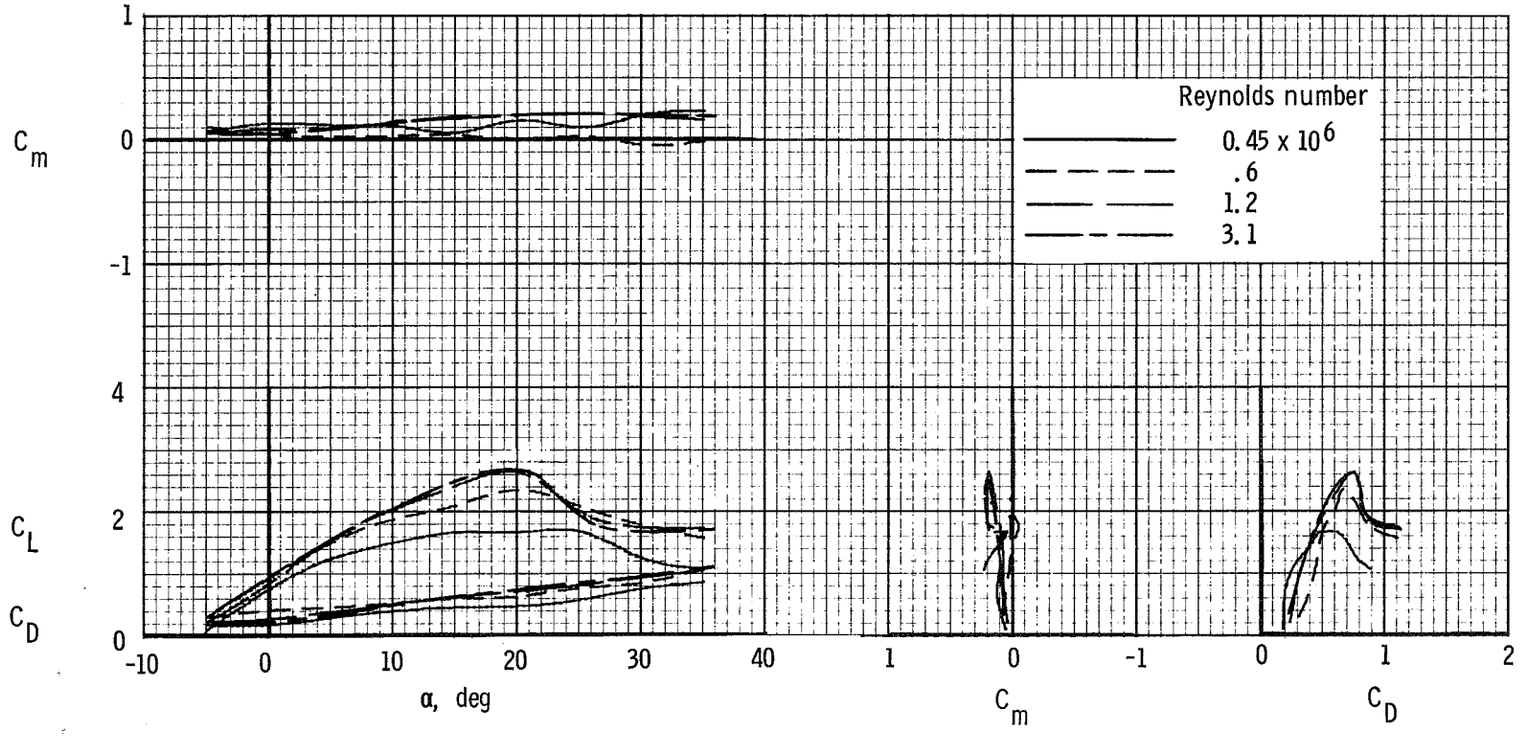

(a) $C_\mu = 0$.

Figure 39.- Effect of Reynolds number on longitudinal characteristics of the model. $\delta_f = 60^o$.

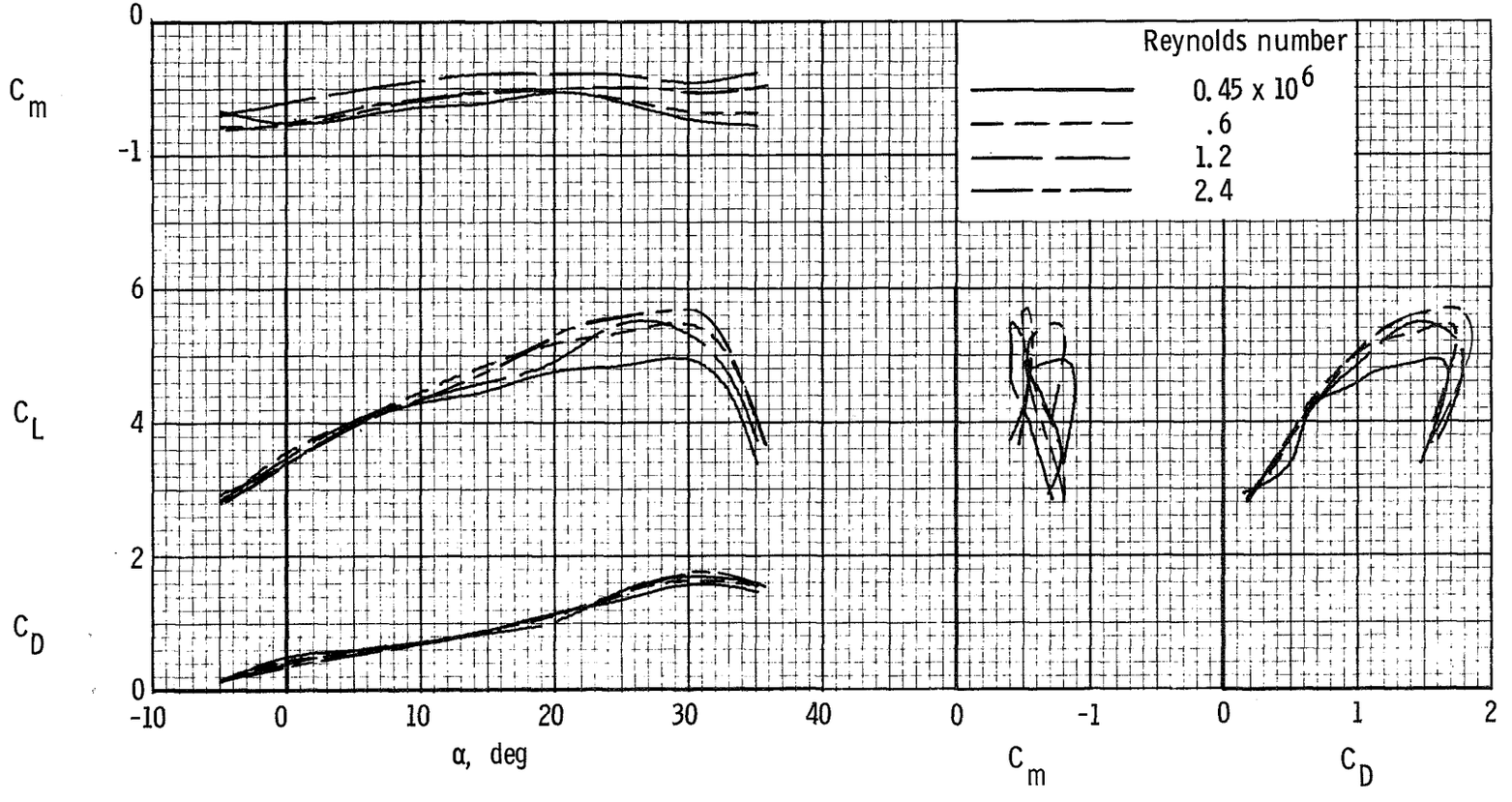

(b) C_μ = 1.0.

Figure 39.- Continued.

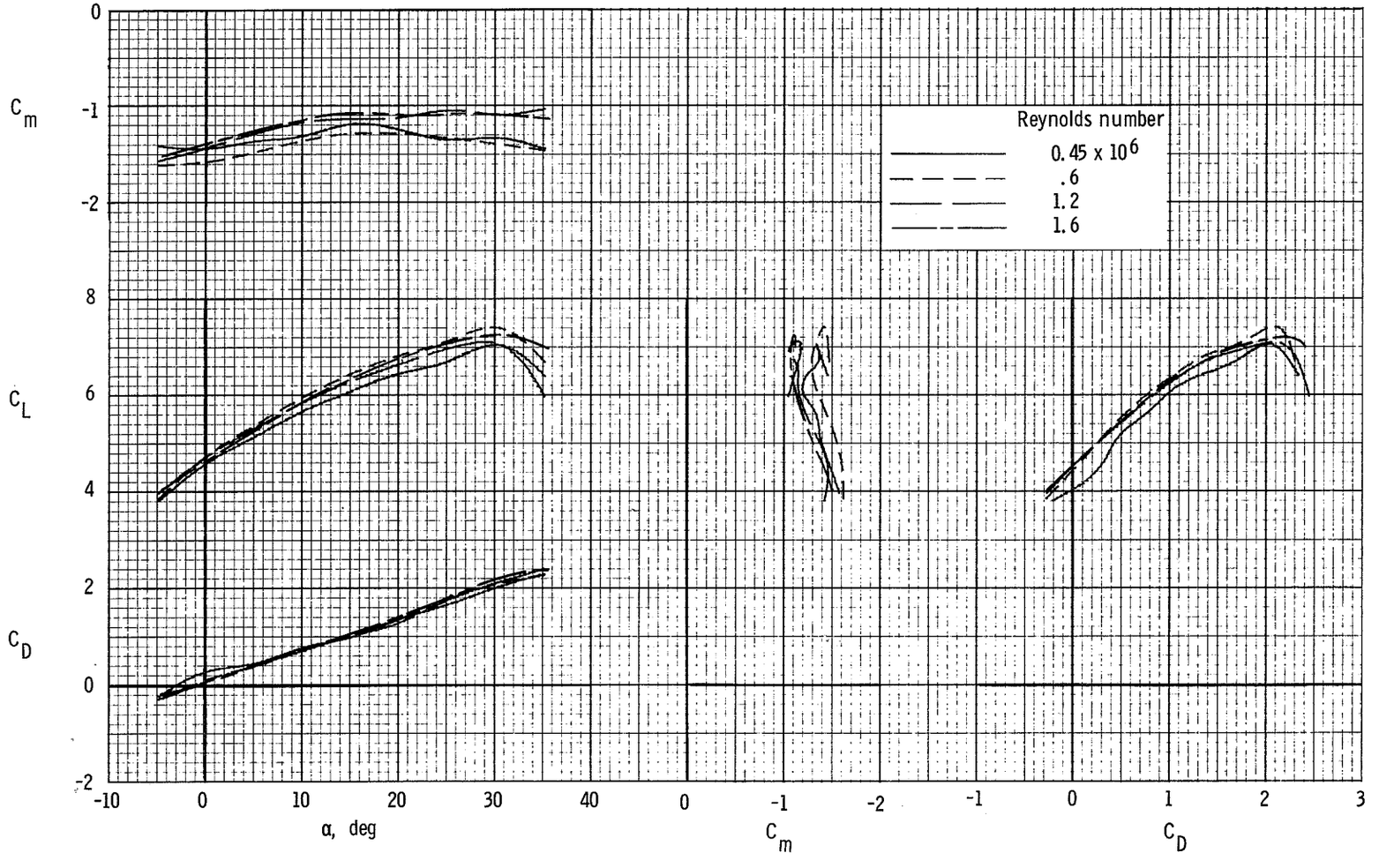

(c) $C_\mu = 2.0$.

Figure 39.- Continued.

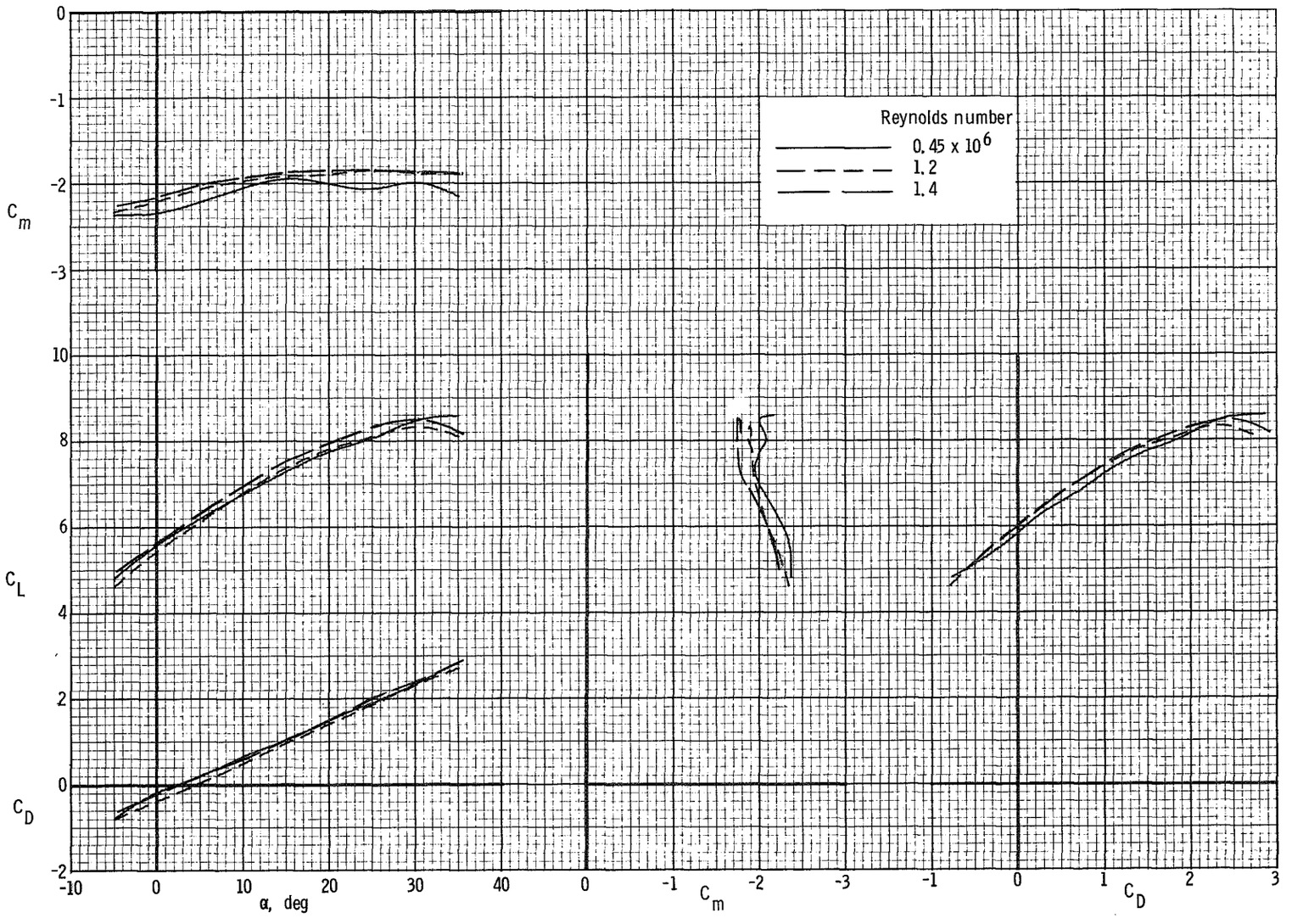

(d) $C_{\mu} = 3.0$.

Figure 39.- Concluded.

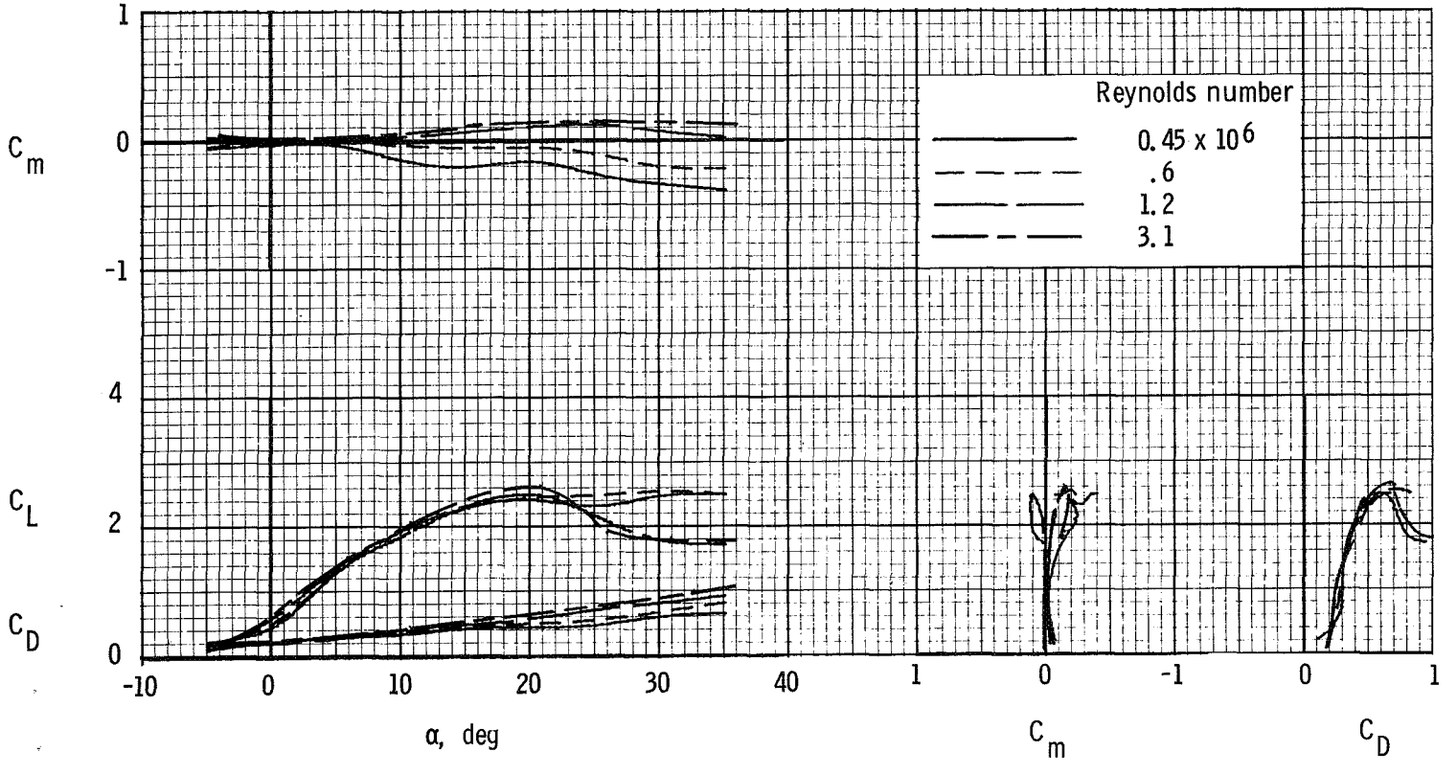

(a) $C_\mu = 0$.

Figure 40.- Effect of Reynolds number on longitudinal characteristics of the model. $\delta_f = 40^o$.

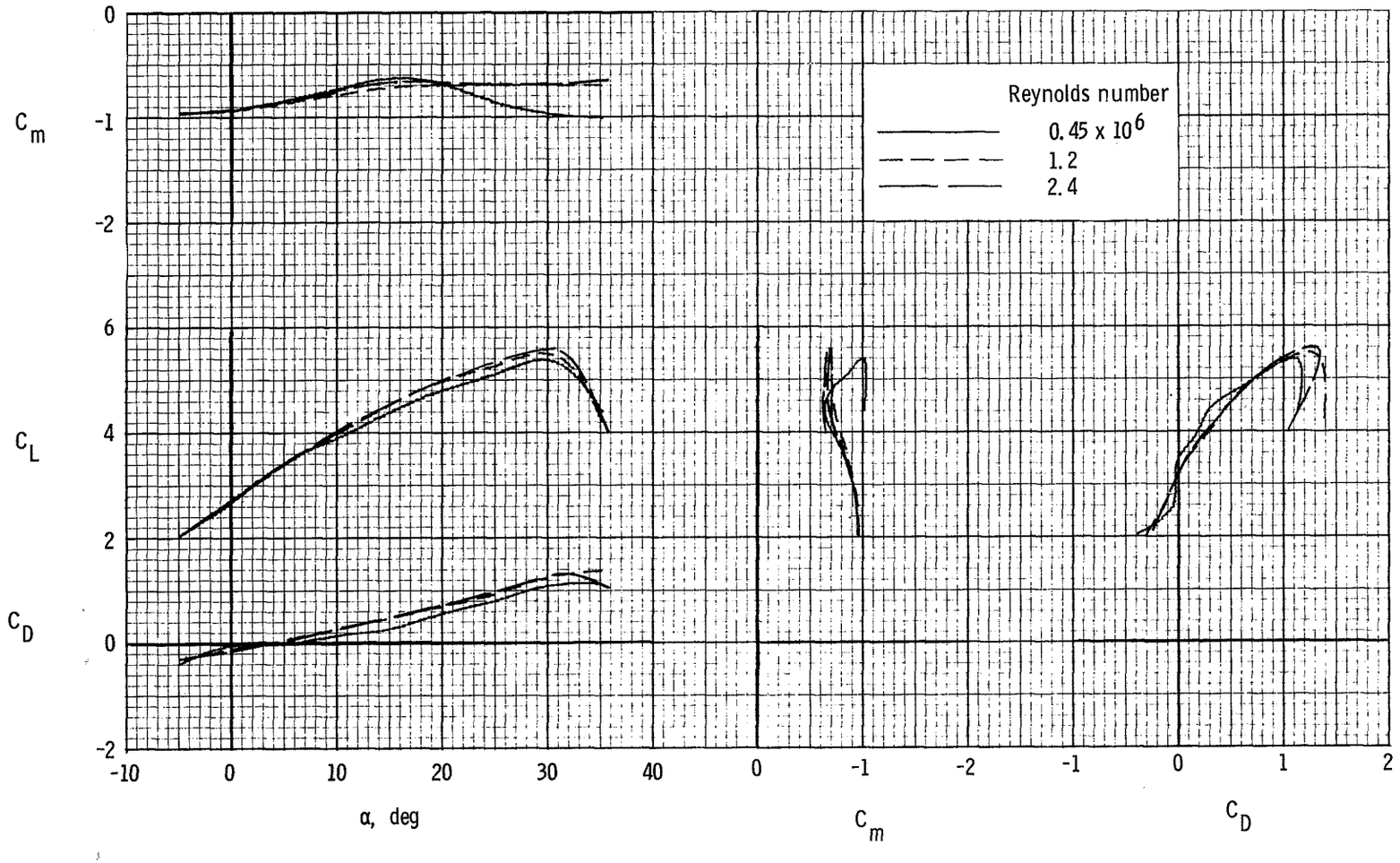

(b) $C_\mu = 1.0$.

Figure 40.- Continued.

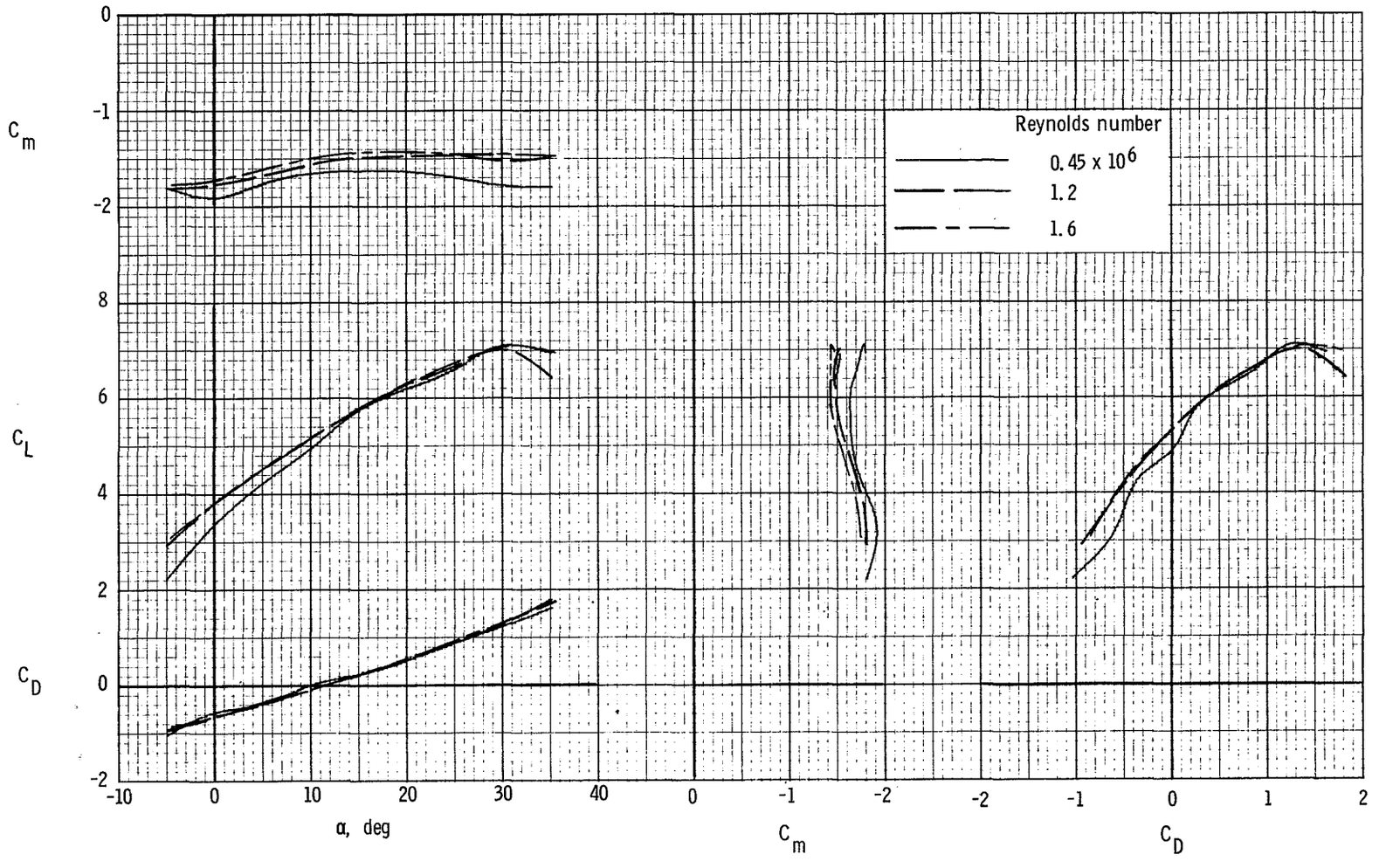

(c) $C_\mu = 2.0$.

Figure 40.- Concluded.

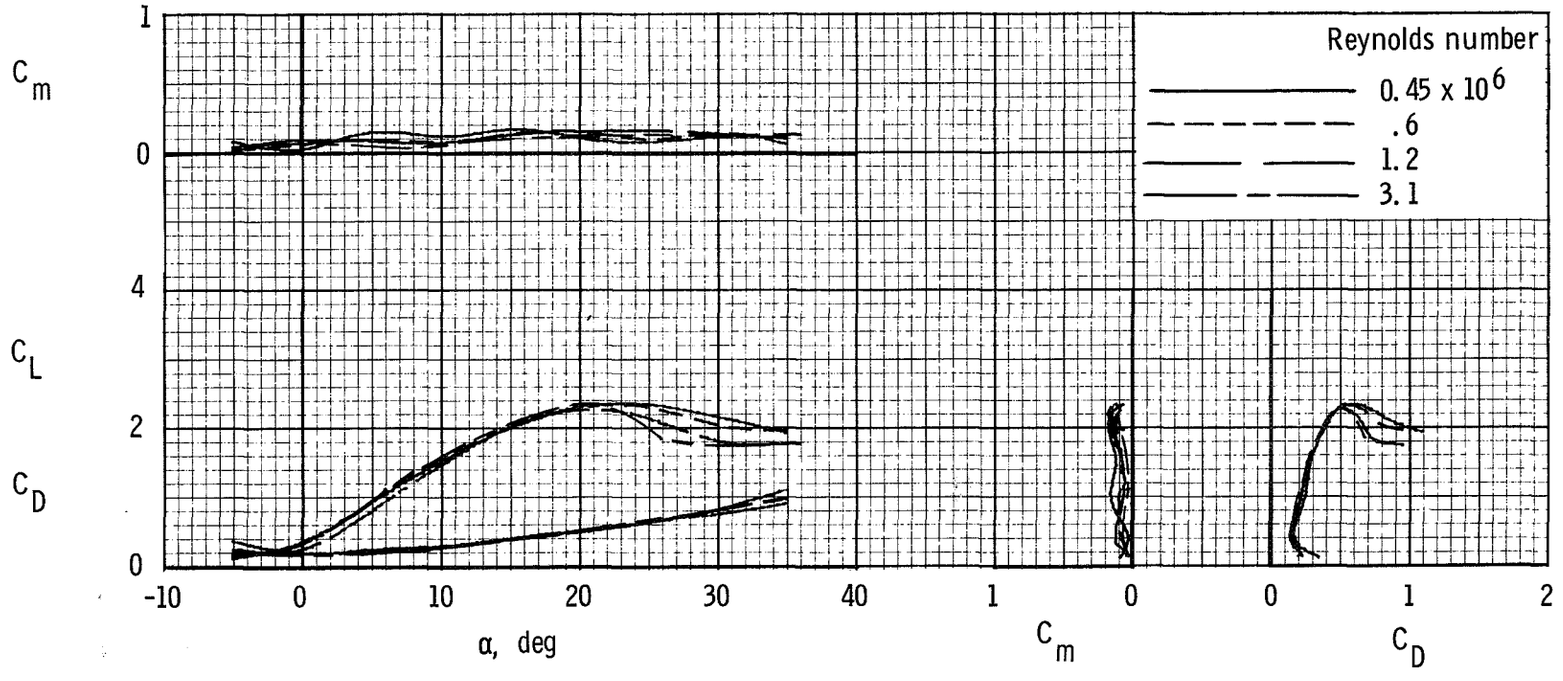

(a) $C_\mu = 0$.

Figure 41.- Effect of Reynolds number on the longitudinal characteristics of the model. $\delta_f = 20^o$.

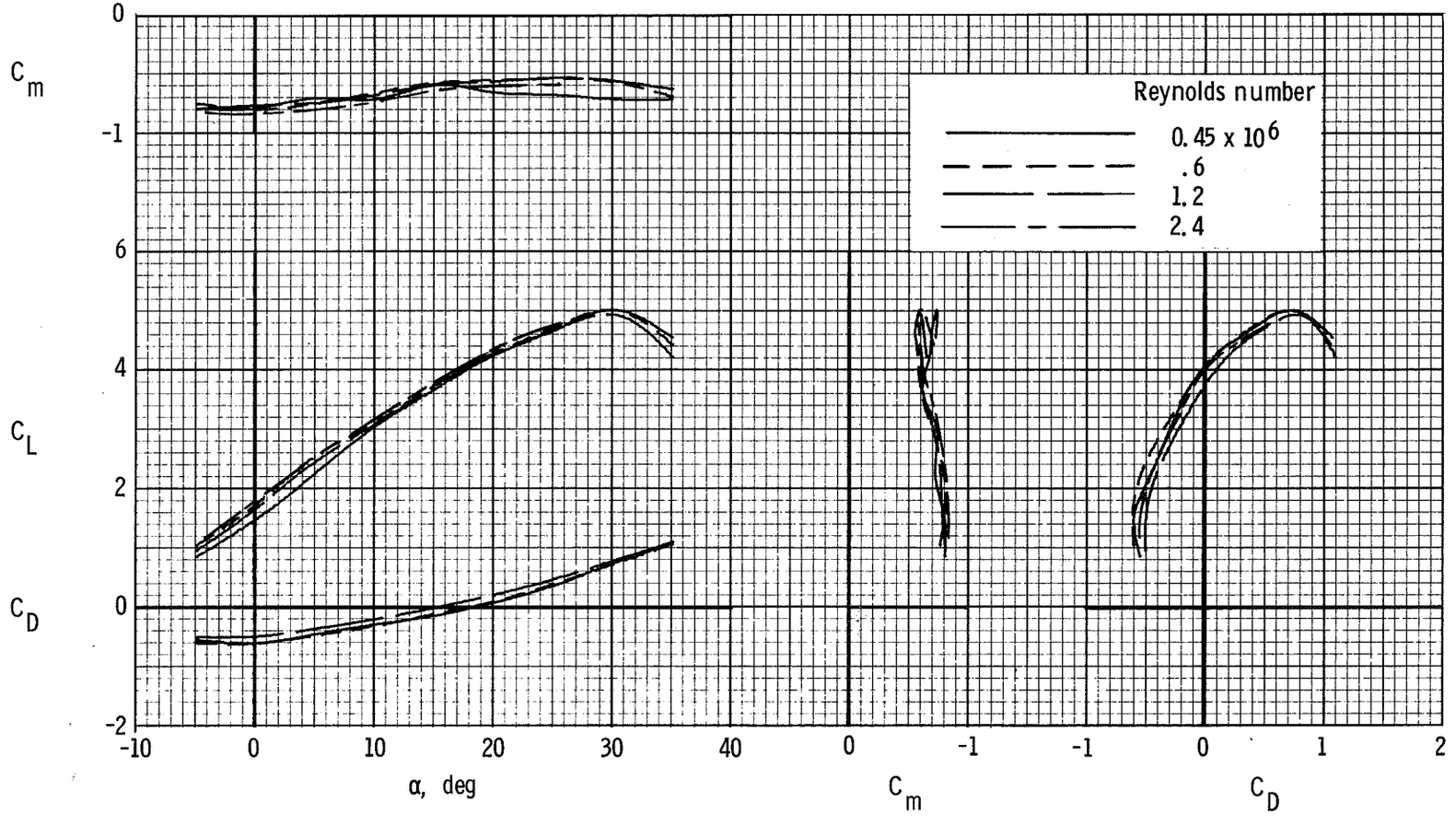

(b) $C_\mu = 1.0$.

Figure 41.- Continued.

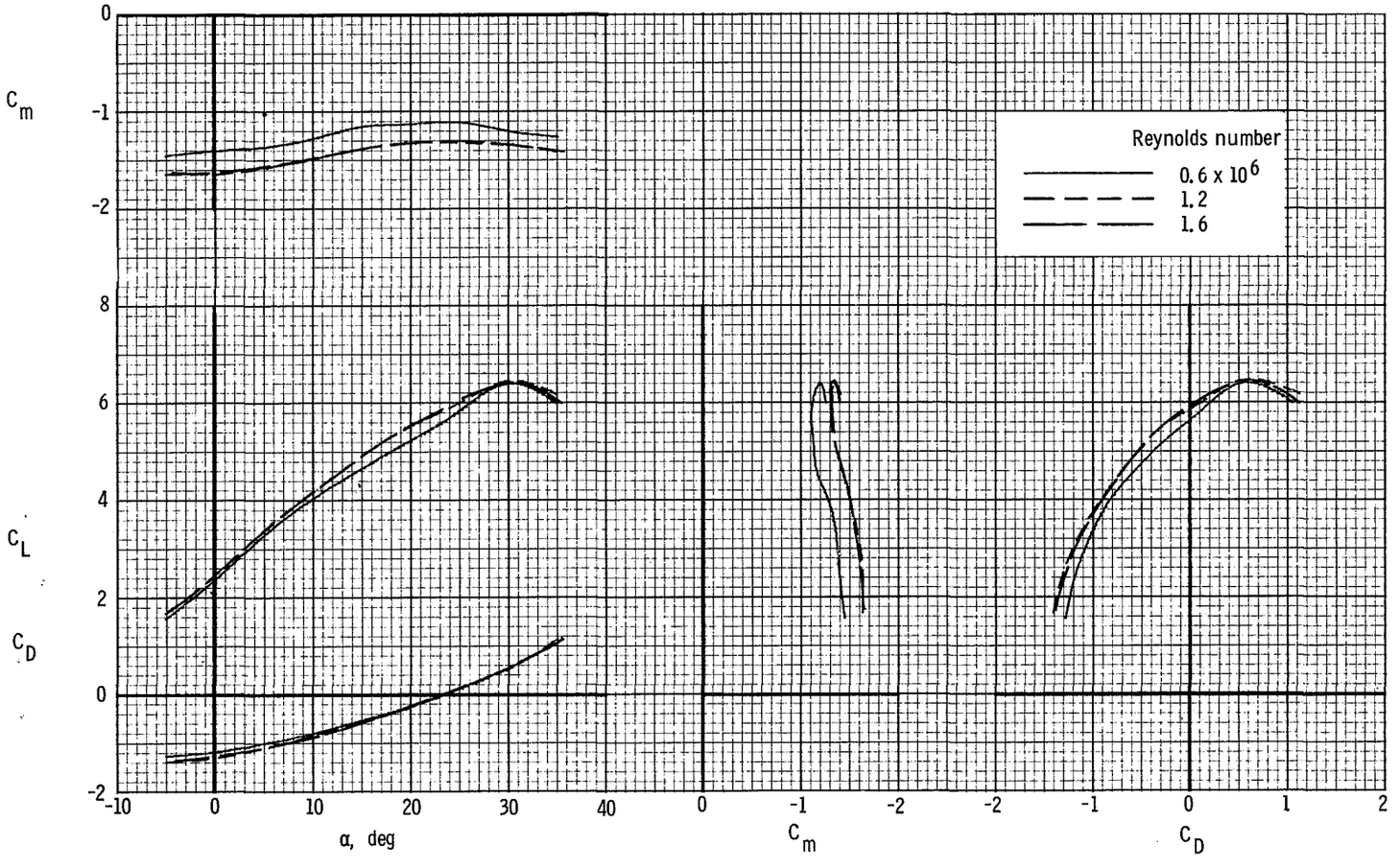

(c) C_μ = 2.0.

Figure 41.- Concluded.

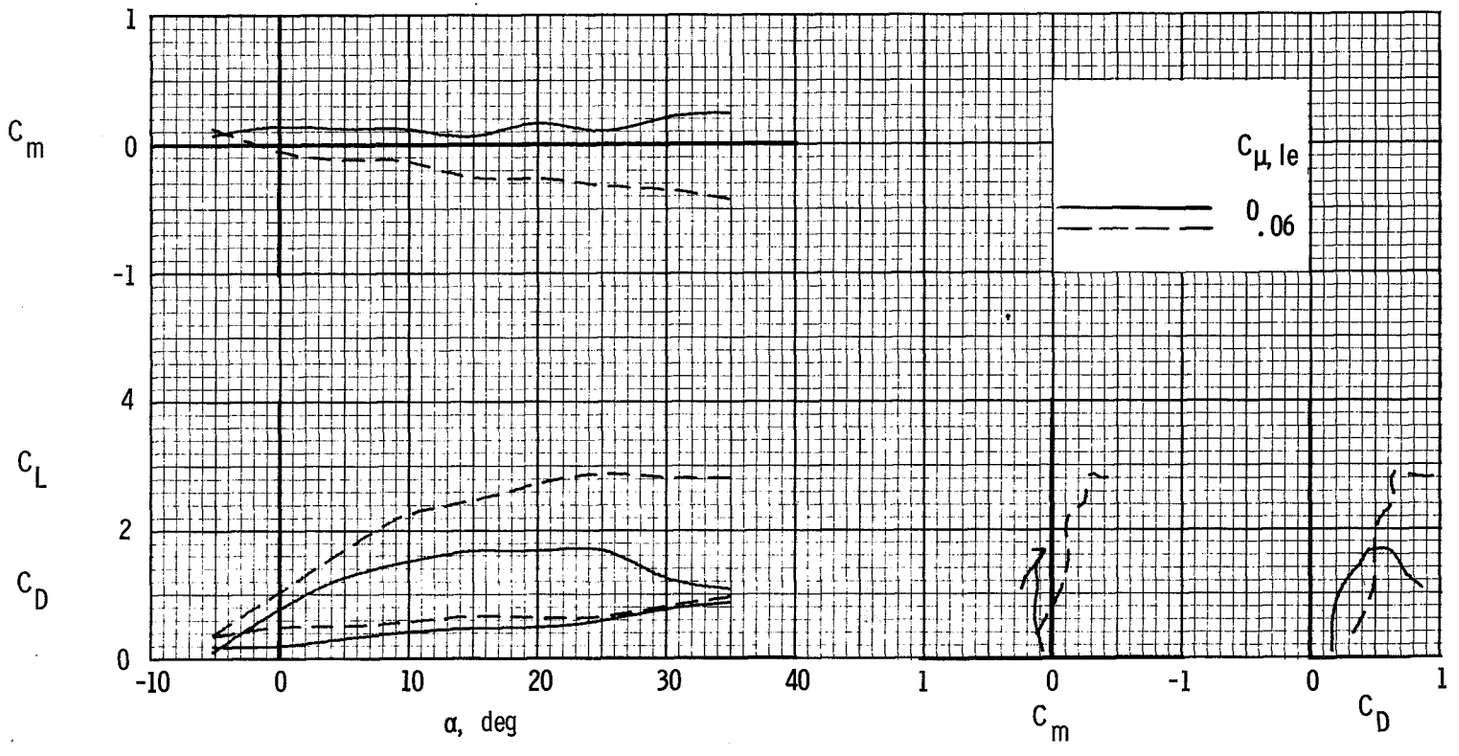

(a) $C_\mu = 0$.

Figure 42.- Effect of leading-edge blowing on longitudinal characteristics of the model at a Reynolds number of 0.45×10^6. $\delta_f = 60^o$.

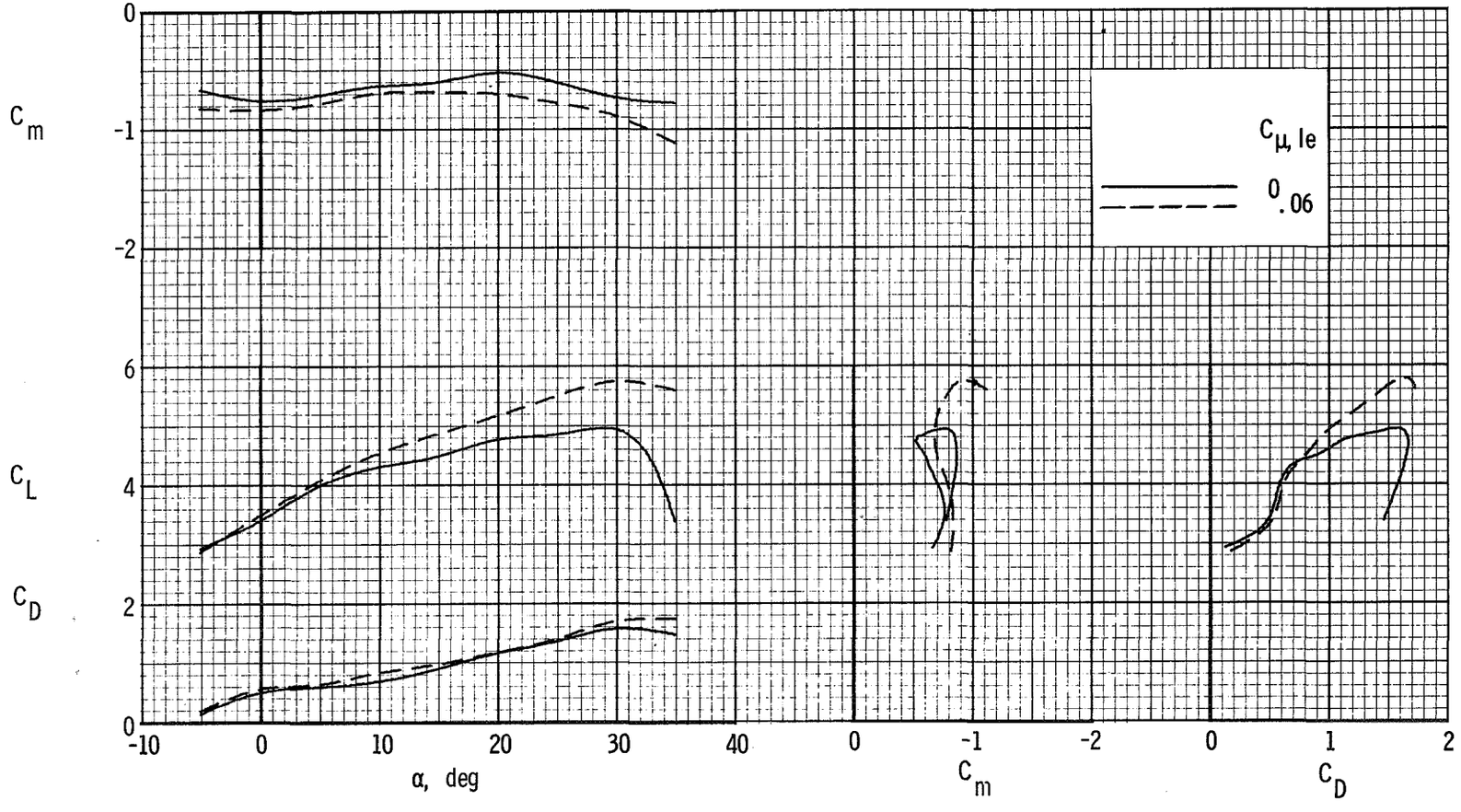

(b) $C_\mu = 1.0$.

Figure 42.- Continued.

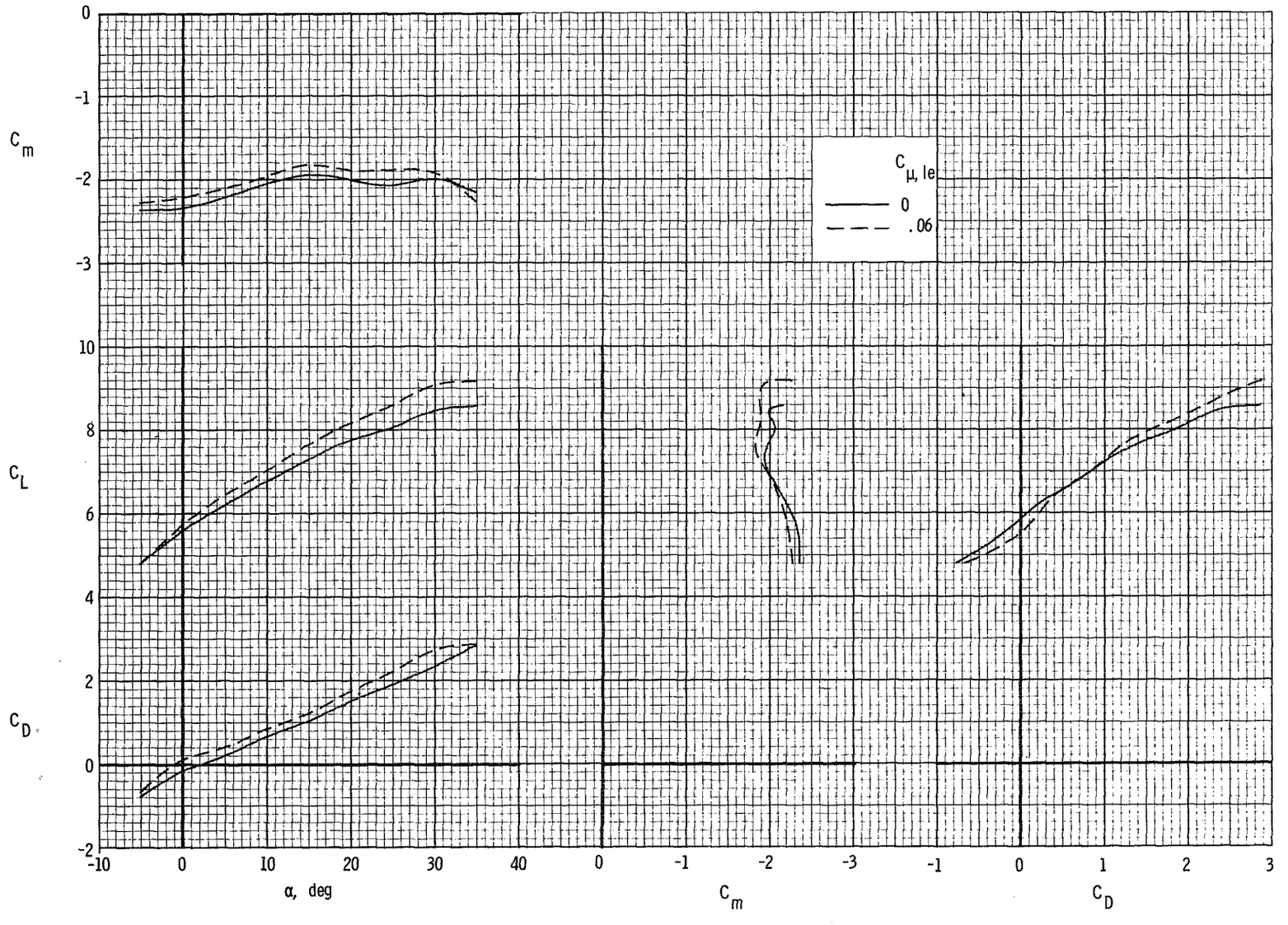

(c) $C_\mu = 3.0$.

Figure 42.- Concluded.

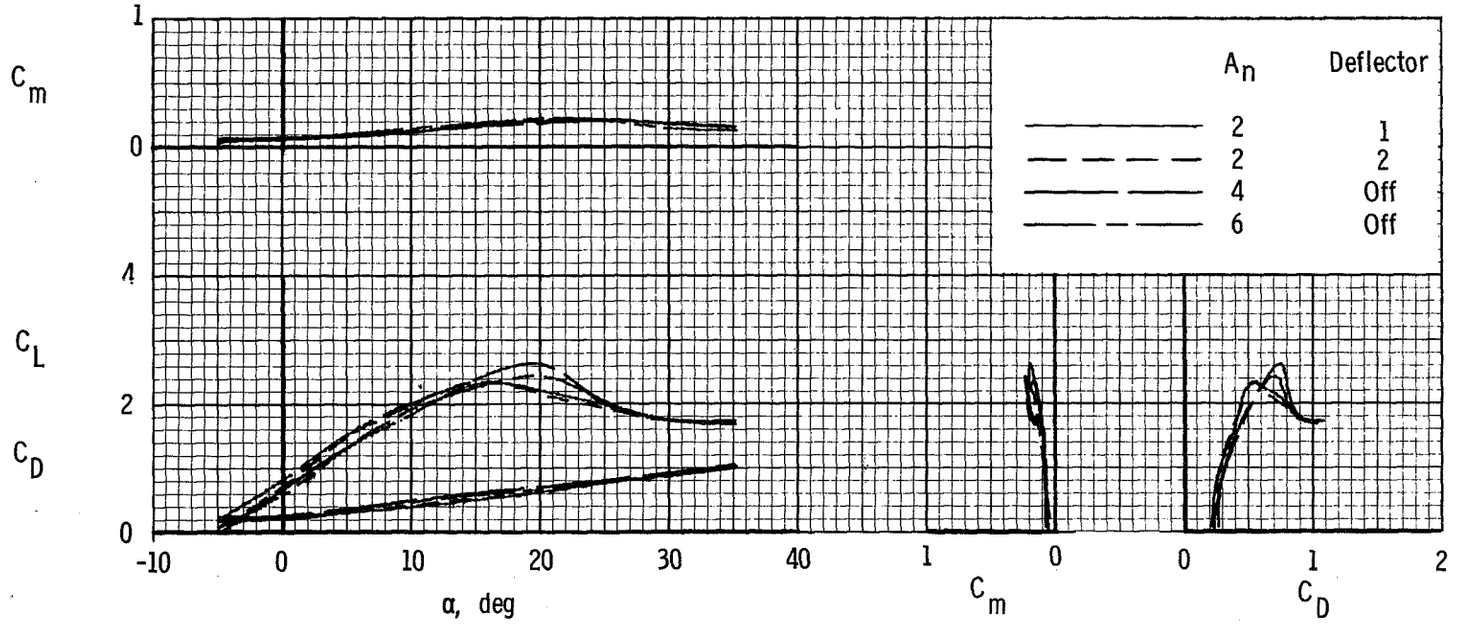

(a) $C_\mu = 0$.

Figure 43.- Effect of nozzle geometry on longitudinal characteristics of the model. $\delta_f = 60^o$.

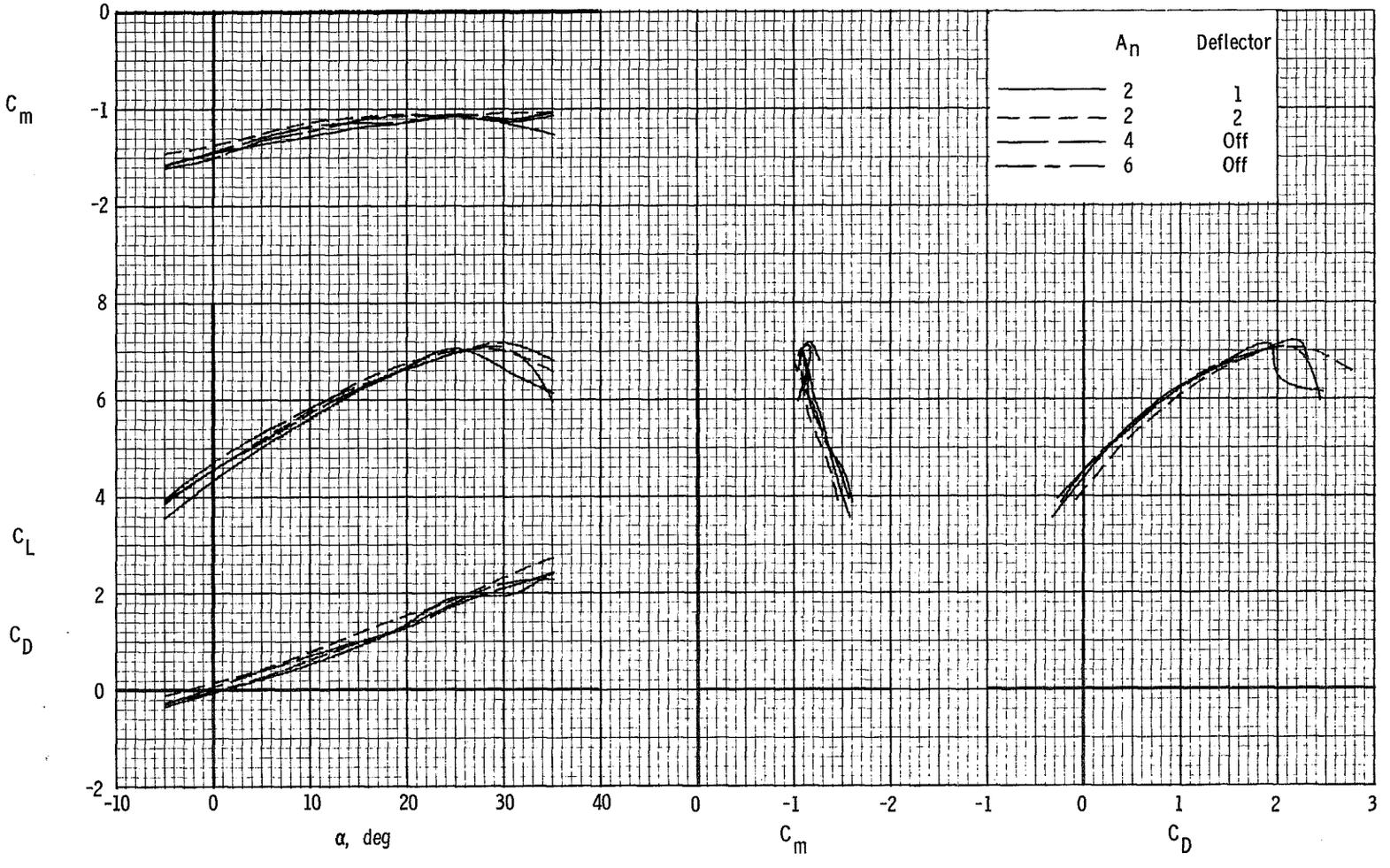

(b) $C_\mu = 2.0$.

Figure 43.- Continued.

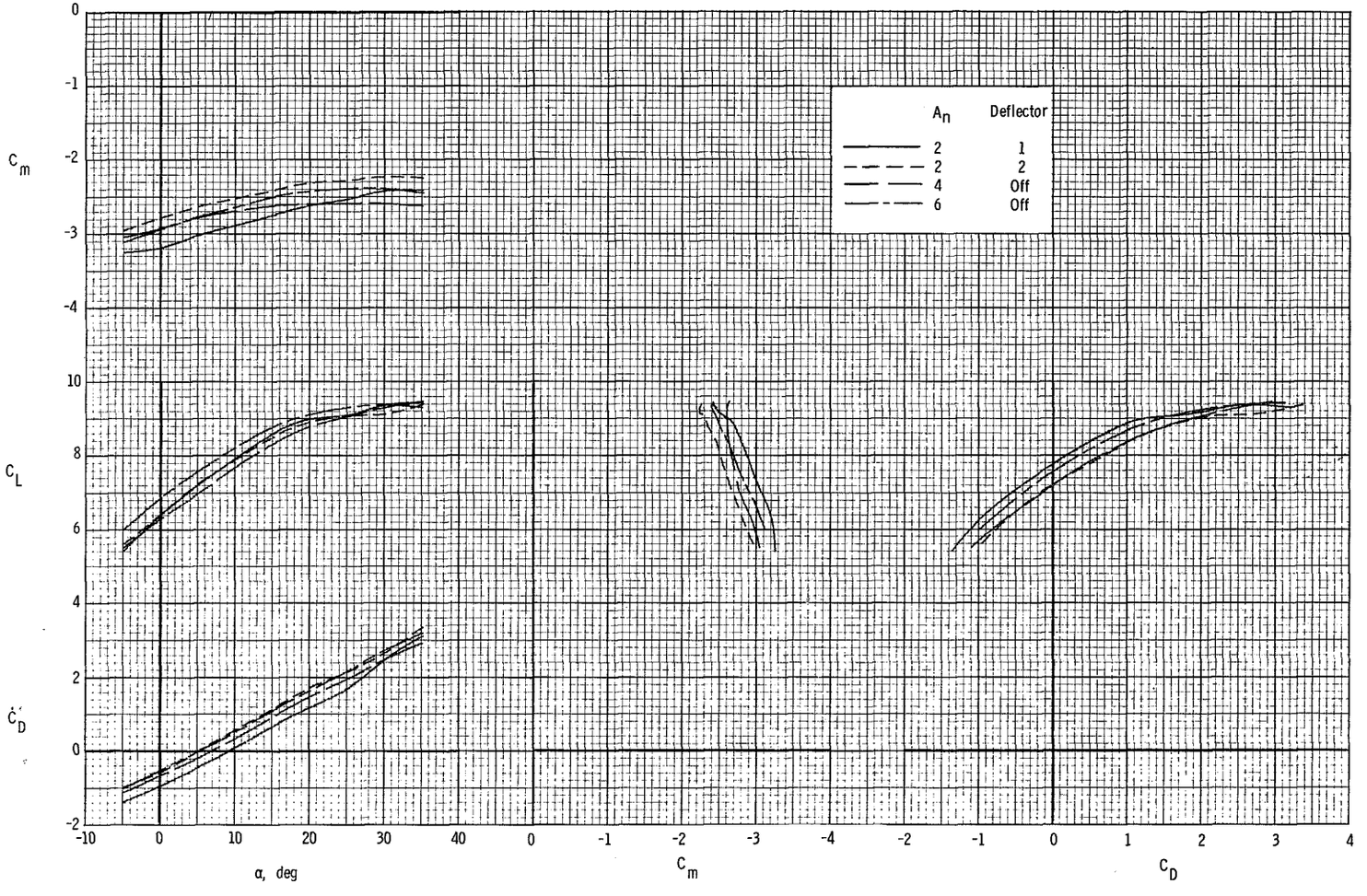

(c) C_μ = 4.0.

Figure 43.- Concluded.

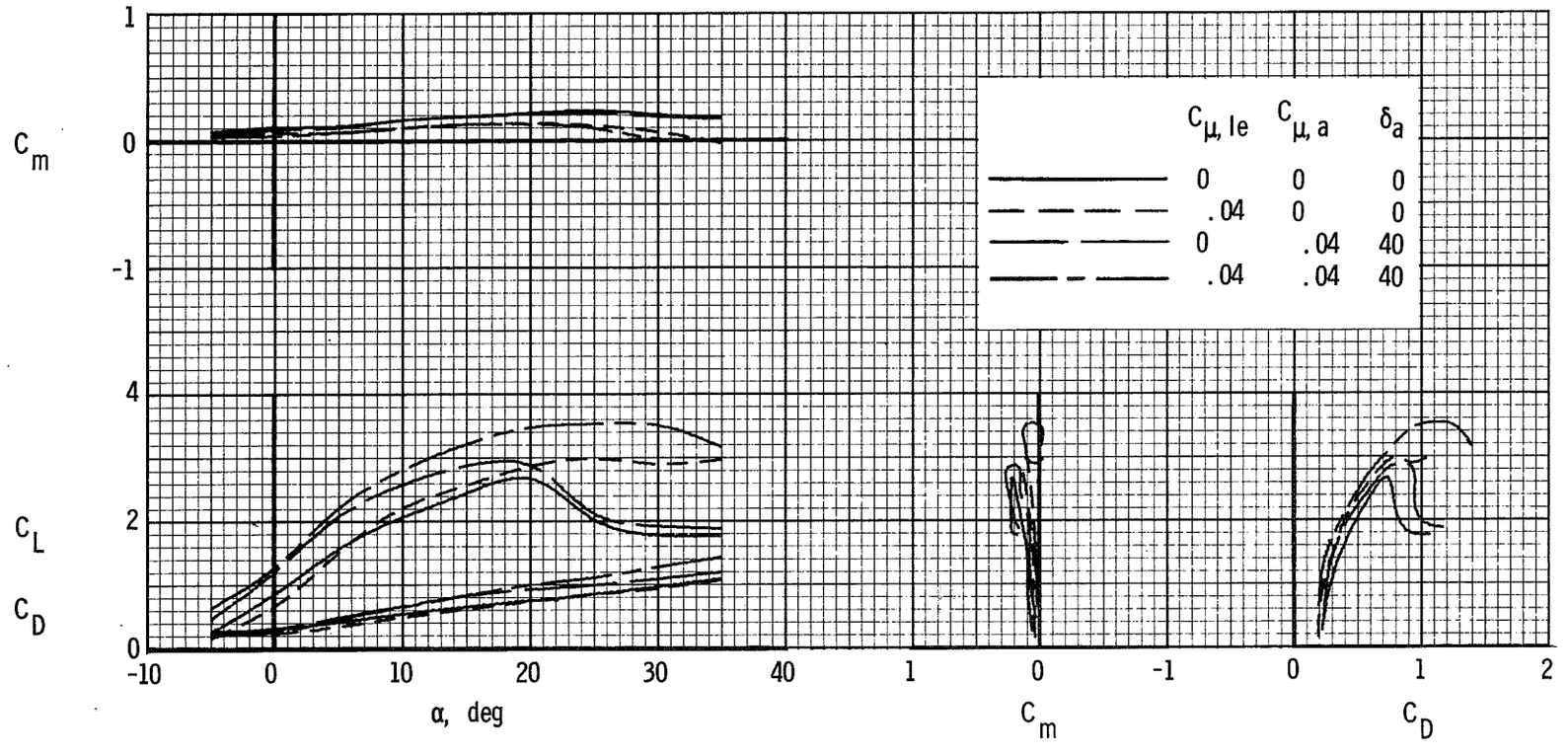

(a) $C_\mu = 0$.

Figure 44.- Effect of leading-edge BLC and drooped aileron on longitudinal characteristics of the model. $\delta_f = 60^o$.

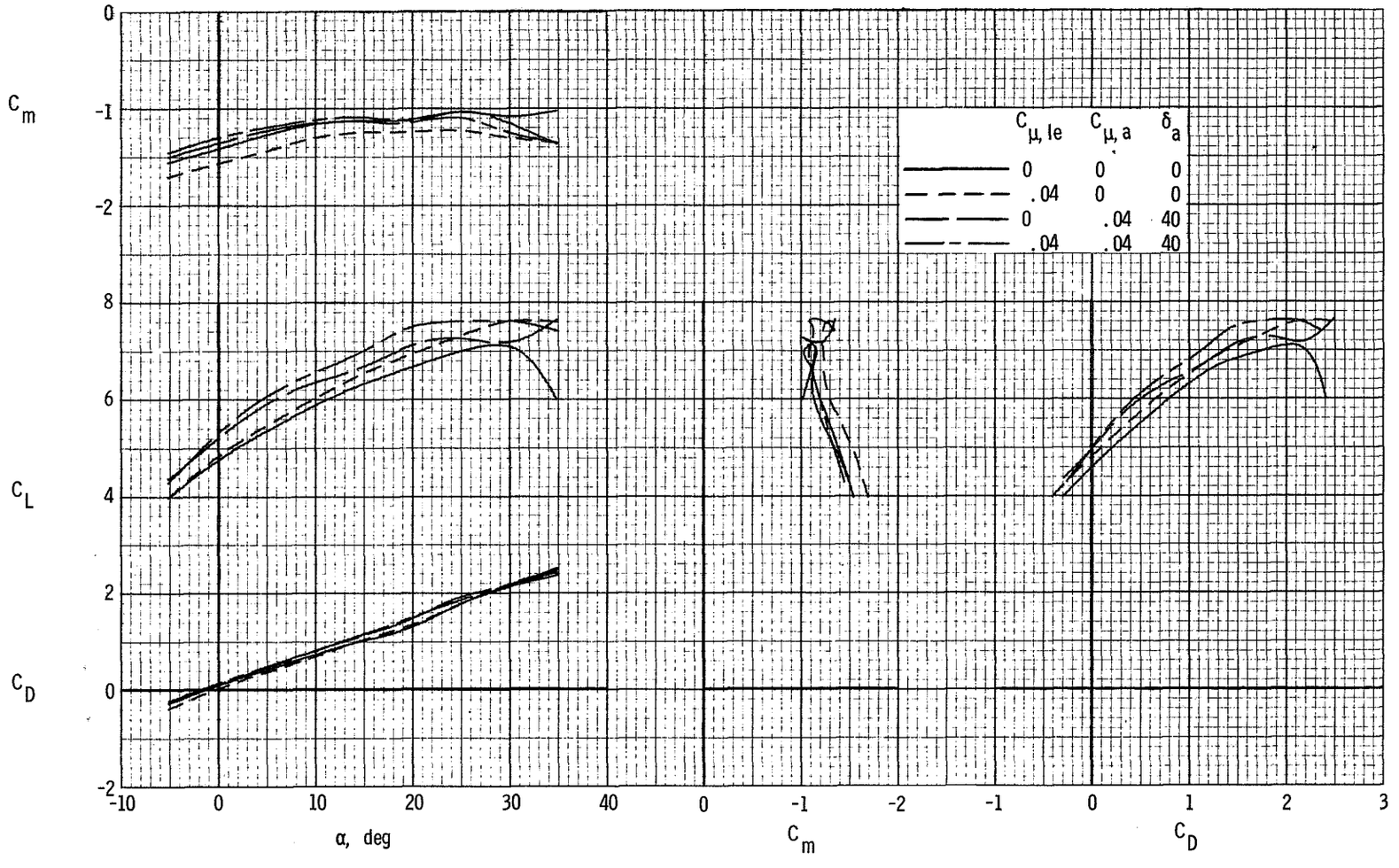

(b) C_μ = 2.0.

Figure 44.- Continued.

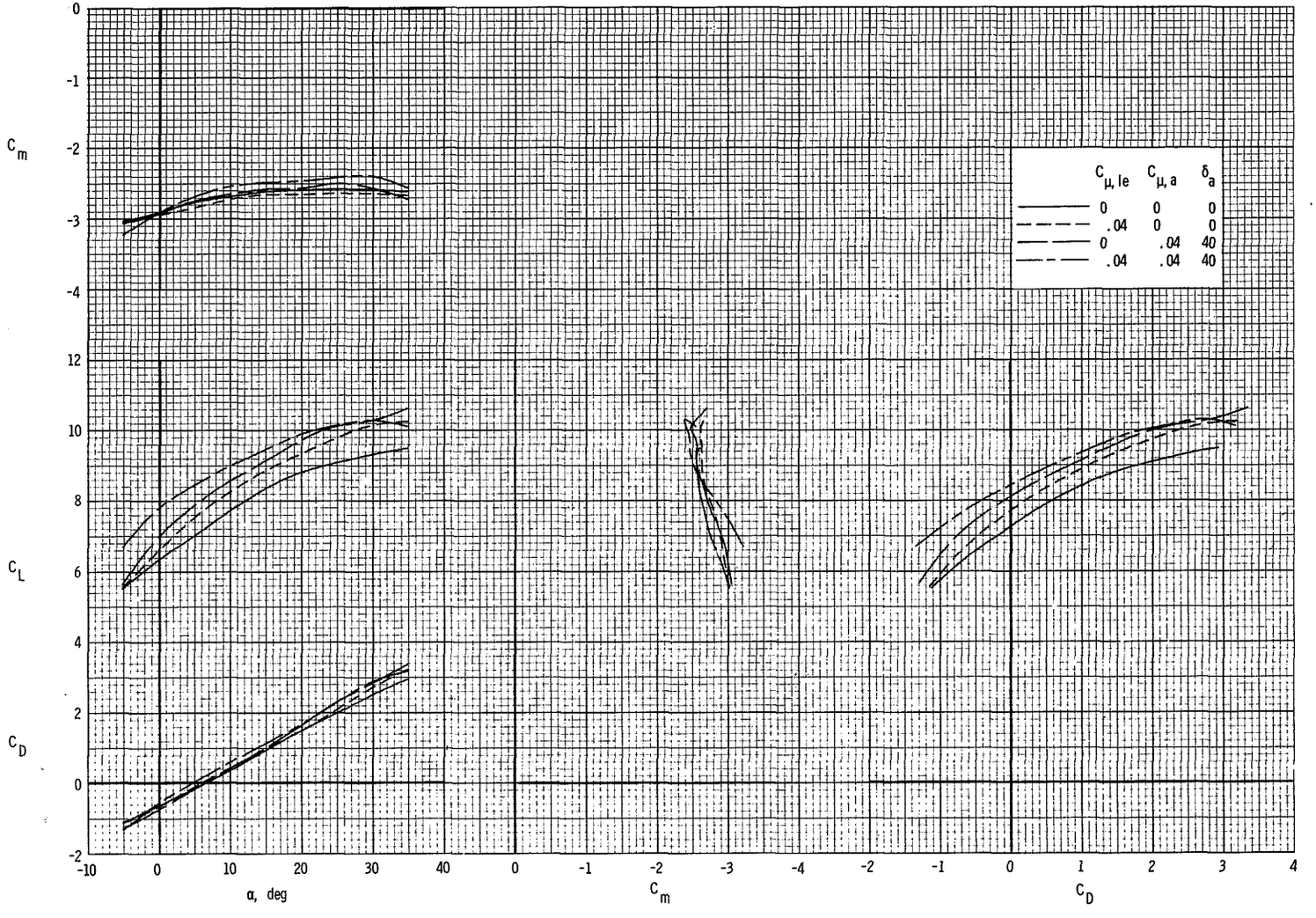

(c) $C_\mu = 4.0$.

Figure 44.- Concluded.

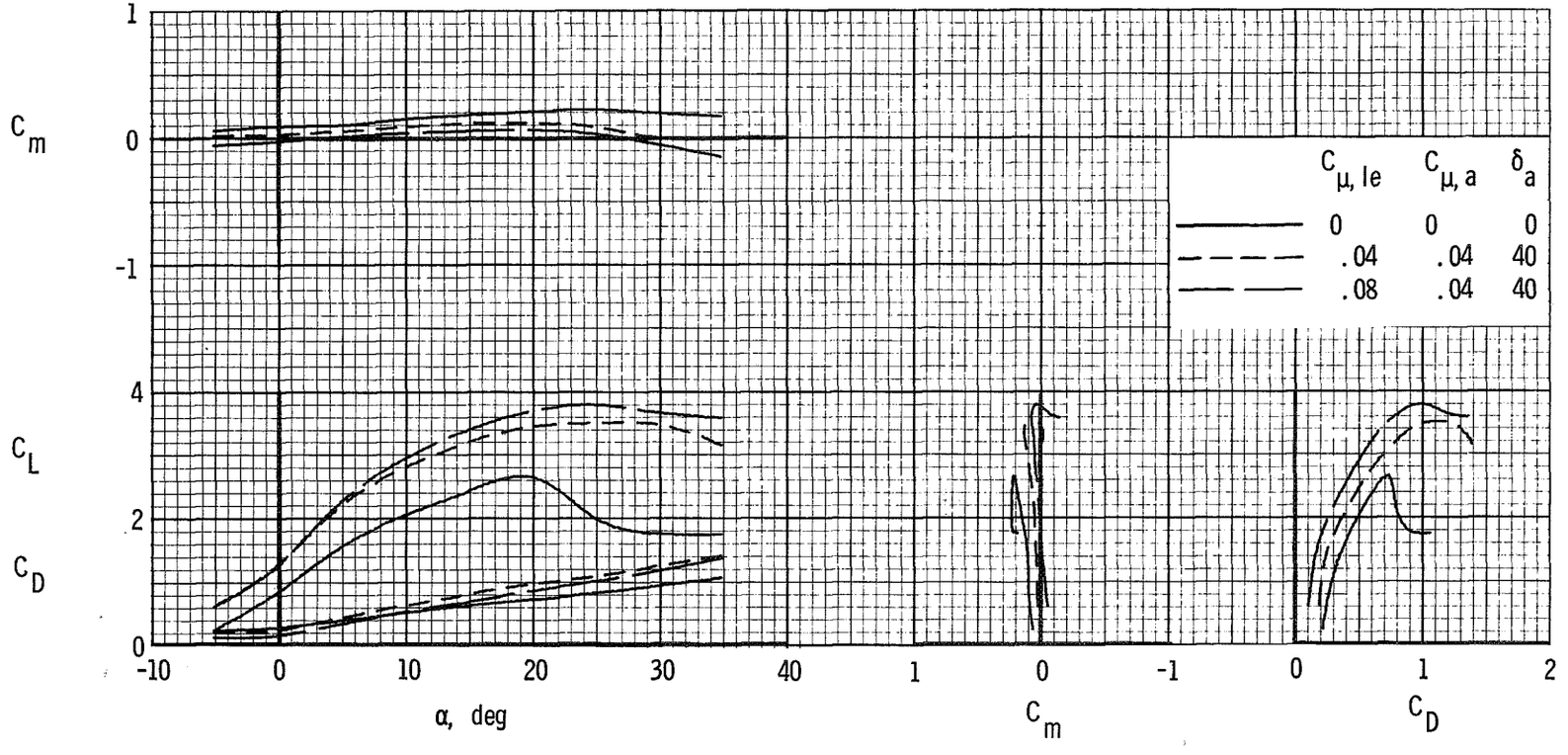

(a) $C_\mu = 0$.

Figure 45.- Effect of increased leading-edge blowing on longitudinal characteristics of the model. $\delta_f = 60^o$.

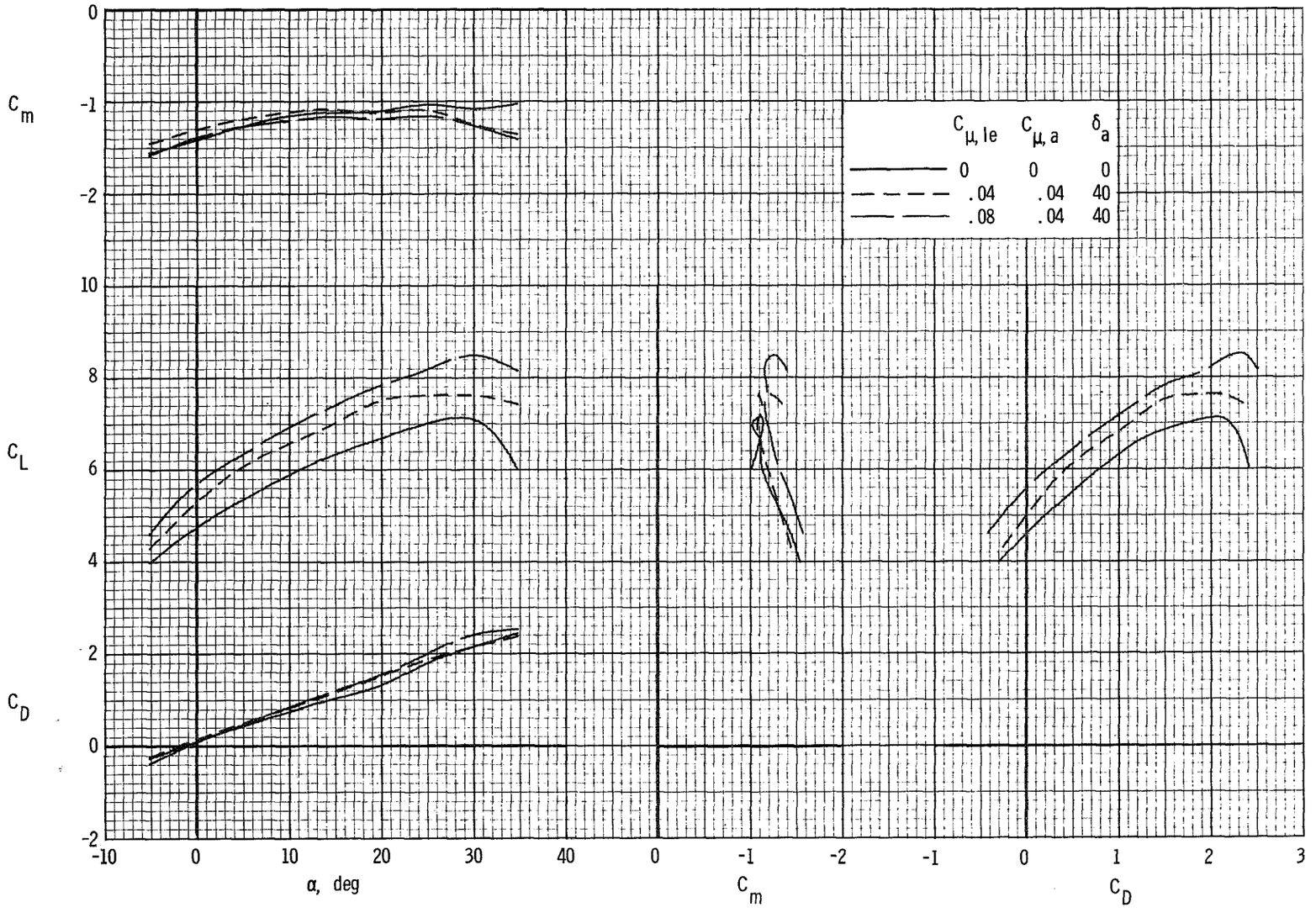

(b) $C_\mu = 2.0$.

Figure 45.- Continued.

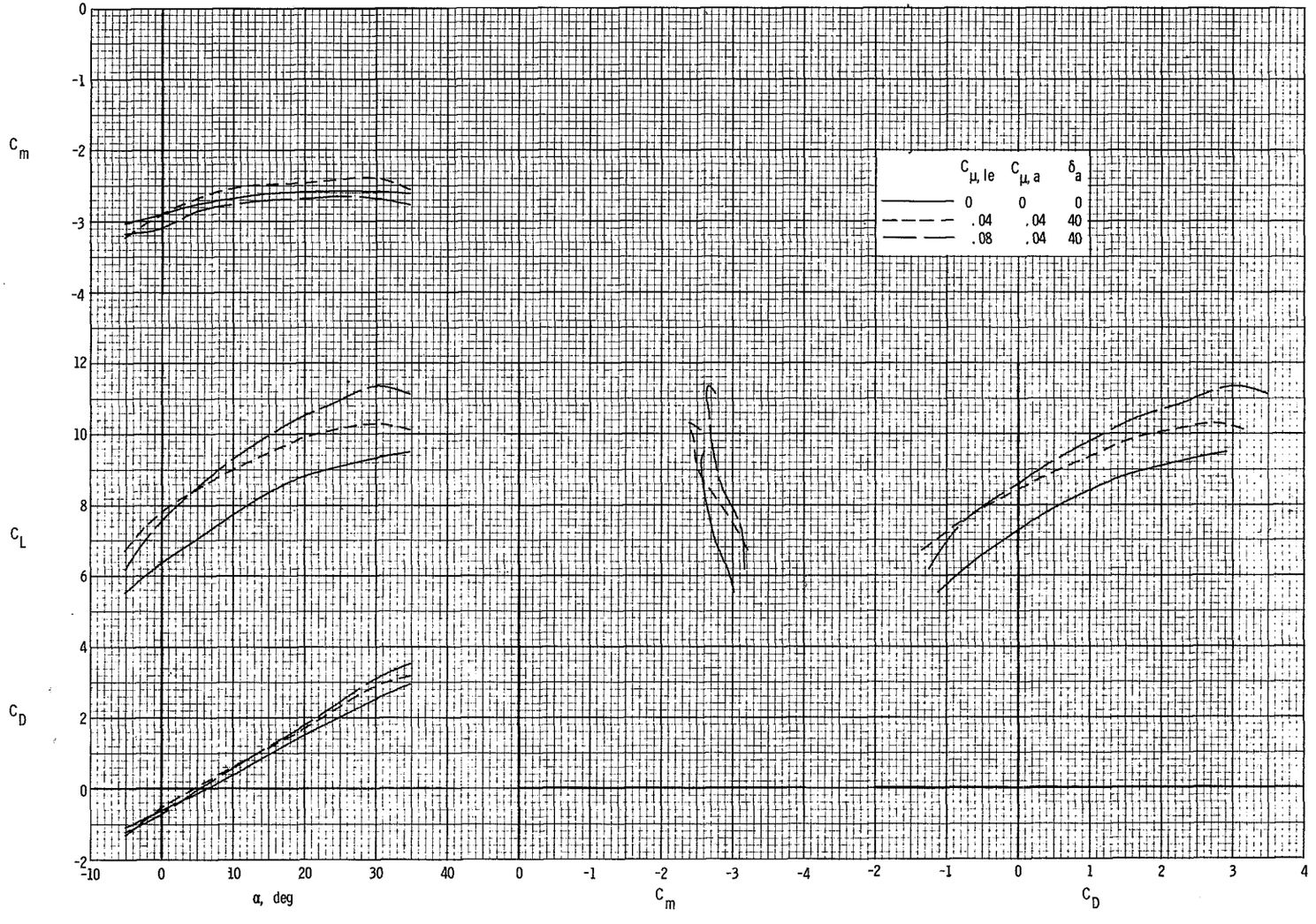

(c) $C_\mu = 4.0$.

Figure 45.- Concluded.

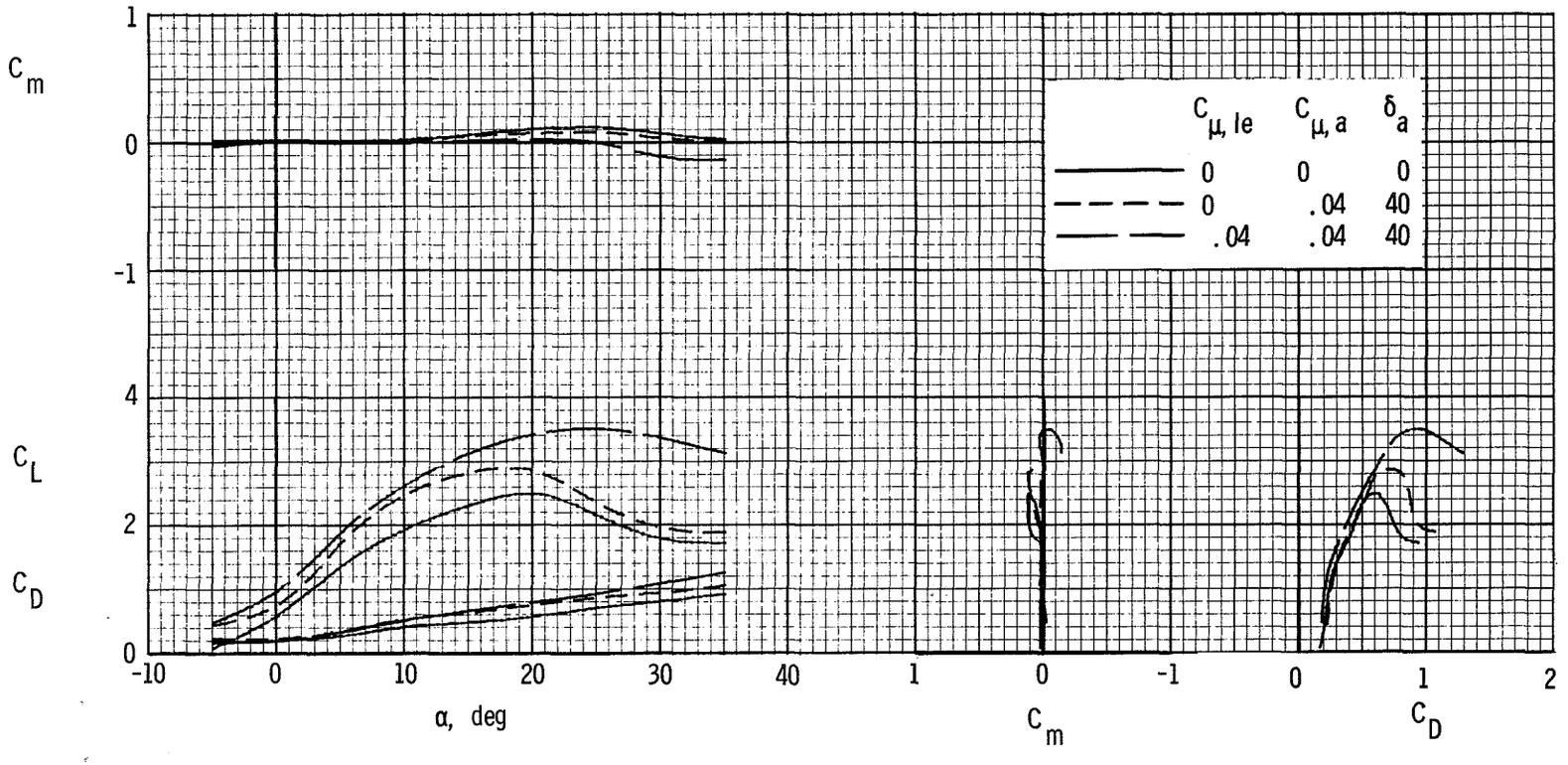

(a) $C_\mu = 0$.

Figure 46.- Effect of leading-edge BLC and drooped blown aileron on longitudinal characteristics of the model. $\delta_f = 40^o$.

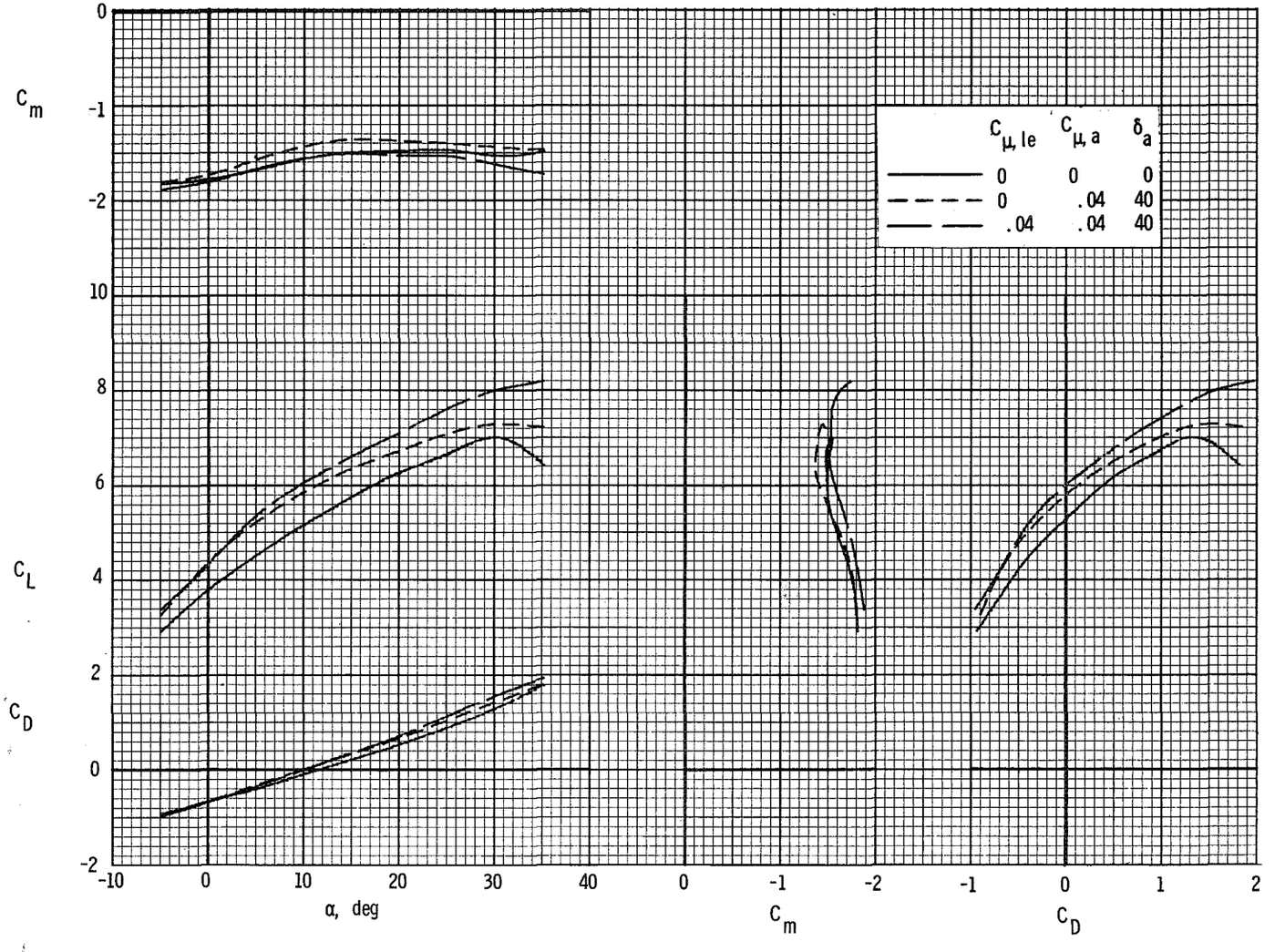

(b) $C_\mu = 2.0$.

Figure 46.- Continued.

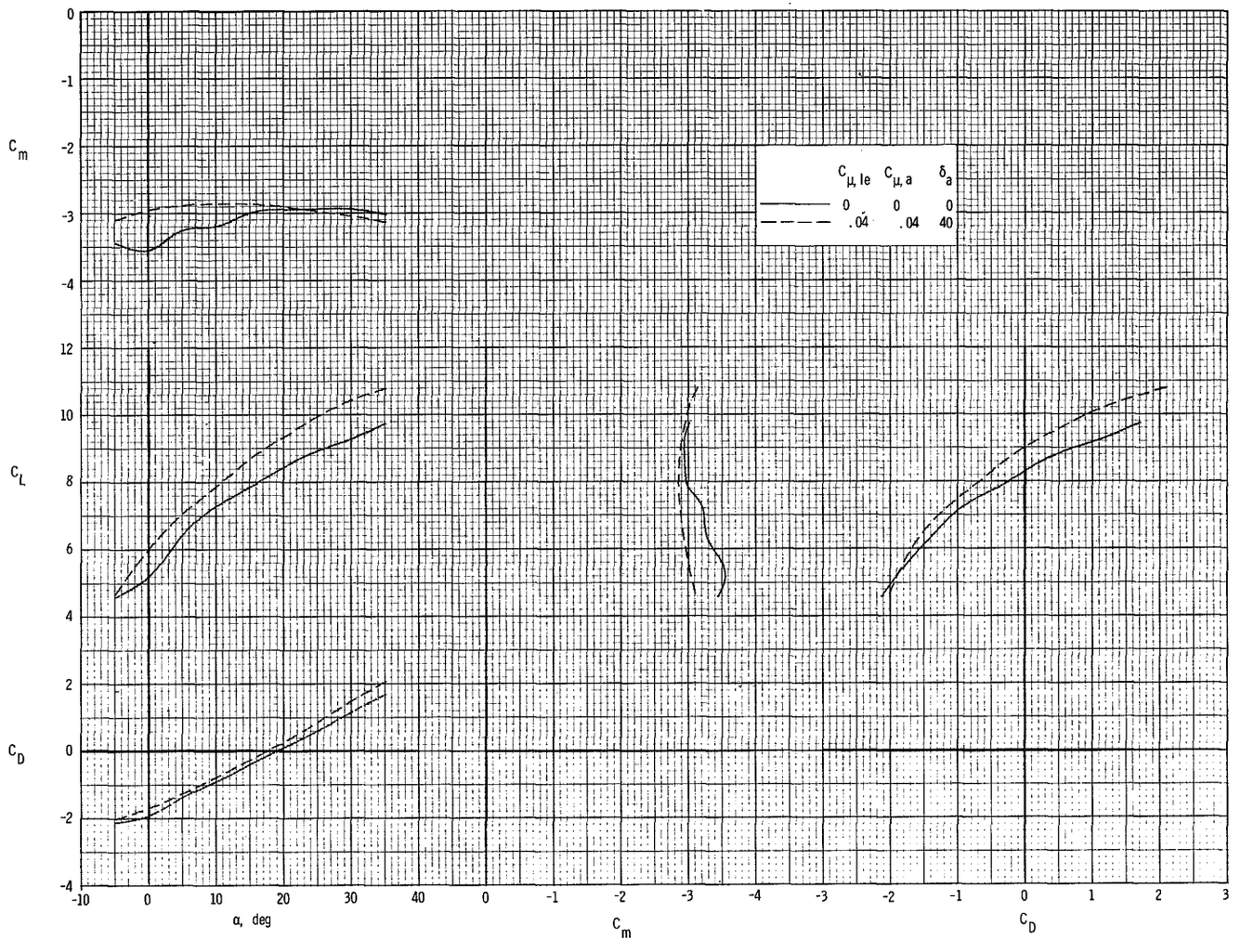

(c) $C_\mu = 4.0$.

Figure 46.- Concluded.

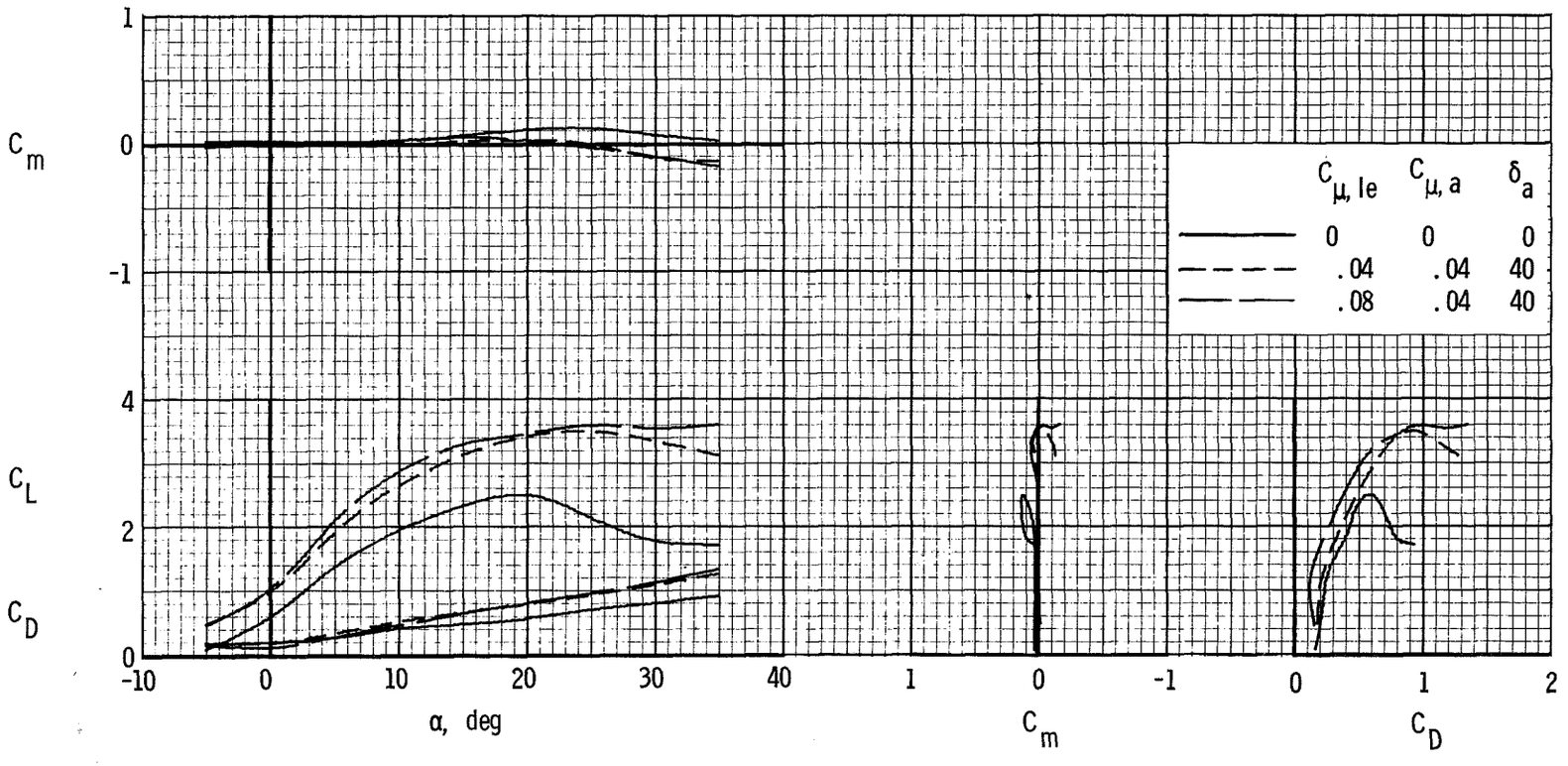

(a) $C_\mu = 0$.

Figure 47.- Effect of increased leading-edge blowing on longitudinal characteristics of the model. $\delta_f = 40^o$.

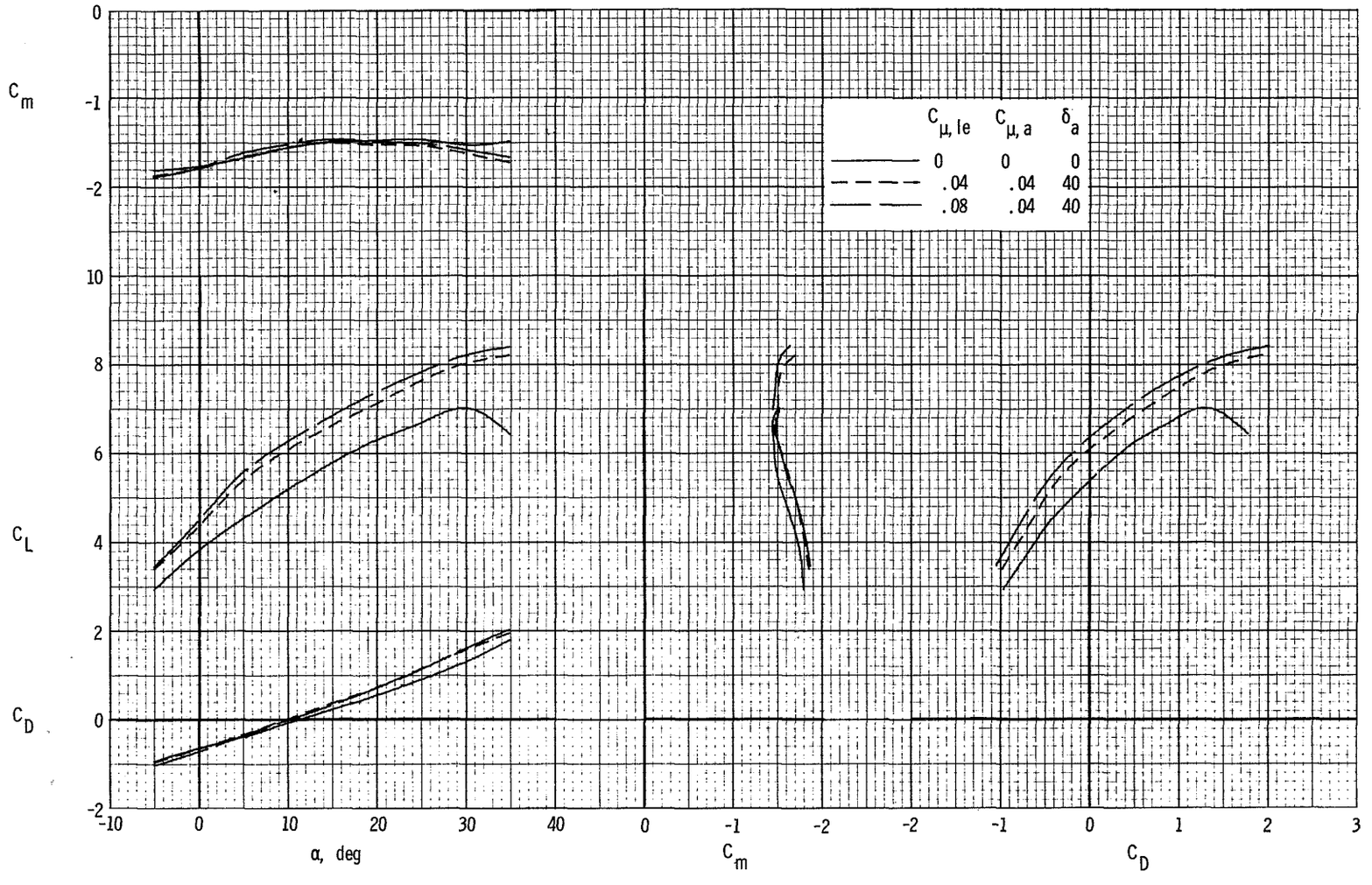

(b) $C_\mu = 2.0$.

Figure 47.- Continued.

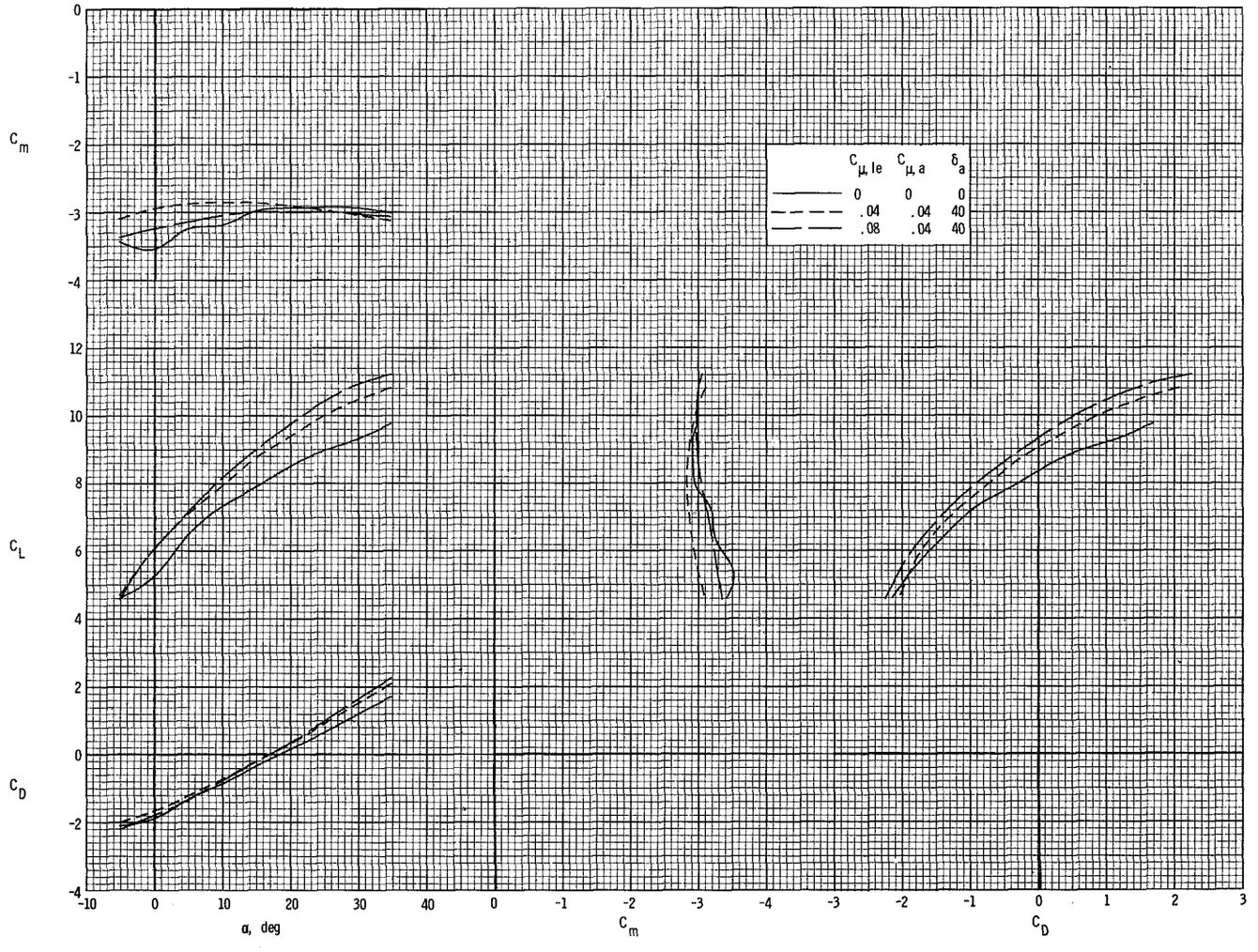

(c) $C_\mu = 4.0$.

Figure 47.- Concluded.

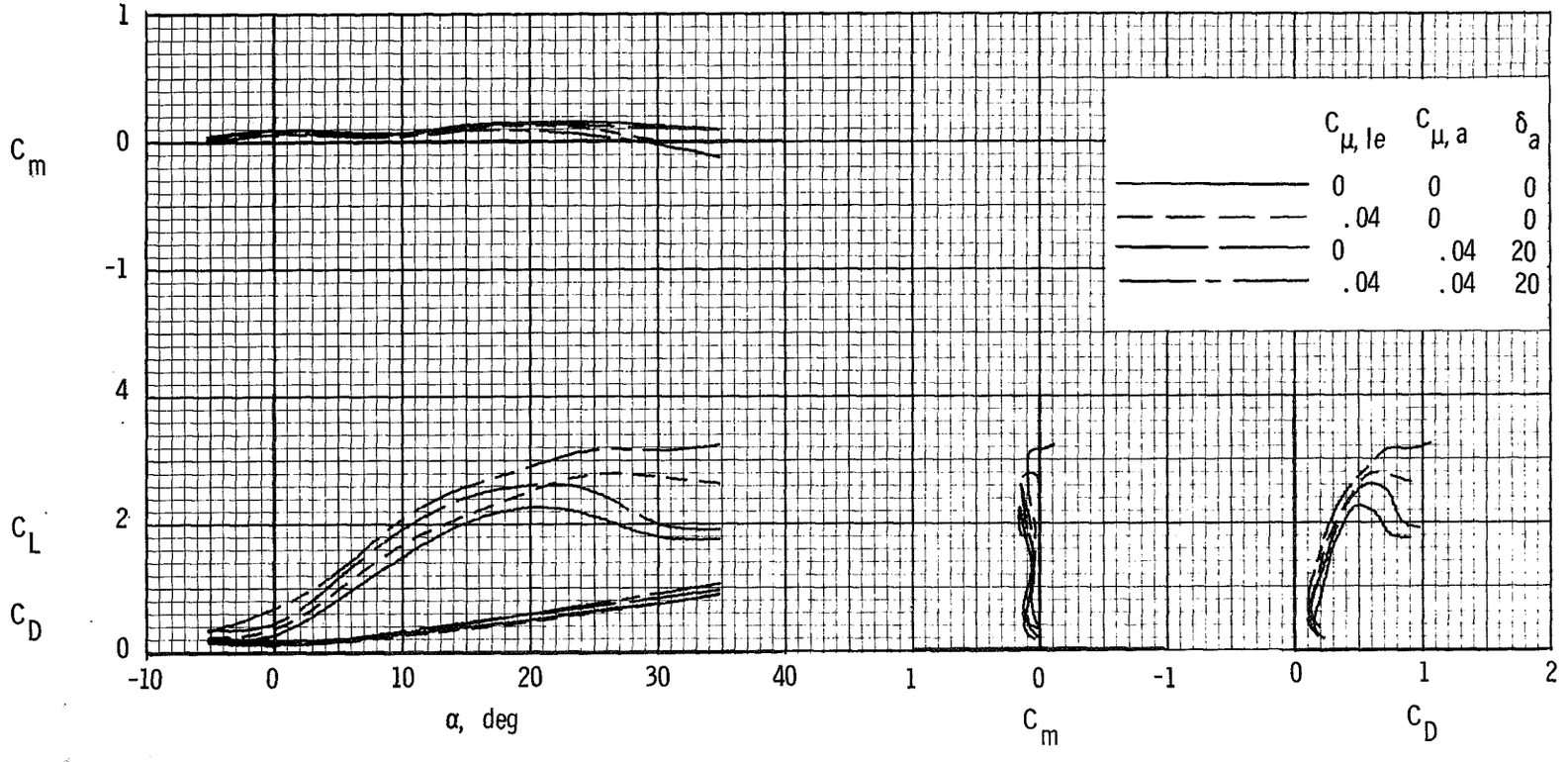

(a) $C_\mu = 0$.

Figure 48.- Effect of leading-edge BLC and drooped blown aileron on longitudinal characteristics of the model. $\delta_f = 20^o$.

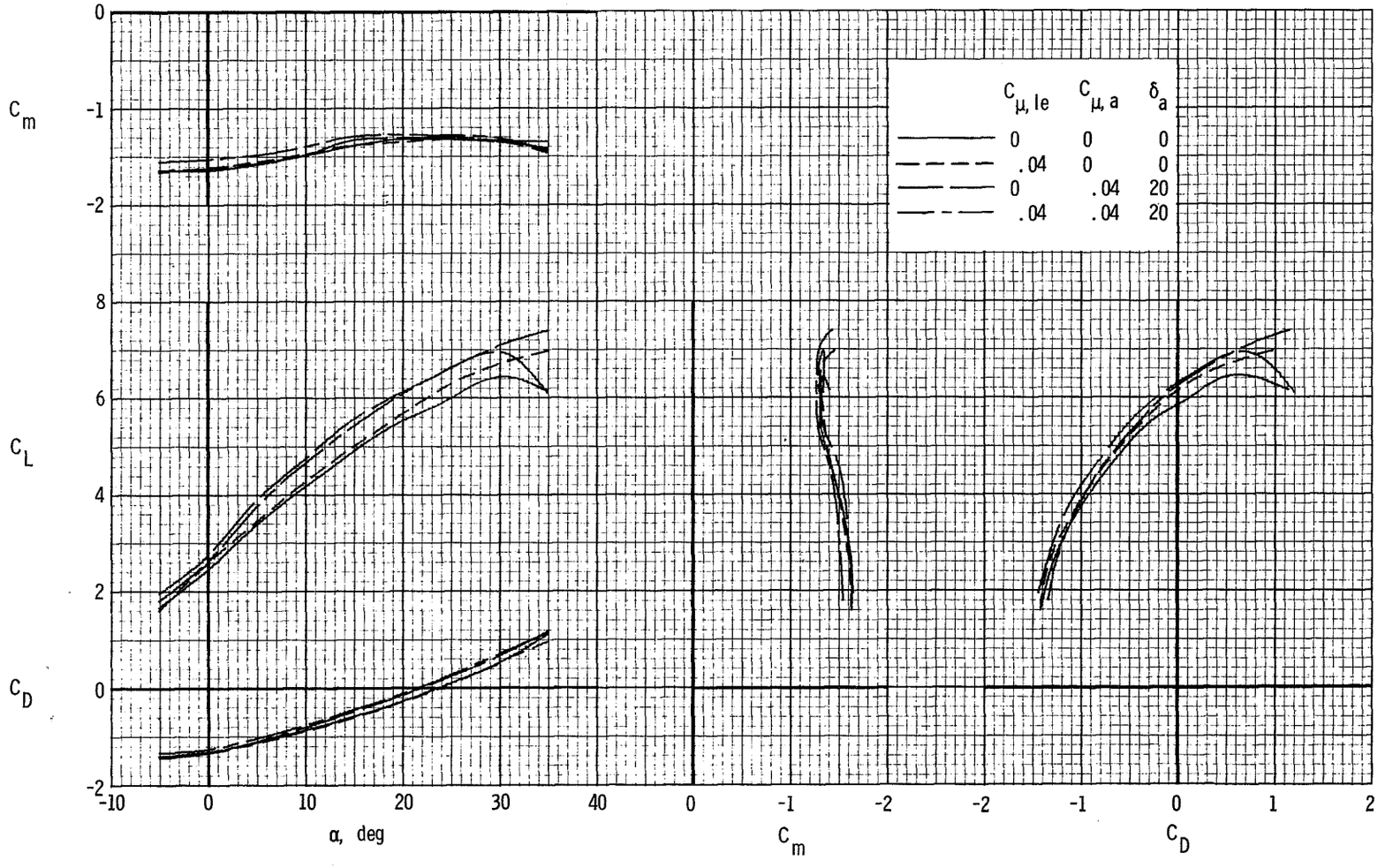

(b) $C\mu$ = 2.0.

Figure 48.- Continued.

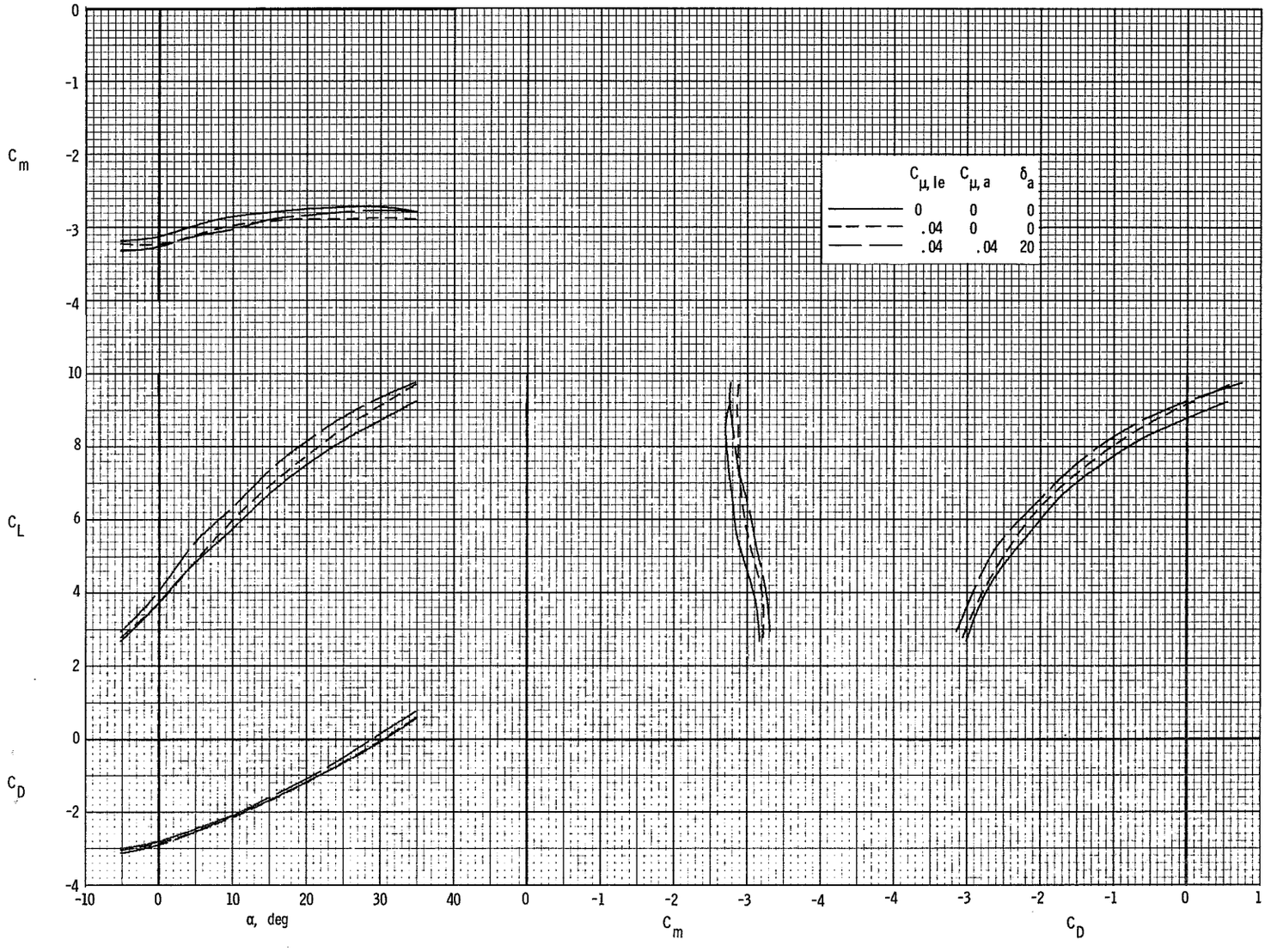

(c) $C_\mu = 4.0$.

Figure 48.- Concluded.

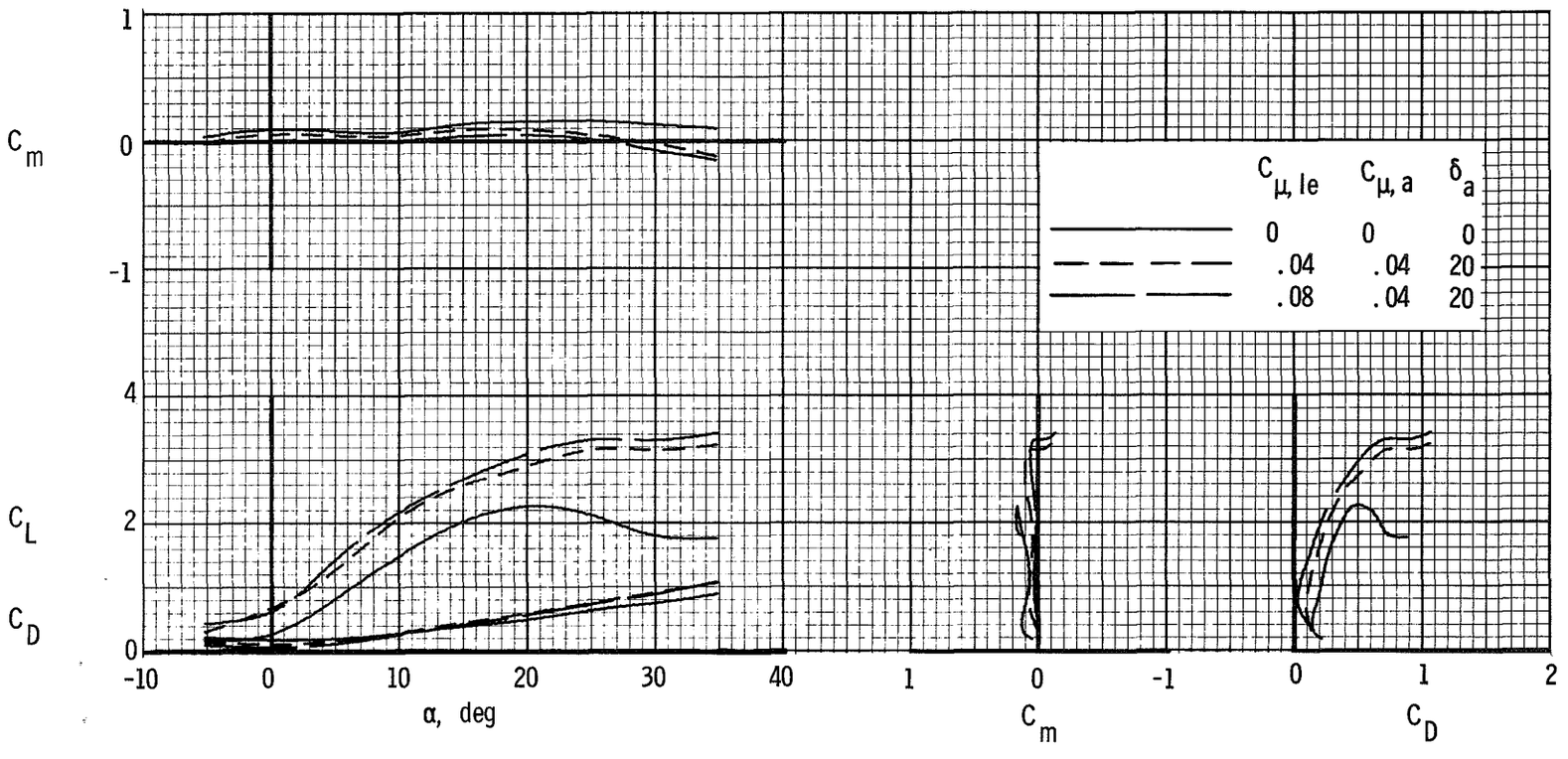

(a) $C_\mu = 0$.

Figure 49.- Effect of increased leading-edge blowing on longitudinal characteristics of the model. $\delta_f = 20^o$.

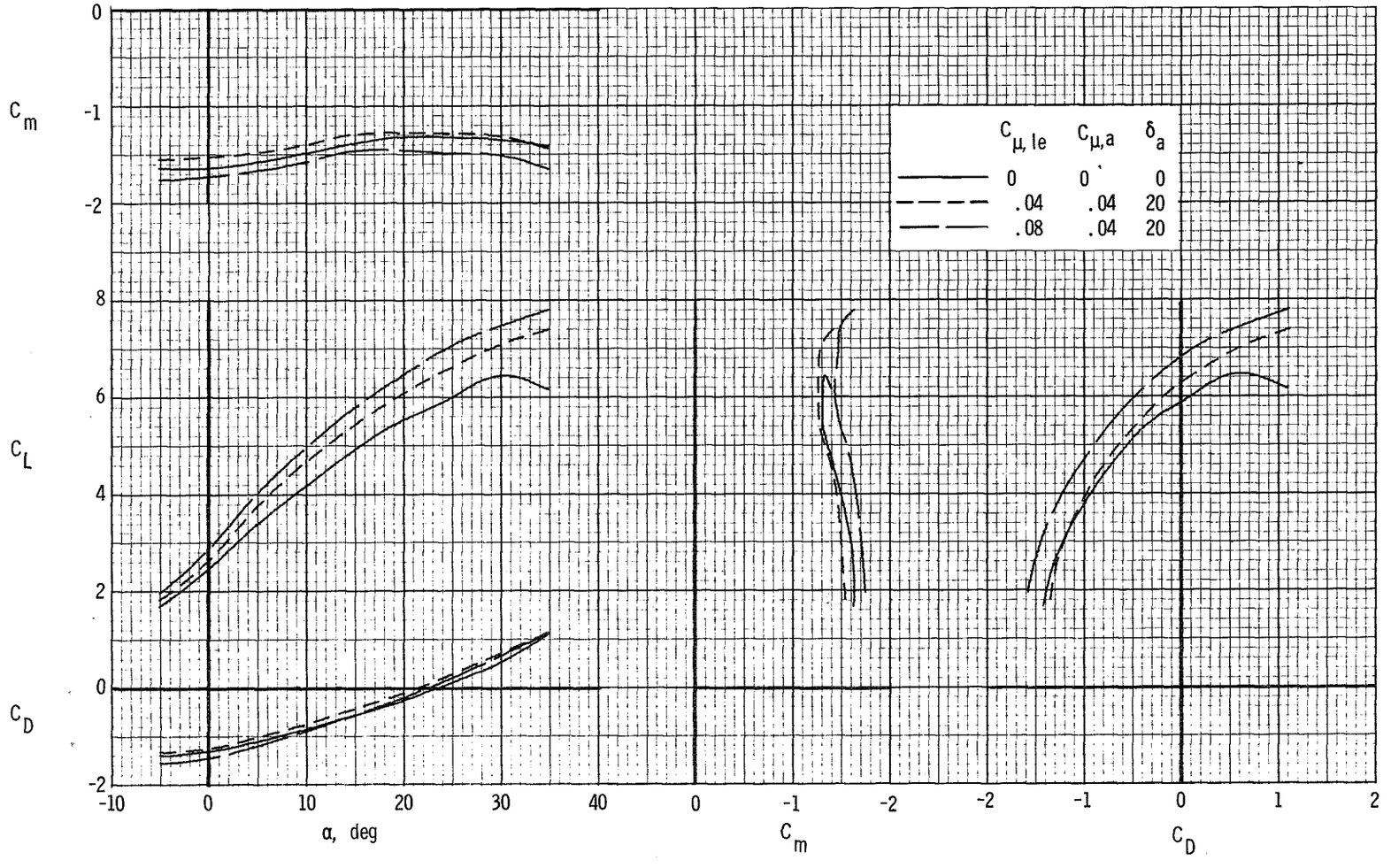

(b) $C_\mu = 2.0$.

Figure 49.- Continued.

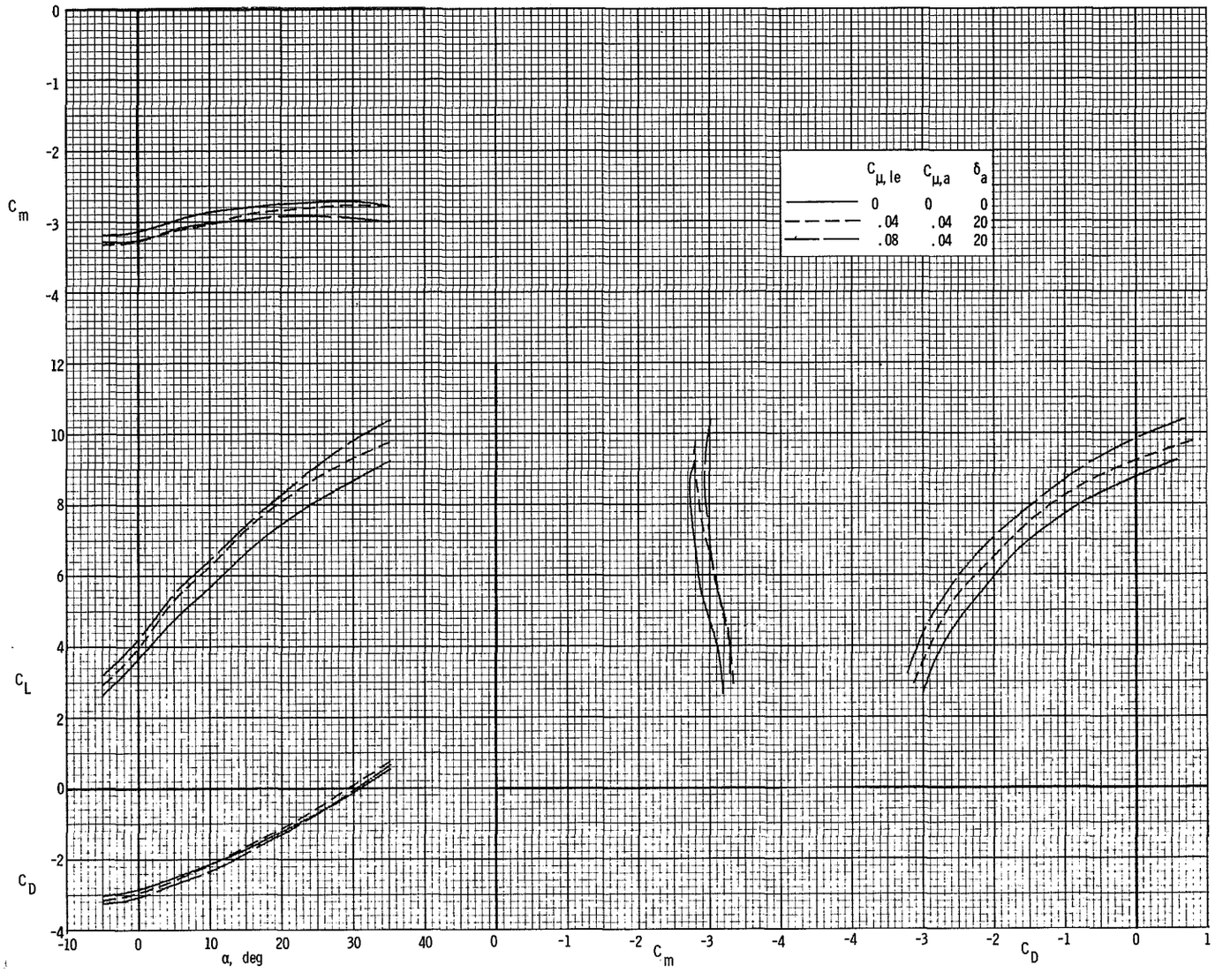

(c) C_μ = 4.0.

Figure 49.- Concluded.

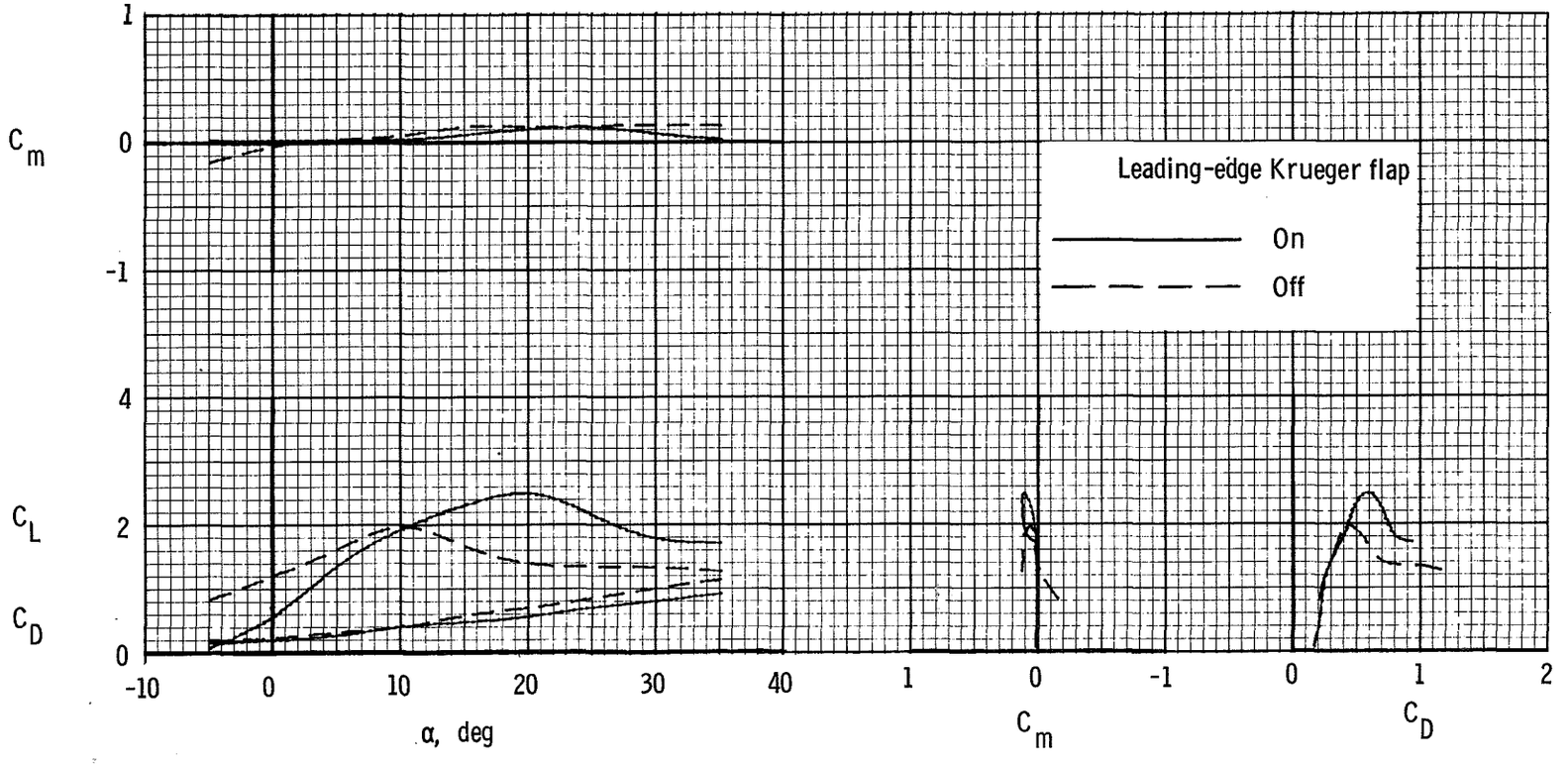

(a) $C_\mu = 0$.

Figure 50.- Effect of leading-edge Krueger flap on longitudinal characteristics of the model. $\delta_f = 40^o$.

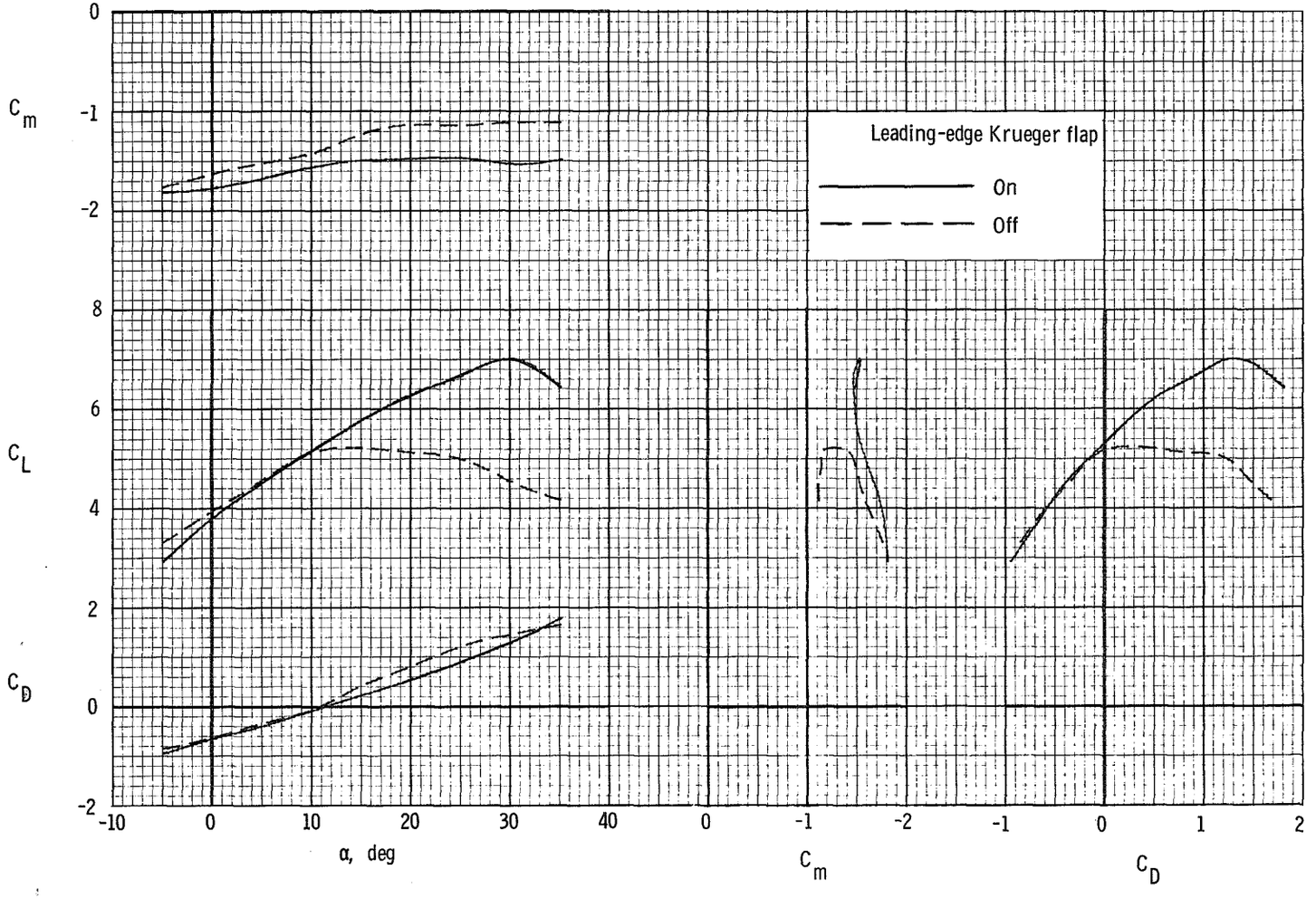

(b) $C_\mu = 2.0$.

Figure 50.- Continued.

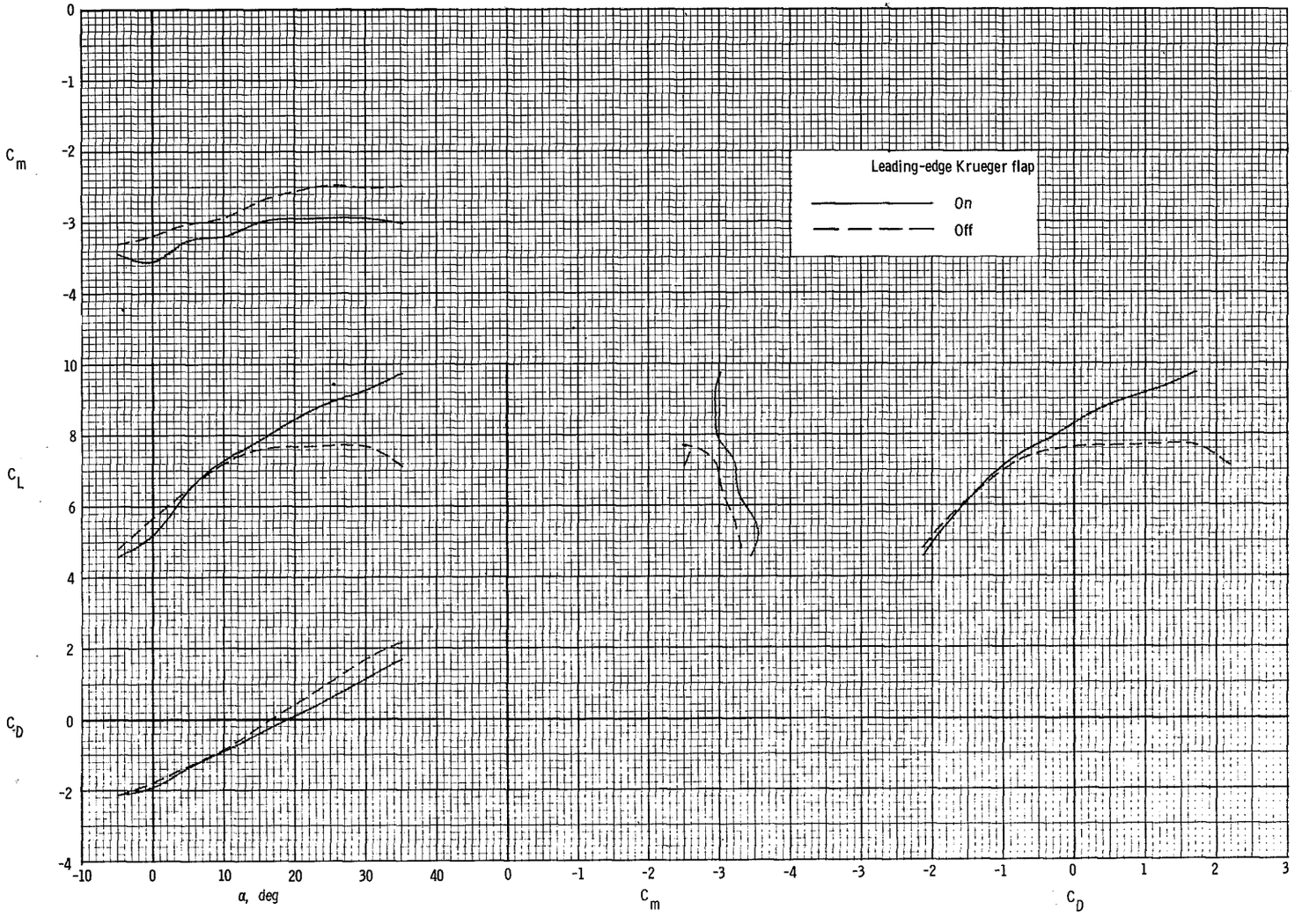

(c) $C_\mu = 4.0$.

Figure 50.- Concluded.

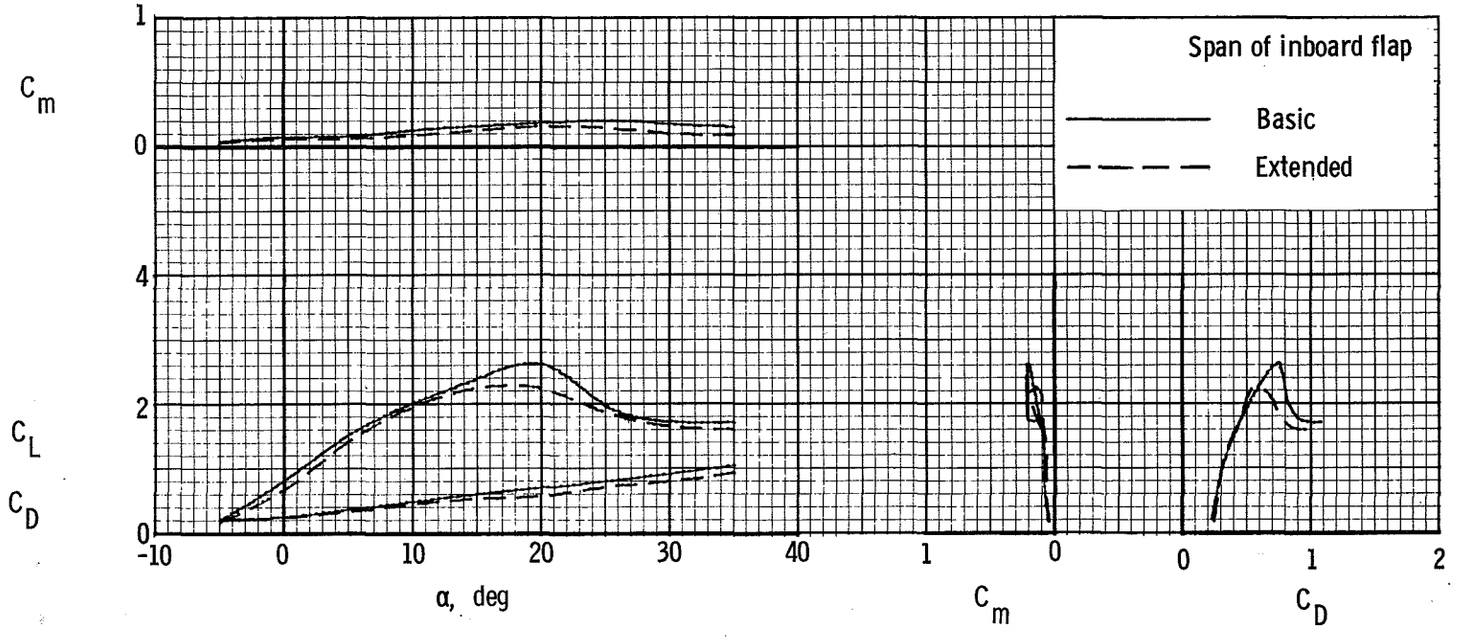

(a) $C_\mu = 0$.

Figure 51.- Effect of span of inboard flap on longitudinal characteristics of the model. $\delta_f = 60^o$.

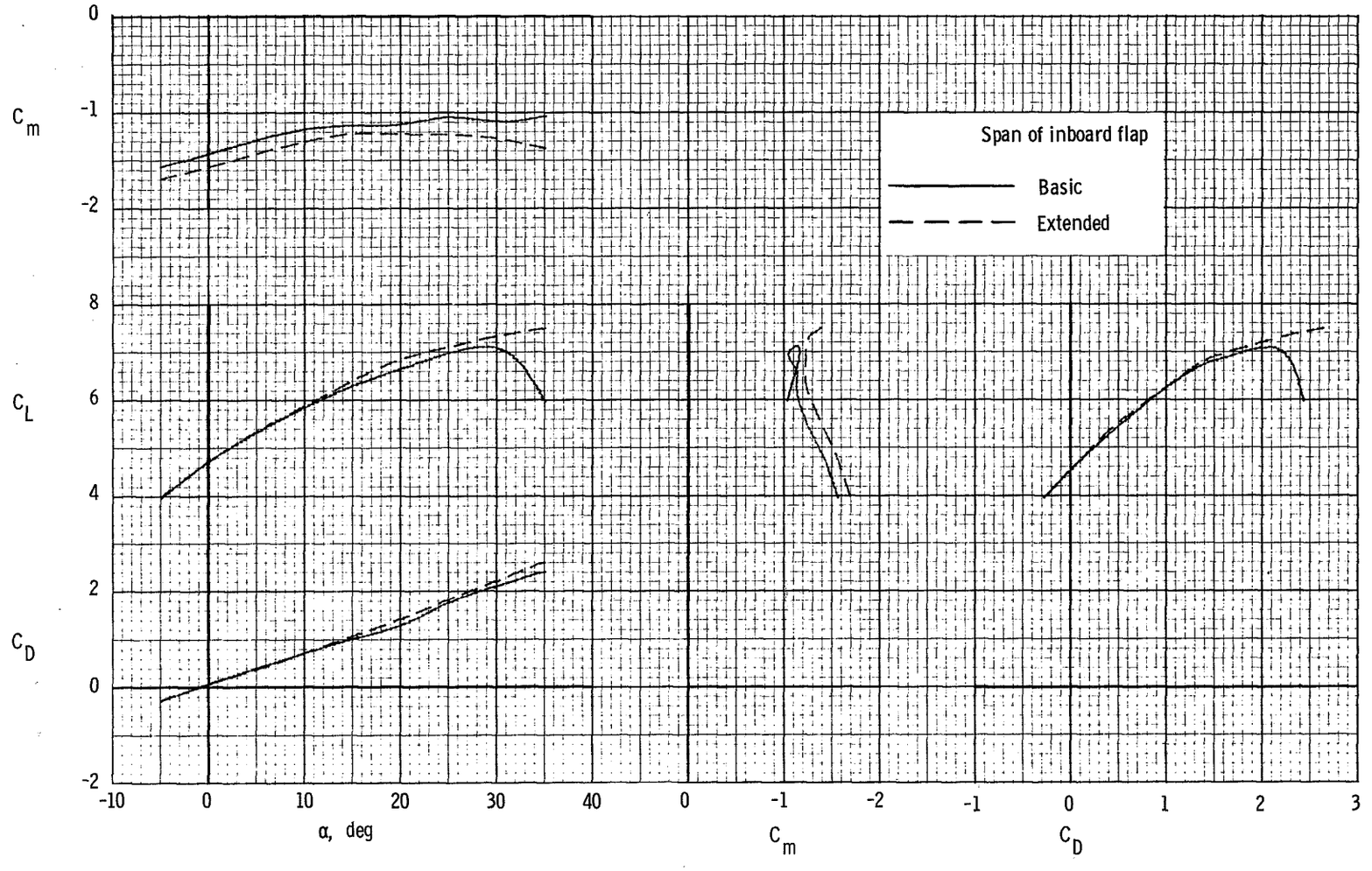

(b) $C_\mu = 2.0$.

Figure 51.- Continued.

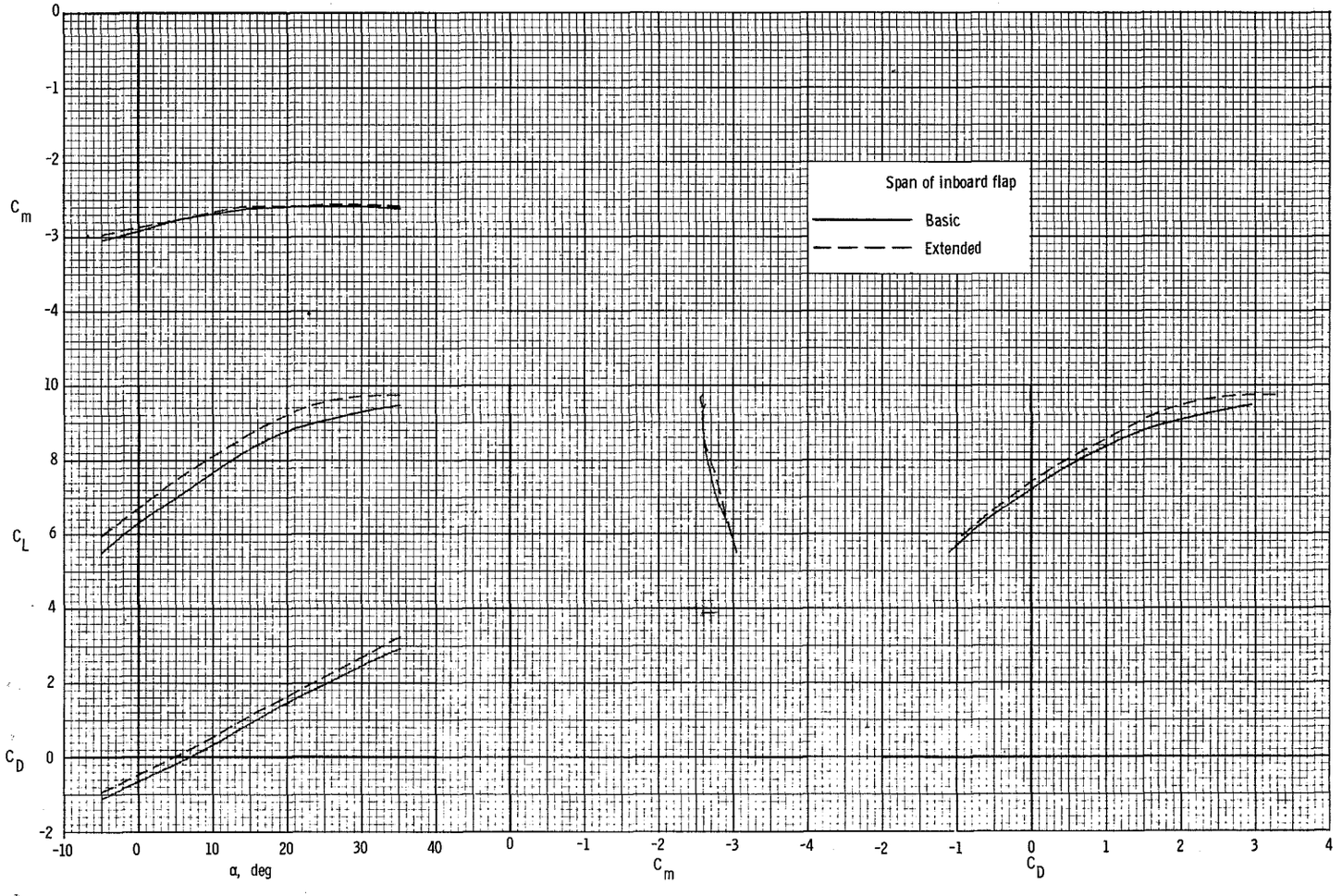

(c) $C_\mu = 4.0$.

Figure 51.- Concluded.

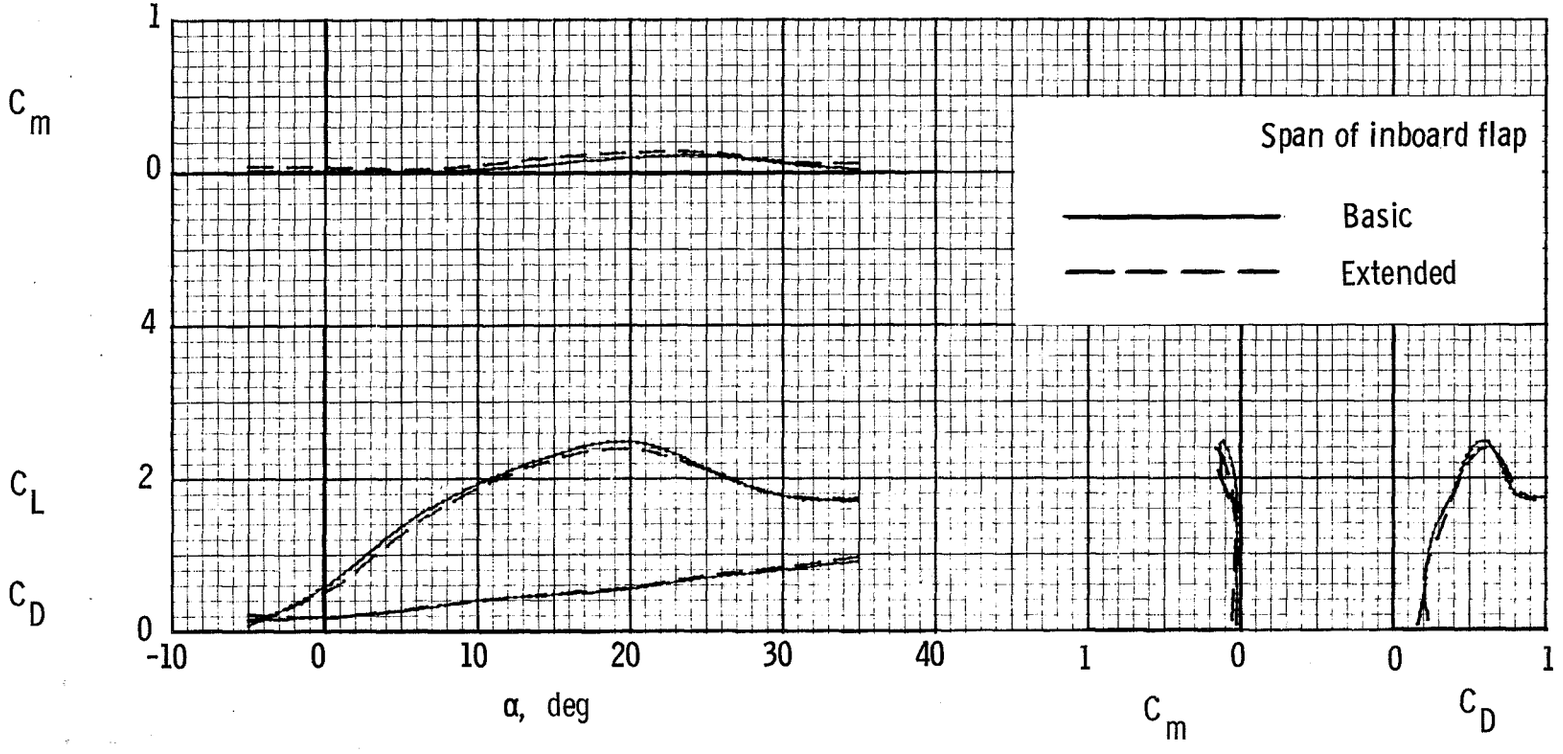

(a) $C_\mu = 0$.

Figure 52.- Effect of span of inboard flap on longitudinal characteristics of the model. $\delta_f = 40^o$.

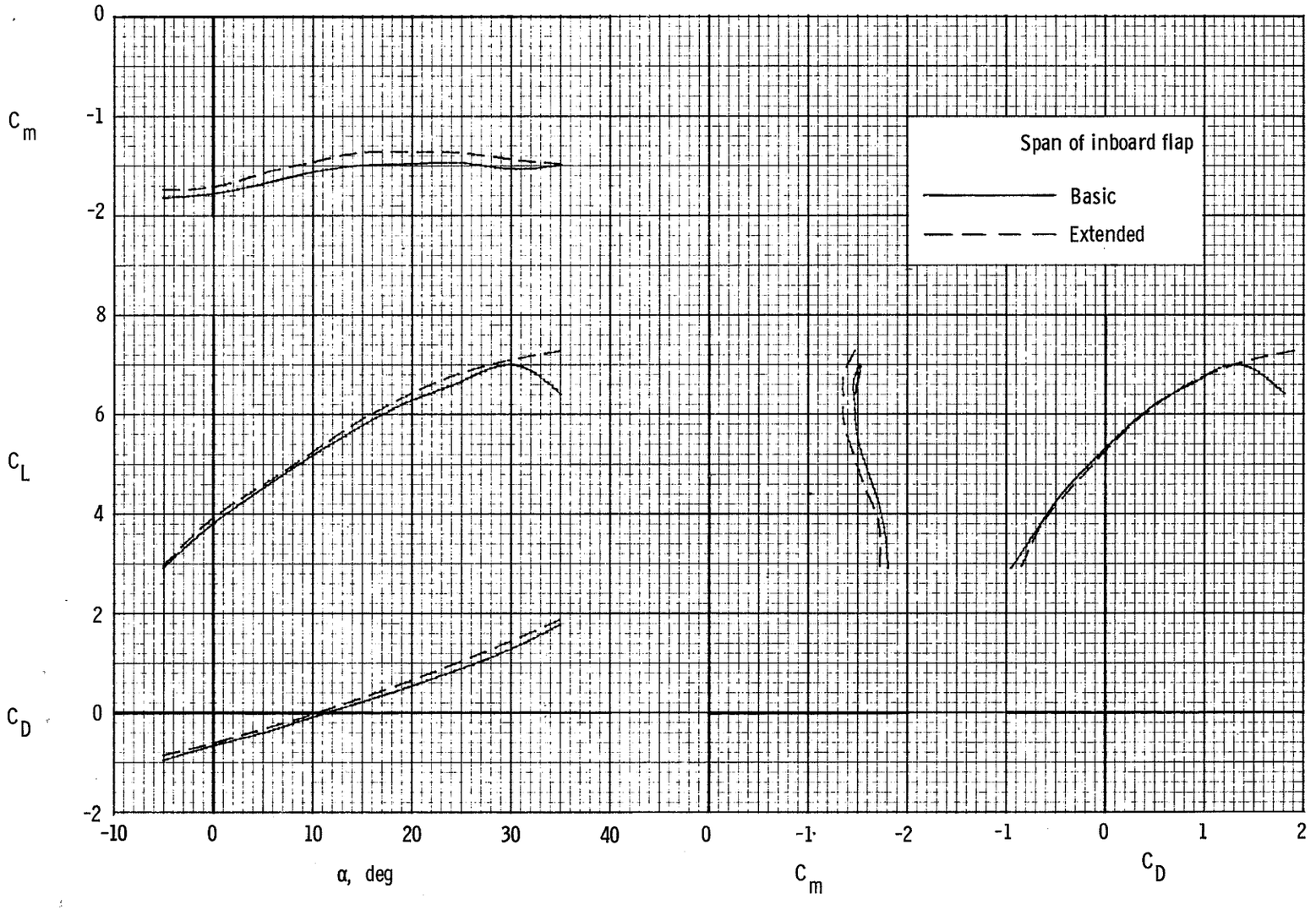

(b) $C_\mu = 2.0$.

Figure 52.- Continued.

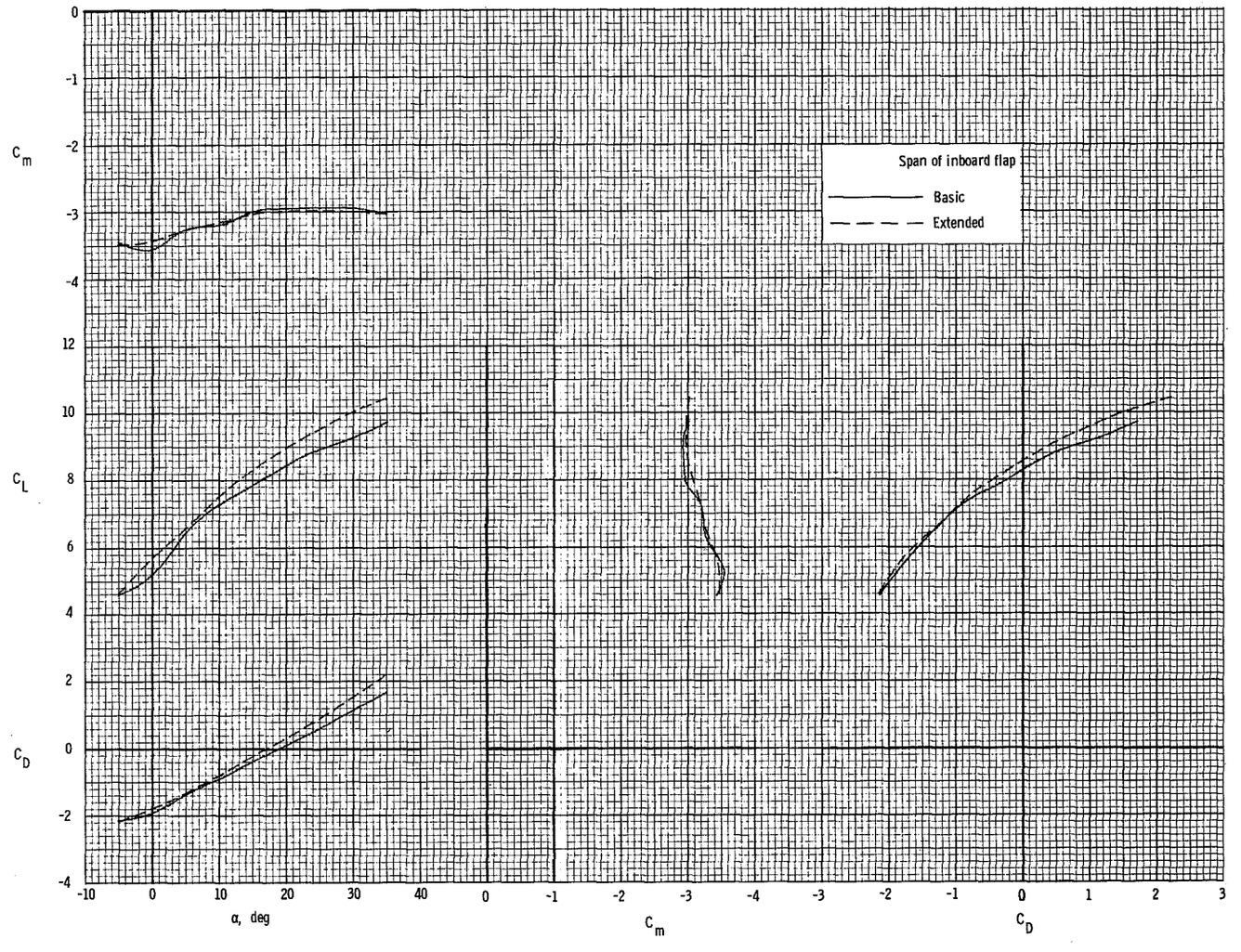

(c) $C_\mu = 4.0$.

Figure 52.- Concluded.

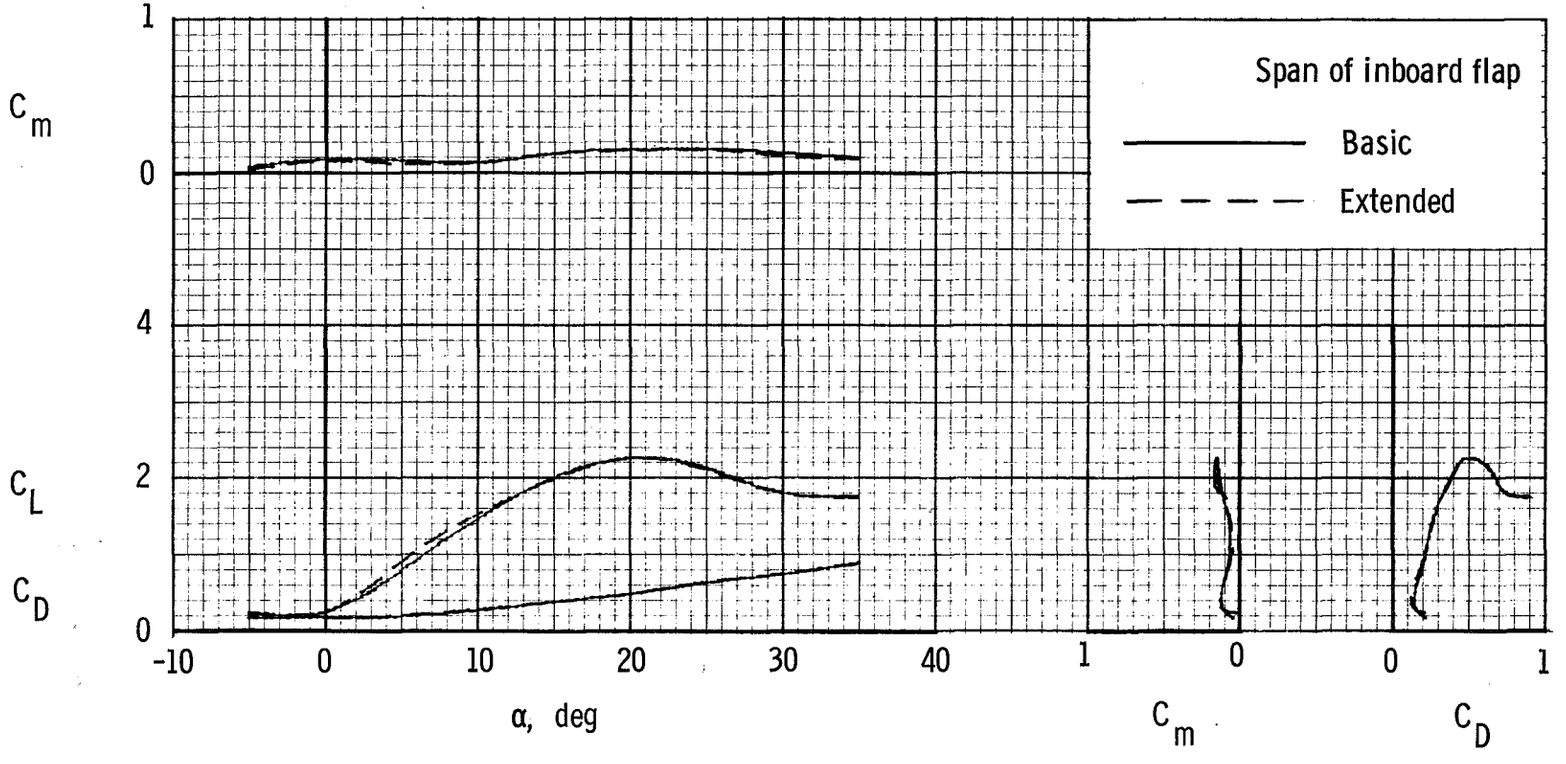

(a) $C_\mu = 0$.

Figure 53.- Effect of span of inboard flap on longitudinal characteristics of the model. $\delta_f = 20^o$.

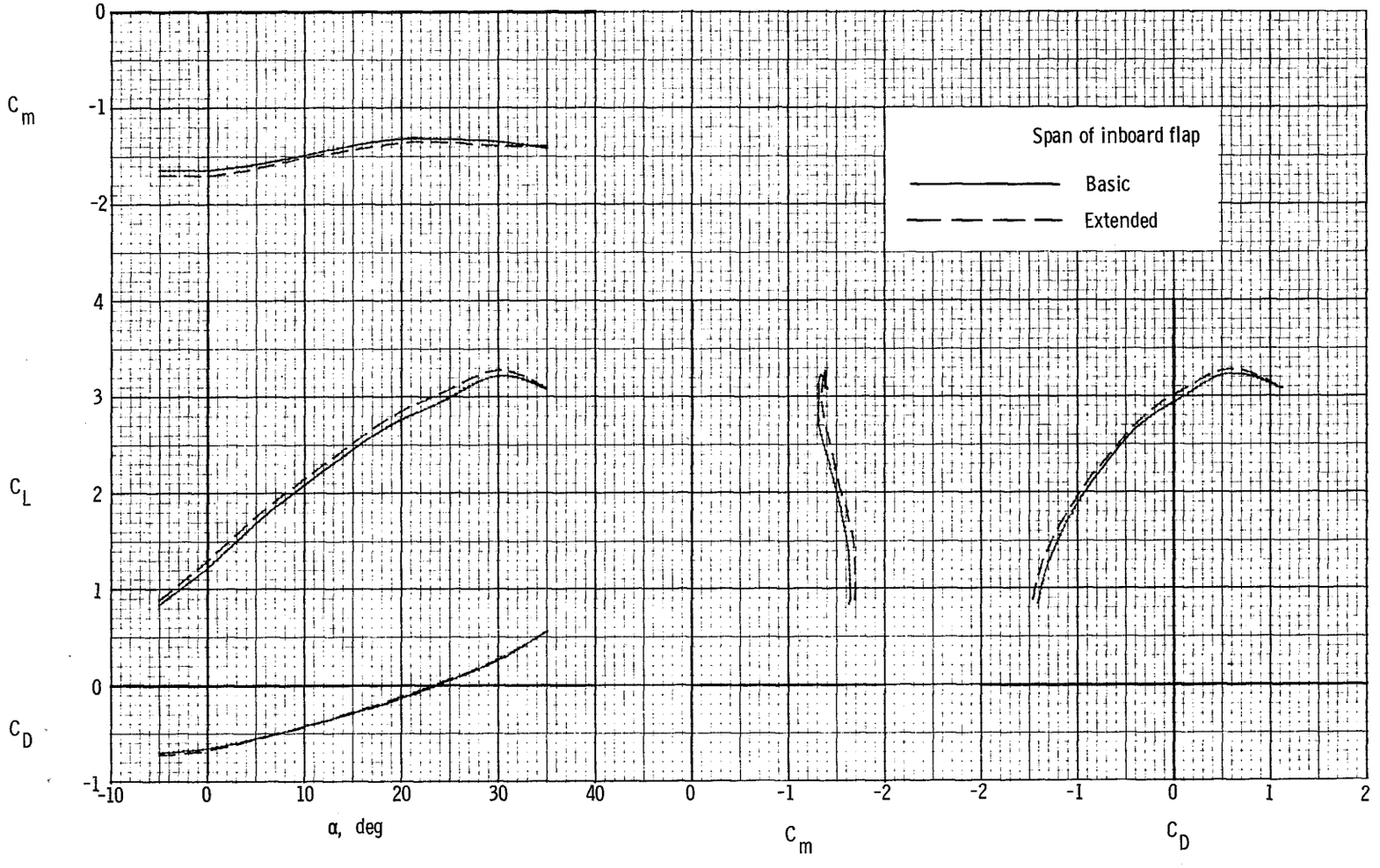

(b) $C\mu$ = 2.0.

Figure 53.- Continued.

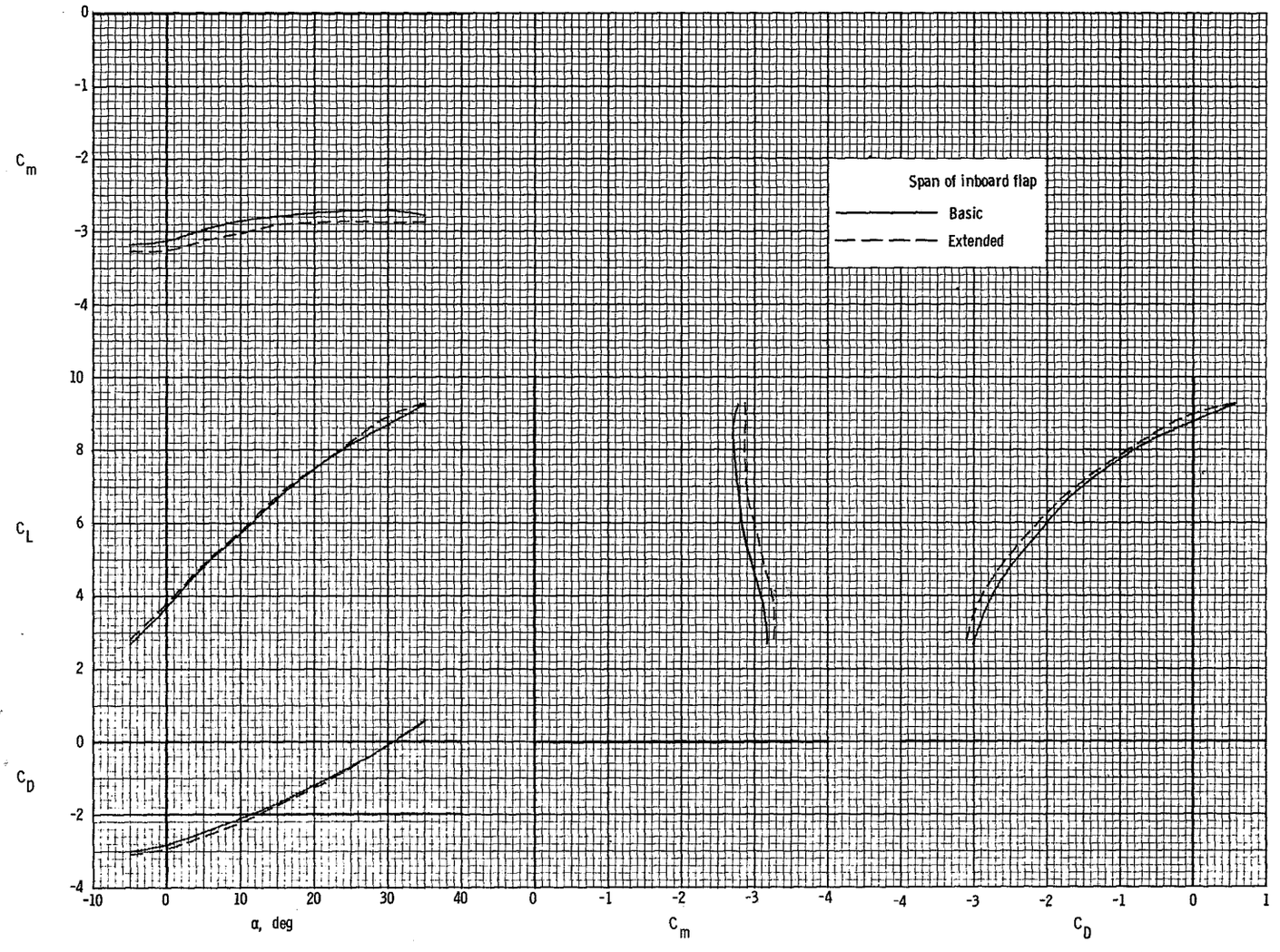

(c) $C_\mu = 4.0$.

Figure 53.- Concluded.

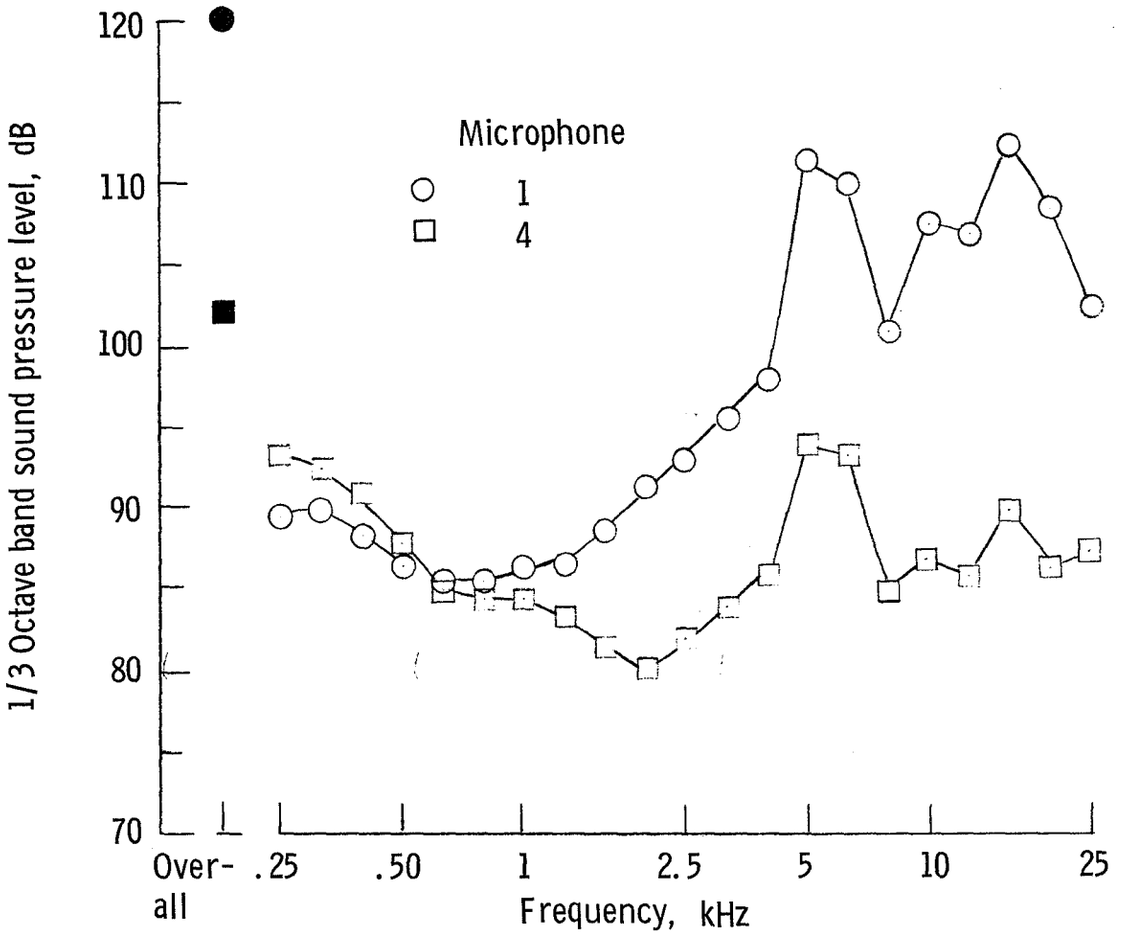

(a) Wind off.

Figure 54.- Comparison of noise measured above and below the wing. $\delta_f = 60^o$; $A_n = 2$; deflector 2; thrust, 1290 N (290 lb). (Solid symbols denote overall sound pressure levels.)

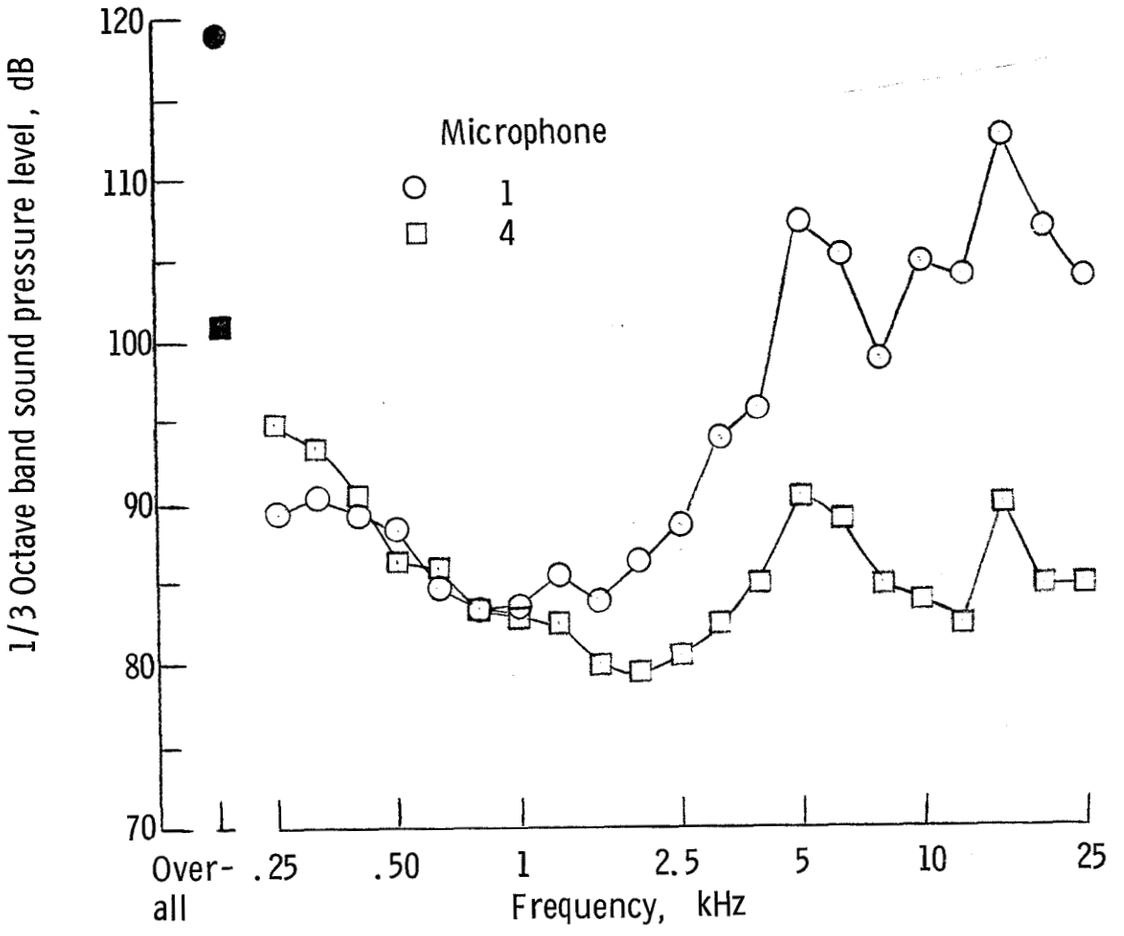

(b) Wind velocity, 7.72 m/sec (25.32 ft/sec).

Figure 54.- Continued.

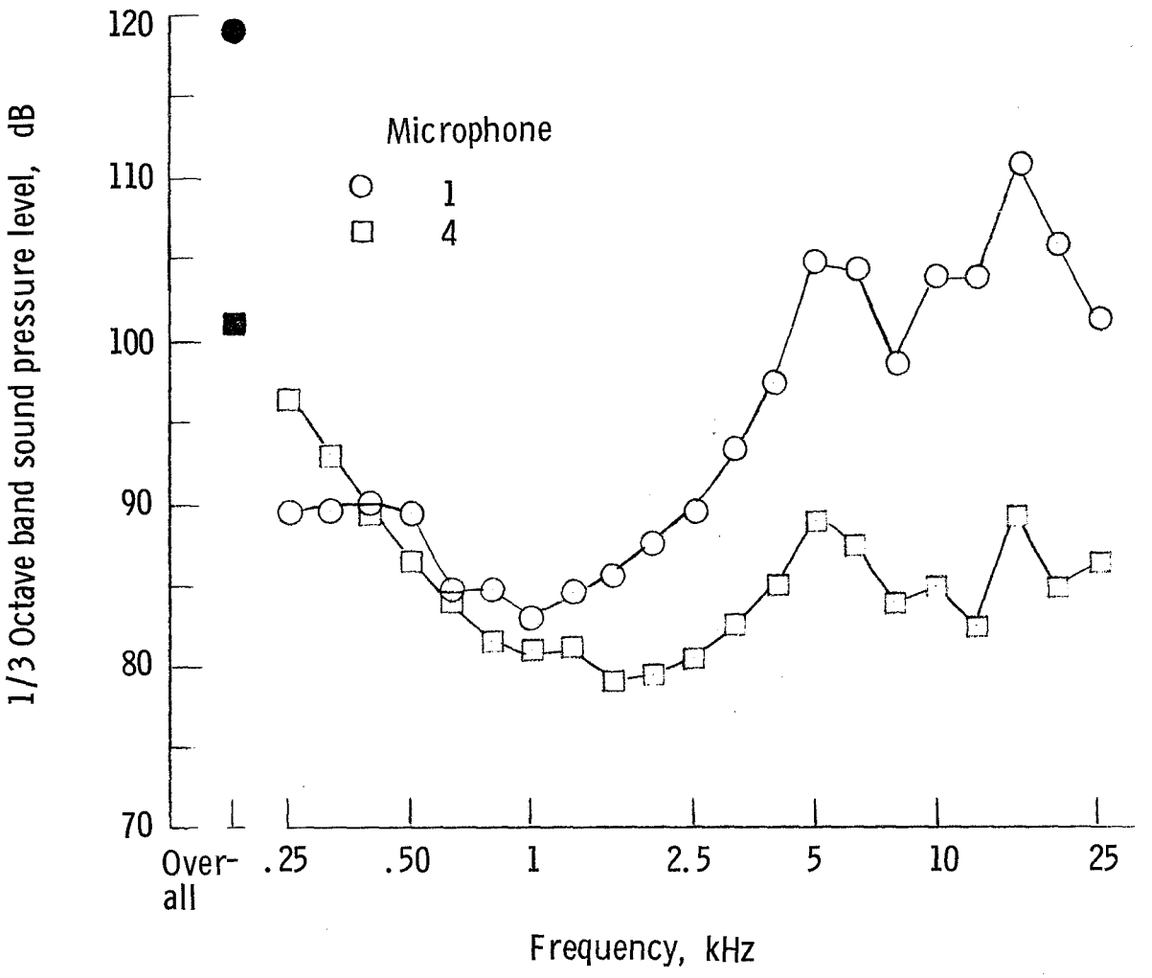

(c) Wind velocity, 15.43 m/sec (50.63 ft/sec).

Figure 54.- Concluded.

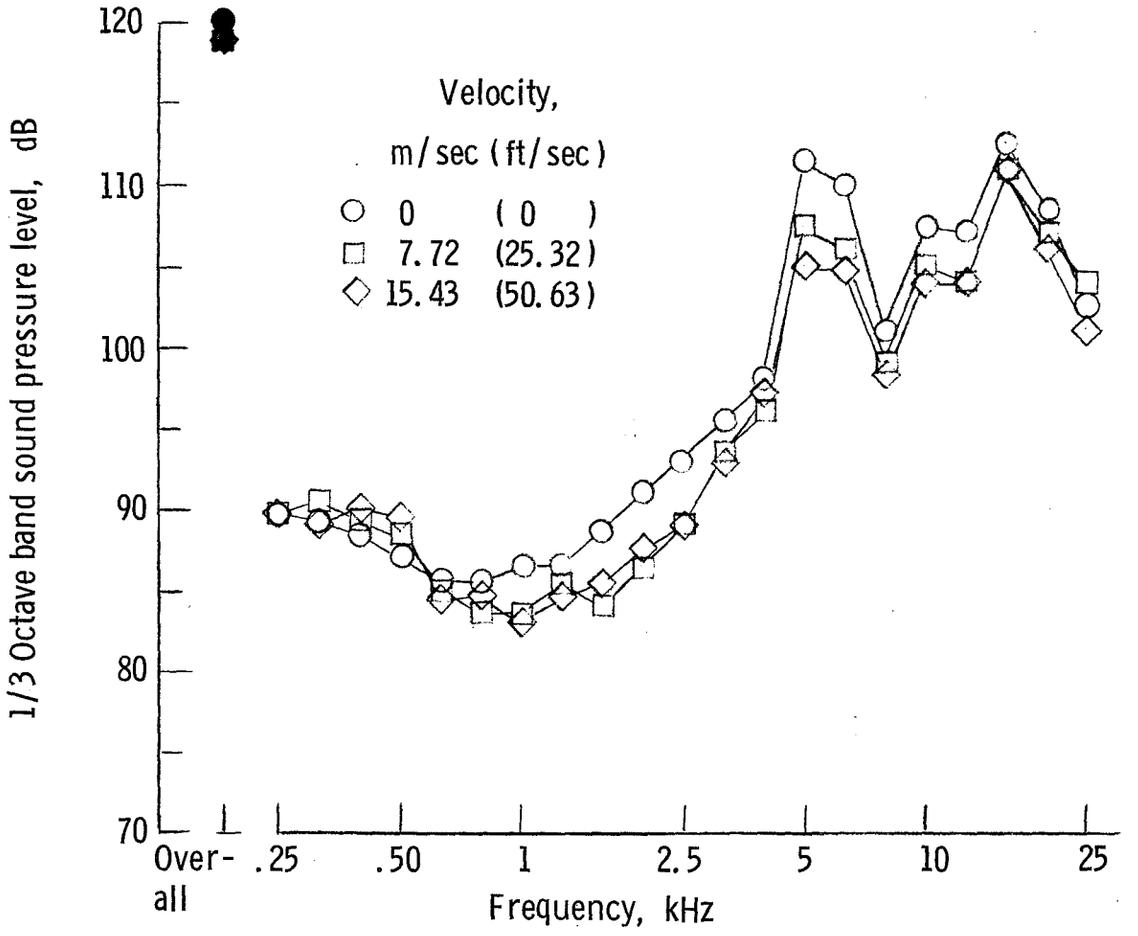

(a) Microphone 1 (above wing).

Figure 55.- Effect of forward speed on noise measured above and below the wing. $\delta_f = 60^o$; $A_n = 2$; deflector 2; thrust, 1290 N (290 lb). (Solid symbols denote overall sound pressure levels.)

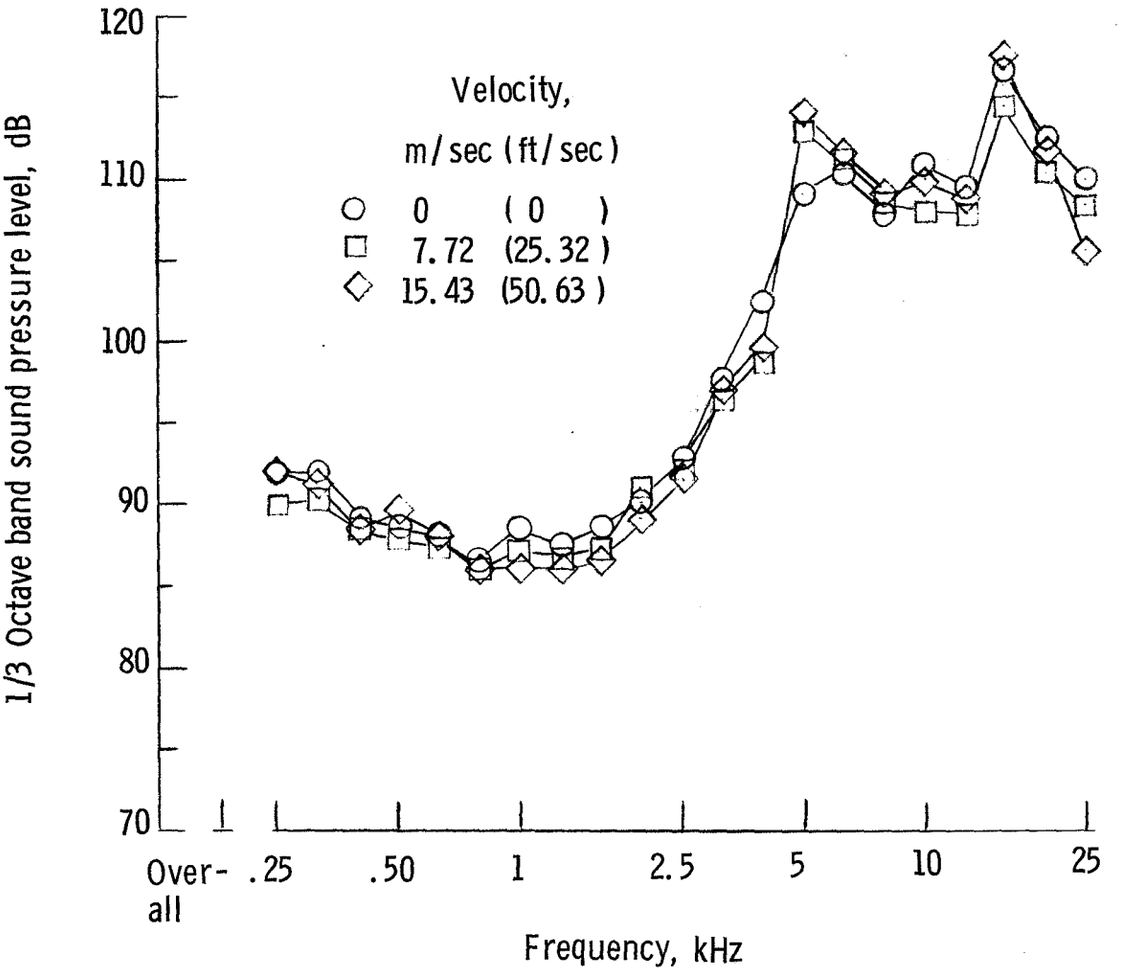

(b) Microphone 2 (above and behind wing).

Figure 55.- Continued.

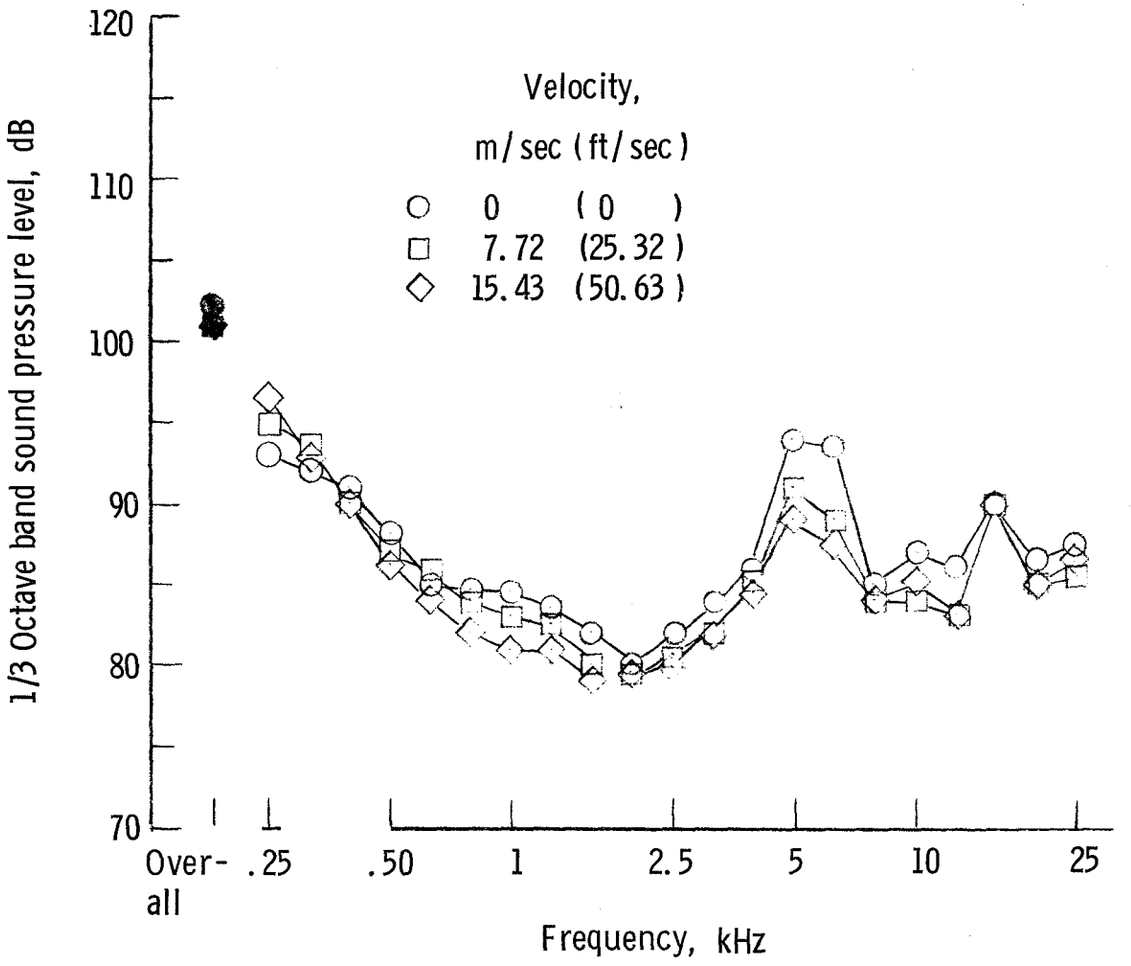

(c) Microphone 4 (below wing).

Figure 55.- Concluded.

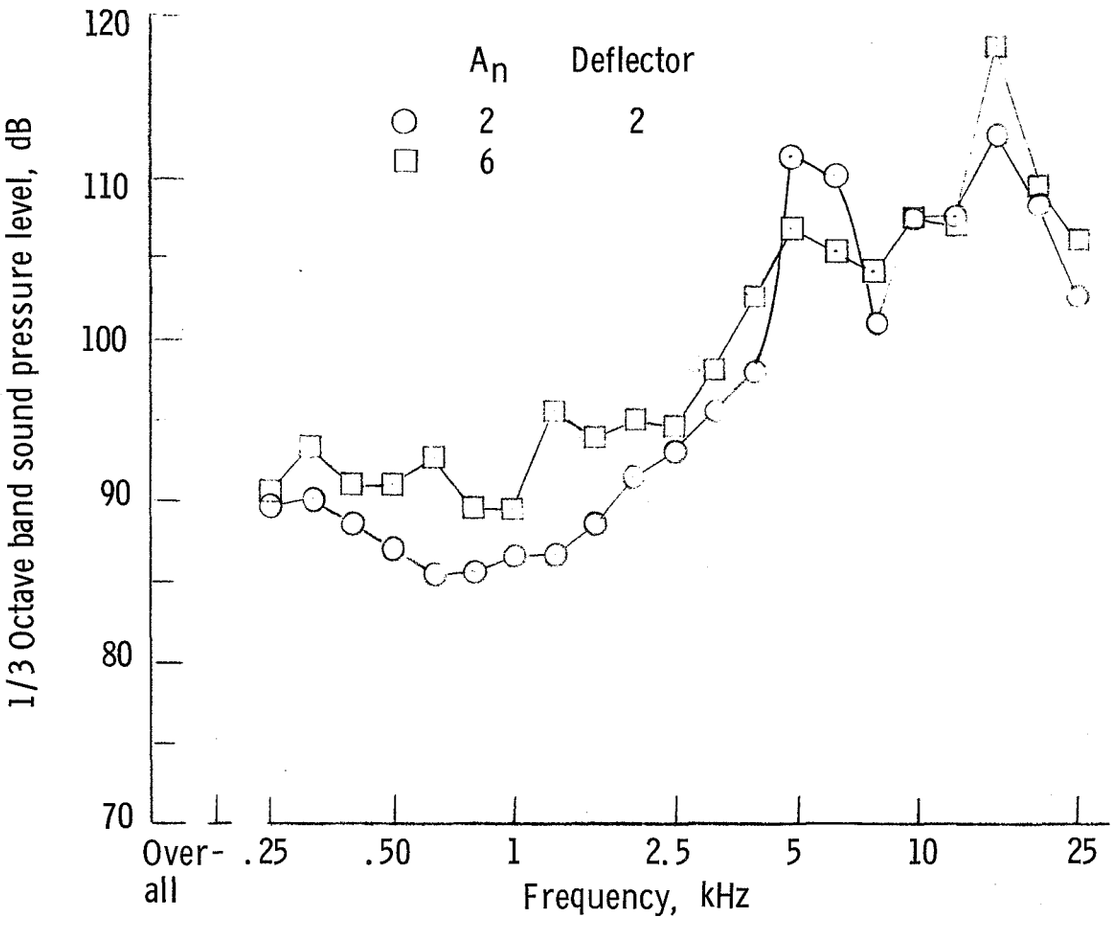

(a) Microphone 1 (above wing).

Figure 56.- Effect of nozzle geometry on noise measured above and below the wing. $\delta_f = 60^o$; wind off; thrust, 1290 N (290 lb). (Solid symbols denote overall sound pressure levels.)

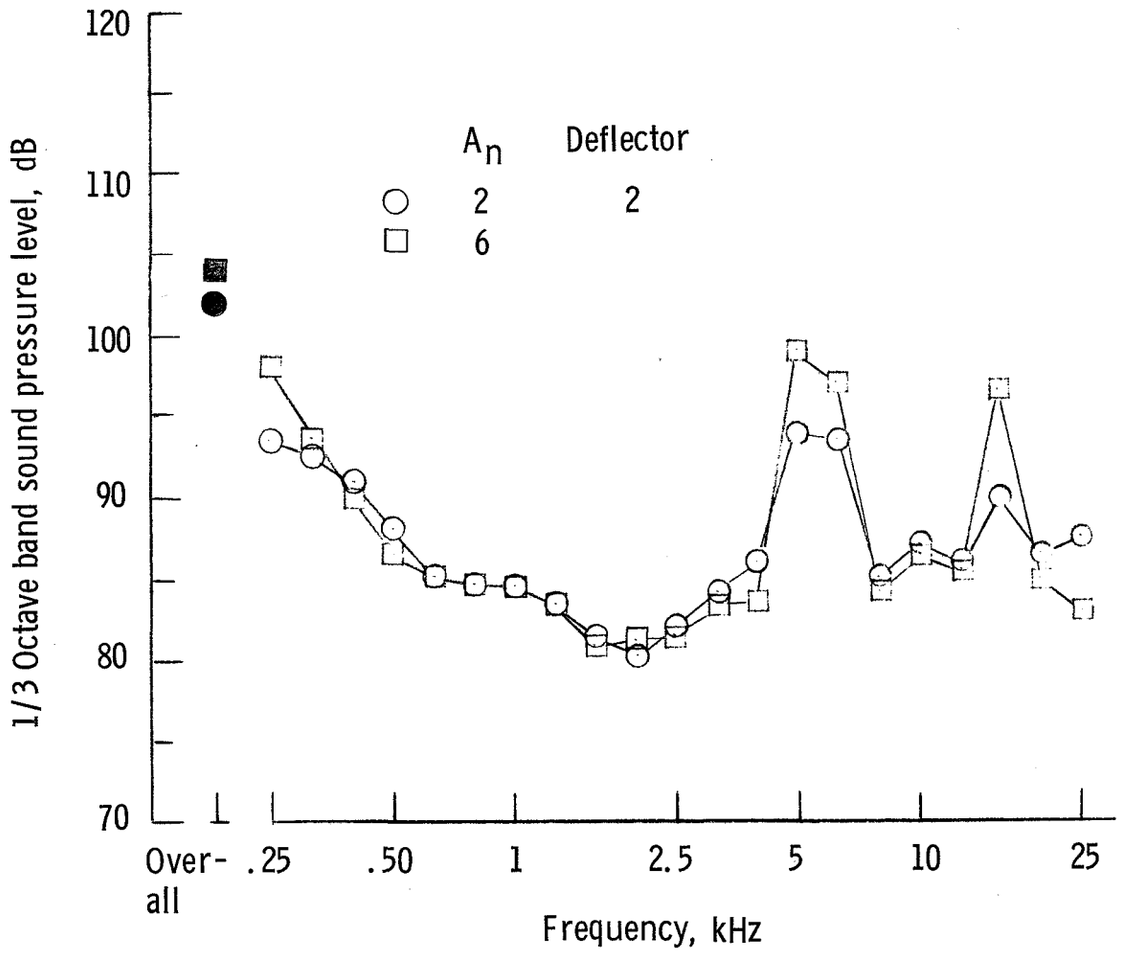

(b) Microphone 4 (below wing).

Figure 56.- Concluded.

NATIONAL AERONAUTICS AND SPACE ADMINISTRATION
WASHINGTON, D.C. 20546

OFFICIAL BUSINESS
PENALTY FOR PRIVATE USE $300

SPECIAL FOURTH-CLASS RATE BOOK

POSTAGE AND FEES PAID
NATIONAL AERONAUTICS AND SPACE ADMINISTRATION
451

U.S.MAIL

POSTMASTER: If Undeliverable (Section 158 Postal Manual) Do Not Return

"The aeronautical and space activities of the United States shall be conducted so as to contribute . . . to the expansion of human knowledge of phenomena in the atmosphere and space. The Administration shall provide for the widest practicable and appropriate dissemination of information concerning its activities and the results thereof."

—NATIONAL AERONAUTICS AND SPACE ACT OF 1958

NASA SCIENTIFIC AND TECHNICAL PUBLICATIONS

TECHNICAL REPORTS: Scientific and technical information considered important, complete, and a lasting contribution to existing knowledge.

TECHNICAL NOTES: Information less broad in scope but nevertheless of importance as a contribution to existing knowledge.

TECHNICAL MEMORANDUMS: Information receiving limited distribution because of preliminary data, security classification, or other reasons. Also includes conference proceedings with either limited or unlimited distribution.

CONTRACTOR REPORTS: Scientific and technical information generated under a NASA contract or grant and considered an important contribution to existing knowledge.

TECHNICAL TRANSLATIONS: Information published in a foreign language considered to merit NASA distribution in English.

SPECIAL PUBLICATIONS: Information derived from or of value to NASA activities. Publications include final reports of major projects, monographs, data compilations, handbooks, sourcebooks, and special bibliographies.

TECHNOLOGY UTILIZATION PUBLICATIONS: Information on technology used by NASA that may be of particular interest in commercial and other non-aerospace applications. Publications include Tech Briefs, Technology Utilization Reports and Technology Surveys.

Details on the availability of these publications may be obtained from:

SCIENTIFIC AND TECHNICAL INFORMATION OFFICE

NATIONAL AERONAUTICS AND SPACE ADMINISTRATION

Washington, D.C. 20546